

HIGH-SPEED ENDOSCOPIC OPTICAL COHERENCE TOMOGRAPHY AND
ITS APPLICATIONS

by
Jiefeng Xi

A dissertation submitted to Johns Hopkins University in conformity with the
requirements for the degree of Doctor of Philosophy

Baltimore, Maryland

April, 2014

© 2014 Jiefeng Xi
All Rights Reserved

Abstract

Optical coherence tomography (OCT) is a real-time high-resolution imaging technology providing cross-sectional images of biological structures at a resolution of <1 to $20\ \mu\text{m}$ and a penetration depth of 1 to 3 mm in most highly scattering tissues. OCT is in general non-invasive and can perform real-time ‘optical biopsy’ with a resolution approaching standard low magnification histopathology but without tissue removal. Conventional OCT requires a bulky imaging probe, which limits most of the *in vivo* applications to ophthalmology and dermatology. The development of miniature OCT imaging probe has greatly expanded the scope of the applications (e.g., cardiology, gastroenterology, etc.). Recent technical advances in OCT has extended the imaging speed from a few kHz to a few hundreds kHz, enabling *in vivo* three-dimensional (3D) imaging.

This dissertation describes the development of a high-speed endoscopic OCT imaging system. The system employs the Fourier domain mode locking laser technology at a wavelength range of 1300 nm to reach an axial resolution of $9.7\ \mu\text{m}$ and an A-scan rate of 220 kHz. A Mach-Zehnder interferometer setup is used to achieve shot-noise limited detection. A generic OCT software platform is developed for data acquisition, processing, display, storage, and 3D visualization. Miniature OCT imaging probes are designed and fabricated for *in vivo* 3D OCT imaging. The utility of the high-speed endoscopic OCT system is demonstrated for clinical and basic researches in pulmonology and

gastroenterology. In addition, an ultrahigh-resolution endoscopic OCT system is developed at a wavelength range of 800 nm to reach an axial resolution of 3.0 μm and an A-scan rate of up to 20 kHz. Furthermore, a novel type of OCT contrast agents, scattering dominant gold nanocages, is developed with the aid of a cross-reference OCT imaging method. Finally, a multimodal endoscopic imaging system combines 1300 nm *en face* OCT and 1550 nm two photon fluorescence is developed.

Compared with most of other imaging modalities, high-speed endoscopic OCT has unmatched advantages including high spatial resolution, imaging speed, and non-invasiveness / minimal invasiveness. The results in this dissertation suggest that high-speed endoscopic OCT may has a great impact on healthcare as well as basic research.

To my family

Intended to be blank

ACKNOWLEDGMENTS

First and foremost, I would like to thank my research advisor, Dr. Xingde Li, for providing me with this opportunity to conduct my Ph.D. work in the Biophotonics Imaging Technologies (BIT) laboratory at the University of Washington and the Johns Hopkins University in the past eight years. None of this could be accomplished without the help and guidance of Dr. Li. He offered me the opportunities to take part in various different research projects. His endless patience, challenges and advice have expanded the horizon of my knowledge and experiences in this multi-disciplinary field. To my thesis committee members, Dr. Wayne Mitzner, Dr. Daniel Herzka, and Dr. Kristine Glunde, I thank you for thoughtful input and advice.

None of my work can be done without the group members who paved the road before me. I would like to thank Dr. Yuxing Leng for introducing me into the world of swept source OCT and passing on all the secrets of a swept source OCT. Henry Fu showed me the fabrication of an OCT imaging probe and helped me make my first one. I would like to thank Dr. Michael J. Cobb for all the helps on electronics and hardware components. The well-organized documents helps me a lot when I first took over his work. Daniel J. MacDonald's software greatly inspired me when I wrote the software code for OCT imaging.

Most of my works are made possible by collaborating with other group members. I owe my great gratitude to Dr. Li Huo, who taught me a lot in fiber optics. Without his mentorship and generous help, several technical challenges in the laser and OCT system are impossible to be solved. I am grateful for the work of Drs. Yicong Wu and Yuying Zhang in development of the multimodal system. I think Dr. Yongping Chen for the animal preparation and the synthesis of gold nanocages. It has also been a pleasure working with Jessica Mavadia, Huiquan Wang, Carmen Kut, Wenxuan Liang. Their support and sense of humor helped me go through the tough times of my Ph. D. study.

Collaboration with outside the group is also essential in all of my works. For upper GI imaging on large animals, I would like to thank Drs. Joo Ha Hwang, Melissa Upton at the University of Washington and Drs. Marcia Canto, Eun Ji Shin at the Johns Hopkins University. I would also like to thank Dr. Shaoyong Yu and Zhenyu Liu for their guinea pig model. The ultrahigh resolution endoscopic OCT imaging would not happen without their generous help. For lower airway imaging, I would like to thank Drs. Rex Yung, Wayne Mitnzer, and Robert Brown for their guidance, all the time and efforts they put into this project. Technical support is sometimes negligible but critical. For that, I thank Laurie Pipitone, Mingying Zheng, Jeff Magula, and Jay Burns. Laurie and Mingying organized the animal studies so well that the experiments almost went smoothly every time. Without Jeff and Jay, none of the OCT imaging probes can be fabricated.

I would like to thank our Ph.D. program coordinator, Hong Lan for her great help in my Ph.D. program transition and generous guidance on being a Ph.D. student.

Finally, I save my last and most appreciative thanks for my family for supporting me during this long journey of eight years. I thank my wife Jing Chen for supporting and believe in me unconditionally even when there were doubts and complaints from others. My son Max is able to make my day no matter what I go through outside. I would also like to thank my parents for encouraging me in pursuit of science and engineering and their support in everyday life.

Intended to be blank

TABLE OF CONTENTS

TABLE OF CONTENTS.....	x
LIST OF FIGURES	xv
LIST OF TABLES	xx
Chapter 1 Introduction	1
1.1 Overview	1
1.2 Endoscopic Medical Imaging.....	3
1.2.1 Surface Optical Endoscopy.....	4
1.2.2 Ultrasonic Endoscopy	6
1.3 Optical Coherence Tomography and Optical Biopsy	6
1.3.1 Brief History of Optical Coherence Tomography	7
1.3.2 Applications of Optical Coherence Tomography	9
1.3.3 Optical Biopsy and Optical Coherence Tomography Endoscopy	10
1.4 Scope of Dissertation	12
Chapter 2 Theory of Optical Coherence Tomography	15
2.1 Introduction	15
2.2 Low Coherence Interferometry	16
2.3 Time Domain Optical Coherence Tomography.....	17
2.3.1 Time Domain OCT Axial Scan Signal [90].....	18
2.3.2 Key Parameters: Axial Resolution, Dispersion Mismatch, Lateral Resolution, Side Lobes, Imaging Depth and Detection Sensitivity.....	20
2.3.3 Disadvantages	24
2.4 Fourier Domain Optical Coherence Tomography.....	25
2.4.1 Fourier Domain OCT Axial Scan Signal [97]	27
2.4.2 Key Parameters: Axial Resolution, Lateral Resolution, Side Lobes, Imaging Depth, Detection Sensitivity and Its Roll-off	28
2.4.3 Comparison between SD-OCT and SS-OCT.....	30
2.5 Summary	32
Chapter 3 Overview of an Endoscopic Optical Coherence Tomography System	33
3.1 Introduction	33

3.2	Choice of Broadband Light Source	34
3.3	Choice of OCT Interferometer Setup	36
3.4	Choice of Miniature OCT Imaging Probe	40
3.5	Summary	44
Chapter 4 High-speed OCT Laser Engine — Fourier Domain Mode-locking Laser		45
4.1	Basic Principles of Wavelength Swept Laser	45
4.1.1	Conventional Wavelength Swept Laser	46
4.1.2	Fourier Domain Mode-locking Laser	49
4.1.3	Buffered Fourier Domain Mode-locking Laser	52
4.2	Design of a Double-buffered Fourier Domain Mode-locking Laser	55
4.2.1	Tunable filter and its Driver	55
4.2.2	Optical Cavity Design	59
4.2.3	Optical Time Multiplexing Design	61
4.2.4	Performance of the double-buffered FDML	62
4.3	Future Improvement	64
4.4	Summary	65
Chapter 5 OCT Interferometers and Detection Electronics		67
5.1	OCT Interferometers	67
5.2	Shot-noise Limited Detection	69
5.3	Real-time Uniform K-space Sampling Method	70
5.3.1	Principle and Method	72
5.3.2	Performance and Results	79
5.4	Summary	82
Chapter 6 High-speed Optical Coherence Tomography Software Platform		83
6.1	Software Platform and High-speed Data Rate Management	83
6.2	Data Acquisition	87
6.3	Data Processing and Display	88
6.3.1	Data Processing Algorithm on GPU	89
6.3.2	Data Display Module on GPU	94
6.4	Data Storage	96

6.5	Summary	98
Chapter 7 Side-viewing Optical Coherence Tomography Imaging Probe		99
7.1	Introduction	99
7.2	Distal End Optical Design of OCT Imaging Probes	100
7.3	Short Working Distance OCT Imaging Probe	103
7.3.1	Paraxial Model	103
7.3.2	Zemax Model	108
7.3.3	Fabrication Steps and Tolerance	110
7.3.4	Proximal End	113
7.4	Large Working Distance OCT Imaging Probe.....	114
7.4.1	Paraxial Model	114
7.4.2	Zemax Model	115
7.4.3	Astigmatism Correction	116
7.4.4	Fabrication Steps and Tolerance	119
7.5	Summary	121
Chapter 8 Endoscopic Optical Coherence Tomography in Lower Airway Imaging		123
8.1	Background and Introduction.....	123
8.2	Material and Methods.....	125
8.2.1	High-speed Endoscopic OCT System.....	125
8.2.2	Animal Protocols	126
8.3	Results	128
8.3.1	In vivo Endoscopic OCT Images of Swine Lower Airways.....	128
8.3.2	Correlation between in vivo OCT images and ex vivo Histopathology ...	131
8.3.3	Dynamic OCT Imaging of Swine Lower Airways	136
8.4	Summary	138
Chapter 9 Endoscopic Optical Coherence Tomography in Upper Gastrointestinal Tract Imaging		139
9.1	Background and Introduction.....	139
9.2	Material and Methods.....	142
9.2.1	High-speed Endoscopic OCT System.....	142

9.2.2	Animal Protocols	144
9.3	Results	145
9.3.1	Endoscopic OCT Esophageal Imaging	145
9.3.2	In vivo Assessment of Cryoablation on Normal Pig Esophagus – A Pilot Study	148
9.3.3	In vivo Assessment of Esophageal Structures in a Guinea Pig Model of Eosinophilic Esophagitis.....	150
9.4	Summary	152
Chapter 10 Ultrahigh Resolution Endoscopic Optical Coherence Tomography Imaging		153
10.1	Introduction	153
10.2	Ultrahigh Resolution Endoscopic OCT System	154
10.2.1	Light Source and Interferometer	154
10.2.2	Linear-in-wavenumber Spectrometer	157
10.2.3	Diffractive Imaging Probe for Ultrahigh Resolution OCT Imaging.....	158
10.3	Results	164
10.3.1	In vivo Endoscopic OCT Esophageal Imaging.....	164
10.3.2	Ex vivo Endoscopic OCT Bronchus Imaging.....	168
10.4	Summary.....	169
Chapter 11 OCT Contrast Enhancement and Endoscopic Multi-modal Imaging		171
11.1	Gold Nanocages as Optical Coherence Tomography Contrast Agent	171
11.1.1	Introduction.....	171
11.1.2	Characterizing Optical Properties by Using Cross-referencing OCT Imaging	173
11.1.3	Scattering-dominant Gold Nanocages	180
11.1.4	Contrast Enhancement of Gold Nanocages	183
11.2	Endoscopic Multi-modal Imaging System: Two-photon Fluorescence and Optical Coherence Tomography.....	185
11.2.1	Introduction.....	185
11.2.2	Endoscope Design.....	186
11.2.3	System Description.....	187

11.2.4	Results.....	189
11.3	Summary.....	193
Chapter 12	Conclusion and Future Perspective	195
12.1	Summary of Thesis Work.....	195
12.2	Future Work.....	198
Appendix A	DDSCAT	201
A.1.	Introduction	201
A.2.	Compilation of DDSCAT 7.0.....	201
A.3.	Applicability of DDSCAT 7.0	202
A.4.	Parameter File of DDSCAT 7.0	203
A.4.1	An example of ddscat.par	203
A.4.2	Explanation of Key Parameters in ddscat.par	205
Bibliography	207
CURRICULUM VITAE	225

LIST OF FIGURES

Figure 1.1 Plot of resolution and penetration depth of the medical imaging modalities....	3
Figure 2.1 Low coherence Michelson interferometer.....	17
Figure 2.2 Schematic of a time domain optical coherence tomography system.....	18
Figure 2.3 Schematics of a spectral domain and a swept source optical coherence tomography system.	26
Figure 3.1 Block schematic of a high-speed endoscopic OCT imaging system.....	33
Figure 3.2 Schematic of fiber optical Michelson interferometer.....	37
Figure 3.3 Schematic of fiber optical modified Michelson interferometer.	37
Figure 3.4 Schematic of fiber optical Mach-Zehnder interferometer.	39
Figure 3.5 Simplified schematics of forward-viewing OCT imaging probe.	42
Figure 3.6 Simplified schematic of side-viewing OCT imaging probe.....	43
Figure 4.1 Simplified schematic of a conventional wavelength swept laser.	46
Figure 4.2 Simplified schematic of a Fourier domain mode locking laser.....	49
Figure 4.3 Simplified schematic of a buffered Fourier domain mode locking laser.	53
Figure 4.4 Schematic of a double buffered Fourier domain mode locking laser.....	54
Figure 4.5 Mechanical frequency response of the Fabry-Perot tunable filter.....	56
Figure 4.6 Schematic of tunable filter driver.....	57
Figure 4.7 Photos of PCB board of the tunable filter driver.	58
Figure 4.8 Schematic of the optical cavity in designed double buffered FDML laser.	60
Figure 4.9 Schematic of the optical time multiplexing setup in designed double buffered FDML laser.....	62
Figure 4.10 Performance of the double buffered FDML laser.	63
Figure 4.11 Representative OCT images of the double buffered FDML laser.....	64
Figure 5.1 Schematic of the endoscopic OCT interferometers.....	67

Figure 5.2 Measurements of electronic noise from the balanced detector.	70
Figure 5.3 Comparison of point spread functions of the SS-OCT system before and after calibration.	71
Figure 5.4 Block diagram of the K-clock generator and its performance.	74
Figure 5.5 Schematic of the K-clock generator circuit.....	75
Figure 5.6 Photos of PCB board of the K-clock generator.	78
Figure 5.7 MZI interference signal and external clock signal.	79
Figure 5.8 Depth dependent point spread function of an FDML-based SS-OCT system equipped with the real-time linear K-space sampling method.....	80
Figure 5.9 Representative images acquired with an FDML-based SS-OCT system equipped with the real-time linear K-space sampling method.....	81
Figure 6.1. Block flow of the OCT software.....	85
Figure 6.2. Schematic of data synchronization among different synchronous modules wrapped in threads.	86
Figure 6.3. Data processing steps on GPU.	90
Figure 6.4. Benchmark results of each step of data processing on an Nvidia GTX 590. .	92
Figure 6.5. Addon features of the OCT software.....	94
Figure 6.6. Real time display of a 2D OCT image and 3D visualizations.....	96
Figure 6.7. Illustration of a RAID0 disk array adopted in the computer and its benchmark results.	97
Figure 7.1. Illustration of a miniature OCT imaging probe.....	101
Figure 7.2. Abstract model of the distal end of the OCT imaging probe.	104
Figure 7.3. Working distance, the spot size, and the maximal beam width within the GRIN lens of the imaging probe controlled by the length of the glass rod spacer.	107
Figure 7.4. Ray tracing results of a short working distance OCT imaging probe.	109
Figure 7.5. Schematic of distal end of a short working distance OCT imaging probe...	110

Figure 7.6. Torlerance model of a short working distance OCT imaging probe.....	112
Figure 7.7. Maximal beam width within the GRIN lens, working distance, and the spot size of the imaging probe controlled by the length of the GRIN lens.	114
Figure 7.8. Ray tracing result of a large working distance OCT imaging probe.....	115
Figure 7.9 Astigmatism effect and its correction in an OCT imaging probe.....	118
Figure 7.10. Schematic of distal end of a large working distance OCT imaging probe..	119
Figure 7.11. Torlerance model of a large working distance OCT imaging probe.....	120
Figure 8.1 An OCT imaging probe assembly under a video bronchoscope.....	127
Figure 8.2 Representative 2D circumferential OCT images of swine segmental bronchi <i>in vivo</i>	128
Figure 8.3 3D reconstruction of a pig segmental bronchi <i>in vivo</i> acquired by the high-speed endoscopic OCT system	129
Figure 8.4 <i>En face</i> images of pig lower airways <i>in vivo</i> from lung parenchyma to distal bronchi	131
Figure 8.5 <i>in vivo</i> OCT images of canine bronchi and their corresponding histopathology micrographs.....	132
Figure 8.6 An exemplary correlation pair of <i>in vivo</i> OCT images of canine bronchi and histopathology micrograph..	135
Figure 8.7 Three <i>in vivo</i> endoscopic OCT images of pig bronchi response before, during, and after methocholine challenge.	136
Figure 8.8 A time course of the luminal area of the pig bronchus response to the methocholine challenge.	137
Figure 8.9 Change of averaged height, width and size of mucosal folding with their standard deviations.....	138
Figure 9.1 Schematic of double lumen balloon.	142

Figure 9.2 Representative 2D circumferential OCT images and 3D reconstruction of pig esophagus <i>in vivo</i>	147
Figure 9.3 Representative 2D circumferential OCT images and 3D reconstruction of human esophagectomy specimen <i>ex vivo</i>	147
Figure 9.4 Representative 2D circumferential OCT images and 3D reconstruction of pig esophagus <i>in vivo</i> after cryoablation.	148
Figure 9.5 <i>En face</i> images of pig esophagus <i>in vivo</i> after cryoablation.	149
Figure 9.6 Representative 2D circumferential OCT images of guinea pig esophagus <i>in vivo</i> at different longitudinal locations and a longitudinal cross sectional OCT images of guinea pig esophagus <i>in vivo</i>	150
Figure 9.7. The thickness measurements of the esophageal layers on a guinea pig model based on the acquired OCT data.	152
Figure 10.1 Schematic of the ultrahigh-resolution spectral-domain endoscopic OCT imaging system and the spectrum of the Ti:Sapphire laser source.	155
Figure 10. 2 Point spread function of ultrahigh resolution endoscopic OCT system.	156
Figure 10.3 Linear-in-wavenumber spectrometer and detection sensitivity fall-off.	158
Figure 10.4 Schematic of the management of chromatic aberration by diffractive optic elements.	159
Figure 10.5 Zemax simulation result of the focal shift of an OCT imaging probe without and with a diffractive lens.	160
Figure 10.6 Schematic of an ultrahigh-resolution OCT imaging probes and their reflected spectra.	162
Figure 10.7 Photo of fiber rotary joint and fluctuation of the double-pass coupling efficiency of the fiber rotary joint.	164
Figure 10.8 Representative snapshot of 800 nm ultrahigh resolution OCT images and 1300 nm high-speed OCT images of a guinea pig esophagus <i>in vivo</i>	165

Figure 10.9 Representative 2D circumferential <i>in vivo</i> OCT image of guinea pig esophagus and its corresponding histology micrograph.	167
Figure 10.10 Cutaway view of a 3D reconstruction of 800 nm ultrahigh resolution endoscopic OCT image of guinea pig esophagus <i>in vivo</i>	168
Figure 10.11 Representative 2D circumferential <i>ex vivo</i> OCT image of guinea pig bronchus and their corresponding histology micrographs	169
Figure 11.1. Angular dependent scattering pattern of silica nanospheres.	178
Figure 11.2. OCT images of the phantoms without nanocages and with nanocages.....	181
Figure 11.3. <i>In vivo</i> OCT images of a mouse ear tumor before and after intravenous injection of gold nanocages, respectively.	184
Figure 11.5. Schematic of TPF/OCT multimodal endomicroscope system.	187
Figure 11.6. OCT and TPF images of A431 cancer cells immunostained with anti-EGFR conjugated ICG micelles.....	190
Figure 11.6. OCT, TPF and superposed images of mouse tissue with local ICG administration.	192

LIST OF TABLES

Table 8.1 Basic parameters of shorter working distance OCT imaging probes.	126
Table 9.1 Basic parameters of four OCT imaging probes used in upper GI studies.	144

Chapter 1 Introduction

1.1 Overview

Medical imaging has greatly improved the accuracy and promptness of medical diagnosis and interventions by providing clinicians with tissue-related anatomical and functional information over the past fifty years. Currently, X-ray computerized tomography (CT), magnetic resonance imaging (MRI), ultrasound (US), and positron emission tomography (PET) are the most widely recognized medical imaging modalities used in common clinical practice, where a non-invasive assessment of tissue structures is achieved at a resolution of 30 μm to 1 mm with a penetration depth of a few centimeters to the whole body [1, 2]. However, although less known, optical microscopy has also been used in clinic for a few hundred years to aid histological examination where a submicron resolution could be reached [3]. Nevertheless, the penetration depth of conventional optical microscopy is virtually negligible so that *in vivo* applications of such technology are rare. Though recent technological advances on optical microscopy (e.g., confocal microscopy, multi-photon microscopy, etc.) has pushed the penetration depth up to a few hundreds of microns, *in vivo* applications still remain limited.

Current oncological diagnosis criteria for disease staging is excisional or *ex vivo*, which requires tissue biopsy followed by histological staining [3]. The whole procedure usually has a relatively long turnover time of a few days and the false negative rate, especially for early cancer detection, may be high due to sampling error where the

cancerous lesion was missed when biopsy specimens were taken[4]. Medical imaging, on the other hand, has the capability of examining the whole organ in a timely fashion. However, such medical demand requires a medical imaging technology capable of assessing tissue microanatomy at a resolution of at least a few microns in a real-time fashion. Unfortunately, none of the technologies mentioned above would meet such requirements. However, optical imaging modalities that have been rapidly developed for the past a few decades showed a great potential of providing high-resolution medical images (such as diffuse optical tomography, confocal fluorescence, nonlinear optical imaging, optical coherence tomography, spectroscopy, and etc.) [5-9]. Besides reflectance and scattering, optical imaging modalities also provide spectroscopic information that presents physiological and molecular function of the tissue. In addition, optical imaging modalities can potentially reduce the instrumentation and operational costs.

This dissertation describes one of the emerging optical imaging modalities, optical coherence tomography (OCT). It is a novel optical technique that provides real-time high-resolution anatomical and functional information of biological tissue at a resolution of <1 to 10 μm and a penetration depth of 1 to 3 mm which bridges the gap between currently used clinical medical imaging technologies and optical microscopy (as illustrated in Fig. 1.1). The OCT technology was proven to be capable of detecting diseases in their early stages on many *ex vivo* tissue models. In addition, recent technological progress on miniature OCT imaging probes greatly expanded the scope of the OCT applications from ophthalmology and dermatology to cardiology, gastroenterology, pulmonology and others.

In this dissertation, the technological development of a compact, high-speed endoscopic OCT imaging system, including an OCT laser source, an OCT interferometer, an OCT software platform, and particularly a miniature OCT imaging probe, are discussed. Clinical applications in gastrointestinal tract and lower airway applications are investigated. OCT contrast enhancement and an endoscopic multi-modal imaging system are also briefly discussed.

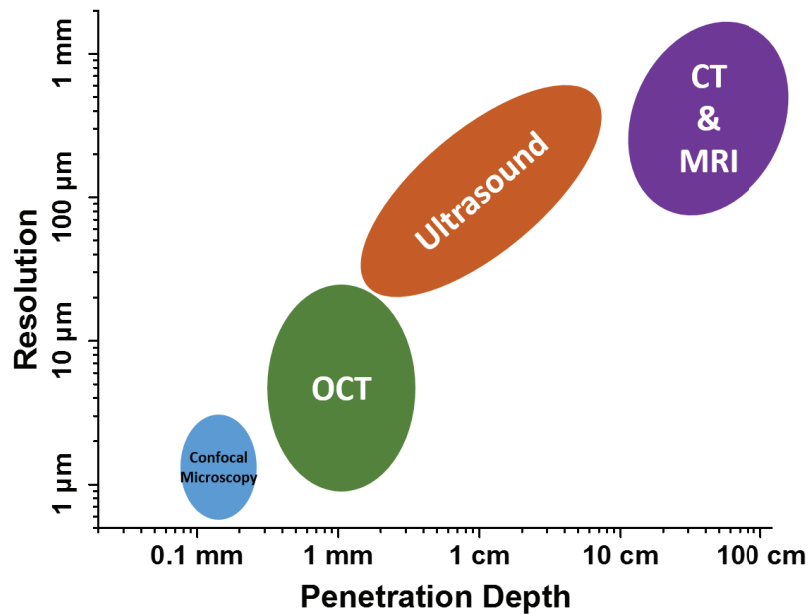


Figure 1.1 A plot between resolution and penetration depth of the medical imaging modalities. OCT bridges the gap between clinically-used medical imaging technologies and optical microscopy.

1.2 Endoscopic Medical Imaging

Endoscopic medical imaging usually refers to the examination of the interior of organs using a miniature medical imaging device directly insert into the human body. Because of the close proximity to the region of interest, endoscopic medical imaging could provide unprecedented diagnostic information to physicians over conventional imaging modalities.

Moreover, due to the small size of the devices used, most of the endoscopic medical imaging procedures are minimally invasive or non-invasive and are therefore safer.

1.2.1 Surface Optical Endoscopy

The idea of a modern endoscope was first proposed in Germany in the nineteenth century for examining canals and cavities of the human body [10]. Due to the technical limitations, the use of rigid endoscopes (e.g., laparoscope, hysteroscope) were first explored in the early twentieth century. In the 1950s, optical fiber bundle made flexible endoscopes (e.g., gastrointestinal endoscope, bronchoscope, etc.) possible by transmitting the light from the distal end of each fiber to the proximal end to form an image [11]. A few decades later, the advent of video endoscope by using charge-coupled devices (CCD) greatly expanded the scope of endoscopic applications in the 1990s [12]. Since then, endoscopes, in particular flexible endoscopes, have been widely adopted.

Conventionally, the light source for illumination used in an endoscope is a white light source (e.g., Xenon lamp) and an endoscope employing such a light source is called a white light endoscope. However, sometimes, a white light endoscope may not provide clinicians with enough image contrast. Therefore, a light source with a narrow optical bandwidth was utilized in endoscopic procedures to improve the image contrast. Clinically, a center wavelength of 415 nm (blue) and 540 nm (green) are commonly used [13]. These two wavelengths were chosen because both wavelengths are the absorption peaks of hemoglobin where narrow-band imaging improves the contrast of cardiovascular vessels.

Alternatively, chromoendoscopy was developed by using stains or dyes topically to enhance the image contrast in order to help clinicians with tissue characterization and differentiation [14]. There are three major stain mechanisms in chromoendoscopy, absorptive stains, contrast stains, and reactive stains. Absorptive stains (e.g., Lugol's iodine, methylene blue, gentian violet) identify specific epithelia cells by preferential absorption or diffusion. Contrast stains (e.g., indigo carmine) permeate between mucosal crevices to highlight surface topography and mucosal abnormalities. Reactive stains (e.g., congo red, phenol red) change the color of a region of interest by binding with specific cellular constituents.

Another type of optical endoscopic techniques are based on fluorescence, including autofluorescence endoscopy, confocal fluorescence endomicroscopy and nonlinear optical endomicroscopy [15, 16]. Autofluorescence endoscopy uses excitation light (i.e., 370-470 nm) to illuminate a region of interest in tissues, which emits fluorescence light of longer wavelength from endogenous fluorophores (e.g., collagen, porphyrins, aromatic amino acids, flavins and NADH, etc.). The image contrast of autofluorescence endoscopy comes from concentration difference of those fluorophores, which helps to differentiate abnormal epithelium from normal mucosa (e.g, Barrett's esophagus). Confocal fluorescence endomicroscopy and nonlinear optical endomicroscopy are newly developed optical imaging techniques. Similarly, both image contrasts come from exogenous or endogenous fluorophores. Unlike autofluorescence endoscopy, they provide much higher resolution microscopic optical images at subcellular scale in both lateral and depth directions.

1.2.2 Ultrasonic Endoscopy

Ultrasonic endoscopy is another major imaging modality in the field of endoscopic medical imaging and has become popular in a variety of clinical applications (e.g., upper gastrointestinal (GI) cancer, lung cancer, and atherosclerosis) [17-21]. In an endoscopic ultrasound (EUS) system, small ultrasonic transducers were packed in an endoscopic form to obtain images of the internal luminal organs inside human body (e.g., wall structures and beyond) and the resolution of EUS is usually in the range of 50 to 100 μm . EUS can be broadly divided into two types: radial and linear EUS. The radial EUS provides an ultrasound image in a plane that is perpendicular to the probe axis and has been widely used in diagnostic procedures (e.g., intravascular ultrasound, and endobronchial ultrasound). Linear EUS produces an ultrasound image in a plane that lies along the probe axis, which is commonly used in image guided procedures (e.g., fine needle aspiration).

1.3 Optical Coherence Tomography and Optical Biopsy

OCT is a recently developed biomedical optical technology capable of providing depth-resolved images of tissue microanatomy [22-24]. It is similar to medical ultrasonic imaging, although the detected signal becomes an optical echo delay signal rather than an acoustic one. Since the speed of light is much faster than the speed of acoustic wave, low coherence interferometry is employed in OCT technology to resolve a small optical echo delay spatially. Therefore, an axial resolution of $<10 \mu\text{m}$ could be achieved in most OCT systems when a proper laser source is used. In addition, with optical heterodyne detection, the

detection sensitivity of an OCT system could reach its quantum limit so that an optical reflection signal as weak as or weaker than 10^{-10} of the incident optical power can be detected.

1.3.1 Brief History of Optical Coherence Tomography

Optical time domain reflectometry (OTDR) is a technique that preceded OCT. It was developed in the 1970s and was first used to characterize optical fiber network [25, 26]. In the 1980s, it was attempted to resolve depth information in biological tissues [27, 28]. In OTDR, an ultrafast laser source was utilized to detect the reflected time-of-flight of ultrashort laser pulses where its depth resolution depends on the narrowness of laser pulses and the bandwidth of a photodetector. The spatial resolution of most commercially available OTDR devices were greater than 5 cm [29]. Although the depth resolution could be improved with a great amount of expenses on the laser source, the detector, and the system, it could hardly exceed 15 μm in biological applications and the detection sensitivity tends to be lower than 70 dB due to the high noise level of a high speed photodetector and the low efficiency of nonlinear optical conversion [28]. Although high power laser source is able to improve the detection sensitivity to some extent, the high intensity that comes with the source may cause tissue damage in biological samples. Consequently, OTDR had very limited applications and was only demonstrated feasible on imaging transparent cornea and superficial skin.

Low coherence interferometry (LCI) is another technique that preceded OCT. It was first proposed in 1987 and was originally developed for high-resolution optical ranging in the same field as OTDR [30, 31]. The technique was sometimes referred to as optical coherence domain reflectometry (OCDR) to distinguish it from a similar technique used in optical fiber sensing, which is also referred to as LCI [32]. Instead of directly detecting time-of-flight of laser pulses, LCI detects an interference signal of reflected light from a sample with light reflection from a mirror, which greatly reduces the complexity of the system and increases the detection sensitivity. A depth resolution of $<10\ \mu\text{m}$ and a detection sensitivity of 120 dB were achieved using this technique. Similar to A-mode ultrasound imaging, LCI (or OCDR) could provide depth resolved informations and was immediately applied in ophthalmology in 1988 to acquire one-dimensional optical imaging (i.e., A-scan) [33].

The idea of OCT was first proposed in 1991 and has been widely adopted for the past 20 years [22]. With an optical imaging lens to focus the beam into a sample, OCT could provide spatial resolved information in lateral direction that is perpendicular to depth direction. A lateral scanning mechanism along with the depth scanning provided by LCI was employed in an OCT imaging system to acquire a two-dimensional optical imaging, providing spatial resolved information that is similar to B-mode ultrasound imaging.

The conventional approach in implementing an OCT system was referred to as time domain OCT (TD-OCT). It requires the mechanical scanning of a mirror to achieve depth scan, which limits the imaging speed of a TD-OCT system (i.e., usually less than a few

thousand A-scan/sec) [34]. In contrast, Fourier domain OCT (FD-OCT), an alternative approach in implementing an OCT system, has no such a requirement. With a line scan detector or a wavelength swept laser source, the imaging speed of a FD-OCT system is significantly faster than a TD-OCT system, reaching as high as a few hundred kilo to a few mega A-scan/sec [35-37]. In addition, given the same imaging speed, a FD-OCT system has a much higher sensitivity, about 20-30 dB higher than a TD-OCT system [38-40].

1.3.2 Applications of Optical Coherence Tomography

Upon invention, OCT immediately drew a lot of attention in dermatology and ophthalmology. Since then, OCT has been widely used from research labs to clinics to image both anterior and posterior segments of the eyes. By quantitatively measuring the thickness of the layered structures, OCT could help with diagnosis in ophthalmological diseases (e.g., age-related macular degeneration, retinoblastoma, etc.) [41-45]. Furthermore, recent technical advances on pushed ophthalmological OCT into a new era with the imaging speed into Mega Hertz [37] and the imaging depth into full eye imaging [46]. In dermatology, OCT has been playing an active role in providing structural and functional information in a micron scale to dermatologist. It has been used to investigate normal skin, dermatitis, burns, wound healing, and skin cancers [47-52].

Although the bulky size of an imaging probe in OCT systems obscures its accessible to many internal organs, the imaging capability of OCT on scattering tissues of the internal organs has been demonstrated by either surgical removal of the tissues (i.e., *ex*

vivo) or surgically opening the organs (i.e., *in situ*). Various types of internal organs, such as GI tract, blood vessel, lung, skeletal muscle, and non-retinal nerve fiber [53-58], have been studied for the purpose of demonstration of new technologies, characterization of both normal and diseased tissue properties, and measurement of physiological parameters.

Besides clinical applications, OCT has also been used in the aspect of basic scientific research. In particular, it was proven to be an invaluable tool for imaging embryo *in vivo* in developmental biology. OCT imaging was performed in *Rana pipiens* tadpoles, *Brachydanio rerio* embryos and eggs, and *Xenopus laevis* tadpole's embryos and its blood flow throughout the beating heart [59-64]. Moreover, OCT was sometimes used in tissue engineering to monitor the development and characterize the optical properties of the engineered tissues non-destructively [65-67].

1.3.3 *Optical Biopsy and Optical Coherence Tomography Endoscopy*

Unlike conventional excisional biopsy, optical biopsy refers to methods using an optical imaging modality (e.g., OCT) to acquire optical images of tissue microanatomy *in situ*, without the removal of the tissue from the body. As opposed to excisional biopsy, optical biopsy has the advantages of non-invasive or minimal invasive, less painful, time efficient, and cost effective. More importantly, with recent technological advances, optical biopsy can easily cover the entire region of interest while excisional biopsy are usually performed in a few discrete sites sampled over the entire region. Compared to other endoscopic

medical imaging modalities (e.g., EUS), optical biopsy can usually provide images of much higher resolution to better assist clinicians in diagnosis.

Among the optical imaging modalities available, OCT is probably one of the most promising techniques to perform optical biopsy in biological tissues *in vivo* [68-74]. In the cases of examining internal organs *in vivo*, an endoscopic form of OCT is required. A key component in such a system is a miniature OCT imaging probe along with a proper lateral scanning mechanism that drives the probe to acquire cross-sectional images of tissue microanatomy.

As a branch of OCT, OCT endoscopy that is developed with the invention of miniature imaging probe greatly expanded the applications of OCT imaging. Now, with OCT imaging system, not only was superficial organ skin and transparent organ (e.g., eye) able to be imaged, but also was internal organs (e.g., blood vessel, lung, esophagus, etc.). In cardiovascular imaging, OCT has been shown to be able to identify various abnormal structures (e.g., measuring luminal structures, identifying vulnerable plaques) and assess treatment outcomes (e.g. stent apposition and neointimal thickening) [75-78]. In esophageal imaging, OCT has been shown to be a unique *in vivo* tool for identification of normal esophageal structures, detection of esophagitis and precancerous lesions, and assessment of disease progression in real time [74, 79-83]. In pulmonary imaging, OCT has also become one of the emerging imaging modalities and provided unprecedented structural and functional information of the lung [84-89].

1.4 Scope of Dissertation

The goal of this dissertation is to investigate the use of OCT for real-time endoscopic assessment of tissue microanatomy *in vivo*. The thesis consists technology development of a high-speed endoscopic OCT system and its clinical potentials.

The dissertation is organized into technology and clinical applications sections. Chapter 2 provides the basic background of OCT imaging system, including the theory behind OCT and an overview of different approaches to OCT (i.e., time domain OCT, Fourier domain OCT). Chapter 3 briefly overviews four key subsystems of an endoscopic OCT system and describes the rationales of choices of the broadband light source, OCT interferometer, and miniature OCT imaging probe. Chapter 4 to 7 cover technical details of the four subsystems in a high-speed endoscopic OCT system. Chapter 4 first reviews the basic principle of a wavelength swept laser source, then introduces one of the wavelength swept lasers (i.e., Fourier domain mode locking laser) at 1300 nm wavelength range, including a wavelength the design of electronic circuit of the tunable filter driver, the optical cavity design, optical time multiplexing design, and the performance of the laser. In Chapter 5, the OCT interferometer is implemented by using a Mach-Zedher interferometer setup to reach a shot-noise limited detection. In addition, a hardware based calibration method (i.e., real-time uniform K-space sampling method) is introduced. Chapter 6 describes a generic software platform specifically designed for high-speed OCT imaging. Chapter 7 discusses the optical designs of the distal end of OCT imaging probes.

Two types of OCT imaging probes with different working distances are then designed and fabricated.

Chapters 8 and 9 describe the investigation of high-speed endoscopic OCT to assess morphological changes in different internal organs. Chapter 8 demonstrates the performance of the high-speed endoscopic OCT in differentiating layered structures of lower airways *in vivo* in animal models. The *in vivo* OCT images can be well correlated with *ex vivo* histopathology results. In addition, high-speed endoscopic OCT can dynamically monitor the acute response of the lower airways to drugs and quantitatively measure the changes, such as airway luminal area and mucosal folding. Chapter 9 focuses on endoscopic OCT applications in upper gastrointestinal tract. The capability of the high-speed endoscopic OCT system is first demonstrated in pig esophagus *in vivo* and human esophagectomy specimen *ex vivo*. An *in vivo* study of cryoablation effect on pig esophagus shows assessment of the cryoablation site in real time. Furthermore, the high-speed endoscopic OCT system is also used for basic research: quantitative assessment of esophageal structures in a guinea pig model of eosinophilia esophagitis *in vivo*.

Besides a high-speed endoscopic OCT system at 1300 nm wavelength range, an ultrahigh resolution endoscopic OCT system at 800 nm wavelength range is introduced in Chapter 10. A better image quality and contrast are demonstrated with the ultrahigh resolution endoscopic OCT system due to the improved axial resolution and potentially high scattering effect. In Chapter 11, two other projects that is related to OCT imaging are described. The first one is a cross-reference OCT imaging method to assess the optical

properties of gold nanocages as OCT contrast agents. And another one is a compact endoscopic multimodal imaging system that combined 1310 nm *en face* OCT and 1550 nm two photon fluorescence imaging.

Chapter 2 Theory of Optical Coherence

Tomography

This chapter describes the basic theory of optical coherence tomography (OCT). A basic principle of low coherence interferometry is first discussed. The OCT interference signal and several key parameters (e.g., axial resolution, detection sensitivity) of a conventional time domain OCT system is then derived. Fourier domain OCT along with its key parameters is also analyzed in details.

2.1 Introduction

OCT is a recently developed optical imaging technology capable of providing high-resolution, cross-sectional imaging of tissue microanatomy *in vivo*. OCT is usually considered as an optical analogy to medical ultrasound (US). In US, acoustic waves are delivered to biological samples and the corresponding echo delays from different depths are measured temporally. Since an optical wave is used in OCT, small optical echo delay (e.g., on the order of femtoseconds) is impossible to measure temporally due to the celerity of the speed of light. In order to solve this problem, OCT employs low coherence interferometry (LCI) or coherence gating. Depending on the broadband light source used, the depth (or axial) resolution of OCT reaches from 1 to 10 μm , which is much higher than US. The imaging depth of OCT depends on the incident wavelength and the optical properties of the tissues and is usually between 1 to 3 mm. Compared to other optical imaging modalities, OCT requires much less level of light that is incident onto a biological

sample (e.g., <1 to 10 mW) to get structural information from the same/similar imaging depth. The major reason that OCT has such an advantage is that LCI provides an optical heterodyne gain to greatly increase the signal level. With a setup of LCI, one can easily reach the detection sensitivity down to a quantum limit — shot noise limit.

Currently, based on detection scheme, there are two types of OCT systems — time domain OCT (TD-OCT) and Fourier domain OCT (FD-OCT). In TD-OCT, only the interference signal of all the wavelengths from a specific depth is detected at each time point. Hence, a depth scanning mechanism, usually mechanical scanning of a mirror, is required to acquire depth resolved information (i.e., axial scan or A-scan), which limits the imaging speed. On the other hand, a FD-OCT system detects the spectrum of the interference signal from all the depths simultaneously and the OCT A-scan is constructed via Fourier transform. Therefore, there is no requirement of a depth scanning mechanism in FD-OCT systems, resulting in 10 to 100 fold increases in imaging speed over TD-OCT systems.

2.2 Low Coherence Interferometry

OCT can be simply considered as a LCI setup with a lateral scanning mechanism of a light beam. A schematic of a LCI setup in Michelson interferometer form is shown in Fig. 2.1a. Light from a broadband light source (e.g., ultrafast laser, superluminescent diode) is sent to a beamsplitter (usually 50/50 to get the best efficiency) and is divided into two beams in two arms. After the beams are reflected back from mirrors in both arms, they are recombined in the beamsplitter. A stable interference signal could be observed once proper conditions are satisfied (i.e., same wavelengths, same polarization states, and a constant phase difference). If the mirror in one of the arms is replaced by a biological sample (named

sample arm) while the mirror in the other arm remains in place (named reference arm), the signal from the sample arm can be coherently gated by the reference arm signal; that is the backscattered light within the coherence length from the sample shows interference pattern whereas the signals outside the coherence length does not. Therefore, signals from different depths can be acquired by moving the mirror position in the reference arm to form depth-resolved information.

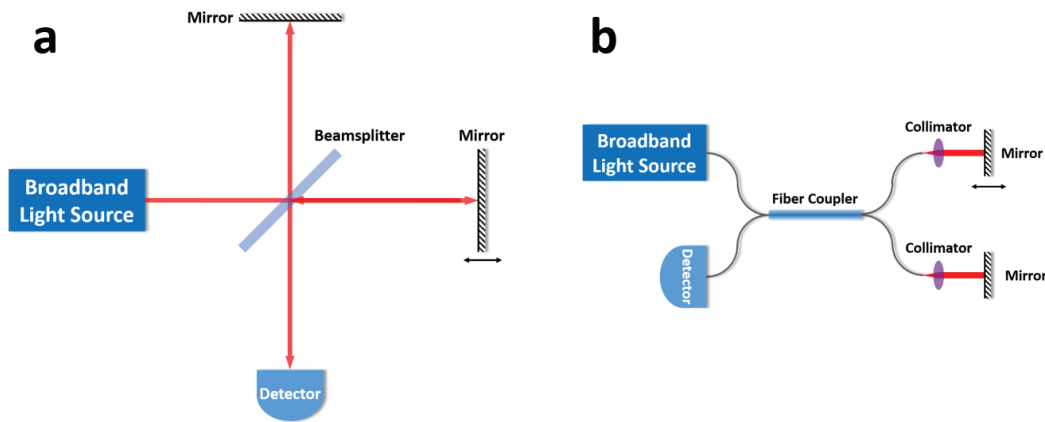


Figure 2.1 (a) A free space low coherence Michelson interferometer and (b) a fiber optic low coherence Michelson interferometer.

The same experimental setup can be implemented in fiber optics. In this design as shown in Fig. 2.1b, the free space beamsplitter is replaced by a simple mode fiber coupler having the same function as the free space beamsplitter in Fig. 2.1a. A fiber optic LCI setup could greatly reduce the size, complexity and the cost of the system and make the system portable, which perfectly fits the need of biological and clinical applications. Therefore, most of experimental setups in OCT field are fiber optical based.

2.3 Time Domain Optical Coherence Tomography

The basic principle of a TD-OCT system is similar to that of LCI, except that OCT introduces a lateral scanning mechanism to get spatial resolved information in both lateral

and axial directions. A schematic of a TD-OCT setup based on a Michelson interferometer is shown in Fig. 2.2. The beam in the sample arm is diverted via a scanning device (e.g., galvanometer scanner) to move the focused beam laterally on the sample. Conventionally, the depth direction is referred to as the z direction while the lateral one is referred to as the x direction.

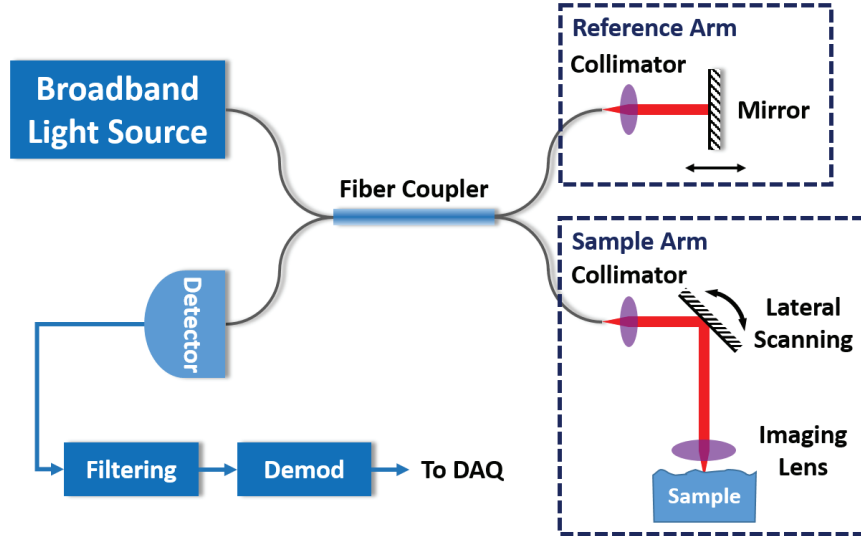


Figure 2.2 A schematic of a time domain optical coherence tomography system

2.3.1 Time Domain OCT Axial Scan Signal [90]

The interference signal in a TD-OCT system can be acquired by moving a mirror in the reference arm with a constant velocity of v_s . The Doppler frequency shift caused by this movement is dependent on the wavelength λ (or angular frequency $\omega = 2\pi c/\lambda$) of the incident light, which is $\omega_d = 4\pi v_s/\lambda = 2v_s\omega/c$, where c is the speed of light. The intensity and electrical field spectra of the incident light to the interferometer are $I_o(\omega)$ and $E_o(\omega)$, respectively. The electric field spectra from both arms are $E_s(\omega) = s(\omega)E_o(\omega)$ and $E_r(\omega) = r(\omega)E_o(\omega)$, where $r(\omega)$ and $s(\omega)$ are the electric field reflection coefficient spectra from the reference and the sample arm, respectively. The spectrum of the total

electric field of the combined signal at the detector is $E_D(\omega) = E_r(\omega) + E_s(\omega)$. The interference signal measured at the detector is time averaged:

$$I_D(t) = \text{Re} \left\langle \int_{\omega} \left[E_r(\omega) e^{i(\omega+\omega_d)t} + E_s(\omega) e^{i\omega t} \right]^2 d\omega \right\rangle_{\omega_d \ll 2\pi/t \ll \omega} \quad (2.1)$$

$$= \underbrace{\int_{\omega} I_o(\omega) \left[|r(\omega)|^2 + |s(\omega)|^2 \right] d\omega}_{DC} + \underbrace{\int_{\omega} 2|r(\omega)s(\omega)| \cos(\omega_d t + \phi(\omega)) d\omega}_{AC}$$

where $\phi(\omega)$ is the phase difference between the reflected beams from two arms and may not be necessarily wavelength independent. The first term in Eq. (2.1) is a DC component because it usually remains constant if the spectrum of the light were kept unchanged. The second term in Eq. (2.1) is an AC component due to the detectable temporal oscillation (i.e., ω_d). In general, the reflectivity of a mirror in the reference arm is independent of the wavelength within the range of interest (i.e., $r = r(\omega)$). In most cases, it is the AC component of the interference signal that we are interested in. Therefore:

$$I_D^{AC}(t) = 2|r| \int_{\omega} \left(I_o(\omega) |s(\omega)| \cos(\omega_d t + \phi(\omega)) \right) d\omega \quad (2.2)$$

$$= 2|r| \int_{\omega} \left(I_o(\omega) |s(\omega)| \cos\left(\frac{2v_s \omega}{c} t + \phi(\omega)\right) \right) d\omega$$

Eq. (2.2) can be converted in spatial domain:

$$I_D^{AC}(z) = I_D^{AC}(v_s t) = \frac{2|r|}{c} \int_k \left(I_o(k \cdot c) |s(k \cdot c)| \cos(2kz + \phi(k \cdot c)) \right) dk, \quad (2.3)$$

where k is the wavenumber of the light. Eq. (2.3) shows that the TD-OCT interference signal contains depth resolved information as the depth dependent signal is the real part of the Fourier transform of the product of the incident light spectrum $I_o(\omega)$ and the sample

reflectivity $s(\omega)$. If the phase difference ϕ is wavelength independent, Eq. (2.3) can be expressed as:

$$I_D^{AC}(2z) \propto \text{Re} \left\{ e^{i\phi} \cdot FT \left[I_o(k \cdot c) |s(k \cdot c)| \right] \right\}, \quad (2.4)$$

which is the mathematical expression of an A-scan signal in TD-OCT.

2.3.2 Key Parameters: Axial Resolution, Dispersion Mismatch, Lateral Resolution, Side Lobes, Imaging Depth and Detection Sensitivity

A few key parameters in OCT system can be deduced from the derivation above.

The axial resolution in OCT, which is defined as the full width half maximum (FWHM) of the image of an infinitely thin reflective surface (e.g., mirror), is also called point spreading function (PSF). It is governed by the bandwidth (or the coherence length) of the light source. The axial resolution can be measured by placing a mirror in the sample arm. Eq. (2.4) can be equivalently rewritten as:

$$I_D^{AC}(z) \propto \text{Re} \left\{ e^{i\phi} \cdot FT \left[I_o(k \cdot c) \right] \right\}, \quad (2.5)$$

which indicates that the axial resolution is inversely proportional to the bandwidth of the light source: $\Delta z \propto 1/\Delta k$. Converting into wavelength dependent form, the axial resolution is proportional to the square of the central wavelength divided by the bandwidth of the light source: $\Delta z \propto \lambda_c^2/\Delta\lambda$. Given the assumption that the spectrum of the light source is Gaussian shaped,, the theoretical limit of the axial resolution is expressed as [90]:

$$\Delta z = \frac{2 \ln 2}{\pi} \frac{\lambda_c^2}{\Delta\lambda} \approx 0.44 \frac{\lambda_c^2}{\Delta\lambda}^* . \quad (2.6)$$

* The derivation of axial resolution is in a unit of optical pathlength, which is equivalent to physical length in vacuum or in air. In a medium, the axial resolution in physical length is equal to the one in optical pathlength divided by the refractive index of the medium (i.e., $\Delta z/n$).

Dispersion, defined as the wavelength dependent velocity, exists in all the materials when the light travels inside them. Unlike most other optical fields, dispersion itself would not deteriorate the axial resolution in an OCT system. Dispersion mismatch between two arms, however, would degrade the axial resolution. If phase difference is expressed as an optical frequency dependency (i.e., $\phi = \phi(k)$), Eq. (2.3) then becomes:

$$I_D^{AC}(z) \propto \text{Re} \left\{ \text{FT} \left[e^{i\phi(k)} \right] \otimes \text{FT} \left[I_o(k \cdot c) |s(k \cdot c)| \right] \right\}, \quad (2.7)$$

where \otimes is defined as the convolution of two functions. It is a common convention to express the phase function as a Taylor expansion around the central wavelength as shown below:

$$\phi(k - k_0) = \phi_0 + \phi_1 \cdot (k - k_0) + \phi_2 \cdot \frac{(k - k_0)^2}{2} + \phi_3 \cdot \frac{(k - k_0)^3}{6} + \dots \quad (2.8)$$

Dispersion mismatch, which can be described as nonlinear terms in phase function $\phi(k)$ (i.e., group delay dispersion ϕ_2 , third order dispersion ϕ_3 , and higher order dispersion shown in Eq. (2.8)), causes a chirping in its phase function $e^{i\phi(k)}$, leading to the broadening of the axial resolution as shown in Eq. (2.7). And the severity of the broadening depends on how much the chirping is. For example, the broadening effect of group delay dispersion ϕ_2 on a Gaussian shaped PSF can be expressed as:

$$\Delta z' = \frac{\sqrt{\Delta z^4 + (\ln 2)^2 \phi_2^2}}{\Delta z}, \quad (2.9)$$

where z' is the actual axial resolution and z is the theoretical limited axial resolution as shown in Eq. (2.6). Eq. (2.9) clearly shows that any GVD mismatch between the two arms in an OCT system could deteriorate the axial resolution.

Unlike other optical imaging techniques, the lateral resolution of an OCT system is independent on its axial resolution as the lateral resolution is still governed by the focusing power of the imaging probe in the sample arm of the OCT system. When the numerical aperture (NA) of the imaging probe in the sample arm is small, the propagating beam in the sample arm can be simply described as a scalar Gaussian beam [91]:

$$I(x, z) \propto \frac{1}{1 + (z/z_R)^2} \exp\left[\frac{-2x^2}{\omega_0^2 \left(\frac{1}{1 + (z/z_R)^2} \right)} \right], \quad (2.10)$$

where $z_R = \pi\omega_0^2/\lambda$ is called the Rayleigh range, ω_0 is the waist size. The lateral resolution can be defined as twice of the waist size:

$$\Delta x = 2\omega_0 = \frac{2\lambda_0}{\pi \text{NA}}. \quad (2.11)$$

And the conversion between this lateral resolution and a FWHM of beam spot in lateral direction is:

$$\Delta x_{FWHM} = \sqrt{\frac{\ln 2}{2}} \Delta x \approx 0.589 \cdot \Delta x. \quad (2.12)$$

Direct measurement of a lateral resolution is sometimes difficult and requires extra instruments. But the lateral resolution can be calculated from measured confocal parameter $b = 2z_R$:

$$\Delta x = \sqrt{\frac{2b\lambda_0}{\pi}} \quad (2.13)$$

Most of the broadband light sources do not have a Gaussian shape spectrum so that side lobes exist next to the main lobe when measuring their PSFs. Side lobe level is a key

parameter of TD-OCT in practical use since the side lobe from a strong scatter would overwhelm the main lobe from a weak scatter next to the strong one. The image quality would be fussy although the axial resolution of the system may not be bad. Although the side lobe is dependent on the spectral shape of the light source, it would be better to set the side lobes at least 20 dB lower than their main lobe.

The imaging depth of TD-OCT is determined by how deep the reference arm is capable of scanning. In general, a deeper imaging depth in TD-OCT means slower imaging speed (i.e., A-scan rate). Several optical techniques (e.g., rapid scanning optical delay line) were employed in TD-OCT systems to achieve both deep imaging depth and fast imaging speed. Depending on the incident wavelength, the imaging depth in most OCT systems is from 1 to 3 mm.

The detection sensitivity in an OCT system is defined as the ratio of a complete reflection (e.g., a mirror) in the sample arm over the noise level when the light from the sample arm is negligible. The overall noise in a photodetector comes from several noise sources, such as shot noise, excess noise, dark noise, thermal noise, $1/f$ noise and etc. Among these, shot noise arises from fluctuation of uncorrelated photons of a light source (e.g., a laser of completely coherent state), which is an inherent property of the light source that cannot be reduced or removed with a classical method. The statistics of shot noise follows Poisson distribution (i.e., $\Delta n \propto \sqrt{n}$, where n is photon number) [92]. Excess noise is another type of noise that comes from the fluctuation of correlated photons of a light source (e.g., thermal light source, chaotic light source). The statistics of excess noise of a thermal light source follows Bose-Einstein statistics (i.e., $\Delta n \propto \sqrt{n^2 + n}$) [92]. A practical light source used in OCT has a photon fluctuation statistics between those two

noises. In order to get the best detection sensitivity, a broadband light source need to be carefully chosen and the power level of the reference arm has to be properly set (i.e., not too large and not too small). On the one hand, the power level has to be set small enough so that shot noise, not the excess noise, from the light source is dominant. On the other hand, since dark and thermal noises arise from either the photodetector itself or its amplification electronics, the power level in the reference arm has to be set large enough so that the shot noise from the light source overwhelms those two noise sources. This can be achieved by setting the power level in the reference arm properly [61]. $1/f$ noise is highly frequency dependent in electronics, which can be removed by carefully choosing a Doppler frequency. Hence, detection sensitivity is shot-noise limited.

In a TD-OCT system employing a Michelson interferometer setup, the shot-noise limited detection sensitivity can be expressed as [93]:

$$\text{D.S.} = 10 \cdot \log_{10} \left(\frac{\eta P_s}{2\hbar\omega \text{NEB}} \right), \quad (2.14)$$

where η is the quantum efficiency of the photodetector, P_s is the optical power of the incident light on the sample, $\hbar\omega$ is the energy of a single photon and NEB is the noise equivalent bandwidth. Practically, as a loss of sensitivity exists in any OCT systems, a measured detection sensitivity is always lower than the above theoretical limit by a few dBs. A typical detection sensitivity of a TD-OCT system is about 100 dB to 110 dB.

2.3.3 Disadvantages

A major disadvantage of the TD-OCT system lies in the imaging speed. In a TD-OCT system, a mirror in the reference arm has to be mechanically scanned to acquire depth-resolved information in the sample. A typical A-scan rate of a TD-OCT is usually on the

order of ~ 100 Hz to 2 kHz, which limits the imaging speed of a TD-OCT system. For example, a B-frame rate of such a system is on the order of 0.1 to 2 Hz. With the aid of a rapid scanning optical delay line and a resonant mirror, TD-OCT may reach up to 16 kHz under an extreme circumstance (e.g., small imaging depth) [94].

Another disadvantage of TD-OCT is a decrease of detection sensitivity that comes with an increase of the A-scan rate. As a higher imaging speed requires higher bandwidth of the detection components in the system, the detection sensitivity would decrease according to Eq. (2.14). Generally speaking, the detection sensitivity of a TD-OCT system with an A-scan rate on the order of a few kHz can be easily degraded to 90 dB and below [95], leading to poor imaging quality.

2.4 Fourier Domain Optical Coherence Tomography

In order to improve the imaging speed of OCT systems without sacrificing the detection sensitivity too much, another type of OCT systems named FD-OCT were developed especially with the aid of the technological advances on the line scan detector array and the wavelength swept laser source after the millennium. Similar to TD-OCT that came from optical coherence domain reflectometry, FD-OCT originated from optical Fourier domain reflectometry (OFDR), which was developed for characterization of the optical fiber and other optical components [30, 96]. In a FD-OCT system, the spectrum of the interference signal from all the depths are simultaneously detected and an OCT A-scan is constructed via Fourier transform from the acquired raw data. Therefore, there is no requirement of a depth scanning mechanism in FD-OCT systems, resulting in 10 to 100 fold increases in imaging speed over TD-OCT systems.

Unlike in TD-OCT, the spectrum of the interference signal is detected in FD-OCT as the raw data in either space (i.e., spectral domain OCT or SD-OCT) or time (i.e., swept source OCT or SS-OCT). The signal from different depths in the sample arm that interferes with the reflected signal in the reference arm shows different frequency in the wavenumber space. A depth resolved signal, therefore, can be computed using Fourier transform. The schematics of both SD-OCT and SS-OCT are shown in Fig. 2.3a and Fig. 2.3b, respectively.

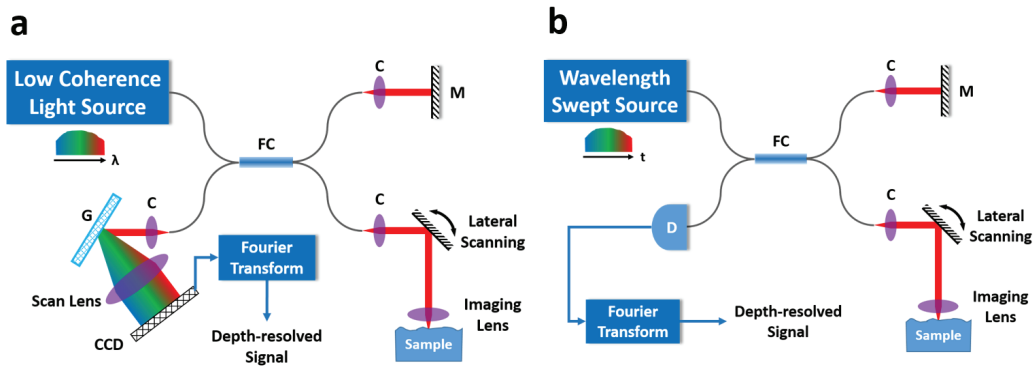


Figure 2.3 (a) A schematic of a spectral domain optical coherence tomography system and (b) a schematic of a swept source optical coherence tomography system. C: collimator; D: detector; FC: fiber coupler; G: grating; M: mirror.

In SD-OCT, the spectral information of a broadband interference signal is decoded via a grating spatially and the dispersive signal is detected via a line scan detector array (e.g., CCD) as a function of the wavenumber (i.e., $k = 2\pi/\lambda$) with respect to the pixel position on the detector array (i.e., $k = k(x)$). In SS-OCT, the spectral information is decoded temporally in a wavelength swept laser source and the swept light is detected by a photodetector as a function of wavenumber with respect to the sweeping time (i.e., $k = k(t)$). Due to the nonlinear mapping between wavenumber and position (or time), most of the FD-OCT systems require a calibration procedure that convert a raw data into

wavenumber space (i.e., K space) before performing Fourier transform. The transformed data, therefore, become depth resolved (i.e., a function of the depth z).

2.4.1 Fourier Domain OCT Axial Scan Signal [97]

For simplicity, we will only derive the interference signal of SD-OCT as shown in Fig. 2.3a and the derivation in SS-OCT is identical. The intensity and electrical field spectra in K space of the incident light to the interferometer are $I_o(k)$ and $E_o(k)$, respectively. The electric field spectra from both arms are $E_s(k, z_s) = s(k, z_s)E_o(k)$ and $E_r(k) = r(k)E_o(k)$, where $r(k)$ is the electric field reflection coefficient spectra from the reference arm, $s(k, z_s)$ is the electric field reflection coefficient with respect to the wavenumber and the optical pathlength in the sample arm. The spectrum of the total electric field of the combined signal at the detector is:

$$\begin{aligned} E_D(k) &= E_r(k) + E_s(k) \\ &= E_o(k) \left[r(k) \cos 2kz_r + \int_{z_s} s(k, z_s) \cos(2kz_s + \phi(k)) dz_s \right], \end{aligned} \quad (2.15)$$

where z_r and z_s are the optical pathlength in the reference and sample arms, respectively.

The interference signal measured at the line scan detector array is then:

$$\begin{aligned} I_D(k) &= I_o(k) \underbrace{\left[|r(k)|^2 + \left| \int_{z_s} s(k, z_s) \cos(2kz_s + \phi(k)) dz_s \right|^2 \right]}_{DC} + \\ &\quad \underbrace{2I_o(k)|r(k)| \int_{z_s} s(k, z_s) \cos[2k(z_s - z_r) + \phi(k)] dz_s}_{AC}, \end{aligned} \quad (2.16)$$

Defining $\Delta z = z_s - z_r$, the AC component in Eq. (2.16) becomes:

$$I_D^{AC}(k) = 2I_o(k) |r(k)| \int_{\Delta z} s(k, \Delta z) \cos[2k\Delta z + \phi(k)] d\Delta z. \quad (2.17)$$

If the reflectivity of the mirror in the reference and the phase difference between two arms are both wavelength independent over the region of interest (i.e., $r(k) = r$ and $\phi(k) = \phi$), Eq. (2.17) is then reduced as:

$$\begin{aligned} I_D^{AC}(k) &= 2I_o(k) |r| \int_{\Delta z} s(k, \Delta z) \cos[2k\Delta z + \phi] d\Delta z \\ &= 2I_o(k) |r| \operatorname{Re} \left\{ e^{i\phi} \operatorname{FT} [s(k, \Delta z)] \right\}, \end{aligned} \quad (2.18)$$

which shows that the FD-OCT interference spectrum is the Fourier transform of the depth resolved reflection coefficient of the sample arm. Therefore, a depth resolved signal can be constructed via an inverse Fourier transform $I_D(z) = \operatorname{FT}^{-1} [I_D^{AC}(k)]$. In particular, the depth resolved signal $I_D(z)$ is proportional to $|r \cdot s(z)|$ when the reflection coefficient in the sample arm is wavelength independent. All the detected raw signals in FD-OCT systems need to be discretized and processed to display on a modern display device. The inversed Fourier transform that is performed to construct the depth resolved signal should be discrete Fourier transform (DFT) in practical.

2.4.2 Key Parameters: Axial Resolution, Lateral Resolution, Side Lobes, Imaging

Depth, Detection Sensitivity and Its Roll-off

Similar to TD-OCT, the axial resolution in FD-OCT is also proportional to the square of the central wavelength divided by the bandwidth of the light source. If a Gaussian shape spectrum of the light source is employed in a dispersion matched OCT system, the axial resolution can also be calculated with Eq. (2.6). The axial resolution in FD-OCT systems would also be degraded when a dispersion mismatch between the two arms exists in the

system (similar to Eq. (2.7) and Eq. (2.9)). Unlike in TD-OCT, however, all the spectral information is acquired in an FD-OCT system so that the dispersion mismatch in an FD-OCT system can be numerically compensated by multiplying a chirped phase function $e^{-i\phi(k)}$ with the Hilbert transform of the signal in K space. However, such a numerical compensation could cause a reduction in the detection sensitivity, especially when the dispersion mismatch is large. The lateral resolution can be identically estimated with Eq.(2.11), Eq. (2.12) and Eq. (2.13) in FD-OCT systems.

Besides the spectral shape of the light source, side lobes in FD-OCT also depend on DFT as a spectral leakage exists in DFT [98]. A numerical manipulation on spectral shape can be performed in FD-OCT to suppress the side lobes. However, such a manipulation usually leads to the broadening of the axial resolution when the side lobes are suppressed. An opposite numerical manipulation on spectral shape could improve the axial resolution with a penalty of the increase of the side lobes. Additionally, the detection sensitivity will be degraded due to the numerical amplification of the noise floor of the raw data.

Unlike in TD-OCT, the imaging depth in FD-OCT is numerically determined by the discretization step of the raw data in wavenumber (i.e., imaging depth $z = \pi/2\Delta k$). However, the discretized step should not be set beyond a physical limit (i.e., spectral resolving power of the FD-OCT system). In SD-OCT, the discretization step cannot be set smaller than the resolving power of the grating. In SS-OCT, the discretization step cannot be set beyond the instantaneous linewidth of the wavelength swept source. Otherwise, the image beyond the physical limit is meaningless and sometimes confusing.

An increase of detection sensitivity of FD-OCT over that of TD-OCT comes from DFT. In order to get the best detection sensitivity, the detection sensitivity of the raw data in FD-OCT should reach shot noise limit, which can be described in the same equation as Eq. (2.14). Since the interference signals of different wavenumbers are constructively added in DFT, the power of the transformed signal is proportional to the square of the effective size of data points M in DFT (i.e., $S \propto M^2$). On the other hand, the power of transformed shot noise is only proportional to the effective size of data points M in DFT due to Wiener–Khinchin theorem. Hence, an M -fold increase in detection sensitivity of FD-OCT over TD-OCT under the same conditions (e.g., electronic bandwidth) is naturally gained from DFT [38-40]. In most FD-OCT systems, the effective data point size is on the order of 1000, which give us a gain of ~ 30 dB. However, the electronic bandwidth in FD-OCT is at least 100 times higher than that in TD-OCT due to its faster A-scan rate. Therefore, most FD-OCT systems have a detection sensitivity of 100 to 120 dB, depending on their A-scan rate.

Unlike TD-OCT, detection sensitivity roll-off, defined as the decay of the detection sensitivity over the imaging depth, is unique in FD-OCT systems. The contributions of detection sensitivity roll-off come from various sources and are different in SD-OCT than SS-OCT systems. In general, detection sensitivity roll-off would be set as small as possible so that the detection capability of a FD-OCT system keeps unchanged when the depth position of a scatter changes.

2.4.3 Comparison between SD-OCT and SS-OCT

There are two implementations in FD-OCT, which are spectral domain OCT (SD-OCT) and swept source OCT (SS-OCT). In SD-OCT, the broadband light is dispersed via a

grating and the dispersive angle is a function of the wavenumber of the light. The dispersive lights are then focused on the pixels of the line scan detector array. Since the position of the pixels can be uniquely mapped into K space, a spectrum of interference signal is then acquired to perform DFT. In SS-OCT, a wavelength swept laser source is required. Since there is a unique relationship between time and wavenumber within a single A-scan, one is able to acquire the spectral data via a point detector to perform DFT. In general, both SD-OCT and SS-OCT systems require a calibration procedure to map the raw data uniformly into K space. But there are a few techniques could avoid this procedure, including directly sampling raw data that is linearly spaced in K space [99, 100] or numerically performing a non-uniform Fourier transform on raw data [101, 102].

Although the basic principles of both systems are very similar, there are two distinct differences between them. First of all, the decisive factor of the imaging speed (i.e., A-scan rate) of a SD-OCT system and a SS-OCT system are different. The A-scan rate of a SD-OCT system is determined by the line scan rate of the detector array while the A-scan rate of a SS-OCT system is determined by the wavelength swept rate of the laser source. Secondly, the contributions of the detection sensitivity roll-off are different in SD-OCT and SS-OCT systems. In SD-OCT system, the roll-off comes from the design of the spectrometer, including the finite size of the detector pixels, the resolving power of the grating and the diffraction effect of the focusing lens in front of the detector array (plus the aberrations existing in the spectrometer in reality). Depending on the bandwidth of the light source and the imaging depth, it usually ranges from 6 to 16 dB [103, 104]. In SS-OCT system, the roll-off mainly comes from the instantaneous linewidth of the laser source and a small portion of the roll-off comes from the electronic bandwidth of the detector.

Depending on the sweeping bandwidth, sweeping rate of the laser source and the imaging depth, it usually ranges from 1 to 6 dB [36, 105-107]. Furthermore, the phase stability of SD-OCT system is better than SS-OCT system since there is no temporal scanning mechanism in SD-OCT.

2.5 Summary

In summary, the basic theories of both TD-OCT and FD-OCT systems were discussed in this chapter. The acquired signals in both OCT systems were derived and the data processing to generate the depth resolved signals were shown. A few key parameters in both OCT systems were mathematically expressed in details, including the axial and lateral resolutions, the effect of dispersion mismatch between the two arms on the axial resolution, side lobes, and detection sensitivity. Finally the disadvantages of both OCT system, such as lower detection sensitivity in TD-OCT and detection sensitivity roll-off in FD-OCT, were also discussed.

Chapter 3 Overview of an Endoscopic Optical Coherence Tomography System

In this chapter, the choices of broadband light source, OCT interferometer, and miniature OCT imaging probe are discussed, mainly focusing on the rationale behind those choices. The technical descriptions of all the subsystems in a high-speed endoscopic OCT system will be introduced in detail in the following four chapters.

3.1 Introduction

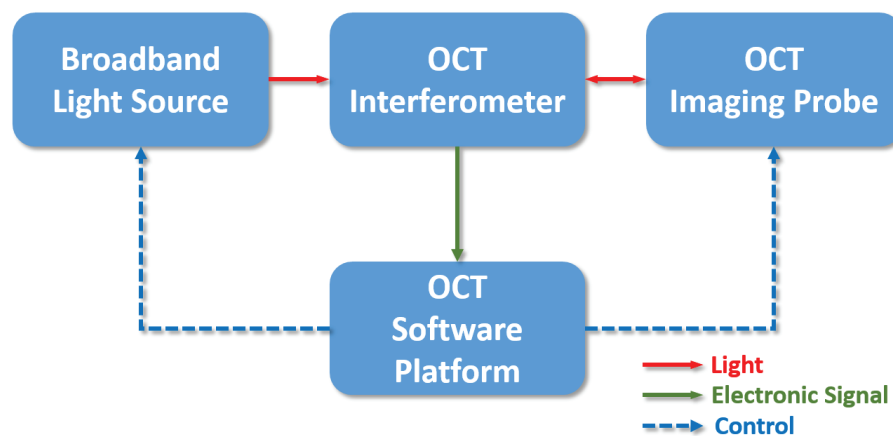


Figure 3.1 A block schematic of a high-speed endoscopic OCT imaging system.

A high-speed endoscopic OCT system, as shown in Fig. 3.1, consists of four essential subsystems including a broadband light source, an OCT interferometer, a miniature OCT imaging probe, and an OCT software platform. A broadband light source has a capability of coherent gating to provide depth-resolved information. An OCT interferometer generates a depth-resolved signal via interfering a weak signal from the sample arm with a stronger signal from the reference arm. A miniature OCT imaging probe can focus the

beam to the internal organs and collect the weak optical signal efficiently while maintaining a small form factor. At last, an OCT software platform controls and synchronizes all the hardware components and is able to acquire, process and save all the OCT data in real time.

3.2 Choice of Broadband Light Source

The wavelength range of the light source is usually discrete due to the availability of the spectra of light sources. Most OCT systems choose a central wavelength at the near infrared (NIR) region at 800 nm, 1060 nm, 1310 nm, and occasionally 1550 nm or beyond [108-111]. The choice of the wavelength range primarily depends on the optical properties of the biological tissue and the requirement of the OCT applications.

There is a tradeoff between the axial resolution and the penetration depth of an OCT system when choosing the incident wavelength of the light source. According to the OCT axial resolution equation (i.e., $\Delta z \propto \lambda^2 / \Delta \lambda$), it is well known that shorter wavelength provides better axial resolution if the spectral bandwidths are the same. However, scattering, which is a dominant optical phenomenon in the NIR region causing exponential decay in biological tissues, highly depends on the wavelength as the scattering significantly increases when the wavelength becomes shorter. For example, Rayleigh scattering cross section is inversely proportional to the fourth order of the wavelength (i.e., $\sigma_s \propto 1/\lambda^4$). Hence, the penetration depth of a longer wavelength is deeper than the one of a shorter wavelength (e.g., an 800 nm OCT system usually has a penetration depth of ~ 1.0 mm in turbid tissue while a 1300 nm OCT system can easily reach a penetration depth of ~ 3.0 mm). Additionally, water absorption is another consideration in biomedical optics. The absorption of water molecules has an increase trend with respect to the wavelength with several absorption peaks in the NIR region [112]. Most OCT imaging in ophthalmology

chooses 800 nm or 1060 nm due to less water absorption and higher axial resolution whereas most OCT imaging of highly scattering tissue (e.g., epithelium) chooses 1310 nm or higher due to less scattering in tissues.

Furthermore, practical considerations have to be taken into account as well. There are two commonly used broadband light sources for TD-OCT and SD-OCT: ultrafast laser and superluminescent diode (SLD)[†]; a wavelength swept laser, which is required for SS-OCT, usually has a gain medium of a semiconductor optical amplifier (SOA) that is equivalent to SLD. In the wavelength range of 800 nm, solid state ultrafast lasers (e.g., Ti:Sapphire, Cr³⁺: LiSAF and Cr³⁺: LiCAF) and AlGaAs SLDs are common choices of the light sources in OCT systems [113-116]. Although solid state lasers usually provide much higher power and broader spectral bandwidth than the SLDs, SLDs have been widely adopted in the OCT community due to their compact size and lower cost (SLDs can be put in parallel to gain broader spectral bandwidth). InGaAs SLDs are commonly used in the range of 1060 nm, but their spectral bandwidths are limited among commercially available choices (e.g., <50nm) [117-119]. Although Nd:YAG solid state ultrafast laser and its family can provide much higher power in this wavelength range, most of them are Q-switch pulse laser so that their spectral bandwidth is too narrow to be used for OCT applications. In the range of 1300 nm or beyond, InGaAsP/InP SLDs are well developed choices due to high demand in telecommunications [120, 121]. For example, a commercially available SLD with a central wavelength of 1310 nm and a bandwidth of ~85 nm can reach an output power above 10 mW from a single mode fiber [122]. Solid state ultrafast lasers (e.g., Cr⁴⁺/Forstertie, Cr⁴⁺:YAG) can also provide a spectral bandwidth that is suitable for OCT

[†] Supercontinuum generation and thermal light source are also sometimes used in OCT systems. But both of them suffers from intensity fluctuation and tends to have higher source noises.

imaging at this wavelength range [123, 124], but their cost is much higher than the SLDs so that they are less commonly used in reality.

In order to achieve high imaging speed, an FD-OCT system was chosen to use in this dissertation. Between the two implementations, SS-OCT system is generally faster than SD-OCT system. Another practical consideration of choosing the type of an FD-OCT is that the availability of line scan detector array and/or light source. Until recently, there is no line scan detector array at the wavelength range beyond 1000 nm [125, 126]. And there is still no practically usable broadband wavelength swept laser source under 1000 nm [127]. Therefore, most SS-OCT systems use a wavelength range of 1060 nm, 1310 nm or beyond while most SD-OCT systems choose a wavelength range of 800 nm.

Since the region of interest in this dissertation is highly scattering tissues in the internal organs, a wavelength range of 1310 nm was chosen to achieve an imaging depth of 2 – 3 mm. In addition, an SS-OCT setup was preferable in order to reach an A-scan rate of a few hundred kHz.

3.3 Choice of OCT Interferometer Setup

There are three fiber-optic based OCT interferometer setups commonly used in most OCT systems: Michelson interferometer, modified Michelson interferometer and Mach–Zehnder interferometer.

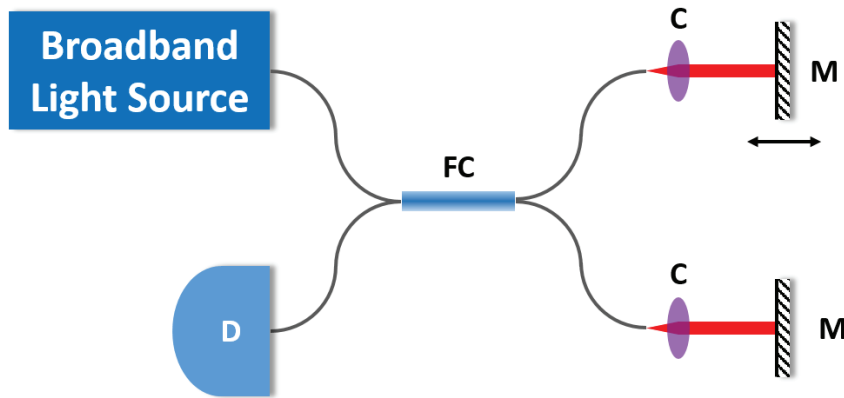


Figure 3.2 A schematic of fiber optical Michelson interferometer. C: collimator; D: detector; FC: fiber coupler; M: mirror.

The simplest interferometer setup as illustrated in Fig. 3.2 is Michelson interferometer, which has been described in the previous chapter. In short, a broadband fiber coupler is employed in this interferometer to split the incident light into sample and reference arms and recombine the reflected lights back from both arms to generate the interference signal. The split ratio of the fiber coupler is usually 50/50 in order to get the best efficiency. One of the disadvantages in this setup is that only half of the interference signal is sent to the photodetector while the other half is wasted by sending back to the laser source.

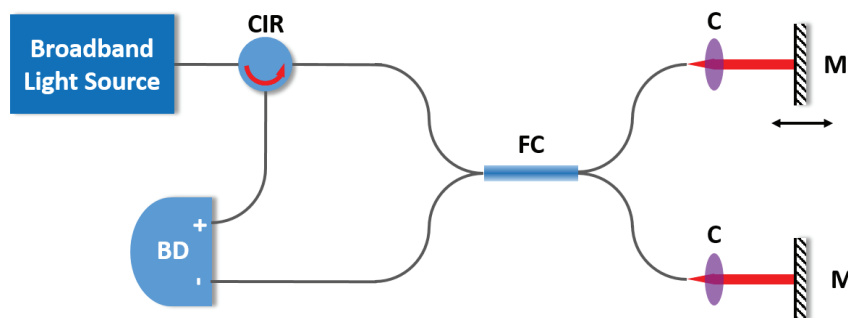


Figure 3.3 A schematic of fiber optical modified Michelson interferometer. BD: balanced detector; C: collimator; CIR: circulator; FC: fiber coupler; M: mirror.

In order to utilize the other half of the interference signal, a modified Michelson interferometer was developed as illustrated in Fig. 3.3. A broadband fiber optic circulator,

where light that travels in the opposite directions takes different optical path, is placed between the light source and the fiber coupler so that the other half of the interference signal is able to be redirected to the photodetector instead of be sent back to the laser source. A balanced detection scheme is employed in this interferometer in order to utilize both interference signals. Due to an intrinsic property of the fiber coupler (i.e., there is a π phase shift between the two split beams in the fiber coupler), the AC components of the two interference signals to the balance detector have a phase difference of π between them while the phases of the DC components remain the same. Because the output of a balanced detector is an amplified signal of the difference between the two optical inputs of the detector, the AC components of the interference signal is doubled while the DC components are cancelled with each other in the balanced detector. Compared to a single detector scheme, the differential mode signal of the balanced detector is doubled whereas the shot noise only increases by $\sqrt{2}$, causing an increase in the detection sensitivity of the OCT system by 3 dB. Another accompanying benefit of balanced detection scheme is the cancellation of non-quantum noises (e.g., 1/f noise) to further improve the performance. However, the availability of a broadband circulator sometimes usually hinders the use of balanced detection scheme (e.g., the choice of a broadband fiber optic circulator at the wavelength of 800 nm is very limited).

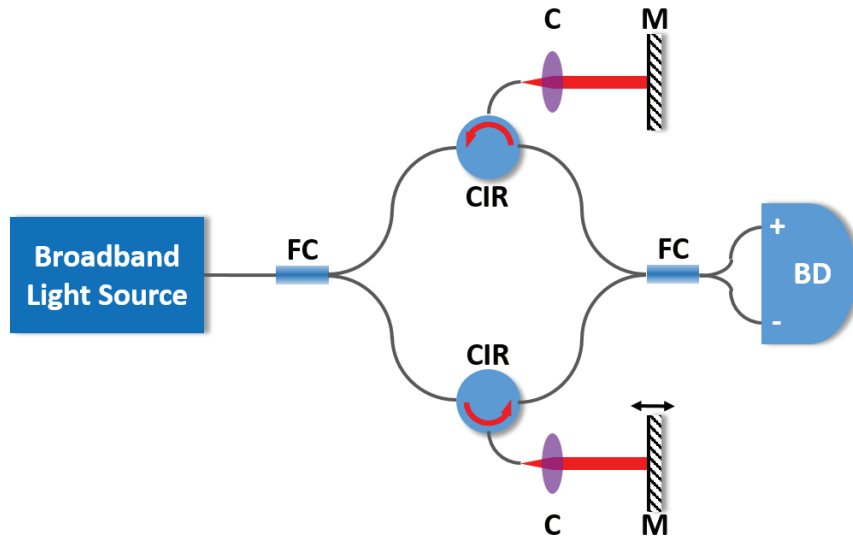


Figure 3.4 A schematic of fiber optical Mach-Zehnder interferometer. BD: balanced detector; C: collimator; CIR: circulator; FC: fiber coupler; M: mirror.

The incident light is evenly split via a 50/50 fiber coupler to the both arms in both aforementioned interferometer setups. But the necessary power to the reference arm is much less than the one in the sample arm in most OCT applications and an attenuator is necessarily inserted into the reference arm to avoid saturation of the detector. In order to optimize the usage of the incident power, a Mach-Zehnder interferometer setup was developed as illustrated in Fig. 3.4. An unbalanced fiber coupler is used to split the incident light into sample and reference arms unevenly (e.g., 90/10) as the majority of the optical power is sent to the sample arm. There are two fiber optic circulators in both arms divert the reflected/backscattered light to the second fiber coupler with a split ratio of 50/50. The second fiber coupler combines the redirected beams from both arms to generate interference signals. A balanced detection scheme is then employed here to remove the DC component of the interference signals and to improve the detection sensitivity as described before.

In summary, we choose to use a Mach-Zehnder interferometer setup in this dissertation.

3.4 Choice of Miniature OCT Imaging Probe

Miniature imaging probes is one of the key components in an endoscopic OCT imaging system. Requirements of a miniature imaging probe for *in vivo* OCT applications includes a high lateral resolution, a compact overall size (including optics, protective components), mechanical robustness and flexibility.

The practical consideration in designing an OCT imaging probe is to minimize its overall size as physical size of the probe is usually limited for *in vivo* applications. For example, the overall size of the entire assembly, including both optical and protective components, usually cannot exceed 2.5 mm for an imaging probe used along with a gastrointestinal endoscope. Unfortunately, a high lateral resolution requires a large optical size in an imaging probe. According to diffraction theory, a smaller spot size comes from higher numerical aperture (NA) of the focusing lens (i.e., $\Delta x \propto 1/NA$), leading to a larger diameter in optics given the same focal length of the lens (i.e., $NA \propto D/f$) [128]. The overall size of the entire assembly of the OCT imaging probe, therefore, would increase if a higher lateral resolution is desirable. Therefore, the primary challenge is to design the distal end optics in an OCT imaging probe in order to utilize a proper optical aperture to reach a desirable lateral resolution when the physical size of the probe is limited. Mechanical robustness and flexibility are, self-explanatorily, also essential for an imaging probe used in *in vivo* applications.

Miniature imaging probes can be divided into forward-viewing and side-viewing probes based on the beam direction in the distal end of a probe. The beam direction in a

forward-viewing probe (as illustrated in Fig. 3.5a) is parallel to the longitudinal axis of the probe so that the field of view (FOV) is in front of the probe; hence it is particularly useful in applications such as image guided surgery. A B-frame image can be acquired via some lateral scanning mechanism at either distal end (e.g., piezoelectric actuator/microelectromechanical systems (MEMS) scanner, MEMS scanning mirror, and angle rotation scanning as illustrated in Figs. 3.5b to 3.5d) [68, 71, 129-135], or proximal end of the probe (e.g., a rigid relay lens or a fiber bundle with galvanometer scanner as illustrated in Fig. 3.5e) [136, 137]. Limited by the size of the scanner, the overall size of forward-viewing imaging probes employing distal end scanning mechanism is usually relatively large (i.e., 1.65 to 7.5 mm in diameter). For forward-viewing probes with proximal end scanning mechanism, a major disadvantage is that they require either a rigid long lens or a fiber bundle, which greatly limits their applications.

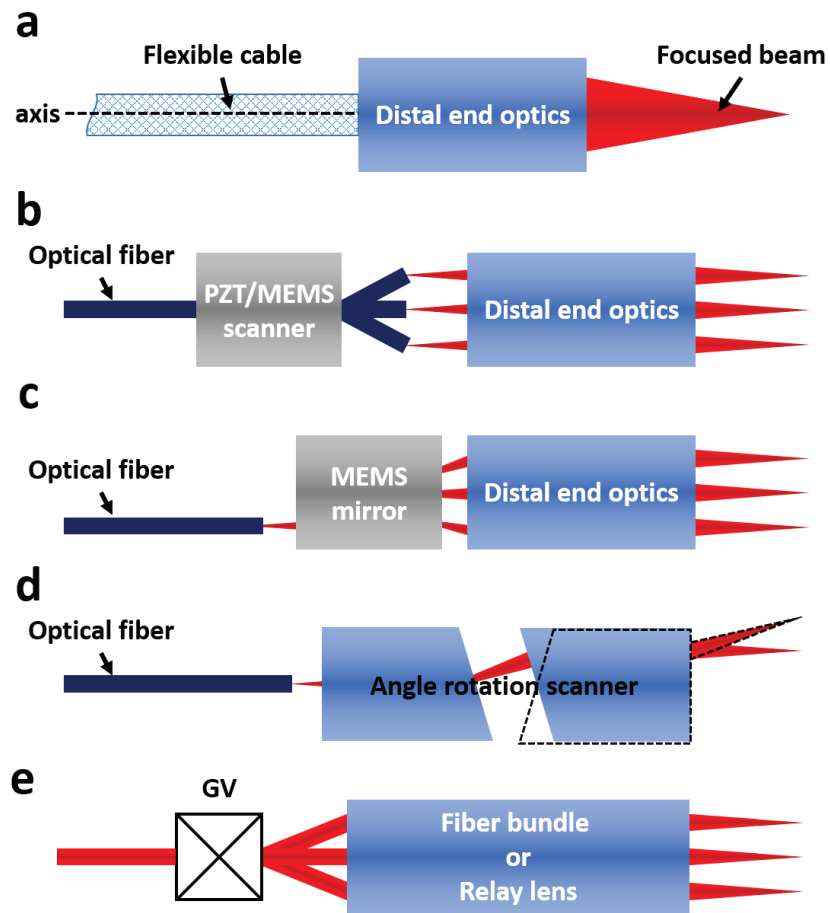


Figure 3.5 (a) A simplified schematic of forward-viewing OCT imaging probe; schematic of (b) PZT scanning probe; (c) MEMS scanning probe; (d) angle rotation scanning probe; and (e) proximal end scanning mechanism in forward-viewing OCT imaging probe. GV: galvanometer scanner.

On the other hand, a side-viewing probe as shown in Fig. 3.6a has a beam direction in the distal end that is perpendicular to the longitudinal axis of the probe, which is usually achieved using a micro reflector in the distal end to divert the beam by $\sim 90^\circ$. The FOV, therefore, is on the side of the probe. The distal end optics of such a probe usually consists of rod lenses to get a desirable working distance. The optical design of the distal end optics includes gradient index (GRIN) lens [73, 74, 83, 138-140], GRIN fiber [141-144], ball lens [145, 146], and multi-element lens assembly [147, 148]. Among these, GRIN lens based

optical design is the most popular choice due to its relatively simple design, ease to assemble, and cost effectiveness. The lateral scanning mechanism in a side-viewing probe can be either linearly translating the OCT imaging probe to acquire side-viewing images as illustrated in Fig. 3.6b [72, 148-151] or rotating the probe to acquire circumferential images as illustrated in Figs. 3.6c and 3.6d. The rotation scanning mechanism can be further divided into rotating the whole probe from the proximal end via a fiber rotary joint as illustrated in Fig. 3.6c [74, 83, 138, 140-145] or only the micro reflector for the distal end via a miniature motor as illustrated in Fig. 3.6d [71, 152-156].

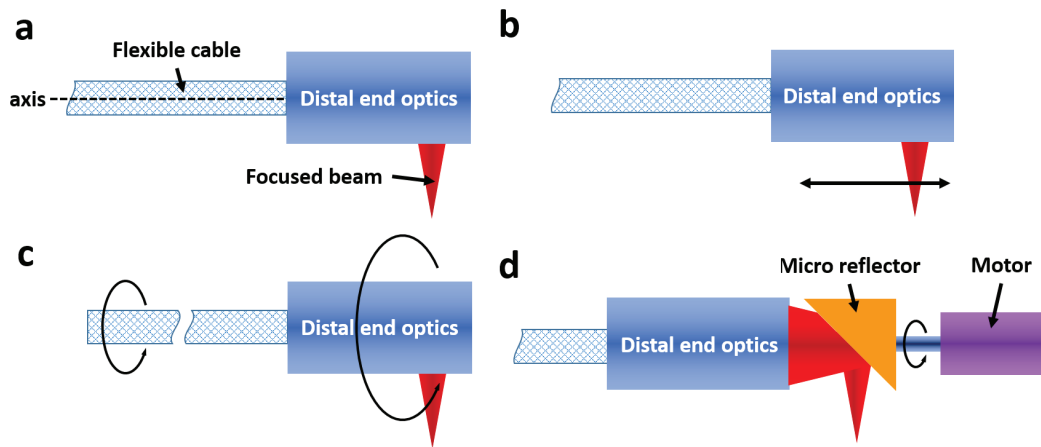


Figure 3.6 (a) A simplified schematic of side-viewing OCT imaging probe; schematic of (b) linearly translational scanning, (c) proximal end scanning, and (d) distal end scanning mechanism in a side-viewing OCT imaging probe.

Since the region of interest of *in vivo* OCT applications is mostly tubular organs (e.g., esophagus, airways and blood vessels), a side-viewing imaging probe with a rotation scanning mechanism is usually preferable to acquire circumferential images of the entire organ lumens. Between proximal and distal end scanning schemes, the overall size of a proximal end scanning probe is usually smaller because a distal end scanner (e.g., DC

motor, MEMS scanner, ultrasound motor) is generally bigger and limits the overall size of a distal end scanning probe[‡].

Therefore, in order to acquire circumferential images while maintaining the probe as small as possible, we consequently choose to use side-viewing miniature OCT imaging probe with proximal end scanning mechanism in the imaging probe designs in this dissertation (as shown in Fig. 3.6c).

3.5 Summary

In summary, we briefly introduced four subsystems in a high-speed endoscopic OCT system. After comparing among different choices, (1) a wavelength swept with a central wavelength of 1300 nm was chosen to be built; (2) a fiber optic Mach-Zehnder interferometer that optimally utilizes the optical power and balanced detection scheme was then used to generate OCT signals, (3) a proximal-end driven, side-viewing OCT imaging probe was chosen in this dissertation. Their technical details will be discussed in the following chapters.

[‡] A motor smaller than 1.0 mm was not commercially available until recently.

Chapter 4 High-speed OCT Laser Engine —

Fourier Domain Mode-locking Laser

This chapter describes the basic principle of wavelength swept lasers. A few essential requirements to ensure a wavelength swept laser working properly were discussed. A double-buffered Fourier domain mode-locking laser was developed to achieve an A-scan rate of ~ 220 kHz. The basic performance of the laser was also tested.

4.1 Basic Principles of Wavelength Swept Laser

SS-OCT is one of the two FD-OCT implementations that greatly increased the imaging speed of an OCT imaging system (i.e., A-scan rate by 10 to 100 folds), which made three dimensional (3D) *in vivo* imaging possible. Among all the components in an SS-OCT system, wavelength swept laser is the optical source engine. Wavelength swept lasers were first used along with an OFDR for inspection of defects in optical fibers and waveguides [157-159]. Since the characteristic size of photonic devices is usually on an order to a few tens of micron and the devices are stationary, the lasers were swept within a very narrow bandwidth at a very slow rate (e.g., a few nanometers with one tenth Hz A-scan rate). Once wavelength swept lasers were adopted into the OCT field, their sweeping bandwidth and rate greatly increased (e.g., an A-scan rate of a few kHz and a bandwidth of >70 nm) [160]. The A-scan rate exceeded 10 kHz and the sweeping bandwidth expanded to >120 nm within a few years [36, 161]. These improvements made the SS-OCT system practically usable for real-time OCT imaging. Sooner after, the invention of Fourier domain mode-locking (FDML) laser and MEMS scanner based short cavity wavelength swept laser

pushed the A-scan rate of the SS-OCT into a few hundreds kHz and expanded the sweeping bandwidth to >150 nm [105, 162-164]; a wavelength swept laser with such a high A-scan rate made in vivo 3D OCT imaging possible. Currently, the A-scan record was updated into multi MHz region [37, 107].

4.1.1 Conventional Wavelength Swept Laser

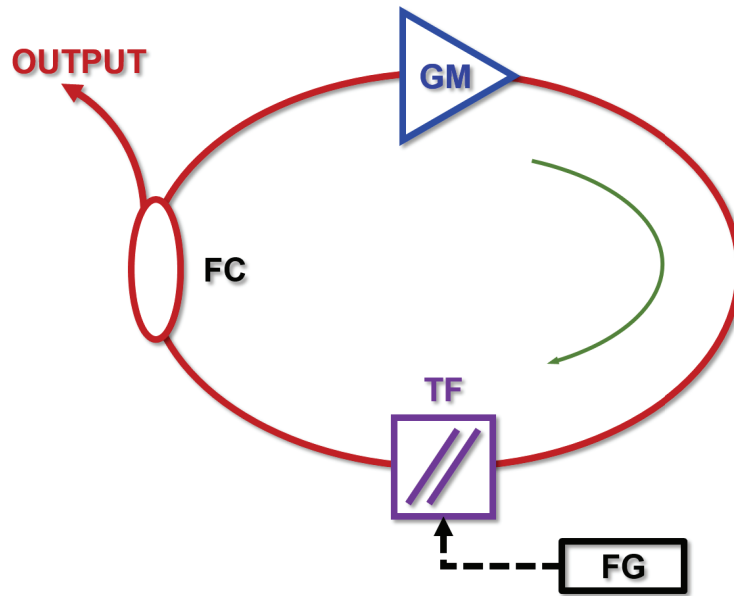


Figure 4.1 A simplified schematic of a conventional wavelength swept laser. The green arrow indicates the light traveling direction inside the cavity. FC: fiber coupler; FG: function generator; GM: gain medium; TF: tunable filter.

A conventional wavelength swept laser is typically made of a broadband high gain medium (e.g., semiconductor optical amplifier, or SOA) and a tunable optical bandpass filter (e.g., fiber optic Fabry-Perot filter) driven by a power function generator to form a laser cavity (e.g., a closed fiber optical loop) as shown in Fig. 4.1. One directional optical component (i.e., usually optical isolator) is utilized to ensure that light travels in a unidirectional direction. The output of the laser comes from a fiber coupler as shown in Fig. 4.1. Before the FDML and short cavity MEMS laser were invented, most of the wavelength swept lasers are setup this way. When laser first starts up, the light first builds up from amplified

spontaneous emission (ASE) inside the gain medium due to its high small signal gain (e.g., at least >20 dB). When the broadband ASE light is sent to the tunable filter, only a very narrow bandwidth of the ASE light (e.g., <0.1 nm) selectively passes through the filter. The selected narrow bandwidth light is then amplified when it travels back to the gain medium. Since the length of the loop is relatively short, the selected light is allowed to travel several times inside the loop to build up enough power of lasing that is close to the saturation level of the gain medium before the tunable filter switches to another wavelength. As the selective wavelength of the tunable filter changes, the old lased light collapses and a new one builds up again. The maximal sweeping rate of a conventional wavelength swept laser is limited by the characteristic frequency for building up laser activity close to its saturation level inside a given optical cavity [36]:

$$f_{sat} \approx \frac{\log(G\rho) \cdot \Delta\lambda_f \cdot c}{\log\left(\frac{P_{sat}\Delta\lambda_{FW}}{\Delta\lambda_f P_{ASE}}\right) \cdot L \cdot \pi \cdot \Delta\lambda_{FW}}, \quad (4.1)$$

where G is the small signal gain of the gain medium, ρ is the fraction of energy fed back into the cavity after each trip, $\Delta\lambda_f$ is the FWHM linewidth of the tunable filter, c is the speed of light, P_{sat} is the saturation power of the gain medium, $\Delta\lambda_{FW}$ is the full-width tuning range of the wavelength swept laser, P_{ASE} is the total ASE power of the gain medium, L is the optical pathlength of the cavity, and π is a constant coming from a sinusoidal driving waveform. Since the driving waveform is usually sinusoidal, one sweeping period of a wavelength swept laser actually contains two wavelength sweeps, which are called forward (short to long wavelength) and backward (long to short wavelength) sweeps.

At any sweeping rate above f_{sat} , the output power of the wavelength swept laser rapidly declines as the laser is driven away from the saturation zone of the gain medium. Keeping increasing the sweeping rate, the laser would reach “single roundtrip limit” [36]:

$$f_{sngl} = \frac{\Delta\lambda_f \cdot c}{L \cdot \pi \cdot \Delta\lambda_{FW}} \quad (4.2)$$

At frequencies near f_{sngl} , the laser output decreases by several orders of magnitude with respect to its saturation limit and most of the laser output is filtered ASE light. A typical conventional wavelength swept laser has a ~8 meter long cavity that is mainly made of SMF28e+ optical fiber. Assuming a gain medium of SOA with a performance shown in [165], a tunable filter of fiber optic Fabry-Perot filter with a fineness of 700, and a 70/30 fiber coupler to pick up the light from the cavity, the saturation limited and single roundtrip limited frequencies calculated are then:

$$\begin{aligned} f_{sat} &= 9.32 \text{ kHz} \\ f_{sngl} &= 11.62 \text{ kHz} \end{aligned} \quad (4.3)$$

Such a sweeping frequency may be high enough for real-time 2D OCT imaging, but insufficient for 3D OCT imaging. As a matter of fact, most conventional wavelength swept lasers work at a sweeping rate of <10 kHz. By reducing the cavity length, the A-scan rate of a wavelength swept laser up to 115 kHz was achieved using a diffractive grating and a rotating polygon mirror as a tunable filter [166]. However, the performance of such a laser at higher sweeping rate is quite poor.

4.1.2 Fourier Domain Mode-locking Laser

In order to increase the maximal sweeping rate of a wavelength swept laser, FDML laser was proposed in 2006, which provided a broad sweeping range, narrow instantaneous linewidth, and high output power [105].

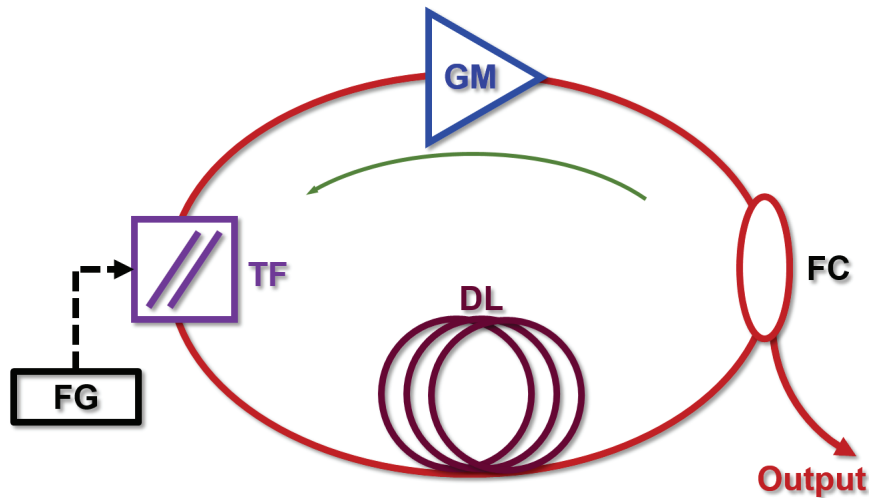


Figure 4.2 A simplified schematic of a Fourier domain mode locking laser. The green arrow indicates the light traveling direction inside the cavity. DL: optical delay line; FC: fiber coupler; FG: function generator; GM: gain medium; TF: tunable filter.

As mentioned in the previous subsection, building up the lasing at each wavelength in a conventional wavelength swept laser takes time and therefore limits the sweeping rate of the laser. The essential concept of a FDML laser takes two steps. First, a very long optical delay line is used to store all the filtered ASE lights of all the wavelengths in a single sweep; the stored lights of all the wavelengths is amplified via the gain medium when the tunable filter selects them sequentially in the next cycle. The lased lights of all the wavelengths are then built up after a few cycles. A FDML laser can be considered as a mode-locking laser with periodic spectral modulation. Based on this concept, a very long dispersion managed optical delay line (e.g., a long spool of single mode fiber) is incorporated into the optical cavity to store the filtered ASE lights of all the wavelengths

as shown in Fig. 4.2. The tunable filter is then driven synchronously at the same period as the cavity roundtrip time (or a harmonic of the roundtrip time).

As mentioned above, FDML operation requires precise synchronization between the roundtrip time of the light inside the optical cavity and the sweeping period of the tunable filter. The driving frequency of the tunable filter is given by [105]:

$$f_d = \frac{1}{\tau_d} = \frac{c}{N \cdot L}, \quad (4.4)$$

where c is speed of light, L is the optical pathlength of the cavity and N is a positive integer representing the harmonic order of the roundtrip time. The synchronization condition can also be expressed as the gating time of the tunable filter at a given wavelength [105]:

$$\tau_g = \frac{\Delta\lambda_f}{\pi f_d \Delta\lambda_{FW}}, \quad (4.5)$$

where f_d is the driving frequency of the tunable filter and the definitions of other variables are the same as in Eq. (4.1). In practice, τ_g must be controlled to less than 10^{-5} of τ_d in order to ensure optimal operation.

Under ideal conditions (i.e., dispersion free and no thermal fluctuation, etc.), consecutive sweeps in a FDML laser should have the same phase and are mutually coherent. Unlike a conventional wavelength swept laser, the gain medium of an ideal FDM laser works deep inside the saturation region, which provides higher output power, narrower instantaneous linewidth, less ASE noise, and better phase stability. In practice, a FDML laser works under a quasi-stationary operational condition due to the existence of dispersion, thermal and polarization fluctuation caused by the long optical delay line, and mechanical instability caused by the tunable filter. When dispersion exists inside the laser

cavity, the lights of most wavelengths in the cavity (except one or two wavelengths) would gradually shift out of the narrow spectral window of the tunable filter when they propagate inside the loop, causing the existed lasing collapses. Meanwhile, a new lasing with slightly wavelength shift builds up. Eventually, these two concurrent processes would complementarily oscillate over time and reach equilibrium. Mathematically, it can be described in a simple model. The maximal variation in roundtrip time is:

$$\Delta\tau_{disp} = \frac{L \cdot D \cdot \Delta\lambda_{FW}}{n_{eff}}, \quad (4.6)$$

where D is the group dispersion delay coefficient of the optical cavity and n_{eff} is the effective refractive index of the cavity at the central wavelength. An FDML laser cannot operate continuously if $\Delta\tau_{disp}$ is greater than the gating time of the tunable filter τ_g .

Therefore the linewidth of the tunable filter $\Delta\lambda_f$ has to be greater than [167]:

$$\Delta\lambda_f \geq \frac{c \cdot \Delta\lambda_{FW}^2 \cdot D \cdot \pi}{n_{eff}}. \quad (4.7)$$

It is noticed that Eq. (4.7) is proportional to the group dispersion delay coefficient D but independent to the length of the optical cavity. Although a longer optical cavity is more dispersive, the gating time of the tunable filter τ_g also increases accordingly. In addition, the requirement in Eq. (4.7) quadratically increases with respect to the full-width sweeping range of the FDML laser $\Delta\lambda_{FW}$, which suggests that the requirement of the linewidth of the tunable filter has to be dramatically increased when a larger sweeping range is needed.

Ideally, a FDML laser can work under any sweeping frequency (A-scan rate) by changing the length of the optical cavity. In practice, the sweeping frequency is limited by the mechanical frequency response of the tunable filter and most commercially available

tunable filter can only be safely driven at a few discrete resonant frequencies under 100 kHz to achieve a broad sweeping spectral range unless it is custom designed or driven under an extreme condition[168]. Therefore, most FDML laser works at a sweeping frequency from 20 kHz to 60 kHz [100, 105, 169].

4.1.3 Buffered Fourier Domain Mode-locking Laser

As discussed in the previous subsection, the sweeping speed of a FDML laser is limited by the mechanical performance of the tunable filter. Unfortunately, it is quite hard for a tunable filter to sweep at a frequency of a few hundred kHz while maintaining a broad sweeping spectral range. Another drawback that exists in a FDML laser as well as a conventional wavelength swept laser, which is less pronounced, is that there are both forward and backward sweeps in each sweeping period. Although they have similar transient power characteristics, the noise floor of forward sweep is significantly higher than that of backward sweep. Hence, a FDML with unidirectional scans is desirable. In order to solve the above problems, buffered FDML was proposed to further improve the A-scan rate of the laser as well as providing unidirectional scans [162]

The schematic of a buffered FDML is shown in Fig. 4.3. In order to get rid of the forward sweeps from a FDML laser, the gain medium in the laser has to be turned off synchronously when the tunable filter is at forward sweeps. Two fiber couplers are placed at evenly spaced locations inside the cavity to get two copies of the backward sweeps that have a time interval of half sweeping period between them (labeled as 1 and 2 in Fig. 4.3). The two copies are then combined together via another fiber coupler outside the cavity and are boosted via an external booster optical amplifier (e.g., SOA). In this setup, the A-scan

rate of the buffered FDML laser is twice as an unbuffered FDML laser at the same sweeping frequency.

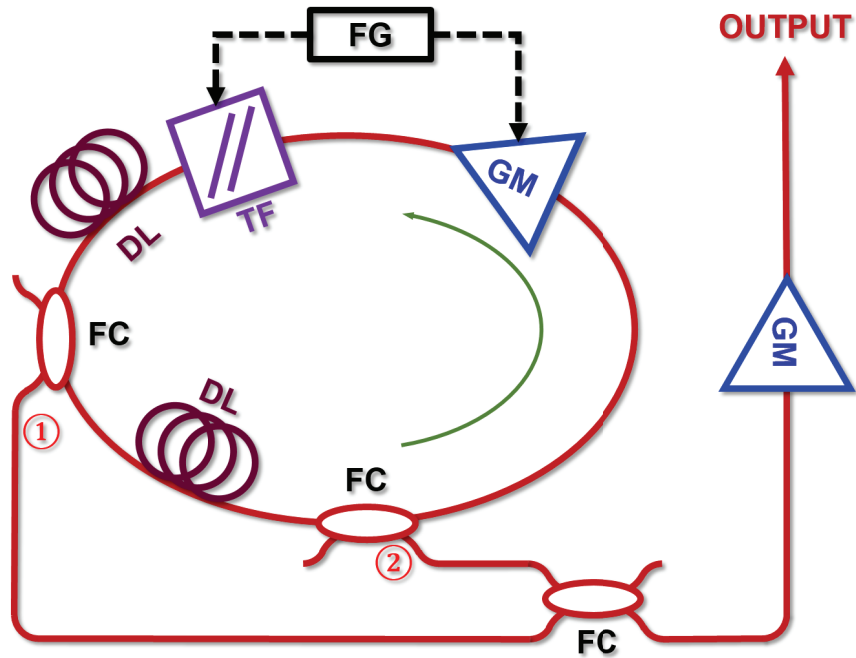


Figure 4.3 A simplified schematic of a buffered Fourier domain mode locking laser. The green arrow indicates the light traveling direction inside the cavity. DL: optical delay line; FC: fiber coupler; FG: function generator; GM: gain medium; ISO: optical isolator; PC: polarization controller; TF: tunable filter.

Moreover, the A-scan rate can be further improved by a FDML laser with a double-buffered cavity setup as shown in Fig. 4.4a. In such an FDML laser, the tunable filter is driven over a wavelength sweeping range that is larger than one free spectral range (FSR) of the backward sweeps; the gain medium inside the cavity is only turned on within the time span covering one FSR or less. Using the same optical cavity design as the one in single buffered FDML (as shown in Fig. 4.3), two copies of the sweeps with a time interval of half sweeping period are outputted from two fiber couplers (labeled as 1 and 2 in Fig. 4.4a and illustrated in Fig. 4.4b). The two copies of the sweeps are then sent to an optical

time multiplexing setup outside the cavity, which consists of two 50/50 fiber couplers and an optical delay line.

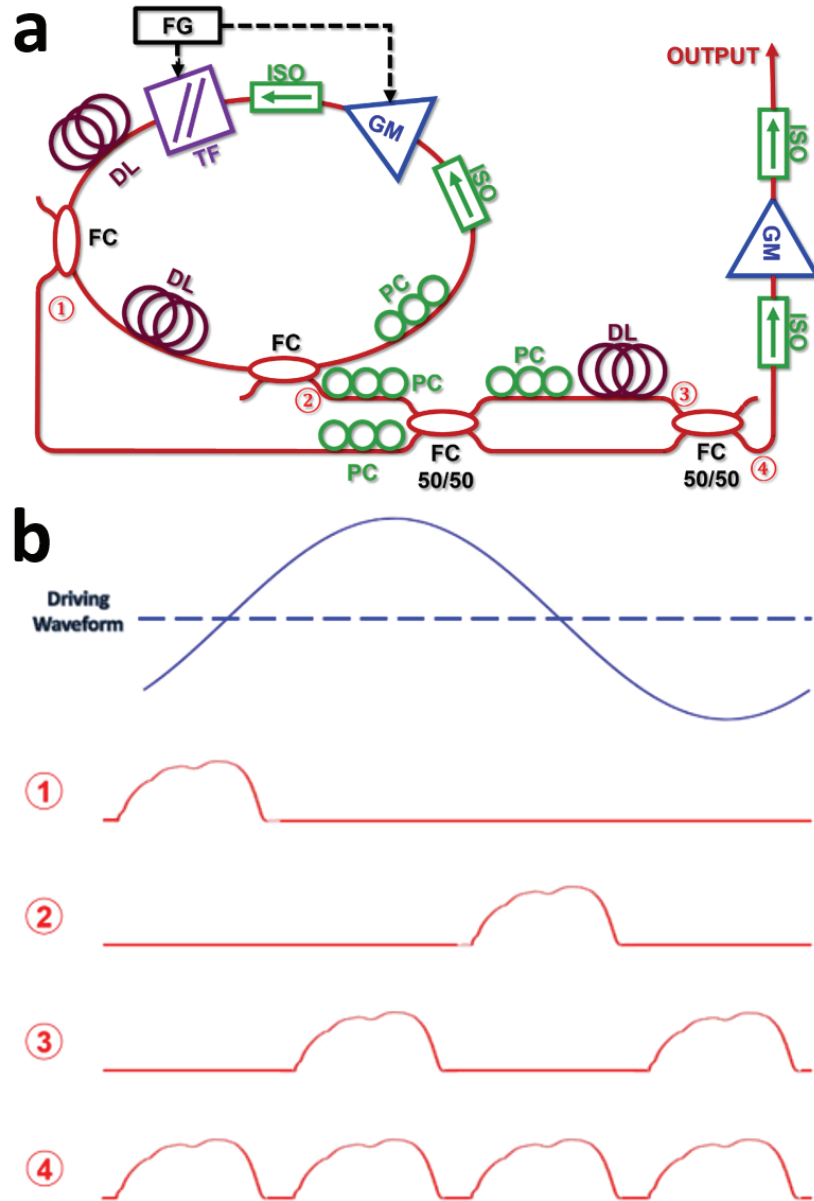


Figure 4.4 (a) Schematic of a double buffered Fourier domain mode locking laser and (b) an illustration of time multiplexing of the double buffered Fourier domain mode locking laser. DL: optical delay line; FC: fiber coupler; FG: function generator; GM: gain medium; ISO: optical isolator; PC: polarization controller; TF: tunable filter.

The basic steps in the optical time multiplexing setup is: (1) mix and split the two copies of the sweeps by the first coupler, (2) delay half of the mixed copies by a quarter of

the sweeping period (labeled as 3 in Fig. 4.4a and illustrated in Fig. 4.4b), and (3) recombine four copies together by the second coupler (labeled as 4 in Fig. 4.4a and illustrated in Fig. 4.4b). Therefore, the A-scan rate of a double buffered FDML laser is quadrupled to its sweeping frequency. Since the two couplers attenuate the light more than 6 dB, another optical amplifier is placed at the end of the optical path to boost the total output power. The buffering order number can be further increased by keep putting optical time multiplexing setups in series [139]; the A-scan rate of a multiple buffered FDML laser is 2^n times of its fundamental sweeping frequency, where n is the buffering order number of the laser.

4.2 Design of a Double-buffered Fourier Domain Mode-locking Laser

In this dissertation, a double-buffered FDML laser was built to achieve an A-scan rate of ~ 220 kHz. The fundamental sweeping frequency of the FDML laser was determined by the mechanical frequency response of the tunable filter. The optical cavity design that is followed by the description in the previous section was chosen to form a single buffered FDML laser. An optical time multiplexing setup was employed to quadruple the A-scan rate to achieve double buffering stage.

4.2.1 Tunable filter and its Driver

The most essential and decisive component in a FDML laser is the tunable filter that can selectively allow a narrow linewidth of light to pass through over a broad wavelength sweeping range (in other words, having a high finesse) at a fast sweeping frequency.

Here we chose a fiber optic Fabry-Perot tunable filter from Lambda Quest LLC [170]. The tunable filter (S/N: X552) has a FSR of 164.0 nm with a finesse of 700, which gives us a linewidth of ~ 0.23 nm. It can be safely driven over a few tens of kHz. The

frequency response of this tunable filter (i.e., sweeping range per unit drive voltage versus sweeping frequency) was measured as shown in Fig. 4.5, where the fundamental resonant frequency is shown to be 53 kHz.

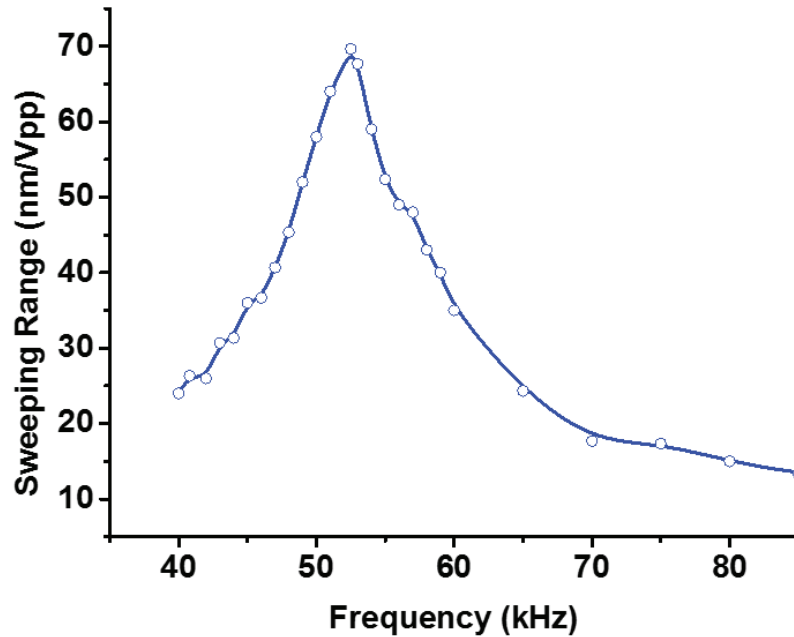


Figure 4.5 Mechanical frequency response of the Fabry-Perot tunable filter (S/N: X552). Its fundamental resonant frequency is at ~53 kHz as indicated by green dashed line. The drive frequency was set at ~55 kHz to avoid instability at the resonant frequency while maintaining a wide sweeping range.

The electric characteristics of the tunable filter is simply equivalent to a capacitor; a higher drive voltage and a higher drive frequency can both lead to a higher drive current. Therefore, its drive frequency cannot be too far away from its resonant frequency in order to maintain a broad sweeping range and an acceptable drive current at the same time. However, a severe instability was observed when the tunable filter was driven too close to its resonant frequency. A drive frequency of 55 kHz was, therefore, chosen to balance the two dilemma. At this frequency, the tunable filter can sweep over 300 nm at a peak-to-peak voltage of 4.5 V and the maximal driving current was measured to be about 700 mA.

Due to the nonlinear response and high hysteresis of the tunable filter, a pure sinusoidal drive waveform is usually preferable. Most modern arbitrary function generators are driven by digital clocks from a phase-locked loop (PLL) circuits, in which jitter inevitably exists. And jitter would cause phase noise in the clock signal, leading to a distortion of sinusoidal waveform. Since the jitter is random, any high order distortion is out of phase with the fundamental frequency of the sinusoidal waveform. This phenomenon would cause instability in a FDML laser. Therefore, the sinusoidal waveform was generated from an ultralow distortion arbitrary function generator (Stanford Research System DS360).

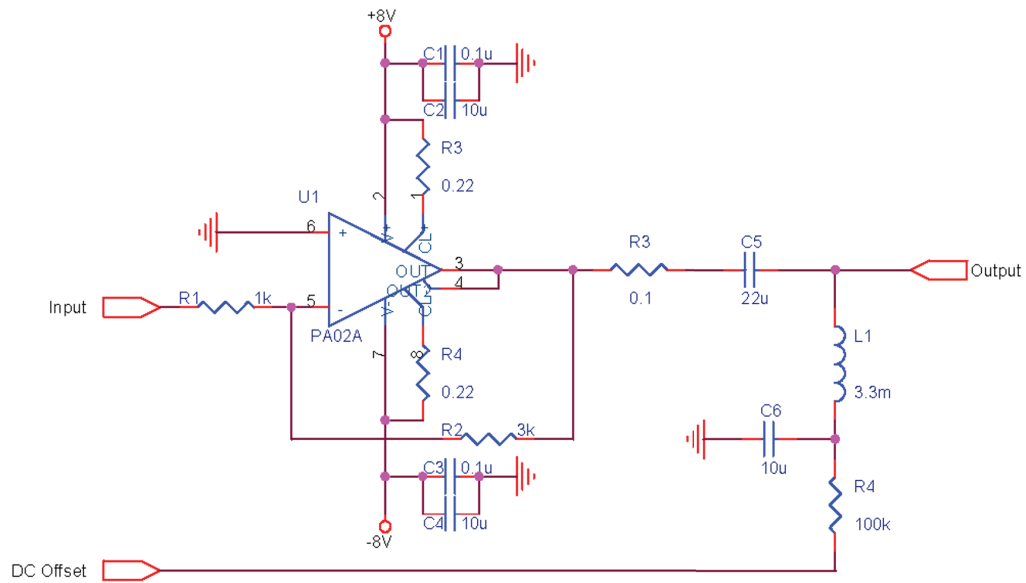


Figure 4.6 Schematic of tunable filter driver. There are three ports, which are input, DC offset, and output, in this circuit. A sinusoidal waveform was first amplified via a closed loop power amplifier; the amplified signal was then combined with a DC offset voltage to drive the tunable filter.

The drive waveform was then amplified via a home built power amplifier, the schematic of which is shown in Fig. 4.6. The operational power amplifier used here was PA02A from Apex Microtechnology, which is a Class A/B power amplifier to balance

between efficiency and linearity. The power amplifier was driven by a $\pm 8\text{V}$ dual power supply with bypass capacitors. It has a gain bandwidth product of 4.5 MHz and can provide power bandwidth of up to 350 kHz. Due to the fact that the tunable filter is a capacitive load, the closed loop gain of -3 was chosen (i.e., R_2/R_1), which provided enough stability margin in the circuit. A small power resistor of $0.3\ \Omega$ (i.e., R_3) was put in series after the power amplifier to provide extra phase margin to keep the circuit stable. In order to avoid overdriving the tunable filter, two current limiting resistors in the circuit (i.e., between pin 1 and 2; pin 7 and 8) clamped the drive current at 2 A. To prevent the two reflective surfaces in the tunable filter from colliding with each other, a drive waveform has to be positively biased. In order to do so, a DC offset was combined with amplified AC signal through a LC bridge (i.e., L_1C_5). However, to eliminate the flyback from the inductor L_1 , the DC offset was slowly charged via a RC circuit (i.e., R_4C_6). Since the noise in the driving waveform greatly affects the performance of the tunable filter driver, a pair of DC power supplies were carefully chosen to ensure minimal voltage ripples.

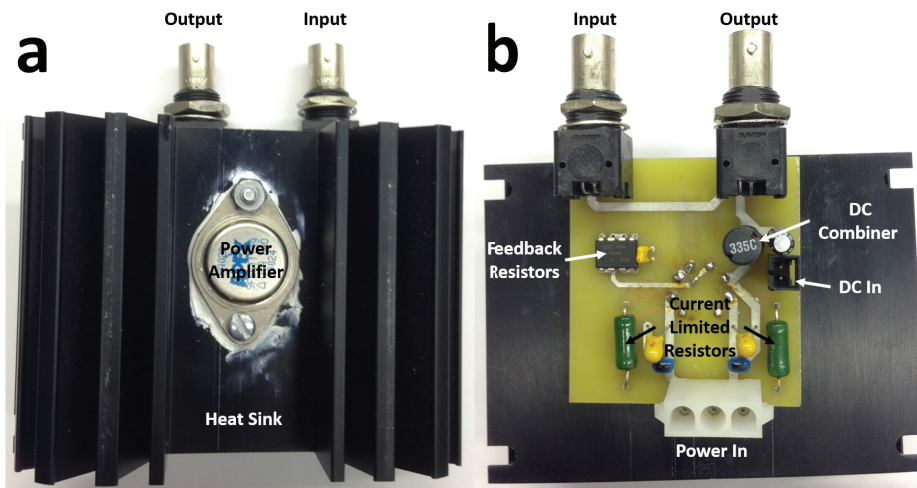


Figure 4.7 Photos of PCB board of the tunable filter driver; (a) front side and (b) back side.

A few practical considerations had to be taken into account when designing the drive. The printed circuit board (PCB) are shown in Fig. 4.7 on both sides. Since the designed working frequency is under 1 MHz, two layered PCB was used. In addition, the tunable filter is a capacitive load so that most of the power is dissipated on the power amplifier. A heat sink, therefore, need to be properly selected and installed. Moreover, resistors array was used as feedback resistors (i.e., R_1 and R_2) to minimize the temperature dependency of the gain. Finally, current limiting resistors (i.e., R_3 and R_4) and DC combiner (i.e., L_1C_5) were carefully chosen to ensure they are able to hold a high current. This driver was tested to work properly with a drive frequency of <200 kHz.

4.2.2 *Optical Cavity Design*

Once the fundamental sweeping frequency was set to ~55 kHz, the total length of the optical cavity was calculated to be 5450.77 meters in optical pathlength. Considering most of the optical cavity is made of optical fiber spools (i.e., SMF28e+), the physical length of the optical cavity was designed to be 3713.82 meters. The schematic of the optical cavity in the double-buffered FDML laser was illustrated in Fig. 4.8. The actual lengths of the two fiber spools in the cavity acting as optical time delay line were chosen to be 1848 and 1856 meters, respectively. The length of the rest cavity, including an SOA, a fiber optical tunable filter, two fiber couplers, and two fiber optic isolators, are approximately 12 meters. Therefore, the actual optical cavity length was ~3716 meter. In order to achieve a stable power output of a double-buffered FDML laser of a sweeping range of 150 nm at a central wavelength of 1310 nm, the requirement for the linewidth of the tunable filter, which was modified from Eq. (4.7) to adopt the double buffered FDML laser, was:

$$\Delta\lambda_f = \frac{164 \text{ nm}}{700} = 0.23 \text{ nm} \geq \frac{c \cdot \Delta\lambda_{FW}^2 \cdot D \cdot \pi}{4n_{eff}} = 0.092 \text{ nm} . \quad (4.8)$$

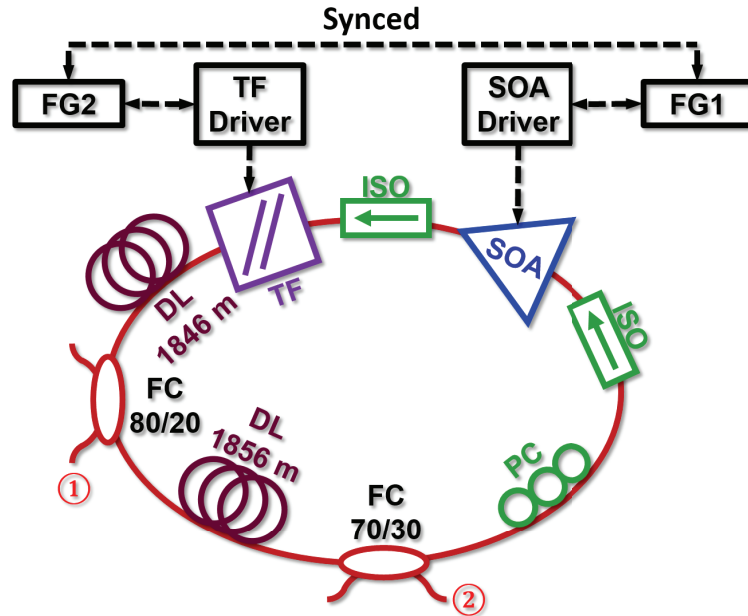


Figure 4.8 Schematic of the optical cavity in designed double buffered FDML laser. DL: optical delay line; FC: fiber coupler; FG: function generator; ISO: optical isolator; SOA: semiconductor optical amplifier; TF: tunable filter.

The SOA (i.e., BOA1132S from Thorlabs Inc.) was turned on less than a quarter of each period (i.e., duty cycle: 22%) by a laser diode driver (LDTC 2/2 E from Wavelength Electronics, Inc.). And the laser diode driver was modulated by a square shaped waveform from an arbitrary function generator that was synchronized with the function generator that drove the tunable filter. Two broadband two-stage fiber optic isolators were placed at both end of the SOA to ensure about 60 dB isolation so that the light travels inside the cavity in a unidirectional way. The tunable filter driven by a home-built driver described in previous subsection was placed in front of one of the isolators to select a narrow linewidth of the light at a given time; its driving waveform was synchronized with the modulation drive waveform of the SOA. Two broadband fiber couplers were used to pick up partial light from the cavity as two half sweeping period apart copies. In order to keep the power levels

from two couplers close to each other, an 80/20 fiber coupler was placed between the first optical delay lines and the tunable filter while a 70/30 fiber coupler was placed between the two optical delay lines. Since the gain medium is a polarization dependent SOA, a manual fiber optic polarization controller was placed in the optical loop to manage the polarization state inside the cavity.

4.2.3 Optical Time Multiplexing Design

Based on the optical cavity design, the two copies of the sweeps from the inner cavity above were separated in half of the period of the driving waveform, which provided an A-scan rate as twice as the driving frequency of the tunable filter. In order to further increase the A-scan rate, an optical time multiplexing setup was implemented as described in previous section. In short, the two copies of the sweeps were mixed via a 50/50 fiber coupler so that both arms of this coupler have two identical copies of the combination of two temporal separated sweeps. One of the copies was then delayed by a quarter of the period of the driving waveform through an optical delay line while another copies was not. These two copies were combined via a second 50/50 fiber coupler to generate four copies of the sweeps. Since there are more than 6 dB loss in this setup, another SOA (i.e., BOA1132S from Thorlabs Inc.) was used to boost the output. In order to manage the polarization states in the optical time multiplexing setup, three polarization controllers were placed in this setup as shown in Fig. 4.9.

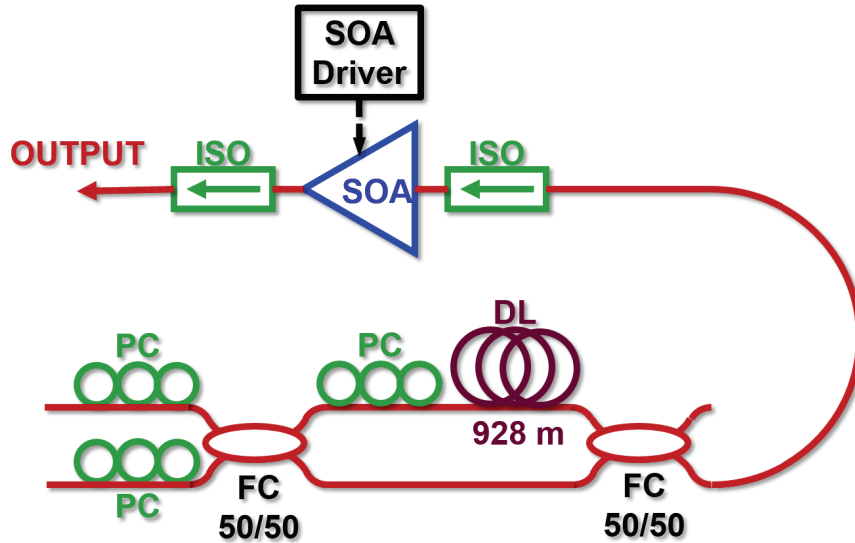


Figure 4.9 Schematic of the optical time multiplexing setup in designed double buffered FDML laser. DL: optical delay line; FC: fiber coupler; ISO: optical isolator; PC: polarization controller; SOA: semiconductor optical amplifier.

4.2.4 Performance of the double-buffered FDML

The actual sweeping frequency of the double-buffered FDML laser was measured to be about 54.95 kHz, which gave us an A-scan rate of 219.8 kHz. The total output power from the laser was measured to be about 65 mW. The optical spectrum from the laser was measured by an optical spectrum analyzer. It was shown in Fig. 4.10a that a full bandwidth of the sweeps is ~135 nm and a FWHM of the bandwidth is ~90 nm. The bandwidth, which determines the axial resolution of the SS-OCT system using such a laser, was limited by the bandwidth of the SOA in the FDML laser. Interference results of the four copies of the sweeps were shown in Fig. 4.10b via a Mach-Zehnder interferometer with an FSR of 30 GHz (i.e., equivalent to an optical pathlength difference of 5.0 mm between its two arms). The copies from different ports in the double buffered FDML laser was indicated with encircled numbers that are defined in Fig. 4.4. Although there were slight differences of

the spectral shape among these four copies of the sweeps, their point spread functions (PSF) were very similar to each other.

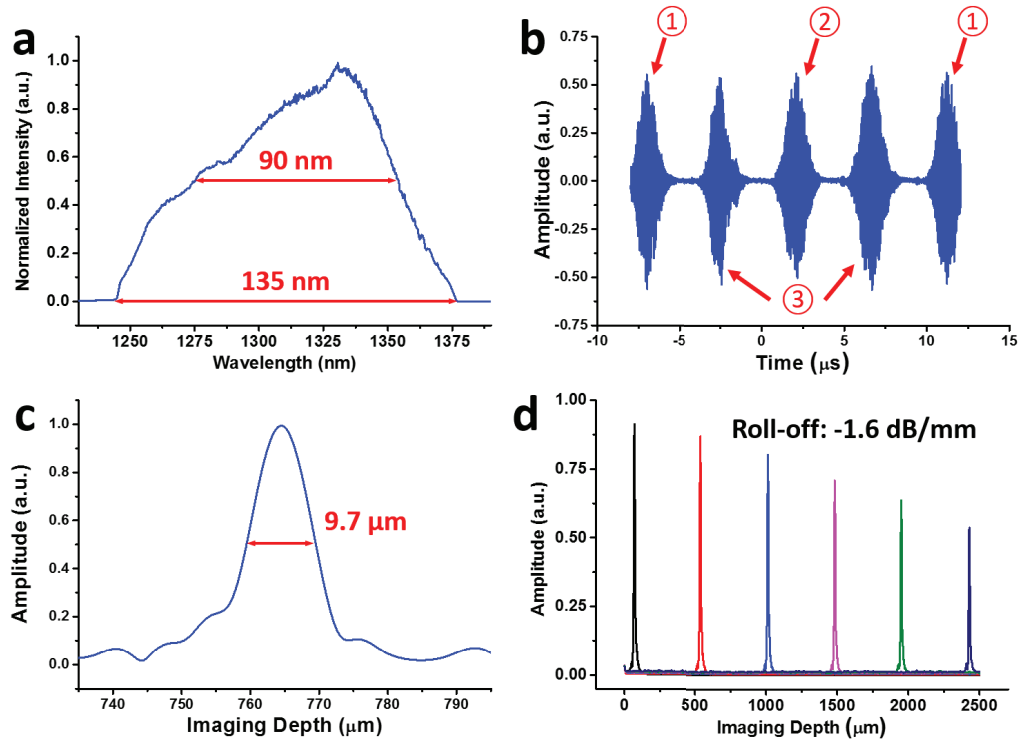


Figure 4.10 (a) Output spectrum of the double buffered FDML laser measured by optical spectrum analyzer. (b) An interference signal of a Mach-Zehnder interferometer with a FSR of 30 GHz. The encircled numbers indicate the four copies of the sweeps as labeled in Fig. 4.4. (c) The point spread function of 9.7 μm at an imaging depth of $\sim 765 \mu\text{m}$. (d) The point spread functions at different imaging depths indicate a detection sensitivity roll-off of -1.6 dB/mm.

A PSF of 9.7 μm at an imaging depth of $\sim 765 \mu\text{m}$ was shown in Fig. 4.10c and a detection sensitivity roll-off of 1.6 dB/mm was measured in Fig. 4.10d, which is close to the reported results [162, 171]. At last, OCT images of a human fingernail were displayed in Fig. 4.11 to test the performance of the FDML laser.

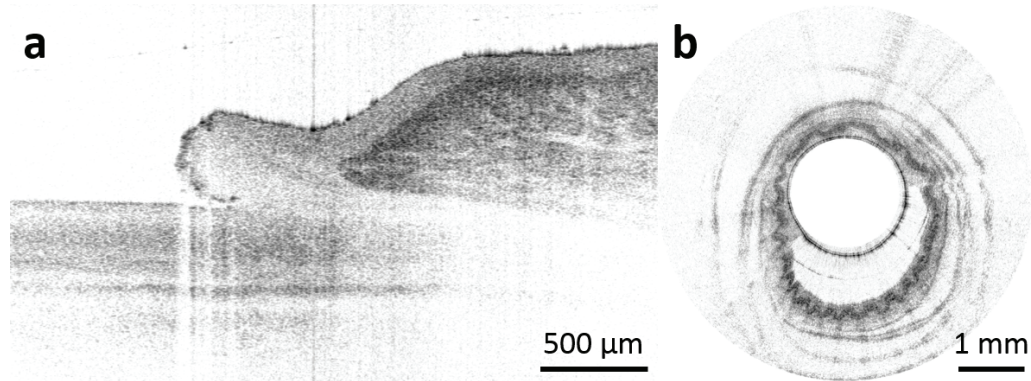


Figure 4.11 (a) A representative OCT image of human finger nailbed *in vivo*. (b) A representative endoscopic OCT image of pig bronchus *in vivo*.

4.3 Future Improvement

There are two major limitations in the FDML laser, which comprises the performance of the laser.

Although this laser works close to the zero dispersion wavelength of the optical fiber (i.e., 1313 nm), there is still some small residual dispersion inside the optical cavity, which decrease the spectral bandwidth and the instantaneous linewidth of the laser. Thus, a dispersion compensation setup can further improve the performance of the FDML laser [106, 172].

Due to the long length of the optical delay lines used in the FDML laser, the polarization state in the laser was influenced by both mechanical vibration and thermal fluctuation. A FDML laser, thus, usually requires lots of degrees of freedom to manage its polarization state. Potentially, however, this could be improved by employing a sigma ring cavity [172]. Such a setup could compensate the polarization state completely when the light travels inside the cavity twice in the opposite directions. Combining with other polarization managed components (e.g., SOA, fiber coupler, etc.), the whole FDML laser can be free of dispersion management.

Unfortunately, these two aforementioned improvements have not been implemented in current FDML setup yet due to the limited bandwidth of a few indispensable components (e.g., chirped fiber Bragg grating and Faraday rotator mirror). The implementation will become feasible in the future when the components with broader bandwidth are developed.

4.4 Summary

In this chapter, we first introduced the basic principle of wavelength swept lasers. Among those wavelength swept lasers, FDML lasers were thoroughly discussed. Based on the conclusions and analysis in the first section, a double-buffered Fourier domain mode-locking laser was developed in the second section to achieve an A-scan rate of ~ 220 kHz and the basic performance of the laser was tested.

Intended to be blank

Chapter 5 OCT Interferometers and Detection Electronics

This chapter describes the OCT interferometer setup used in the high-speed endoscopic OCT system used in this dissertation and demonstrated how to achieve a shot-noise limited detection in the imaging system. Real-time uniform K-space sampling, a hardware based method that was developed for calibration of the OCT interference signal is introduced.

5.1 OCT Interferometers

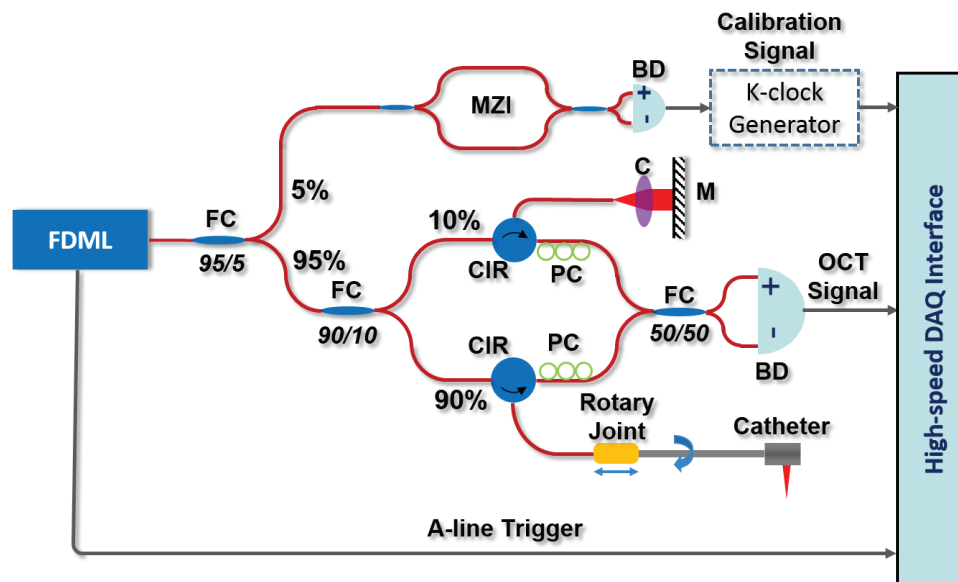


Figure 5.1 Schematic of the endoscopic OCT interferometers. BD: balanced detector; C: collimator; CIR: optical circulator; FC: fiber coupler; M: mirror; MZI: Mach-Zehnder interferometer; PC: polarization controller.

The endoscopic OCT interferometer setups that were employed in the high-speed endoscopic OCT system is illustrated in Fig. 5.1, which consists of two Mach-Zehnder interferometers. 5% of the light from the double buffered FDML laser described in the last

chapter was sent to an auxiliary interferometer to generate a calibration interference signal of a free spectral range (FSR) of 60 GHz by an all-fiber Mach-Zehnder interferometer with a 5-mm optical pathlength difference between its two arms; the rest 95% of the light was delivered into the OCT interferometer to generate the OCT interference signals. The calibration signal was directly sent to the high-speed digitizer to calibrate the OCT data. Alternatively, an optional K-clock generator can convert the calibration signal into digital clock signal that drives the digitizer, which will be described in Section 5.3. The light to the OCT interferometer was split via a 90/10 fiber coupler (Dual window wideband coupler from LIGHTEL), where 90% of the light was sent to the sample arm and 10% of the light was sent to the reference arm. Two fiber optic circulators were placed in both arms to redirect the reflected/backscattered light from both arms to a 50/50 fiber coupler (Ultra flat dual window wideband coupler from LIGHTEL) where the interference signal was generated. Two manual polarization controllers was placed on the two arms to match and optimize the polarization states of both signals. A balanced detection scheme was employed at the end of the interferometer. It should be pointed out that there are three major advantages using this interferometer setup. First of all, the majority of the light power was sent to the sample arm so that the OCT signal detection would not suffer from power deprivation. Secondly, the balanced detection scheme can remove the DC components as well as some types of the noises from the total interference signal. Finally, the balanced detection scheme can also improve the detection sensitivity of the system by 3 dB if shot noise limited detection is assumed.

5.2 Shot-noise Limited Detection

In order to display OCT images on a screen, the optical interference signals have to be first converted into electronics via photodetectors. Detection electronics in a SS-OCT system is essentially balanced detectors, which is consisted of a pair of balanced PIN photodiodes and amplification electronics. Currently, most detection electronics used in SS-OCT systems are commercially available ones. In the OCT interferometer, a balanced detector (PDB430C from Thorlabs Inc.), which has an optical spectral range from 800 to 1700 nm and an electronic bandwidth of 350 MHz, detects the OCT signals. In the auxiliary interferometer, another balanced detector from Newport Corp. (1617-AC-FC), which has an optical spectral range from 900 to 1700 nm and an electronic bandwidth of 800 MHz, detects the calibration signals.

In order to get the best detection sensitivity in an OCT system, detected signal has to be set into a shot noise limited detection region, which is mainly adjusted by setting a proper optical power level in the reference arm. The noise level of the balanced detector in the OCT interferometer (i.e., Thorlabs PDB430C) was measured as a function of the incident optical power to the detector in Fig. 5.2. A shot noise model was also built in Fig. 5.2 as a blue dash line, which has a 5 dB/decade slope. The shot noise limited detection region was indicated as blue area in Fig. 5.2 (i.e., when the incident optical power is greater than 30 μ W). On the other hand, the incident optical power in the reference arm should not be set too large for two reasons: (1) excess noise might become dominant; and (2) the optical heterodyne gain may become too high and the detector will be electronically

saturated easily. Therefore, the incident optical power in the reference arm was finally set to be around $50 \mu\text{W}$.

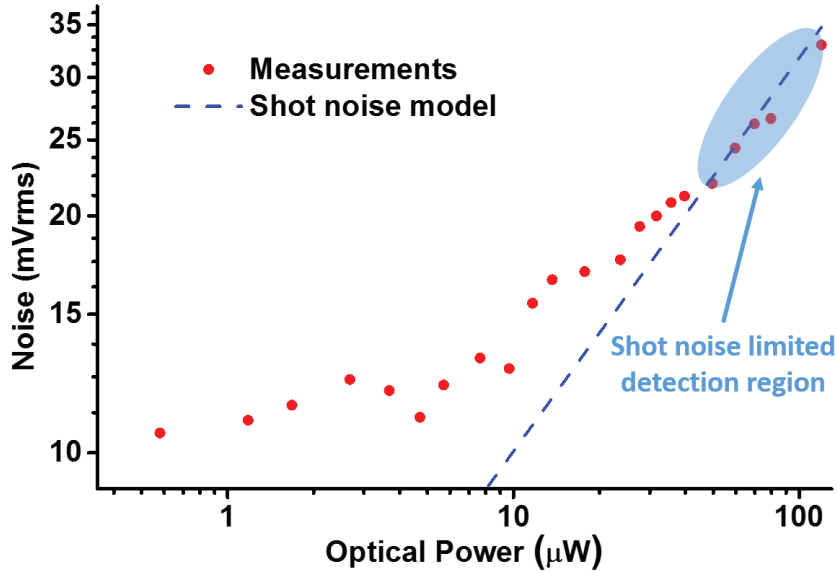


Figure 5.2 The measurements of electronic noise from the balanced detector (Thorlabs PDB430C) versus the incident power to the detector. A shot noise model is shown as blue dash line that has a 5 dB/decade slope.

5.3 Real-time Uniform K-space Sampling Method

The method and results described in this section have been published in [100].

Since the driving waveforms in most wavelength sweeping lasers are sinusoidal and frequency response of the tunable filters are usually nonlinear and hysteretic, the wavenumber sweeping speed is not linear with respect to time, which requires a calibration procedure prior to Fourier transform. The axial resolution, otherwise, would be severely degraded without calibration (i.e., red curve in Fig. 5.3); an uncalibrated point spread

function usually looked skewed with lots of big side lobes, which represented the raw data is chirped in time.

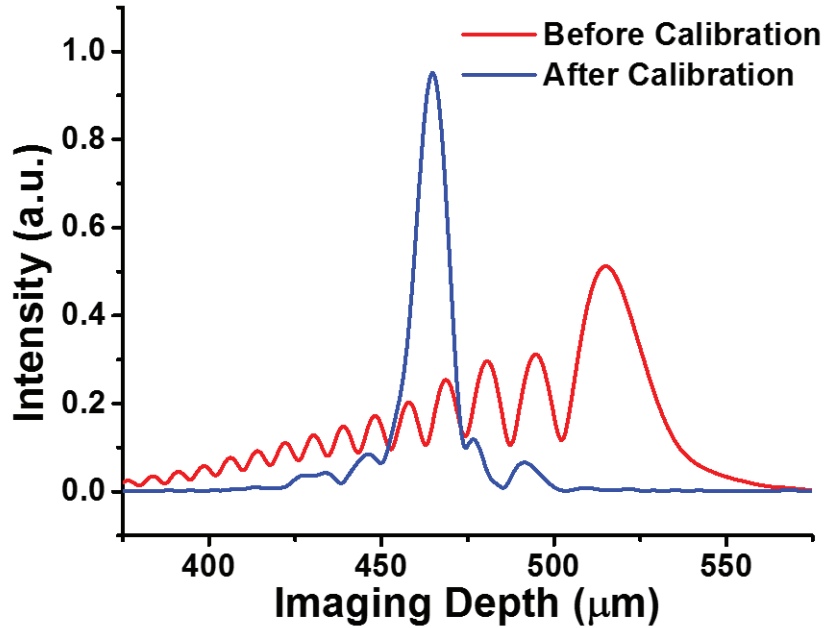


Figure 5.3 A comparison of point spread functions of the SS-OCT system (a) before calibration and (b) after calibration.

An interference signal was generated via an auxiliary interferometer with a fixed optical pathlength difference (i.e., 5.0 mm) to calibrate actual OCT interference signal into a linear-in-wavenumber fashion. After calibration, the discrete signal became uniformly distributed and the point spread function recovered to its theoretical limit (i.e., blue curve in Fig. 5.3). The software based numerical calibration algorithm will be discussed in the next chapter. Here we focused on a hardware based data acquisition method, which is real-time uniform wavenumber space (K-space) sampling method using high-speed digital electronics in order to control the digitizer to sample the data in a non-uniform fashion in temporal space but uniform in K-space.

5.3.1 *Principle and Method*

The basic idea of the hardware based method is to use the interference signal from the auxiliary interferometer to generate a digital clock signal (K-clock) to drive the high speed digitizer. Although the period of the clock signal varies in temporal space, it keeps the same in K-space. Therefore, the actual OCT interference signal should be uniformly digitalized via a high speed digitizer driven by the K-clock.

There are three major design considerations in order to implement such a method. Conventionally, the numerical calibration algorithm usually uses the calibration signal to identify two data points on the OCT signal with equal K-spacing for every fringe cycle of the calibration signal (e.g. the extrema or zero-crossing points). Under the Nyquist sampling theorem the imaging depth is thus the same as the optical path difference in the auxiliary interferometer. For the same reason, the uniform K-space sampling method requires two clock cycles with an equal K-space interval for each fringe cycle of the calibration signal. The second one is related to high-speed digitizer. Most high-speed, high resolution digitizers use an ADC with a pipeline architecture that requires a clock duty cycle close to 50% to prevent the ADC from malfunctioning and prevent degradation of the spurious-free dynamic range (SFDR). Moreover, as most high-speed digitizers prefer to operate in a continuous mode in order to avoid repeated reset of internal circuitry (and the associated loss of speed), a dummy clock signal is thus needed to fill the idle gap between two consecutive OCT A-scans. Other two practical considerations are the propagation delay and jitter time of the external clock circuitry. Since the optical frequency

information is encoded in time in an SS-OCT system, the propagation delay time of the external clock relative to the OCT signal must be carefully calculated and compensated. In addition, the electronic jitter time also needs to be minimized to avoid random triggering of the ADC. Thus a high-speed logic gate with minimal jitter time becomes critical for generating a stable external clock signal.

The block diagram of the K-clock generator is shown in Fig. 5.4a. In order to generate two clock cycles for each period of the calibration signal, a broadband 90° phase shifter was employed to produce a quadrant signal from the original calibration signal. The original and quadrant signals (Fig. 5.4b) were sent to two separate zero-crossing detection devices (Fig. 5.4a), which output two square-waves with “level high” corresponding to the positive portion of the original and the quadrant signal, respectively (Fig. 5.4c). The two square waves were then combined through an exclusive OR (XOR) gate, which generated an external clock pulse when the two square waves overlap (Fig. 5.4d). This method produced two clock pulses for each period of the calibration signal. To fill the empty gap on the external clock between adjacent A-scans, a dummy clock signal (the pulses in green color in Fig. 5.4d) was generated within the time duration complementary to the time gate for the zero-crossing detection, and then combined with the zero-crossing clock signal by a XOR gate to form a final external clock (both the green and black pulses in Fig. 5.4d), which triggered a high-speed digitizer on the rising edges for uninterruptedly digitization in a uniform K-space fashion.

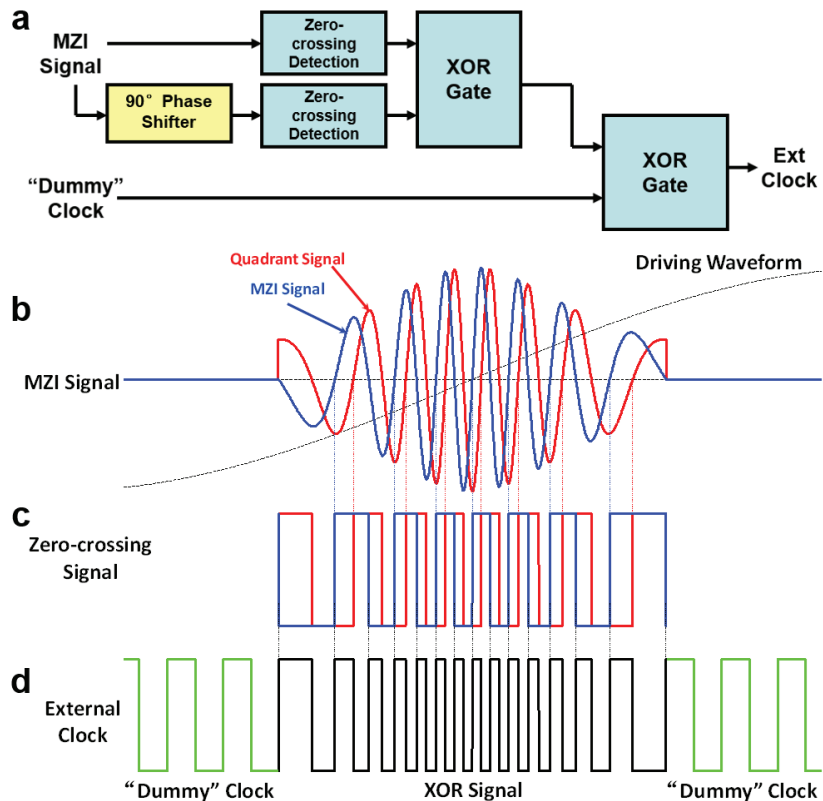


Figure 5.4 (a) Block diagram of the K-clock generator. (b) Illustration of the original MZI signal (blue line) and its quadrant signal after the broadband 90° phase shifter (red line). (c) Illustration of zero-crossing signals generated from the MZI and quadrant signals in (b). (d) External clock signal that combines the XOR gate output with a gap-filling dummy clock. The vertical dotted lines indicate the rising edges of the signals.

The schematic of the K-clock generator circuit is shown in Fig. 5.5. The circuit is a mixed signal circuit where the phase shifter (JSPQ-65W + from Mini-Circuits) and the input of the zero-crossing detectors (MAX9693 from Maxim Integrated Products, Inc.) is analog and the rest of the circuit is digital. In order to suppress the interference between analog and digital circuit, the analog and digital ground are connected via a 10 μ H inductor (i.e., L_1). The digital logic level used in this circuit was emitter-coupled logic (ECL).

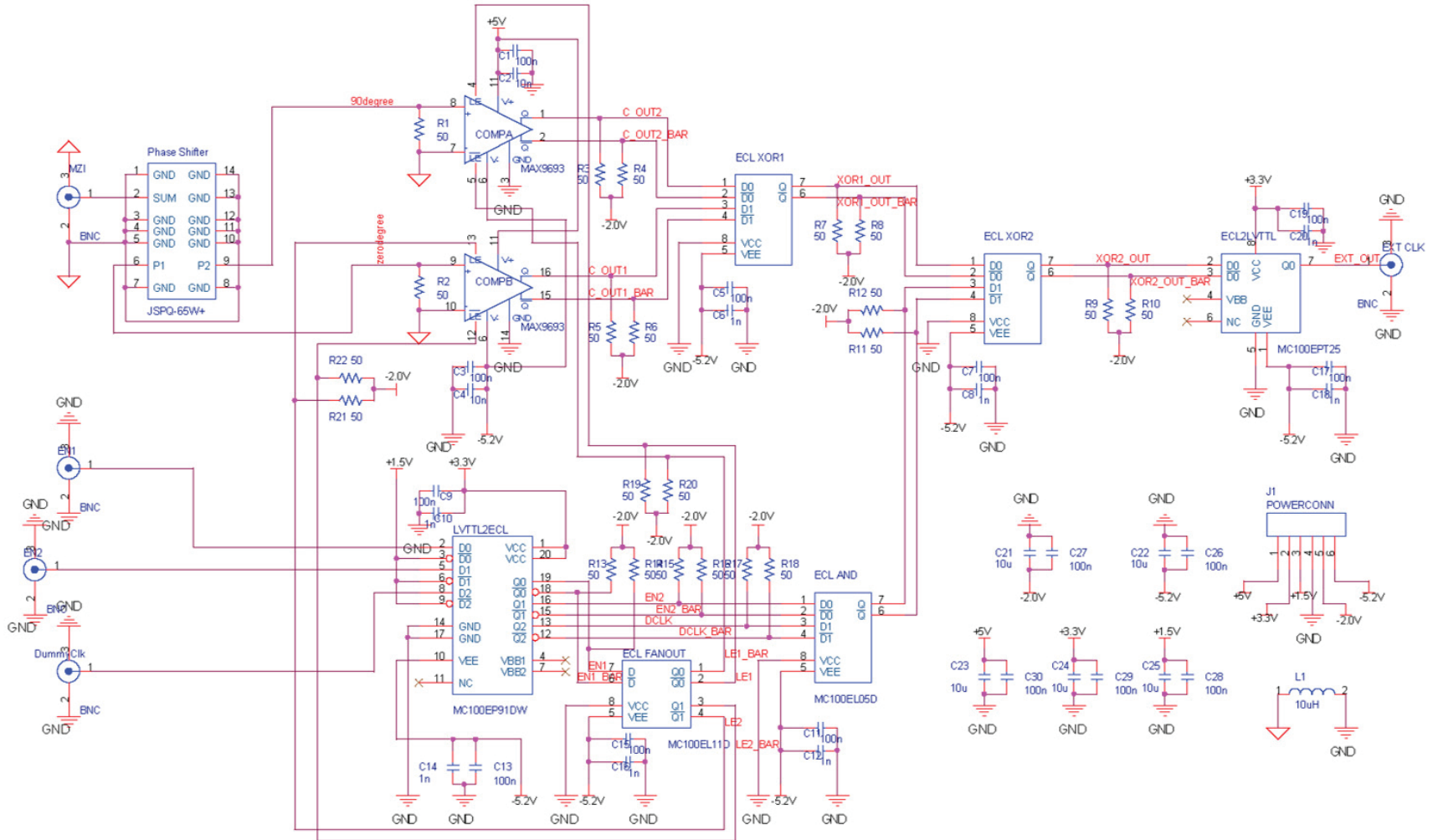


Figure 5.5 Schematic of the K-clock generator circuit

Unlike commonly used logics (e.g., TTL and CMOS), the transistors in the ECL logic are never in saturation so that the change of states in ECL is very fast (i.e., propagation time is usually less than 1 ns and jitter is usually on the order of 10 ps). The combination of a quadrant phase shifter and an XOR gate (MC100EL08 from ON Semiconductor) ensures the external clocks have an ~50% duty cycle. For our current off-the-shelf simple phase shifter, the change in phase unbalance over more than 3 octaves (5 MHz to 65 MHz) is less than 2° , and the resulted duty cycle only varies around $50\% \pm 0.3\%$, which helped maintain and maximize the SFDR of an ADC during the entire A-scan. As a result, the designed circuitry can generate a clock signal for A-scan rates from 20 to 100 kHz. The dummy clock and the ENABLE window signal[§] that generated externally in low-voltage transistor-transistor logic (TTL) were first converted into ECL logic via a logic converter (MC100EP91 from ON Semiconductor). The inverted ENABLE window signal was used to turn off the zero-crossing detectors via a fan-out device (MC100EL11 from ON Semiconductor). Meanwhile, the dummy clock was gated by the ENABLE window signal via an AND gate (MC100EL05 from ON Semiconductor). The K-clock signal was then combined with the gated dummy clock signal via an XOR gate (MC100EL08 from ON Semiconductor). A XOR gate was used here instead of an OR gate because the logic of the K-clock signal was random when the zero-crossing detector was disabled. At last, the

[§] Two ENABLE signals are shown in the schematic only for debugging purpose. They are identical when the K-clock generator properly works.

combined signal was converted to low-voltage TTL via a logical convertor (MC100EPT25 from ON Semiconductor) so that the signal can be accepted by the high-speed digitizer (ATS9462 from Alazartech Inc.).

A few practical considerations had to be taken into account when designing the generator. Since the circuit work close to 100 MHz, a four layered printed circuit board (PCB) are designed as shown in Fig. 5.6 on both sides. The most of the lines on the top layer of the PCB is mostly signal; the middle two layers are digital ground and -5.2V power layers; other power layers and bypass capacitors are laid out on the bottom layer. The footprint of all the discrete components on the board were small surface mount to reduce their parasitic capacitance. In order to further minimize the noise in analog portion in the circuit, an analog ground was poured around the phase shifter. Additionally, all the lines that transmit the digital signals were transmission lines, which means that the line width were carefully chosen to match the input impedance among the IC chips (i.e, 50 Ω) in order to minimize the reflection among the chips. This circuit was tested to work properly with a frequency of <130 MHz.

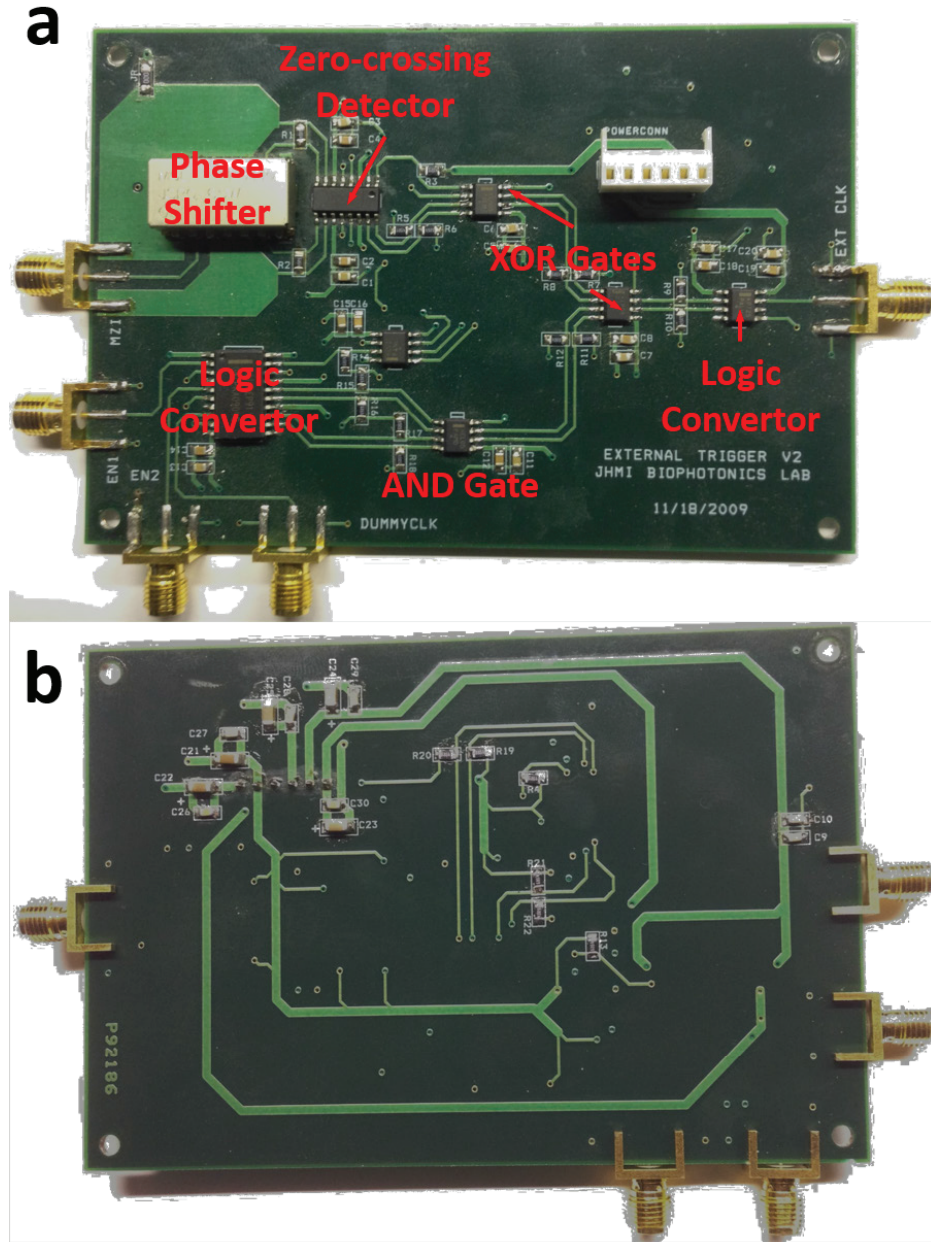


Figure 5.6 Photos of PCB board of the K-clock generator; (a) front side and (b) back side.

5.3.2 Performance and Results

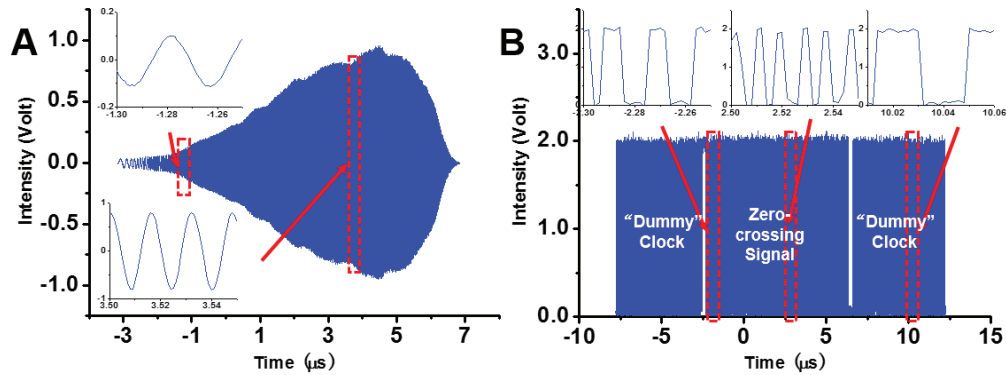


Figure 5.7 (a) MZI interference signal. The upper and lower insets show the MZI signal at the beginning (or end) and the center of an A-scan, respectively, indicating that the MZI signal frequency varies during wavelength scanning. (b) External clock signal during forward wavelength scanning with the FFP-TF driven by a 40 kHz sinusoidal wave. The insets show the duty ratio of the external clock keeps very close to 50% which is essential to keep the high-speed digitizer working properly and continuously.

The K-clock signal was measured with an FDML laser of a sweeping frequency of 40 kHz. The total number of fringe cycles of the forward scan signal is 409 and the corresponding number of the sampled data points per A-scan is therefore 818. It is noted that the frequency of the MZI signal varies a lot, e.g., the frequency of the slow fringe region (~ 25 MHz) with a zoomed-in version shown in the upper inset of Fig. 5.7a is less than half of the fast fringe region (~ 55 MHz) with a zoomed-in version shown in the lower inset. The external clock signal is shown in Fig. 5.7b which was to trigger the high-speed digitizer in a point by point fashion. The trigger frequency in the middle portion of the clock signal is about 110 MHz, while the clock frequency slows down to about 50 MHz at the edge of each A-scan. The frequency of the “dummy” clock should be high enough to fill in enough clock cycles in order to keep the digitizer working continuously, and in our case it was chosen to be 28 MHz or higher. It should be noted that the duty ratio of the external clock over the entire

A-scan is close to 50% as shown in the insets in Fig. 5.7b, which is required for maintaining a good FSDR for a high-speed digitizer as mentioned previously.

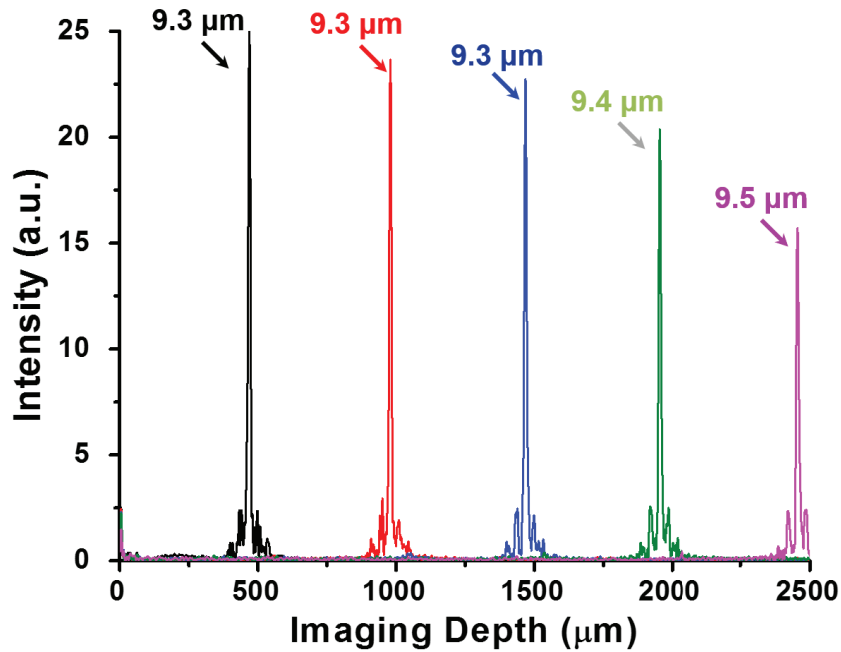


Figure 5.8 Depth dependent point spread function of an FDML-based SS-OCT system equipped with the real-time linear K-space sampling method revealing no axial resolution degradation throughout the imaging depth of 2.5 mm.

The measured axial resolution is 9.3 to 9.5 μm in air as shown in Fig. 5.8 for a FDML laser of a sweeping frequency of 40 kHz, and the axial resolution remains almost the same throughout the entire imaging depth of 2.5 mm and the detection sensitivity roll-off is about -1.55 dB/mm (as shown in Fig. 5.8).

The performance of the real-time linear K-space sampling method in an FDML-based SS-OCT system was demonstrated by imaging human fingertip and nail fold. The imaging beam was delivered to and scanned over the tissue with a handheld probe. The raw data of each A-scan of about 818 points are processed in real time via 4096 points fast Fourier transform after zero-padding, and the transformed A-scan size is 2048 pixels corresponding to an optical path of 2.5 mm. Representative OCT images are shown in Fig.

5.9. Both images have been rescaled along the depth direction by the average tissue index of refraction (i.e. ~ 1.4). The final image size is about 1024×1700 pixels corresponding to a physical dimension of 2×1.4 mm (lateral \times depth). Structures such as sweat duct (SD), stratum corneum (SC), epidermis (E), nail fold (NF), and nail root (NR) can be clearly identified.

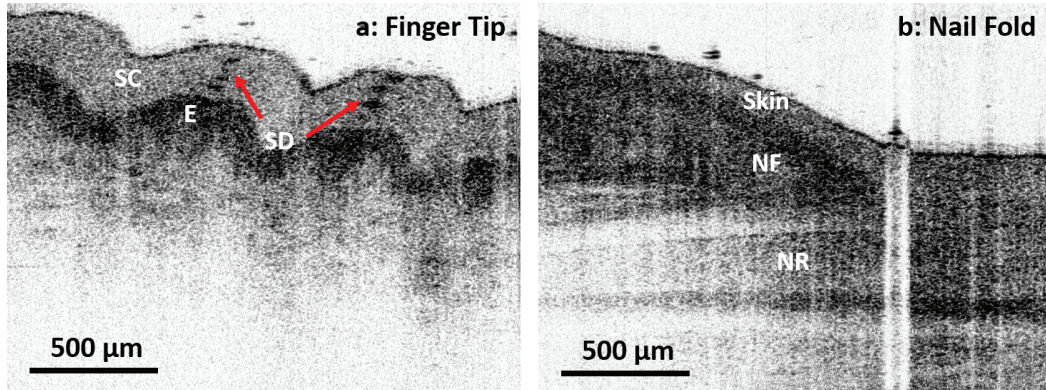


Figure 5.9 Representative images acquired with an FDML-based SS-OCT system equipped with the real-time linear K-space sampling method. (a) Finger tip and (b) finger nail fold of a human volunteer.

Comparing to software based calibration algorithm, this method has two advantages. Firstly, it reduces the speed demand in OCT signal digitization, data transfer, processing and real-time saving because it does not require oversampling as in the software based calibration algorithm. Secondly, this method in principle may provide a better phase stability.

Although this method was only tested under an SS-OCT system with an A-scan rate of 40 kHz, the home-built electronic circuit can support up to 100 kHz A-scan rate under the same circumstances (e.g., same sweeping wavelength range, same imaging depth, etc). The same principle of this method can be applied to another circuit that supports higher A-scan rate.

5.4 Summary

In this chapter, we first described the Mach-Zehnder interferometer setup used in the high-speed endoscopic OCT system. A power level on the reference arm was properly set up in order to get a shot-noise limited detection. In addition, besides commonly used software based calibration method, a hardware based method, i.e., real-time uniform K-space sampling, was developed for calibration of the OCT interference signal was demonstrated.

Chapter 6 High-speed Optical Coherence

Tomography Software Platform

This chapter describes basic mechanism of the software platform, including the choice of the software development kits, the synchronous mechanism among different modules in the software and the data flow transferred in the software. Data acquisition, data processing, data display and data storage modules are further discussed in details to show how to achieve real-time data acquisition, processing, display and storage in a high-speed OCT system.

6.1 Software Platform and High-speed Data Rate Management

Data throughput has been significantly increased by several orders and reached the era of gigabyte per second since the development of FD-OCT systems with a few hundreds of kHz A-scan rate. Accordingly, the requirements of data flow management in an OCT software, including data acquisition, processing, and storage, has also become higher. Due to the technical advances on computer and semiconductor industry, the requirements can be fulfilled in a relatively simple and cost-effective way.

In this dissertation, an OCT software program written in C++ on a personal computer with a Windows® operating system was developed to provide a software platform in order to (1) control and synchronize all the hardware components (e.g., high-speed digitizer, fiber rotary joint, translational stages, etc.); (2) process acquired raw data and display the processed data in real-time; (3) save acquired raw data into a permanent

storage device continuously in real-time; and (4) synchronize the data flow among the functions in the software (e.g., acquisition, processing, display and saving). The basic block flow of the OCT software is illustrated in Fig. 6.1. Basic functions (e.g., data acquisition, data processing, etc.) in the software are encapsulated into different modules. There are five essential modules including core, data acquisition, data storage, data processing, and display modules to make the software work properly. Except the core module, each module can be categorized into synchronous and asynchronous modules. A synchronous module, which controls a large amount of data (e.g., data processing), was executed in a separate thread on the CPU; the high-speed data was flown among the synchronous modules that was controlled by a core module to synchronize with other synchronous modules. On the other hand, an asynchronous module, which controls low speed external devices (e.g., translational stage control), was directly called by the core module whenever necessary.

The basic data flow in the software is described as follows. The raw data was first acquired by the high speed digitizer and transferred into the buffer on the computer memory in data acquisition module. The raw data was then shared between data storage and data processing modules when the buffer was full; The raw data was directly written into an external permanent storage device (e.g., hard drive) through data storage module while it was also transferred into the graphic processing unit (GPU) to be processed in data processing module. The processed data was shown on a display device controlled by OpenGL when it was ready. A histogram of the processed data was also evaluated in real time and transferred back to CPU in order to control the contrast of the final images.

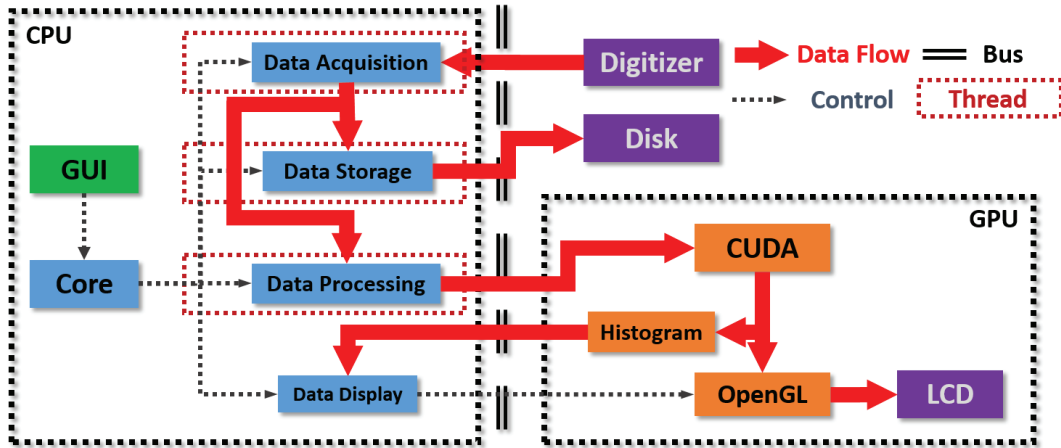


Figure 6.1. Block flow of the OCT software. Modules are shown as blue blocks; hardware components are shown as purple blocks; GPU modules are shown as orange blocks. Red arrow: high-speed data flow; blue dotted line: control commands from the core module; red dotted block: thread; double dashed line: computer bus.

The graphic user interface (GUI) of the software was developed using Qt development framework 4.8 [173] under GNU lesser general public license (LGPL) v2.1 [174]. When the program started, the GUI in the software first loaded a configuration file written in extensible markup language (XML) format [175], which contained all the preset parameters for each module. One of the advantages of using configuration file is that the software is able to flexibly load various combinations of the modules based on the requirements of different experiments. After tuning the parameters by the user (if necessary), the software initiates all the modules that has been loaded accordingly. The initialization includes buffer allocation in CPU and GPU, testing and setting hardware components, etc. When each module was successfully initiated, the software was then ready to acquire and process the data.

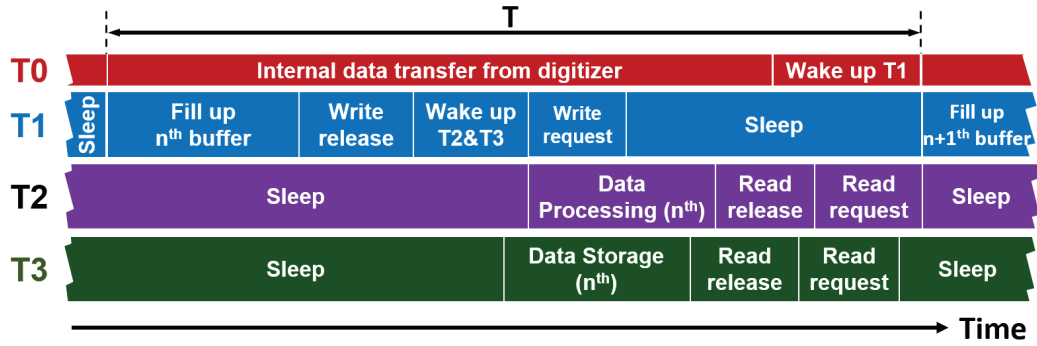


Figure 6.2. Schematic of data synchronization among different synchronous modules wrapped in threads. T0: internal thread of the digitizer driver for data acquisition; T1: data acquisition; T2: data processing; T3: data storage.

In order to manage the high-speed data flow efficiently, a buffer was created during initiation of the software and shared among all the synchronous modules. The basic schematic of data flow in the software is illustrated in Fig. 6.2. The synchronization flow was ultimately regulated by an internal thread of the digitizer driver for data acquisition (i.e., T0 in Fig. 6.2), the period time of which was usually a multiple of B frame period. The threads controlling the data acquisition module (i.e., T1 in Fig. 6.2) was woken up whenever the internal thread finished. T1 quickly filled up the buffer shared among other threads and released the write access to this buffer afterwards; it then woke up other threads and sent out a write request for the next buffer; T1 finally went to sleep after it finished every tasks in this cycle. Meanwhile, the data storage and processing threads (i.e., T2 and T3 in Fig. 6.2) that were woken up by T1 gained the read access to the shared buffer, started saving and processing the raw data in the buffer simultaneously, and released the read access after their jobs were complete; they then sent out a read request for the next available buffer before they went to sleep. T1, on the other hand, would not be woken up until the internal thread finished. It would automatically gain the write access to the buffer since it requested the control before it went to sleep.

In order to make the data flow work properly as described above, a synchronization object was needed to guard the shared buffer. The synchronization object used in the software was slim reader/writer (SRW) locker [176]. Comparing with other synchronization objects (e.g., mutex object, critical section object), SRW locker is more efficient and has much less overhead time (e.g. $< 50 \mu\text{s}$). The SRW locker was locked in the exclusive mode when acquired raw data was filled into the buffer so that other threads cannot be granted access to the same buffer. But the raw data was locked in the shared mode during processing, saving the data so that other synchronous modules can share the buffer among them.

6.2 Data Acquisition

The data acquisition in the high-speed endoscopic OCT system was achieved via a high-speed digitizer (i.e., Alazartech ATS9360) [177]. The averaged data acquisition rate reached 880 Megabytes per second with the 220 kHz FDML laser reported in Chapter 4. The software program controlled the high-speed digitizer via the software development kit library ATS-SDK v6.1.0 from the vendor [2]. The digitizer was programmed in the NPT AutoDMA mode in order to acquire the data and transfer the data from board into computer memory in a high trigger repetition rate fashion. In the NPT AutoDMA mode, the thread that controls the data acquisition module in the program (i.e., T1 in Fig. 6.2) pushed a list of internal buffers, each of which as big as a B frame size, into a first in-first out (FIFO) queue in the user mode of Windows® operating system via calling a function related to the digitizer's driver in the kernel mode (i.e., T0 in Fig. 6.2). After entering the kernel mode in T0, the digitizer driver digitized the analog OCT signal while filling up the digitized data into the internal buffer simultaneously. As mentioned, T1 then was kept asleep until the

internal buffers were full and returned to the user mode. The digitizer can work very efficiently in such a mode and the only overhead exists in this mode is a reset time of about 10 clock cycles between two consecutive triggered records.

Once the internal buffers were full, T1 transferred the data from the internal buffer into the buffer shared among the other modules with the guard of the SWR locker so that other modules would not be able to read the buffer accidentally. Due to the fact that Windows® operating system is not a real time operating system (i.e., thread scheduling on Windows NT® runs at an interval of 10 or 15 ms) [178], a frequent thread switching (e.g., thread sleep and waking up) is undesirable and should be avoided whenever possible. Meanwhile, the frame rate in a high-speed OCT system is usually very high (e.g., 50 to 1000 fps). Therefore, frequently switching all the threads for every frame is unrealistic and potentially causes the loss or corruption of the acquired data during thread switching. In order to solve this challenge, the size of the shared buffer was set to be a multiply of the B frame size. Therefore, the shared buffer clustered multiple B frames to increase the switching time among different threads so that it was greater than the thread scheduling interval time.

6.3 Data Processing and Display

High data throughput from the digitizer requires high performance data processing solution and real time display in order to help researchers and potentially the clinicians in the future to assess the results in real time. In the past decade, technological advances on semiconductor industry has greatly improved the performance of the field-programmable gate array (FPGA), digital signal processor (DSP) and general purpose graphic processing unit (GPU) while significantly reducing the cost. Theses electronics have all been brought

into the OCT field to improve the data processing speed [179-186]. Meanwhile, programmable shading languages, such as OpenGL GLSL [187], Nvidia Cg [188], Microsoft HLSL [189], designed for 3D computer graphics have been also greatly advanced. Unlike traditional fixed graphic rendering pipeline (e.g., prior to OpenGL 2.0, DirectX 9.0), such high level shading languages provide us with a more powerful and flexible rendering pipeline to visualize the processed data in either 2D or 3D fashion. In this dissertation, we chose to use a GPU-based data processing solution using compute unified device architecture (CUDA) developed by Nvidia along with OpenGL GLSL shading language to process and display the OCT data on a single consumer level graphic adaptor (e.g., Nvidia GTX 590, \$<800 when purchased in 2011). Comparing to FPGA and DSP solutions, there are three advantages using a GPU-based data processing solution. First of all, it is more cost-effective for developing an OCT platform in a laboratory based environment. Secondly, GPU-based data processing solution is naturally integrated with the data display module employing the shading language on the same hardware component. At last, both GPU and shading language support a development environment of C/C++, which is compatible with our software development environment.

6.3.1 Data Processing Algorithm on GPU

Unlike commonly known CPU that usually has only one large and complex algorithm logic unit (ALU) per core, GPU contains hundreds to thousands of small and simplified ALUs which are dedicated to fixed and floating point algorithmic operations. Therefore, GPU excels at parallel processing of multiple data through the same procedure, which perfectly fits the need of OCT data processing (i.e., multiple A-scans of data follow the same data processing steps).

Once the thread that handles data processing module (i.e., T2 in Fig. 6.2) was woken up via SWR locker, there were two steps in CPU-based processing for calibration data and four steps in a GPU-based data processing pipeline for OCT data as shown in Fig. 6.3. Since the driving waveforms in most wavelength sweeping lasers are sinusoidal and frequency response of the tunable filters are usually nonlinear and hysteretic, the wavenumber sweeping speed is not linear with respect to time, which requires a calibration procedure prior to Fourier transform. In order to calibrate the OCT data into uniformly distributed wavenumber space (i.e., K-space), the calibration data were generated from a Mach-Zehnder interferometer with a fixed optical path difference between two arms (i.e., $I(k) = \cos k\Delta z$ where Δz is constant). They was interpolated into denser sampling rate in order to accurately find the extrema (i.e., $k\Delta z = n \cdot \pi$), which are evenly spaced in the K-space (i.e., $\Delta k = \pi/\Delta z$). Since the wavelength swept laser is sweeping every A-line with the same drive waveform, the calibration data needs be only acquired and processed once before processing the OCT data. Therefore, these two steps could be placed in CPU. The only data need to be transferred to GPU for OCT data processing is the positions of these extrema points.

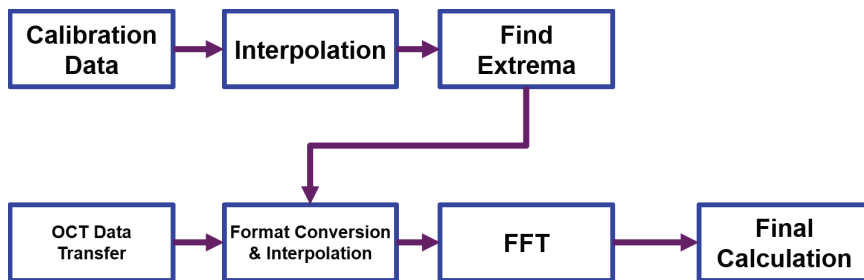


Figure 6.3. Data processing steps on GPU.

The data processing steps for OCT data in GPU can be divided into four steps: 1) all the acquired raw data was first transferred from the computer memory to graphic device

memory. 2) Every A-scan of the raw data was converted from 16-bit integer into single-precision floating point format and then calibrated based on the extrema data positions of the calibration signal so that all the data was uniformly spaced in K-space. This procedure could be bypassed if uniform K-space sampling method as described in Chapter 5 is employed during data acquisition. 3) One dimensional fast Fourier transform (FFT) operation was then performed on each A-scan of the calibrated data to form a two dimensional data of complex number, which was depth-resolved in the transformed direction. 4) The depth-resolved intensity and phase information can be extracted from the 2D data of complex number and then normalized between 0 and 1.

The GPU SDK used in the software is Nvidia CUDA v4.2. The first step could be directly implemented by calling a single function from the CUDA library. The second step required its own kernel function to perform such an operation. In this step, the raw data was mapped into a texture memory because interpolation in a texture memory was accelerated via specialized designed texture filtering units in GPUs. Due to the fact that the calibrated data was not evenly spaced in the original raw data, this method provided much faster interpolation than any other conventional methods implemented on GPUs. In the third step, a built-in FFT library (i.e., CUFFT) in CUDA SDK was used to perform a single-precision FFT operation. At last, a kernel function was written in the fourth step to calculate the amplitude and the phase of the depth-resolved data from complex FFT transformed data as well as to rescale the calculated results between 0 and 1. The final results were directly mapped into texture memory for the purpose of data display via OpenGL. The benchmark test of each steps in the data processing took place on an Nvidia GTX 590 GPU. A high performance GPU timer, which provides time stamps with an accuracy of $<1 \mu\text{s}$,

was placed among the aforementioned steps in the data processing pipeline. Hence, the consumed time of each step can be accurately recorded. Buffer consisting of 4096 A-lines was processed in this benchmark test and the processing time of each step was scaled to the time of each A-line. Both linear and cubic interpolation methods were tested in the benchmark. The effective number of data points after the interpolation was about 900 and 2048-point FFT operation was performed in this test with zero padding. The benchmark test results (i.e., Fig. 6.4a) showed: 1) the cubic interpolation took about 70% more time than the linear interpolation in the interpolation step; and 2) data transfer from computer memory to graphic device memory is the most time consuming among all the data processing steps, which is larger than the summation of the rest three steps.

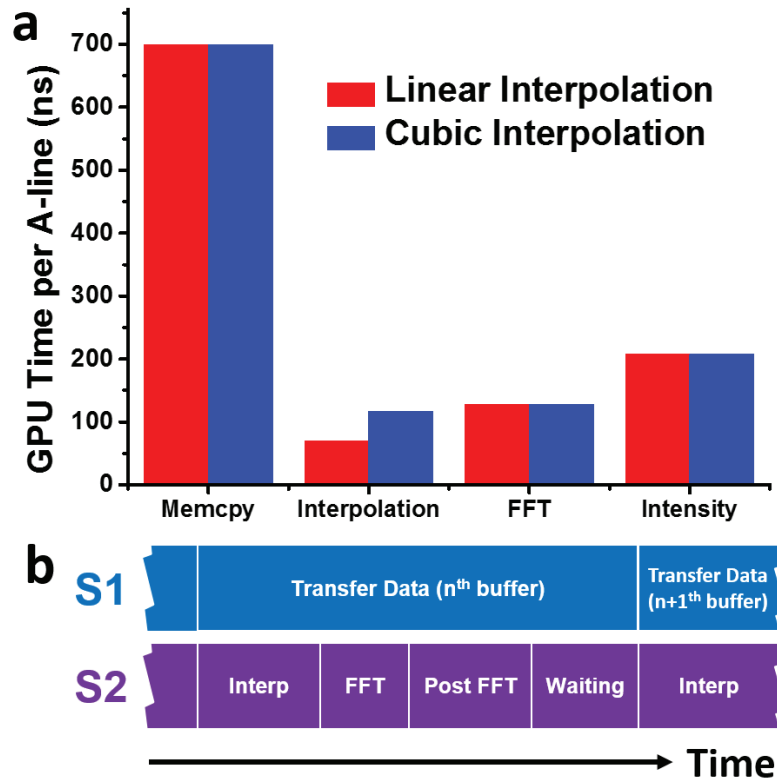


Figure 6.4. (a) Benchmark results of each step of data processing on an Nvidia GTX 590 GPU and (b) parallel streaming on GPU to accelerate data processing. Interp: interpolation.

Since the most time consuming step is data transfer, the GPU wastes most of its time in waiting for data transfer completion. It would be better if data transfer can be executed in parallel with the rest three data processing steps. Since CUDA v4.0, a concept of stream on GPUs, which is analogous to thread on CPU has been introduced in GPU programming. Based on the benchmark results in Fig. 6.4a, the most time consuming step among those four steps above was data transfer from computer memory to device memory as the bus interface of PCI Express v2.0 used by Nvidia GTX 590 limits its data transfer rate. Therefore, these four steps could be organized into two streams in GPU to further accelerate the data processing procedure at a cost of allocation of multiple buffers for storage of the intermediate results shared between streams (as shown in Fig. 6.4b). After the optimization, the performance of the data processing module was benchmarked to be 1.5 M A-scan/sec on Nvidia GTX 590 and data processing speed reached 2.4 M A-scan/sec if only the last three steps on GPU are taken into account (under a condition of a cubic interpolation with 1k resampling rate)** . The benchmark results showed such a data processing module running on Nvidia GTX 590 greatly exceeded the requirement of the designed high-speed endoscopic OCT system (i.e, 220 k A-scan/sec). The extra computing power on the GPU was used to calculate other time consuming tasks, such as *en face* projection, speckle variance OCT, etc. (as shown in Fig. 6.5).

There are two major advantages using the data processing pipeline as described above. First of all, the data processing module is completely compatible with any Nvidia graphic card released later than late 2010 (i.e., supports CUDA v4.0 or later), which means

** The benchmark were taken in July 2011. With the new technologies used in newer GPU, the results can be significantly improved with a newest graphic card. Similar results can be achieved with a mainstream Nvidia graphic card that costs ~\$300.

the source code can be compiled and run successfully without any modification. The optimization for different GPU can be automatically achieved during compilation. Secondly, the data processing module is scalable as the number of streams used in the data processing module can be expanded and more data processing steps can be added into the streams and re-arranged among the streams. Hence the data processing speed can be further improved when necessary.

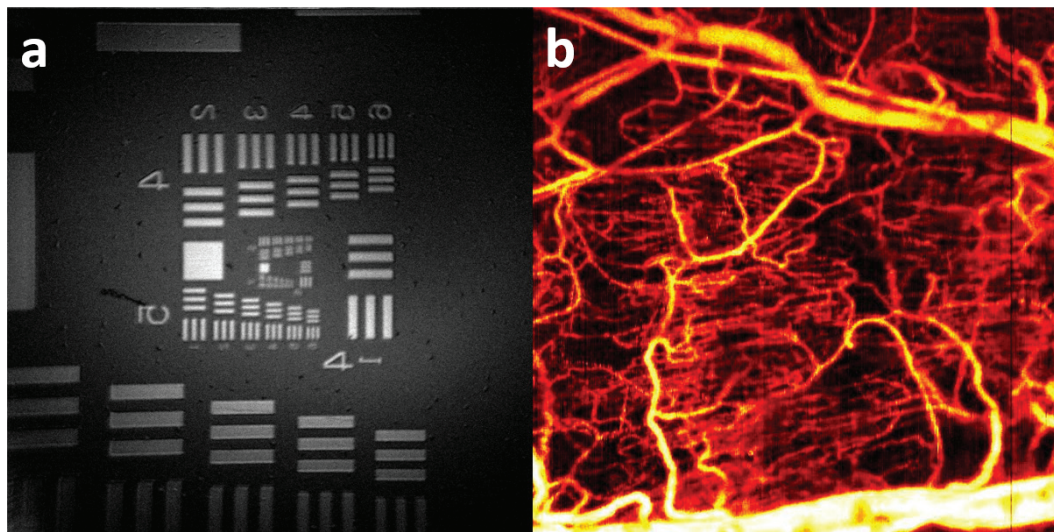


Figure 6.5. *En face* projection of (a) OCT intensity images of a USAF 1951 resolution chart in real time and (b) speckle variance OCT images of mouse ear in real time.

6.3.2 Data Display Module on GPU

The processed data was stored in the texture memory on the GPU, which can be directly accessed via OpenGL shading language GLSL. One of the benefits using texture memory is that a texture can be mapped onto any geometric shaped surface flexibly and efficiently in GLSL. Therefore a single B frame of the processed data can be displayed in either a rectangular or a polar view (as shown in Fig. 4.9). However, the working mechanism of the data display module was slightly different between a 2D and a 3D display mode.

In the 2D display mode, the data display module worked asynchronously with respect to the data processing module. Since multiple B frames are accumulated and processed simultaneously, the display module was woken up at the same frequency as the frame rate by a preset timer. Each time the display module was waken, it only displayed a single B frame of data from the processed data in the texture memory that contained multiple B frames of data. A double buffered texture memory was set up to avoid write/read conflict between data processing and display module. Eventually, all the B-frames in the texture memory would be displayed on the screen. In order to display a 2D image with different colormaps (i.e., grayscale, inverted grayscale, hot, etc.), the B frame data was first displayed onto an intermediate OpenGL pixel buffer object (PBO). With a simple secondary 1D texture mapping in GLSL, various colormaps can be applied onto the image in the OpenGL PBO and a final image was displayed on an actual display device by mapping the OpenGL PBO as a texture onto a rectangular surface (as shown in Fig. 6.6a).

In the 3D display mode, the data display module worked synchronously with the data processing module, which means that the module was only waken up after the data processing was completed. The processed data that contains multiple B frames of data was stored in a 3D texture memory. A 3D rendering algorithm was applied to display the 3D dataset onto a 2D OpenGL PBO in a perspective view. Then similar to the operation in 2D display model, a selected colormap was applied onto the image in the OpenGL PBO and a pseudo colored image can be displayed on an actual display device (as shown in Fig. 6.6b and 6.6c).

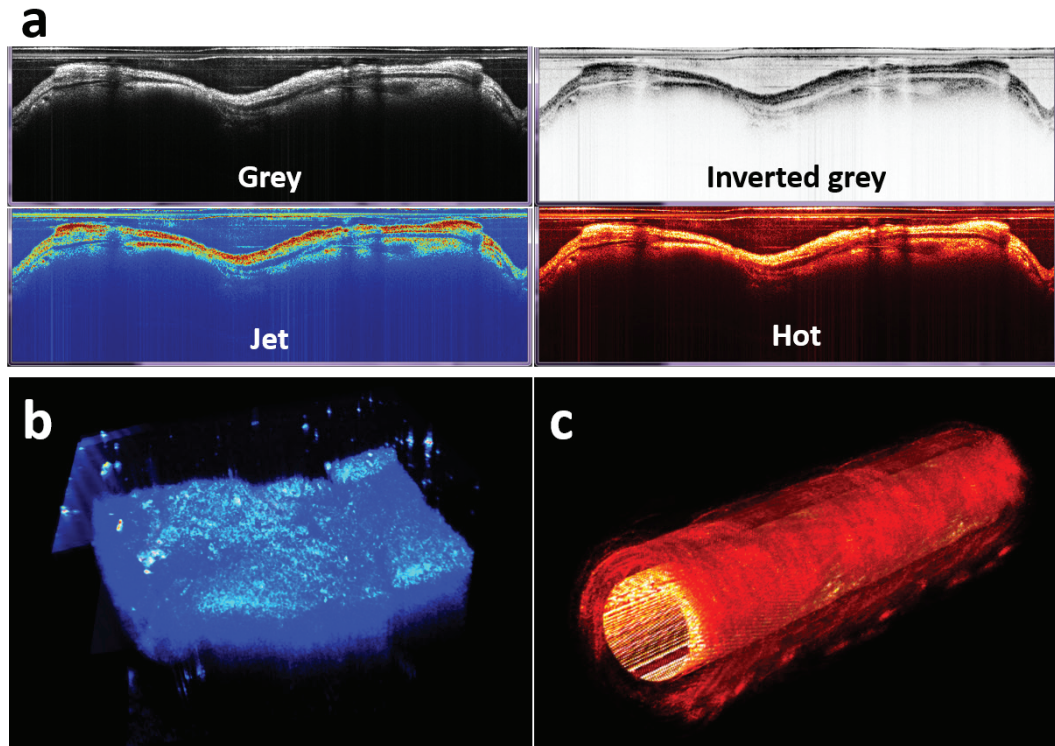


Figure 6.6. Real time display of (a) a 2D OCT image of an pig bronchus *in vivo* in four different colormaps in a rectangular view, (b) a 3D visualization of an OCT dataset of human brain tissue *ex vivo* and (c) a 3D visualization of an OCT dataset of pig bronchus *in vivo*.

6.4 Data Storage

The information of the data may be partially lost when the data is in the data processing pipeline (e.g., conversion from integer to floating point, interpolation, etc.). In order to be able to perform more comprehensive data processing (e.g., averaging, speckle reduction, Doppler, etc.), only the raw data was stored in a permanent storage device on the computer.

As mentioned in the previous section, the averaged raw data rate is about 880 MB/sec for the designed SS-OCT system with an A-scan rate of ~ 220 kHz. And it needs to be noted that data with such a data rate cannot be sustainably stored to any common external storage device on a personal computer (i.e., hard drive). Here a cost effective storage solution on a personal computer was proposed: to use a solid state disk (SSD) array.

Unlike a conventional hard drive, SSD does not require a disk head and disc spinning to write data into the disk. Therefore, SSD usually has a constant read/write speed across the whole disk. Recent technical advances on SSD enabled a sustainable write speed of a high-end consumer level SSD about 300 – 400 MB/sec with an affordable cost of \$1 to \$2 per GB. Although a single SSD still does not have enough write speed for the designed OCT system, RAID can further improve the write speed by forming a disk array and writing data into multiple disks in parallel.

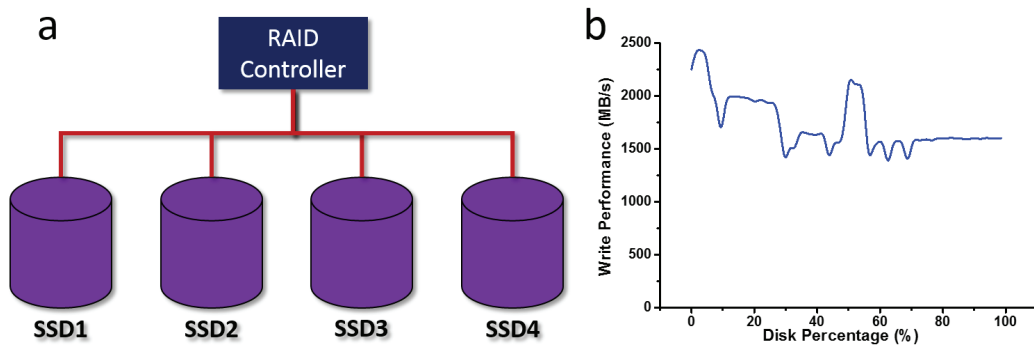


Figure 6.7. (a) An illustration of a RAID0 disk array adopted in the computer. (b) Random data write performance test of the RAID0 setup over the whole disk array.

In the computer built for the designed OCT system, a RAID controller (3ware 9750-4i) combined four SSDs (OCZ Technology Vertex 3Mxx) into a RAID0 disk array to expand the write speed as illustrated in Fig. 6.7a. The array cluster size and block size of the file system used on the disk array were finely tuned to further optimize the write performance of the disk array. The write performance was tested by writing random data into the disk array over the entire array by a free software (i.e., ATTO from ATTO Technology) as shown in Fig. 6.7b. At the beginning of the test, an increase of the write speed, due to the fact that the data is first stored in on-board memory of the RAID controller, was observed. When more data was sent to the controller, the data was eventually written

into the disk array. The sustained write speed of the disk array was tested to be at least 1.5 GB/sec, which is much greater than the design requirement.

Similar to the data processing module, the data storage module also runs in a synchronous thread (i.e., T3 in Fig. 6.2). It was woken up via a SWR locker by data acquisition module when the shared buffer that stored the raw data were ready. In order to get the best write performance of the disk array, the raw data had to be written into the disk array in fixed size blocks, that is, the buffer that contained the raw data was divided into blocks of 1MB size, which were sequentially written into the disk array. A benchmark was also performed to test the actual write performance in the software and a result of 1.57 GB/sec was achieved.

6.5 Summary

In this chapter, we first described the software platform designed for the high-speed endoscopic OCT system in order to acquire, process, display, and save the data in real time, mainly focusing on how to manage the high speed data rate (i.e., 880 MB/sec) and synchronize the data among the different modules in the software. Data acquisition, data processing and display, and data storage modules were then discussed in details in separate sections. All modules were tested to ensure they were able to handle such a large data rate with enough design margin.

Chapter 7 Side-viewing Optical Coherence

Tomography Imaging Probe

This chapter briefly compares a few approaches in fabricating a miniature side-viewing OCT imaging probe. Short and large working distance OCT imaging probes are then discussed in details. Paraxial models of the distal end of imaging probes are developed and validated by using ray tracing models. Fabrication of OCT imaging probes are introduced as well as the measurements of a few key parameters. At last, the design of the proximal end of imaging probes are discussed.

7.1 Introduction

Miniature OCT imaging probe is one of the most critical components in an endoscopic OCT system. Its optical performance directly affects the lateral resolution, signal-to-noise ratio (SNR), and overall quality of the OCT images. And its mechanical properties (e.g., size and robustness, etc.) limit the applicability of the endoscopic OCT imaging.

Based on the beam direction on the distal end of the imaging probe, OCT imaging probes are commonly categorized into forward-viewing [129, 190-192] and side-viewing probes [68, 80, 138, 193-199]. One advantage of side-viewing OCT imaging probes over forward-viewing ones is that it can provide B-frame OCT images in a full circumferential view (or at least a majority of the full circumferential view); such a field of view provided is more convenient for visualization since the shape of most internal organs is tubular. In order to acquire a full circumferential B-frame OCT image, a scanning mechanism needs

to be implemented in the endoscopic OCT system by either driving a micro motor where a mirror is attached to the distal end of the probe [195, 199] or rotating the entire probe from its proximal end [193, 194, 198]. Until last year [200], the relatively large physical dimension of the micro motor remained a big obstacle for the distal end scanning imaging probe to be applied to *in vivo* applications as their diameter can hardly be smaller than 2.0 mm. Therefore, in this chapter, we focused on side-viewing OCT imaging probes that are driven from their proximal end.

7.2 Distal End Optical Design of OCT Imaging Probes

The physical dimension of the OCT imaging probe may be the limiting factor for the *in vivo* application of OCT imaging in many cases. From the clinical perspective, the imaging probes should be as small as possible to minimize their intervention with the imaged internal organs. From the optical perspective, on the other hand, the small dimension of an imaging system would limit the size of stop aperture of the optics (i.e., numerical aperture or NA), and will lead to a poor lateral resolution. Therefore, one of the most important criteria in designing a miniature OCT imaging probe is to increase the effective NA of the probe by expanding the beam width within the micro optics with a limited diameter.

There are a few approaches to build a miniature probe, all of which based on a similar concept: focusing the expanded beam from a single mode fiber to a designed focal plane as illustrated in Fig. 7.1. The beam from a single mode fiber first passed an optical component to expand the beam width; the expanded beam was then focused by a micro focuser, which could also be achieved via several other ways. A micro prism or reflector was placed at the distal end to deflect the beam by about 90° to achieve side-viewing.

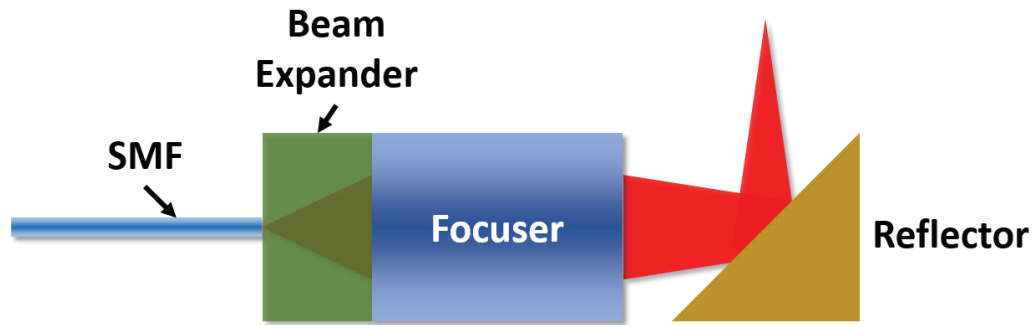


Figure 7.1. An illustration of a miniature OCT imaging probe. The beam from a single mode fiber first passes an optical component to expand the beam width. The expanded beam was then focused by a micro focuser. A micro prism or reflector was placed at the distal end to deflect the focused beam. SMF: single mode fiber.

The first approach is the fused fiber lens design. In this design, the distal end of the imaging probe is constructed with a single mode fiber, a multimode fiber, and a gradient index (GRIN) fiber [141-143, 197, 201]. By thermally fusing these fibers together, the multimode fiber acts as a beam expander and the GRIN fiber acts as the focuser. The optical size of the imaging probe in this design is usually smaller than 300 μm and the overall size can be controlled under 1.0 mm or even smaller. Such a probe has been used in intravascular imaging [202], imaging guided fine needle aspiration [143], and parenchymal lung imaging [142]. Due to the limited diameter in this design, the working distance of the imaging probe is usually designed to be small in order to maintain an acceptable lateral resolution. One technical difficulty of this design is that thermal fusion, which changes the optical properties of the hot zone between fibers, usually causes a reduction of coupling efficiency and a degradation of the beam profile. Therefore, a lot of practical considerations and fine tuning are required to build such an imaging probe.

Another approach to build an OCT imaging probe is to use standard miniature spherical lens or lenses, including ball lens [145, 146, 196]. In this design, a short length of air/fiber gap between the single mode fiber and the miniature spherical lens acts as a

beam expander and a spherical lens or lens group acts as the beam focuser. Although one can borrow a lot of examples and experiences from conventional bulky lens designs, the limited choice of small size spherical lenses hinders the applicability of this design (i.e., the spherical lenses less than 2.0 mm is very limited). Moreover, in order to keep the rigid part at the distal end of the OCT imaging probe short, the focal length of the lens has to be small enough (e.g., <5.0 mm), which would cause severe spherical aberration. Although the aberration may be reduced by using multiple lenses to split the focusing power, the optical design is complicated and the cost is increased. Therefore, multiple lenses were usually only used when high lateral resolution and chromatic aberration are critical. Nevertheless, due to a relatively complicated design, the applications of this type of imaging probes are limited, with its primary applications in the large GI tract [196]. The ball lens design can be implemented in very small OCT imaging probes [145]. Similar to miniature spherical lens, however, ball lens also suffers from severe spherical aberration. In addition, ball lens can be only used to form a very short working distance OCT probe due to its fabrication limitation.

The third approach, which is the most commonly used, is to use GRIN lens as a beam focuser [68, 80, 138, 141, 194, 197, 198]. In this design, a glass spacer is sometimes applied before the GRIN lens to form a compound lens in order to fully utilize the available NA within the GRIN lens. Since both the GRIN lens and the glass spacer have planar surfaces, it is much easier to customize such optical components into various lengths and the alignment is more tolerable than spherical lens. It is also much easier to find commercially available GRIN lens smaller than 1.0 mm in diameter so that the overall size of the probe using this design can be controlled under 2.0 mm. This type of OCT imaging

probes have been applied in various applications, such as cardiovascular, GI imaging, and pulmonary imaging, etc.

In this chapter, we choose using a compound lens that consists of a glass rod spacer and a GRIN lens to build OCT imaging probes. Two types of OCT imaging probes were designed and built based on different application requirements: short working distance imaging probes (i.e., working distance is shorter than 4.0 mm) and long working distance imaging probes (i.e., working distance is longer than 8.0 mm)^{††}.

7.3 Short Working Distance OCT Imaging Probe

A short working distance OCT imaging probe is designed for imaging internal organs with a small luminal area (i.e., $D < 6-7$ mm), such as lower airways, blood vessels, etc. A compound lens, which consists of a glass rod spacer and a GRIN lens with a diameter of 1.0 mm, was used to exploit the available NA in the micro optics in order to make a lateral resolution of the imaging probe comparable to the axial resolution. The design is similar to previously reported papers [89, 194, 198].

7.3.1 Paraxial Model

The distal end of the OCT imaging probe is first modeled using first-order, paraxial approximation. There are several paraxial approximation methods, such as Newton equations, Gaussian optics, etc. For convenience, here we chose to use ray transfer matrix analysis (also known as ABCD matrix analysis). In ABCD matrix analysis, optical components between two planes can be described as a 2×2 matrix while each ray at any plane can be written as a 1×2 vector, which describes the distance from the optical axis and

^{††} Working distance used in this chapter is commonly defined as the distance from the exit plane of the last optical component that focuses the beam (e.g., GRIN lens) to the focal plane unless it is defined otherwise.

the angle with the optical axis. By multiplying every matrices of simple optical components, we can get a 2×2 matrix that describes the whole optical system. One advantage of using ABCD matrix analysis is that it can describe a paraxial Gaussian beam as well as optical rays in ray optics. So key parameters, such as working distance and beam spot size at the focal plane (i.e., lateral resolution), can be simply derived from the final matrix. Since the beam from the single mode fiber is very similar to a Gaussian beam and the NA in an OCT imaging probe is usually smaller than 0.1, ABCD matrix analysis gives us a very accurate prediction on those parameters.



Figure 7.2. An abstract model of the distal end of the OCT imaging probe that consists of three optical components and two optical surfaces as described.

Figure 7.2 describes an abstract mode of the distal end of the OCT imaging probe^{‡‡}, where the ABCD matrices describe each optical component and optical surface with the glass rod spacer as M_s , the surface between the glass rod spacer and the GRIN lens as M_{s-g} , the GRIN lens as M_g , the surface between the GRIN lens and the air as M_{g-a} , and the air between the GRIN lens and the focal plane as M_a :

^{‡‡} The micro reflector only changes the beam propagating direction so that it is not included in this model.

$$\begin{aligned}
\mathbf{M}_s &= \begin{bmatrix} 1 & L_s \\ 0 & 1 \end{bmatrix} & \mathbf{M}_{s-g} &= \begin{bmatrix} 1 & 0 \\ 0 & n_s/n_g \end{bmatrix} & \mathbf{M}_g &= \begin{bmatrix} \cos \alpha L_g & \sin \alpha L_g / \alpha \\ -\alpha \sin \alpha L_g & \cos \alpha L_g \end{bmatrix} \\
\mathbf{M}_{g-a} &= \begin{bmatrix} 1 & 0 \\ 0 & n_g/n_0 \end{bmatrix} & & & \mathbf{M}_a &= \begin{bmatrix} 1 & L_{wd} \\ 0 & 1 \end{bmatrix}
\end{aligned} \quad , \quad (7.1)$$

where L_s , L_g , and L_{wd} are the length of the glass rod space, the GRIN lens, and the air (i.e., working distance), respectively, n_s and n_0 are the refractive indices of the glass rod space and air, n_g is the on-axis refractive index of the GRIN lens, and α is the alpha value of the GRIN lens (i.e., $n = n_0(1 - \alpha \cdot r^2/2)$). Therefore, the final matrix describes the whole imaging probe is:

$$\begin{aligned}
\mathbf{M} &= \begin{bmatrix} A & B \\ C & D \end{bmatrix} \\
A &= \cos \alpha L_g - \frac{\alpha \cdot L_{wd} \cdot n_g \sin \alpha L_g}{n_0} \\
B &= L_s \cdot \left(\cos \alpha L_g - \frac{\alpha \cdot L_{wd} \cdot n_g \sin \alpha L_g}{n_0} \right) + \frac{n_s \cdot \sin \alpha L_g}{\alpha \cdot n_g} + \frac{L_{wd} \cdot \cos \alpha L_g}{n_0} \\
C &= -\frac{\alpha \cdot n_g \cdot \sin \alpha L_g}{n_0} \\
D &= \frac{n_s \cdot \cos \alpha L_g - \alpha \cdot L_s \cdot n_g \sin \alpha L_g}{n_0}
\end{aligned} \quad (7.2)$$

The complex beam parameters q_s and q_f of Gaussian beams from the single mode fiber and at the focal plane are both purely imaginary, which can be expressed as:

$$q_f = \frac{Aq_s + B}{Cq_s + D} \quad (7.3)$$

Since q_f and q_s are purely imaginary (i.e., $q_f = i \cdot z_f$ and $q_s = i \cdot z_R$, where z_f and z_R are the Rayleigh range of the Gaussian beam at the focus and of the single mode fiber, respectively), we have:

$$-z_f z_R C + i \cdot z_f D = B + i \cdot z_R A. \quad (7.4)$$

Since all the elements in the ABCD matrix are real, Eq. (7.4) can be written as:

$$\begin{aligned} -z_f z_R C &= B \\ z_f D &= z_R A \end{aligned} \quad (7.5)$$

From Eq. (7.5), the Rayleigh range of the Gaussian beam of the single mode fiber z_R can be derived as:

$$z_R = \sqrt{-\frac{B \cdot D}{A \cdot C}}. \quad (7.6)$$

From Eq.(7.6), we can solve the working distance L_{wd} and the spot size of the beam at the focal plane Δx_f is^{§§}:

$$\Delta x_f = 2\omega_0 \cdot \sqrt{\frac{n_s}{n_0} \frac{A^2 + (B \cdot z_R)^2}{A \cdot D - B \cdot C}}, \quad (7.7)$$

where $2\omega_0$ is the beam width from the single mode fiber (i.e., $1/e^{-2}$), which is 9.2 μm at a wavelength of 1310 nm.

^{§§} The spot size is defined here as the twice of the radius location when the intensity is $1/e^2$ of the central intensity. The FWHM spot size should be converted accordingly (i.e., $0.589 \cdot \Delta x_f$).

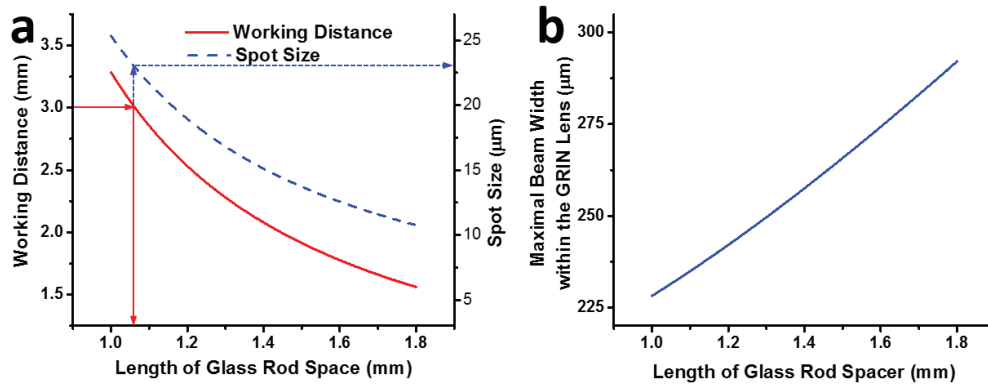


Figure 7.3. (a) The working distance and the spot size of the imaging probe is controlled by the length of the glass rod spacer when the length of the GRIN lens is preset to be 2.2 mm. (b) The maximal beam width within the GRIN lens is also controlled by the length of the glass rod.

Two of the parameters in the above formula are usually variables when fabricating an OCT imaging probe: the length of the glass rod spacer L_s and the length of the GRIN lens L_g . In practice, we usually first polishes a set of GRIN lenses with a fixed length, 2.20 mm in this case. By changing the length of the glass rod spacer L_s , the working distance can be set from 1.5 to 3.0 mm and the spot size can be tuned from 10 to 23 μm accordingly. For example, for a working distance of 3.00 mm, the length of the glass rod spacer needs to be tuned to ~1.05 mm with the corresponding spot size of 23.4 μm as shown in Fig. 7.3a.

One thing need to be pointed out is that ABCD matrix analysis is for an optical system without aperture limit. Therefore, beam vignetting has to be examined by using ABCD matrix analysis to calculate the maximal beam width inside the optical system (i.e., inside the GRIN lens). A monotonic relationship between the length of the glass rod spacer and the maximal beam width inside the GRIN lens as shown in Fig. 7.3b indicates that the maximal beam width increases as the length of the glass rod spacer increases. It is noticed in Fig. 7.3b that the NA of the micro optics (i.e., <300 μm) was not fully utilized in

designing short working distance probe because a too tightly focused beam would greatly reduce the depth of focus (DOF), and a short DOF would degrade the imaging quality where it is out of focus in an OCT image. Here, a lateral resolution was intentionally chosen to be comparable with the axial resolution (e.g., 9.5 μm).

7.3.2 Zemax Model

Zemax® is a commercial optical design software by ray tracing every rays passing through the optical system. It can simulate the optical performance of an optical system in an almost realistic fashion. Optical aberrations, such as spherical and chromatic aberrations, can be calculated within the software. Therefore, a Zemax model was built based on the parameters from the ABCD matrix analysis to validate the paraxial results.

Shown in Fig. 7.4 is the Zemax simulation results of an OCT imaging probe with a diameter of 1.0 mm and a designed working distance of 3.0 mm. As shown in Fig. 7.4a, the actual working distance was calculated as 3.07 mm, which is only 70 μm larger than the result of the ABCD matrix analysis. The difference merely comes from the different definitions of the focus; in the Zemax model, the focus is defined as the smallest RMS spot size while defined as a paraxial focus in ABCD matrix analysis. The maximal beam width within the GRIN lens calculated was about 230 μm^{***} , which was also consistent with the ABCD matrix analysis shown in Fig. 7.3b. Shown in Fig. 7.4b is the spherical aberration in such a design. Comparing with the diffraction limited spot size (i.e., 23.4 μm), the spherical aberration was negligible. The chromatic aberration calculated was also

*** The NA of the beam from the single mode fiber (i.e., SMF-28e+) is 0.092 in Zemax model instead of 0.14 shown in the specification of the fiber. The definition of the NA in SMF-28e+ fiber specification is 1% power level of a 1D far-field scan. But the definition of the NA used here is taken from Gaussian beam and the encircled energy is only ~86%. Therefore the NA used here is smaller than the one in the fiber specification.

negligible compared with the confocal parameter of $657\ \mu\text{m}$ as shown in Fig. 7.4c. . Other short working distance OCT imaging probes with different working distances were also validated with Zemax® software (data not shown) and the Zemax results showed a good consistency between ABCD matrix analysis and real ray tracing results. Therefore, it is suggested that the actual optical model of a short working distance OCT imaging probe can be accurately predicted by the ABCD matrix analysis and Zemax models can provide fine tuning when finalizing the parameters, such as actual working distance or spot size.

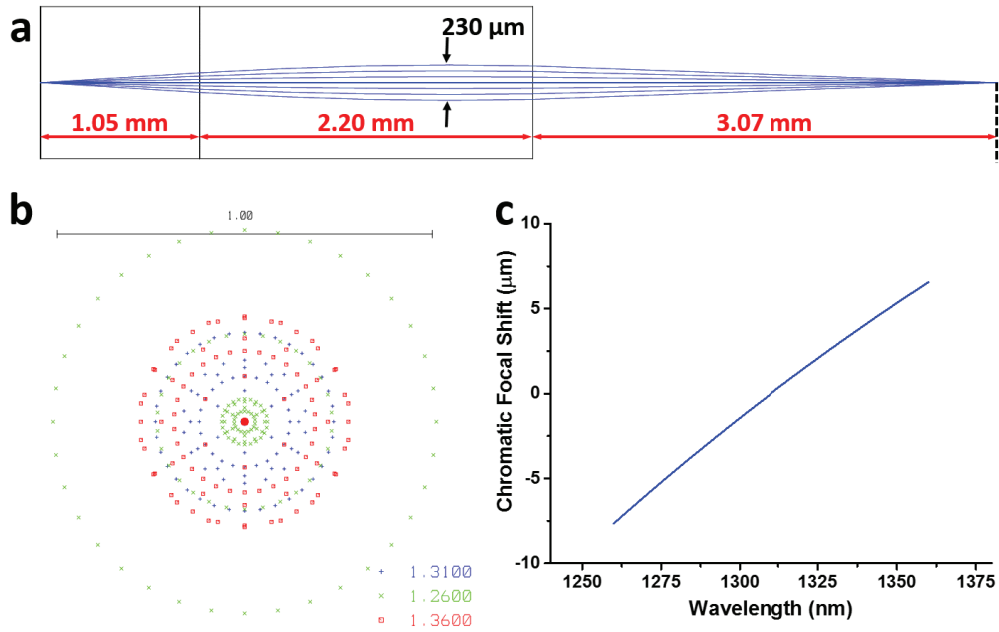


Figure 7.4. (a) Ray tracing result of an OCT imaging probe consists of a 1.05 mm glass rod spacer and a 2.2 mm GRIN lens (SLW-1.0) shows a working distance of 3.07 mm and that the maximal beam width within the GRIN lens is about $230\ \mu\text{m}$. (b) beam spot size at the focal plane at different wavelengths ($1310\pm 50\ \text{nm}$) with a scale bar of $1.0\ \mu\text{m}$. The diffraction limited spot size is $23.4\ \mu\text{m}$ from ABCD matrix analysis. (c) Chromatic focal shift over 100 nm wavelength region is about $14.2\ \mu\text{m}$ while the confocal parameter of the focused Gaussian beam is $657\ \mu\text{m}$.

A short working distance OCT imaging probe with micro optics of 0.7 mm in diameter was also designed followed by the same procedure as discussed above.

7.3.3 Fabrication Steps and Tolerance

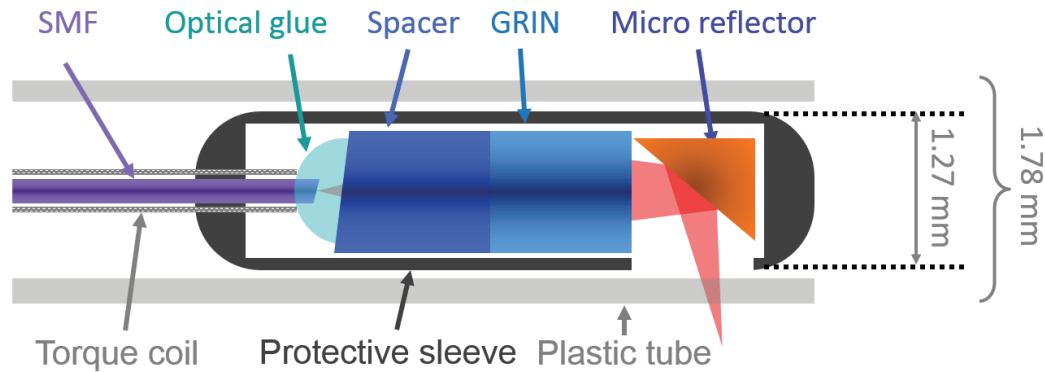


Figure 7.5. A schematic of the distal end of a short working distance OCT imaging probe. The optical portion consists of a single mode fiber, a glass rod spacer, a GRIN lens, and a micro reflector. All the optical components were packed into an 18 Ga hypodermic tube with a window opens on side. The whole assembly was then inserted into a transparent plastic tube.

The final design of the distal end is shown in Fig. 7.5. During the fabrication of the distal end of the imaging probe, both the glass rod spacer and the GRIN lens were first polished to designed lengths. Since it is important for endoscopic OCT imaging to minimize the back reflection from any optical surface in the imaging probe, the entrance plane of the glass rod spacer was polished with an angle of 8° to reduce the back reflection from this surface. The compound lens, which was made by gluing the glass rod spacer and the GRIN lens together, was connected via optical glue with a single mode fiber (i.e., SMF-28e+® from Corning Inc.) inside a hollow torque coil that delivers the rotation from the proximal ends to the distal ends. The end of the single mode fiber was also cleaved into an 8° angle to further reduce the back reflection. After curing the optical glue, the working distance was experimentally confirmed to be close to the designed value (i.e., $\pm 50 \mu\text{m}$). The spot size was then calculated from the measured confocal parameter, which should also be close to the designed value. A large deviation of the spot size from its designed value is usually

caused by defected optical components or poor alignment among them, both of which could be avoided. The double pass efficiency of the imaging probe was measured by measuring the back reflection with a reflective mirror placed at its focal plane, and it should be kept as high as possible in order to achieve the best imaging performance. When fabricating short working distance OCT imaging probes, the double pass efficiency can usually be controlled between -1.5 and -2.5 dB. The back reflection was also measured and is required to be lower than -50.0 dB for proper OCT imaging. Angled polishing the end surface of the single mode fiber and the first surface of the glass rod spacer could further reduce the back reflection down to -55.0 to -62.0 dB.

A micro rod reflector was placed in front of the compound lens to diverge the beam about 90° . The diverging angle should be close to but not exactly equal to 90° in order to avoid specular reflection from the plastic tube and the angle difference away from 90° should be no less than half the angle of the focused beam cone, which is approximately equal to the NA of the focused beam. The whole optical components, glued to the torque coil, were housed inside an 18 Gauge stainless hypodermic tube (i.e., inner diameter: 1.02 mm; outer diameter: 1.27 mm) with a window that opens on one side. The whole assembly was then put into a transparent plastic tube (i.e., inner diameter: 1.30 mm; outer diameter: 1.78 mm) for insulation and protection from the biological tissue during *in vivo* experiments.

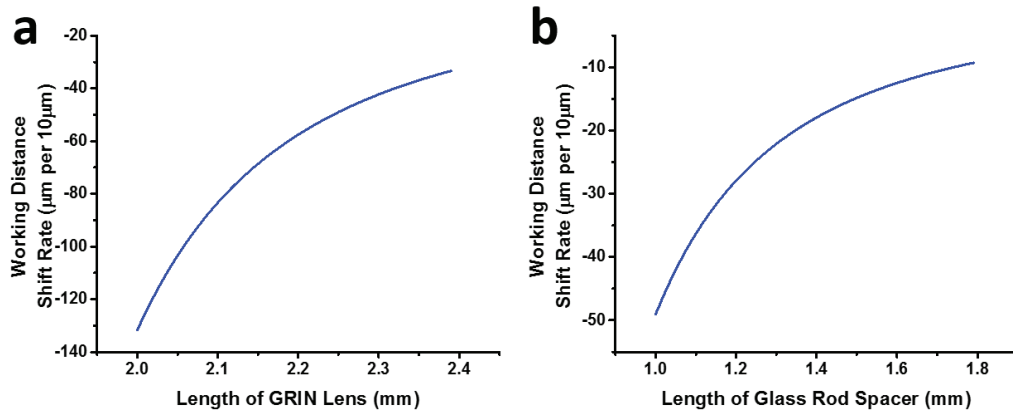


Figure 7.6. (a) The change of working distance with respect to the change of the length of the GRIN lens at different length when the length of the glass rod spacer is 1.05 mm. (b) The change of working distance with respect to the change of the length of the glass rod spacer lens at different length when the length of the GRIN lens is 2.2 mm.

Inconsistencies between the actual OCT imaging probe and the designed model may arise due to fabrication errors. To evaluate how severe the error might be, a simple tolerance model was developed based on ABCD matrix analysis as shown in Fig. 7.6. Taking as an example an imaging probe with a working distance of 3.0 mm described in previous subsections, the working distance shifts at a rate of about $-70 \mu\text{m}$ every $10 \mu\text{m}$ increase in GRIN lens length when the length is around 2.20 mm. Meanwhile a similar phenomenon was also observed when the length of the glass rod spacer changes (i.e., about $-55 \mu\text{m}$ per $10 \mu\text{m}$ increase in glass rod spacer length when the spacer length is around 1.05 mm). Therefore, an error up to $\pm 125 \mu\text{m}$ in working distance may be introduced as the inaccuracy of glass rod spacer and GRIN lens polished in the lab is about $\pm 10 \mu\text{m}$. To improve the accuracy of working distance, we come up with a neat strategy where the glass rod spacer is intentionally polished shorter (i.e., $\sim 100 \mu\text{m}$). The variation in working distance, thus, are subsequently compensated by changing the distance between the single mode fiber and the glass rod spacer which is filled with optical glue. As the distance between the single mode fiber and the glass rod spacer is usually of a few hundred microns

in a short working distance probe, there is enough flexibility in the adjustment of working distance. The final working distance acquired using this approach is usually close to the designed value (i.e., $\pm 50 \mu\text{m}$).

7.3.4 Proximal End

A flexible torque coil consists of multiple layers of counter-wound wires that delivers rotational and pull back motion from the proximal end of the probe to the distal end of the probe. When selecting a proper torque coil, there is a tradeoff between the stiffness that delivers precise rotation and translation and the flexibility that helps the incorporation of the imaging probe with standard video endoscope. A more stiffness torque coil may be preferable in upper GI applications whereas a more flexible torque coil is desirable in pulmonary applications. Here we chose to use two types of torque coils with different designs. The first type has an outer diameter of 0.83 mm and an inner diameter of 0.36 mm, which is suitable for a rotation speed of up to 60 revolutions per second. The second type has an outer diameter of 0.75 mm and an inner diameter of 0.30 mm, which is suitable for a lower rotation speed of up to 20 revolutions per second. The overall length of shorter working distance probes is about 1.5 meters, which makes them compatible with conventional video endoscope.

A piece of 16 Gauge hypodermic tube was used at the proximal end of an imaging probe to 1) bridge between the FC/APC fiber connector and the torque coil to deliver the rotational and translation motion, and 2) protect the fused fiber at the proximal end. The hypodermic tube needed to concentrically align with the ferrule in an FC/APC fiber connector to ensure that rotational motion can be smoothly delivered without any off-axis spinning even at a high rotation speed.

7.4 Large Working Distance OCT Imaging Probe

A large working distance OCT imaging probe is designed for imaging internal organs with a large luminal area (i.e., $D > 15$ mm), such as esophagus, colon, etc. Similar to a short working distance OCT imaging probe, a compound lens that consists of a glass rod spacer and a GRIN lens with a diameter of 1.0 mm, was also used. But due to the limited aperture size in the large working distance OCT imaging probe, the available NA in the micro optics has to be fully utilized in order to improve the lateral resolution as high as possible.

7.4.1 Paraxial Model

The same ABCD matrix model was analyzed as described in Fig. 7.2. Unlike in short working distance OCT imaging probes, to design the probe, we first increase the length of the glass rod spacer to fully utilize the available NA of the GRIN lens.

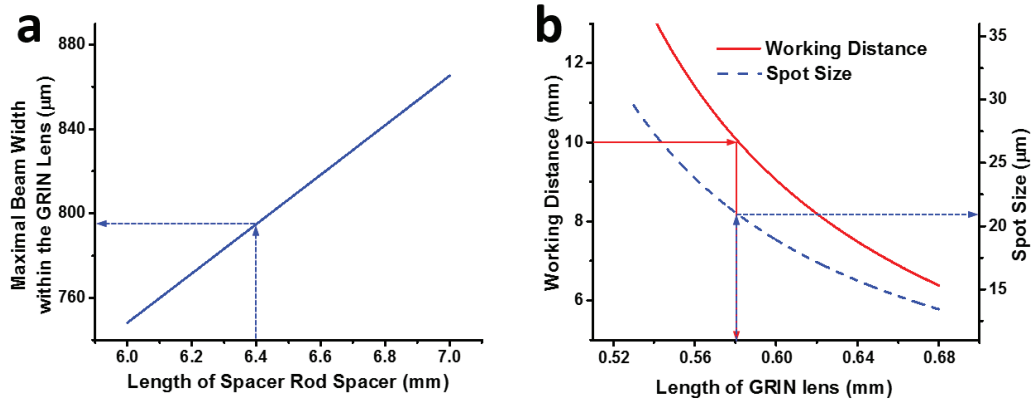


Figure 7.7. (a) The maximal beam width within the GRIN lens is also controlled by the length of the glass rod. A 6.40 mm glass rod spacer gives a maximal beam width within the GRIN lens of ~ 795 μm . (b) The working distance and the spot size of the imaging probe is controlled by the length of the GRIN lens when the length of the glass rod spacer is preset to be 6.40 mm.

Due to the manufacture limitation, the effective area in a GRIN lens is usually no more than 80% of the diameter of the GRIN lens (i.e., 800 μm). Therefore, the maximal beam width within the GRIN lens should be set at close to 800 μm by optimizing the length

of the glass rod spacer to 6.40 mm as shown in Fig. 7.7a. Once the length of the glass rod spacer is fixed, the working distance and the spot size can be tuned by changing the length of the GRIN lens. For example, the length of the GRIN lens needs to be ~ 0.58 mm when the working distance is designed to be 10.0 mm, and the corresponding spot size is then $21.4 \mu\text{m}$ as shown in Fig. 7.7b.

7.4.2 Zemax Model

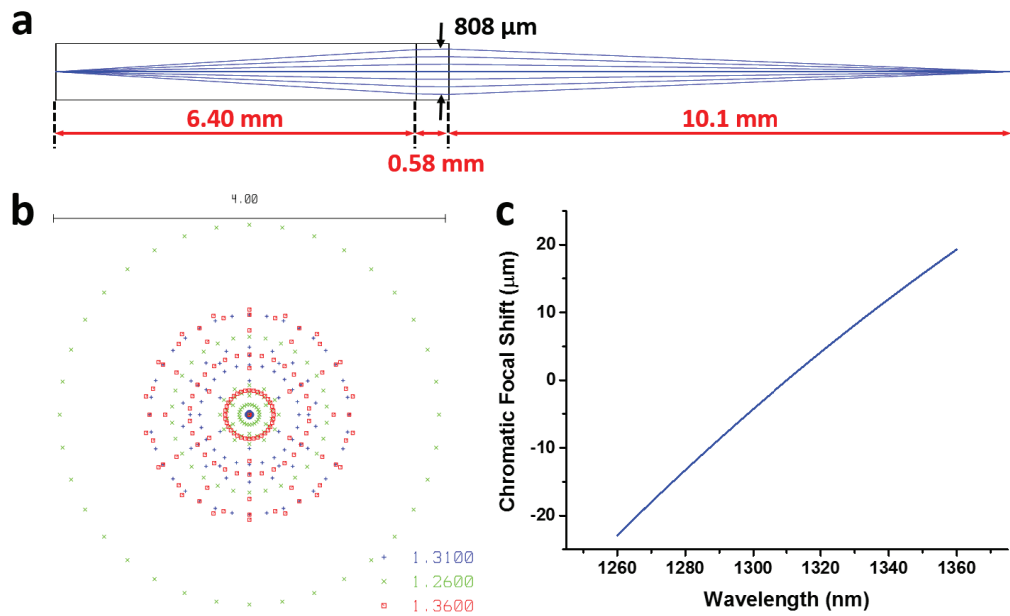


Figure 7.8. (a) Ray tracing result of an OCT imaging probe consists of a 6.40 mm glass rod spacer and a 0.58 mm GRIN lens (SLW-1.0) shows a working distance of 10.0 mm and that the maximal beam width within the GRIN lens is about $808 \mu\text{m}$. (b) beam spot size at the focal plane at different wavelengths (1310 ± 50 nm) with a scale bar of $4.0 \mu\text{m}$. The diffraction limited spot size is $21.4 \mu\text{m}$ from ABCD matrix analysis. (c) Chromatic focal shift over 100 nm wavelength region is about $42.2 \mu\text{m}$ while the confocal parameter of the focused Gaussian beam is $549 \mu\text{m}$.

Similarly, a Zemax model was created to validate the ABCD matrix analysis results. Shown in Fig. 7.8 is the Zemax simulation results of an OCT imaging probe with 1.0 mm in diameter and a designed working distance of 10.0 mm. As shown in Fig. 7.8a, the actual working distance was calculated as 10.1 mm, which is $100 \mu\text{m}$ larger than the result of the

ABCD matrix analysis. The maximal beam width within the GRIN lens is about 808 μm , which is also very close to the ABCD matrix analysis results shown in Fig. 7.7b. The spherical aberration in such a design was shown in Fig. 7.8b; the aberration is larger than the one in a short working distance probe as shown in Fig. 7.3b. Seidel aberration coefficients analysis in Zemax suggested that the aberration mainly comes from the larger beam width within the GRIN lens, which is consistent with the theoretical analysis [203, 204]. Nevertheless, the spherical aberration has negligible effect on the broadening of the spot size (i.e., a diffraction limited spot size of 21.4 μm). The chromatic aberration was calculated in Fig. 7.8c, which is also smaller than the confocal parameter of 549 μm . The Zemax results showed a good consistency between ABCD matrix analysis and real ray tracing results.

7.4.3 *Astigmatism Correction*

The method and results described in this section have been published in [198].

In conventional side-viewing OCT imaging probe, the beam is diverted by 90° with a reflector and then passes through a transparent plastic protective tube. The tube, however, acts as a negative cylindrical lens, which diverges the beam along the azimuthal direction perpendicular to the longitudinal axis of the catheter [140]. This common effect is imperceptible in a short working distance probe because the diverging power of the plastic tube is negligible compared with the focusing power of the probe. However, it is much more problematic in a large working distance probe when the diverging power of the plastic tube is able to counteract the focusing power of the probe. The degradation of the beam can often be severe, in particular when the transparent tube has a small radius and a relatively thick wall. For a plastic tube with a 0.7 mm radius and an ~ 190 μm wall thickness,

the calculated ratio of the beam spot size in the azimuthal direction to the one in the longitudinal direction (defined as the astigmatism ratio) is ~ 40 as shown in Fig. 7.9a, which was observed on the beam profile photograph captured on the target focus plane as shown in Fig. 7.9c. To compensate for the astigmatism, the beam needs to be refocused along the azimuthal direction. One solution is to replace the commonly used flat reflector with a cylindrical reflector. The numerical simulations show that a cylindrical reflector with an ~ 20.5 mm radius of curvature would fully compensate for the cylindrical effect caused by the plastic tube as shown in Fig. 7.9b. The beam profiles before and after the correction of astigmatism by using a cylindrical mirror are shown, respectively, in Figs. 7.9c, 7.9d, which clearly demonstrate that the proposed approach can effectively correct the astigmatism and restore the round shape of the beam profile.

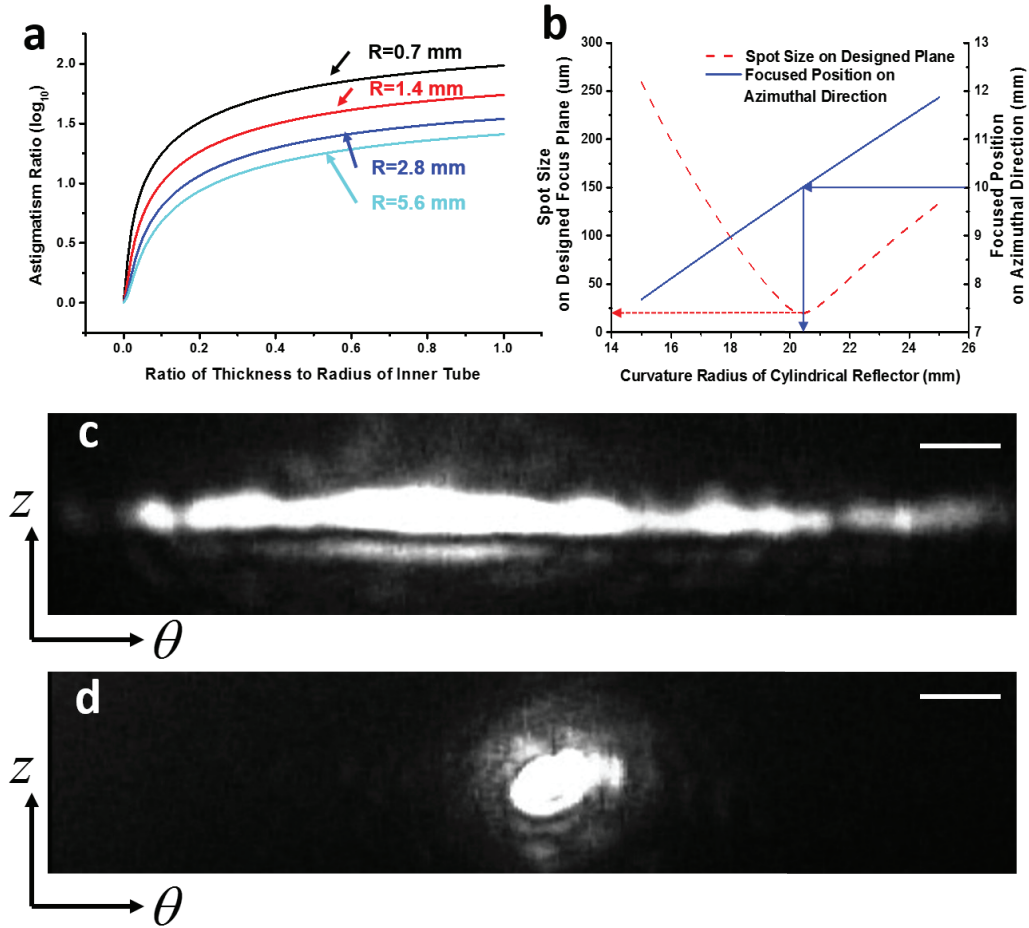


Figure 7.9 (a) Logarithm of the calculated astigmatism ratio versus the ratio of the tube thickness ΔR to tube radius for several tube radii R . The results show that the beam profile distortion increases with the ratio of $\Delta R/R$, and the distortion becomes more severe for a tube of a smaller radius. (b) Calculated beam spot size in the azimuthal direction on the target focus plane (i.e., 10 mm away from the GRIN lens and perpendicular to the beam axis) and the actual focused position on the azimuthal direction versus the curvature radius of the astigmatism-correcting cylindrical reflector. Simulation shows that a cylindrical reflector with an ~ 20.5 mm radius could refocus the beam back to the target working distance. (c) Photograph of the beam profile on the target focal plane when a conventional flat reflector was used in the catheter, where severe distortion was evident. (d) Photograph of the beam profile when a cylindrical concave reflector of an ~ 20.5 mm radius was used, where an approximately circular beam profile was restored.

7.4.4 Fabrication Steps and Tolerance

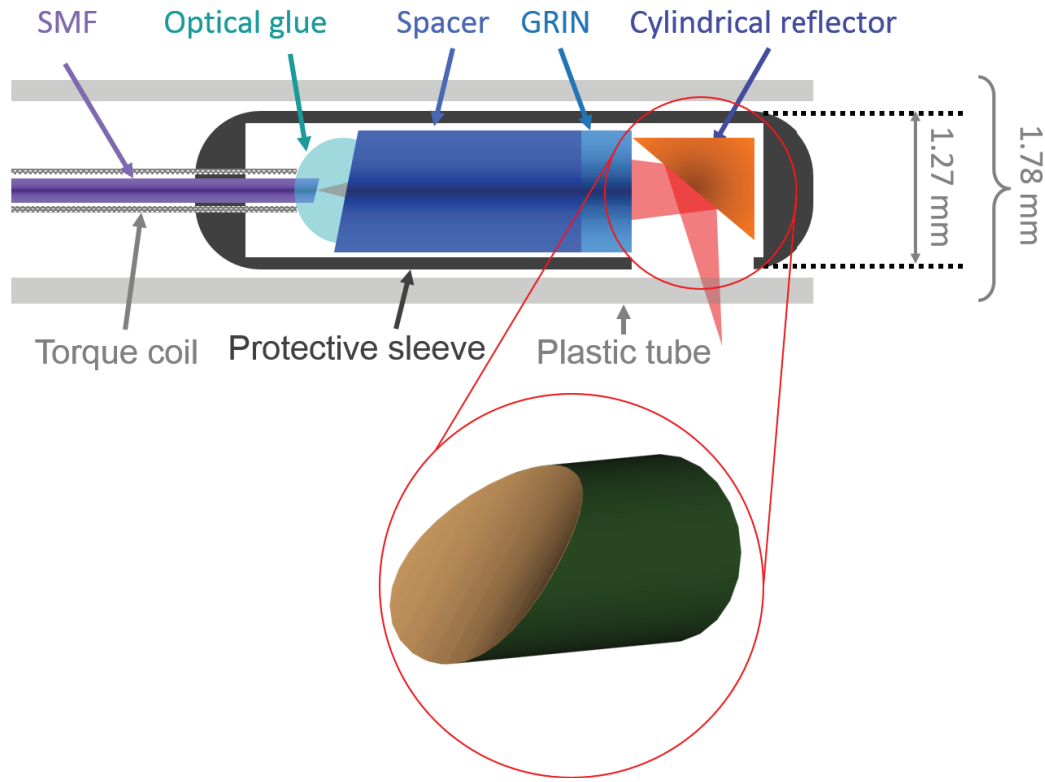


Figure 7.10. A schematic of the distal end of a large working distance OCT imaging probe. The optical portion consists of a single mode fiber, a glass rod spacer, a GRIN lens, and a cylindrical reflector. All the optical components were packed into an 18 Ga hypodermic tube with a window opens on side. The whole assembly was then inserted into a transparent plastic tube.

Shown in Fig. 7.10 is the final design of the distal end of a large working distance OCT imaging probe. Most of the fabrication steps and parameter specifications are similar to those described in subsection 7.3.3 except that a curved micro reflector was used to deflect the beam instead of a flat micro reflector. A cylinder of a diameter of 20.5 mm, which was made of stainless steel, was first manufactured as a mold and polished via different grades of polishing pastes. The finest polishing paste was 1.0 μm . A rod of 1.0 mm in diameter, which was made of softer material (e.g., plastics, aluminum, etc.), was chosen to make the curved micro reflector. The rod was first cut into small length piece (i.e., 2.0 mm in length)

and its one side was grinded as angled flat surface (e.g., 40°). The angled curved surface was then grinded and polished from the flat surface via the diamond polishing compounds on the spinning stainless cylindrical mold. The diamond compounds used here were 10, 5, 3, 1, $0.25\ \mu\text{m}$ in the order of from coarse to fine. Finally, the curved surface was coated with a protective gold or silver reflective layer. The double pass efficiency of a large working distance probe can usually be controlled between -3.0 to -4.0 dB owing to the larger beam width inside the GRIN lens and the larger spherical aberration. The total length of a large working distance probe is usually ~ 2.2 m, which is compatible with an upper GI endoscope.

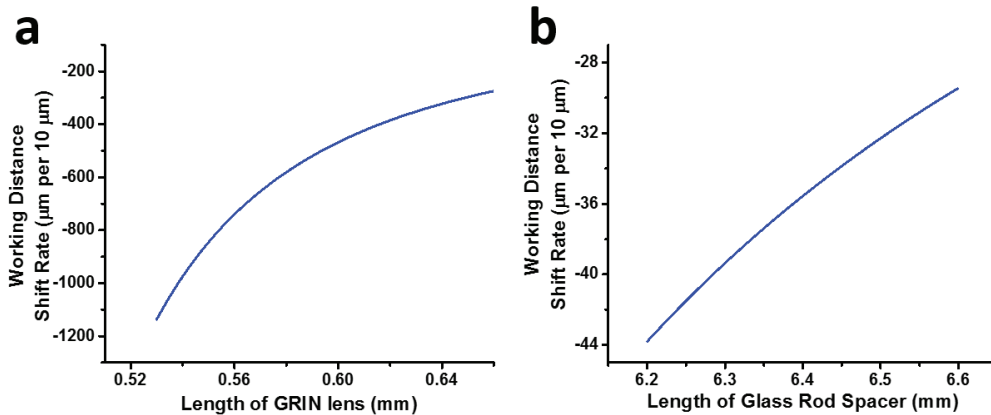


Figure 7.11. (a) The change of working distance with respect to the change of the length of the GRIN lens at different length when the length of the glass rod spacer is 6.40 mm. (b) The change of working distance with respect to the change of the length of the glass rod spacer lens at different length when the length of the GRIN lens is 0.58 mm.

Similarly, tolerance errors were also modeled as shown in Fig. 7.11. Taken as an example a large working distance probe with a working distance of 10.0 mm as described in previous subsections, the working distance shifts at a rate of about $-570\ \mu\text{m}$ every $10\ \mu\text{m}$ increase in GRIN lens length when the length is around 0.58 mm as shown in Fig. 7.11a. This rate is almost one order of magnitude higher than that in a short working

distance probe. However, the working distance shift rate of the glass rod spacer, as shown in Fig. 7.11b, is still on the same order of magnitude as that in a short working distance probe. Therefore, the length tolerance need to be more tightly controlled in a large working distance OCT imaging probe (i.e., a tolerance of $\pm 5 \mu\text{m}$ is desirable). Using the same method proposed in subsection 7.3.3, the working distance can still be controlled to the designed value within $\pm 200 \mu\text{m}$.

7.5 Summary

In this chapter, we first compared two approaches in fabricating a miniature side-viewing OCT imaging probe. A compound lens that is consisted of a glass rod spacer and a GRIN lens is preferably chosen. Short and large working distance OCT imaging probes are then discussed in the following sections. In each section, a paraxial model of the distal end of imaging probes was first developed to optimize the optical design quickly. A ray tracing model was then built in Zemax in order to validate the paraxial model results. In the large working distance probe section, astigmatism was discussed and corrected using a home built curved micro reflector. In addition, we discussed the fabrication steps of OCT imaging probes and a few key parameters that was monitored during the fabrication. A simple tolerance model was developed based on the paraxial model to show which parameter was more sensitive to the design target and guide the practical fabrication work. At last, the design of the proximal end of imaging probes was discussed.

Intended to be blank

Chapter 8 Endoscopic Optical Coherence

Tomography in Lower Airway Imaging

This chapter first briefly reviews the importance of lower airway imaging and the limitations of current imaging modalities. The OCT system and animal protocol we use are then discussed, followed by results from three studies conducted in the lower airways in animal models, including high-speed OCT imaging of lower airways, correlation between *in vivo* OCT images and *ex vivo* histopathology, and dynamic OCT imaging of lower airways.

8.1 Background and Introduction

Obstructive lung diseases (OLD) are a category of respiratory diseases characterized by airflow limitation often associated with pathological changes in the lower airways of the lungs. One of the two major subsets of OLD are chronic obstructive pulmonary disease (COPD) characterized by irreversible airflow obstruction and persistent inflammation to noxious environmental stimuli (e.g., cigarette smoke) [205]. COPD encompasses a spectrum of diseases, where chronic bronchitis and emphysema lay at both ends of, with most individuals fall in between. COPD affects 12 to 16 million people in the United States and is the 4th most common cause of morbidity and mortality among adults in the United States [206]. The other major subset in OLD, asthma, is a common chronic inflammatory disease of the airways characterized by variable and recurring symptoms including reversible airflow obstruction and bronchospasm. It affected more than 24.6 million people

including 7.1 million children in 2009 [207]. Although it is well known that there are morphological changes in OLD (e.g., hypertrophy and hyperplasia of airway smooth muscle, airway epithelial remodeling, and hyperplasia and hypersecretion of goblet cells), little is understood about how those changes affects the pathophysiology of the diseases, such as airway remodeling and the change of elastic properties of the airways [205]. Quantitative analysis of the structure of the airways, which includes the luminal area, the wall thickness, and wall morphology, plays an important role in helping physicians to understand the pathogenesis of the OLD. Currently there is a great diagnostic and therapeutic value for developing and applying technologies such as OCT imaging to monitor the morphological changes of the lower airways *in vivo* real-time.

Lower airway imaging has greatly advanced in the past decade. Flexible white light bronchoscope (WLB) allows physicians to examine lower airways from trachea to segmental bronchi of the 4th to 5th generations. However, it is a semi-quantitative imaging tool due to the image distortion from the bronchoscope lens and the image display system. In addition, WLB could only accesses the luminal surface of relatively large lower airways [88, 208]. Biopsy guided by flexible WLB is prone to sampling error and may cause complications including bleeding and persistent air-leak. High-resolution computed tomography (HRCT) has also been widely adopted for thoracic imaging; it provides an imaging resolution of 0.25 mm at the highest with a slice thickness of 0.75 mm [209]. Thus, HRCT could only resolve airways with a diameter greater than 1 to 2 mm under optimal conditions, and is limited to gross anatomical identification of the diameter changes.

As mentioned in previous chapters, endoscopic OCT holds a strong promise for assessment of lower airways in a minimally invasive fashion [84, 85, 87, 88]. In particular,

a micrometer scale resolution of endoscopic OCT enables precision measurements of the airway luminal area, wall thickness, as well as airway smooth muscle and other layered structures. Of greater interest, OCT is capable of differentiating tissue components of the airway wall such as cartilage, epithelium and potentially the airway smooth muscle. High-speed endoscopic OCT developed in this dissertation makes it possible to perform three-dimensional imaging and hence dynamic volumetric assessment of the structural changes of the airway in real time.

8.2 Material and Methods

In this chapter, we aimed to visualize and assess wall thickness and luminal area of lower airways as well as dynamically monitor changes in these structures in animal models.

8.2.1 High-speed Endoscopic OCT System

The high-speed endoscopic OCT system used in this chapter was described in Chapter 3 to 7. Imaging parameter varied due to system upgrades (e.g., FDML laser sweeping speed). In short, two home built FDML laser sources were used here. Both have a central wavelength of 1310 nm and a full range sweeping range of ~ 150 nm, which provided an axial resolution of ~ 9.3 to 9.5 μm in air. The sweeping frequencies are 40 kHz and 220 kHz, respectively. Such swept laser sources provide a frame rate of 10 to 55 frames per second when each frame contains 4096 A-scans. Four short working distance OCT imaging probes were designed and built with different working distances for acquiring 3D *in vivo* full circumferential OCT images of lower airways of various diameters. The basic parameters of these four imaging probes are listed in Table 8.1.

Probe No.	OD (mm)	WD1 (mm)	WD2 (mm)	Δx (μm)	BR (dB)	2-Pass Efficiency (dB)
1	1.78	1.84	0.45	16.0	< -58.9	> -1.74
2	1.78	2.42	1.03	20.5	< -59.8	> -1.66
3	1.78	2.95	1.56	23.4	< -60.2	> -2.50
4	1.27	1.75	0.62	16.9	< -58.6	> -2.0

Table 8.1 Basic parameters of shorter working distance OCT imaging probes. OD: overall diameter (including plastic tubing); WD1: working distance between the GRIN lens and the focal plane; WD2: working distance from the outer surface of the plastic tubing to the focal plane; Δx : lateral resolution ($1/e^2$); BR: back reflection; 2-Pass Efficiency: double pass efficiency.

The overall diameter of the OCT imaging probe including the protective plastic tubing has to be less than 2.0 mm, which is smaller than the diameter of the working channel on the commonly used bronchoscope (i.e., 2.0 – 2.8 mm). The total imaging depth was set at either 2.5 or 5.0 mm based on the calibration/clock signal from the Mach-Zehnder interferometer. The detection sensitivities of these OCT imaging probes were above 120 dB with 40 kHz FDML laser and above 110 dB with 220 kHz FDML with an incident power of 15 – 20 mW at the sample arm. All the raw data generated from the high-speed endoscopic OCT system were processed, displayed and saved real-time.

8.2.2 *Animal Protocols*

Since swine lower airways is anatomically similar to humans, 11 pigs was used to test the performance and robustness of the high-speed endoscopic OCT system for lower airways imaging. During the experiment, a female pig was anesthetized and placed on a table in one of the animal facilities at John Hopkins University. An endotracheal tube (ETT) was introduced into the trachea through an oral route to maintain ventilation and oxygenation. A bronchoscope was inserted via the ETT to visually inspect central trachea and primary

bronchi, lobar and segmental bronchi. Before OCT imaging, the protective plastic tubing surrounding the OCT imaging probe was marked with an interval of 1 cm. One of the OCT imaging probe surrounded by the marked plastic tubing was delivered through the working channel of the bronchoscope (as shown in Fig. 8.1a) so that the imaging probe can be monitored on the video screen during OCT imaging (as shown in Fig. 8.1b). Once the OCT imaging probe was deployed into the target region, endoscopic OCT imaging was performed by rotating and pulling back the OCT imaging probe. Therefore, 3D dataset of the swine lower airways was acquired. Among the pigs, 4 of them were injected with one or multiple boluses (5 ml each) of 0.08 mg/ml methocholine intravenously to simulate an episode of acute asthma attack. The OCT imaging probe was positioned at the same location to dynamically monitor the response of the lower airway to methocholine. Repeated 2D OCT images were acquired during the experiment.

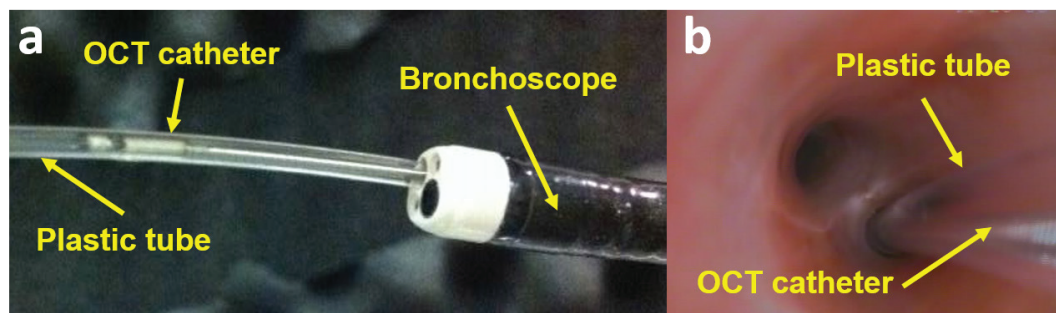


Figure 8.1 (a) An OCT imaging probe assembly including the plastic tubing passes through the working channel of a video bronchoscope. (b) A snapshot of the video acquired from a video bronchoscope showing an OCT imaging probe assembly is deployed into one bronchi.

For certain pulmonary diseases, pig bronchus may not be the best model as it contains more cartilages than human's. Dog airways, on the other hand, has more physiological similarities to human's than pig's. Therefore, a canine model was also explored to first perform a correlation study between *in vivo* endoscopic OCT images and

standard *ex vivo* histopathology. After a female dog was anesthetized, a bronchoscope was used to map the bronchial network structure prior to performing OCT imaging. The protective plastic tubing was marked with an interval of 5 mm and the OCT imaging probe with the marked tube was passed through the working channel of the bronchoscope and into the lower airways. During the OCT imaging, the location of the imaged bronchus was recorded. Afterwards, the whole lung was dissected and fixed in 10% formalin under a normal physiological pressure for 24 hours following the OCT imaging. The lung specimens were located according to the mapped bronchial network structure after fixation, followed by hematoxylin and eosin staining. The OCT images were then compared with the corresponding histology slides.

Animal handling was performed in accordance with Johns Hopkins University institutional animal care and use committee (IACUC).

8.3 Results

8.3.1 *In vivo* Endoscopic OCT Images of Swine Lower Airways

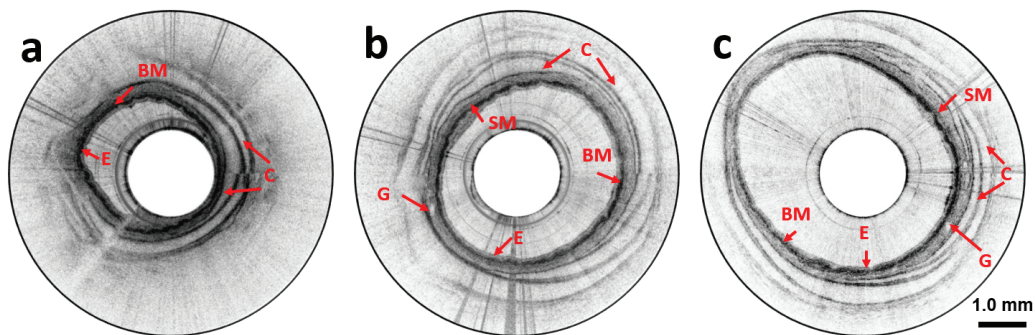


Figure 8.2 Representative 2D circumferential OCT images of swine segmental bronchi *in vivo* with various diameters: (a) ~2.5 mm, (b) ~3.5 mm, and (c) ~4.5 mm. E: epithelium; BM: basement membrane; SM: smooth muscle; C: cartilage; G: gland. Scale bar: 1.0 mm

Microarchitectural structures of pig bronchus can be visualized *in vivo* in a cross sectional fashion with an endoscopic OCT imaging system. The OCT imaging probe has to be

carefully chosen based on the diameter of the bronchus in order to get an optimal imaging quality. Figure 8.2 shows three representative OCT image snapshots of pig segmental bronchus with different diameters between ~ 2.5 to ~ 4.5 mm. Pig segmental bronchus structure is characterized by C-shaped cartilages as shown in Fig. 8.2a-c. Other layered structures can be clearly identified, such as epithelium, basement membrane, and bronchial glands. Thin layers of smooth muscle present between basement membrane and cartilage can sometimes be visualized as well (as shown in Fig. 8.2b-c).

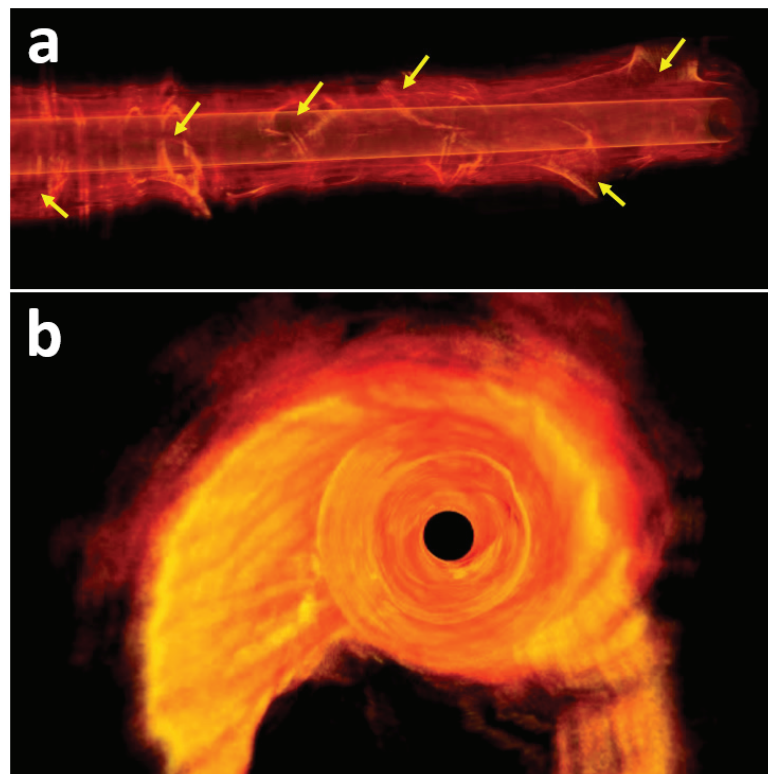


Figure 8.3 3D reconstruction of a pig segmental bronchi *in vivo* acquired by the high-speed endoscopic OCT system in (a) a side view and (b) fly-through view. Yellow arrows in (a) indicate bronchial branching

Animal respiration is one of the most critical problems in *in vivo* 3D endoscopic OCT imaging. One of the advantages that high-speed endoscopic OCT system provides is that 3D dataset can be acquired within a short period of time where animal respiration can be held manually. The reconstruction of one representative 3D dataset is visualized in Fig.

8.3 with two different views. More global information can be directly visualized from 3D reconstruction (e.g., yellow arrows in Fig. 8.3a indicate bronchial branching).

Another way to visualize the *in vivo* 3D dataset is to show *en face* images by unwrapping the airway along the circumferential direction in an orthogonal view. Figure 8.4 shows three *en face* images at different imaging depths of pig lower airways from lung parenchyma to distal bronchi. In the left portion of *en face* images in Fig. 8.4b and c where the lung parenchyma is (i.e., ~ 4 mm long), alveoli can be visualized as the sac-like structures and a blood vessel passing through the alveoli can also be identified. In the middle portion of the *en face* images where the respiratory or terminal bronchiole is (i.e., ~7 mm long), blood vessels and their branches can be identified with a negative image contrast due to the high absorption of blood. Alveoli sometimes can be seen at a deeper depth (as shown in Fig. 8.4c). In the right portion of the *en face* images where distal bronchi is (i.e., ~ 4 mm long), cartilages can be seen with a large size and a negative imaging contrast due to their low scattering in Fig. 8.4b; small glands could also be detected under the cartilages in Fig. 8.4c. The zigzag patterns shown in Fig. 8.4 comes from the heart beat and the high torque from tortuous bronchial network.

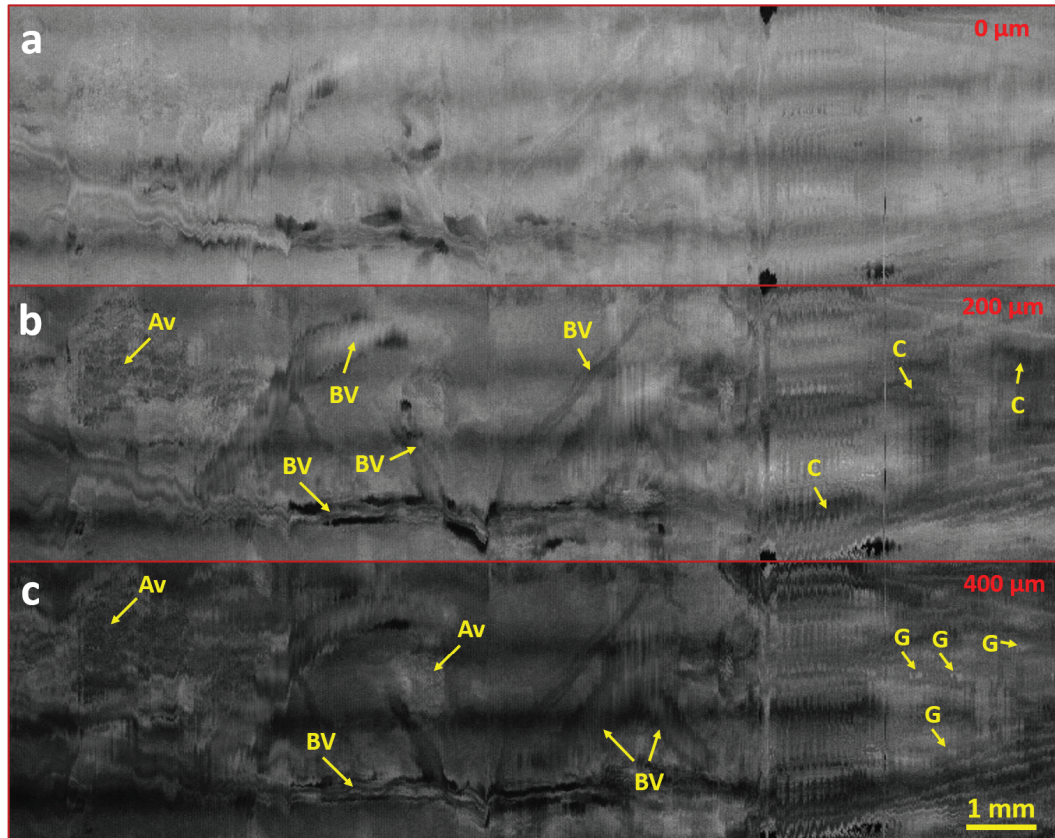


Figure 8.4 *En face* images of pig lower airways *in vivo* from lung parenchyma to distal bronchi at (a) 0 μm , (b) 200 μm , and (c) 400 μm below the airway surface in an orthogonal view. Total field of view: $4.0 \times 15 \times 2.5$ mm (circumferential \times longitudinal \times depth). Av: alveoli; BV: blood vessel; c: cartilage; G: gland. Scale bar: 1.0 mm

8.3.2 Correlation between *in vivo* OCT images and *ex vivo* Histopathology

Although the OCT images in previous subsection have shown a great capability of OCT imaging in resolving and identifying layered structures in lower airways, an experiment was performed to confirm that the layered structures seen on OCT images can be correlated with the golden standard: *ex vivo* histopathology. Figure 8.5 shows two examples of the correlation between *in vivo* OCT images and *ex vivo* histopathology. Shown in Fig. 8.5a is an *in vivo* OCT image of dog bronchus with its corresponding histopathology micrograph shown in Fig. 8.5b. Several features, such as epithelium, cartilage, smooth muscle and

adjacent blood vessel and bronchi that are identified on the OCT image can be confirmed on the corresponding histology.

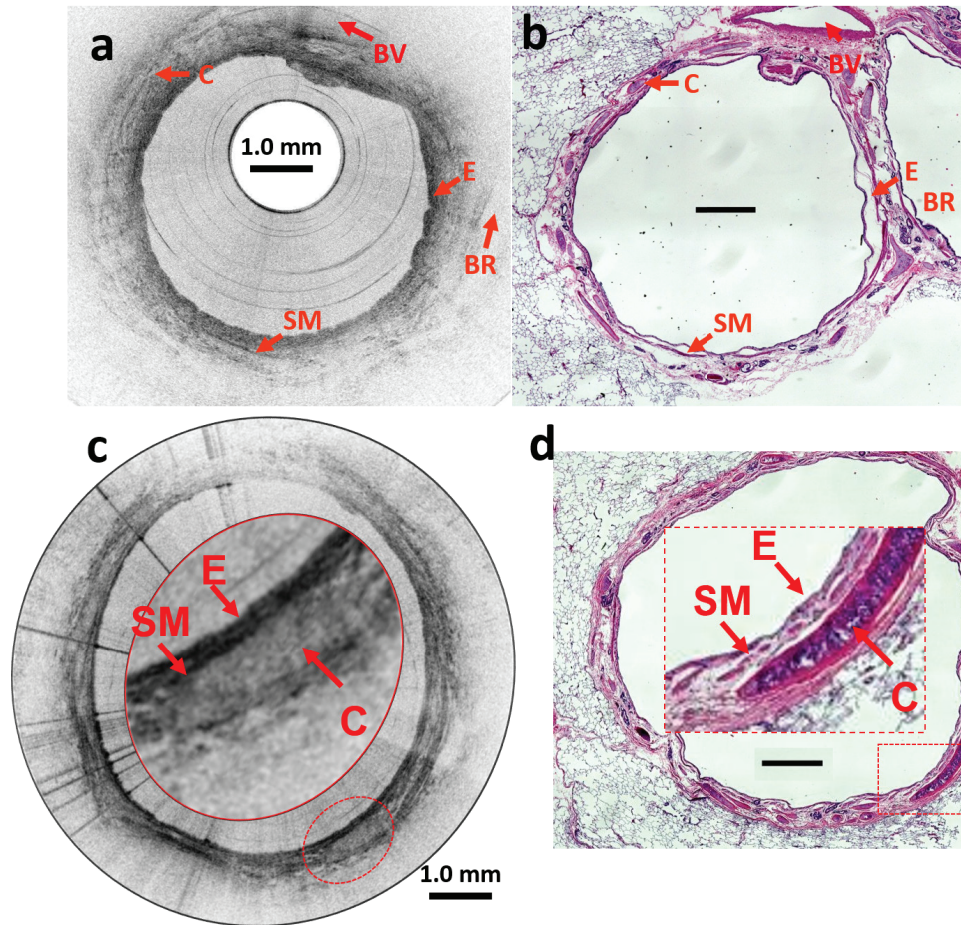


Figure 8.5 (a and c) *in vivo* OCT images of canine bronchi and (b and d) their corresponding histopathology micrographs. The insets in (c) and (d) are 3X zoomed in of the regions encircled in (c) and (d). E: epithelium; C: cartilage; BV: blood vessel; SM: smooth muscle; BR: bronchi. Scale bar: 1.0 mm.

Shown in Fig. 8.5c and 8.5d is another example of *in vivo* OCT image with its corresponding *ex vivo* histopathology. In the insets of Fig. 8.5c and 8.5d, which are the 3X zoomed in images of the regions encircled in those figures, structures like epithelium, smooth muscle, and cartilage, can be identified from the OCT image and confirmed on the corresponding histopathology micrograph.

Moreover, wall thickness was measured in both OCT images and their corresponding histopathology micrographs. An example is given in Fig. 8.6a where an OCT image of a small dog airway and its corresponding histopathology micrograph are shown. The measurements of wall thickness were taken at the locations where there are clearly distinct local similarity between two walls on both images. Since the OCT images are displayed in a scale of optical path, all the measurements of wall thickness on OCT images were divided by an average group refractive index of 1.38. When the results were quantitatively analyzed, it is noticed that the measurements are consistent between OCT images and histopathology if there are clear boundaries at both sides of the bronchial wall (e.g., labeled in yellow in Fig. 8.6a) whereas the measurements have relatively larger errors if the boundaries are unclear (e.g., labeled in red in Fig. 8.6a). A total of 25 bronchial walls were measured among 4 correlation pairs. Among these results, 10 measurements came from the wall with clear boundaries while 15 are from the wall without clear boundaries.

A scatter plot shows a nice correlation between OCT and histology measurements of wall thickness. A linear fitting with an intercept of zero (i.e., $y = a \cdot x$) shows a slope of 1.01 ± 0.02 with an adjusted coefficient of determination (i.e., adjusted R^2) of 0.994, showing that the OCT and histology measurements are surprisingly consistent. A slope statistically significantly larger than 1.0 was originally expected because shrinkage of tissue usually happens during the histology sample preparation. However, it is possible that the averaged group refractive index of the bronchial tissue was overestimated and therefore lowered the slope close to 1. Nevertheless, if the measurements on histology micrographs are considered as golden standard, relative error is then defined as:

$$\frac{\text{OCT Measurement} - \text{Histology Measurement}}{\text{Histology Measurement}} \times 100\% . \quad (8.1)$$

A histogram of the relative error is displayed in Fig. 8.6c where all of the errors are within 20%, suggesting a great correlation between OCT and histology measurements if clear boundaries are able to be identified.

The data in Fig. 8.6d are more scattered than those in Fig. 8.6b and the adjusted R^2 of 0.961 is worse than the one in Fig. 8.6b, suggesting that the OCT measurements became less accurate when the boundaries are hard to be identified. This finding is confirmed by the histogram as shown in Fig. 8.6e, where relative errors became larger as well. In addition, the linear fitting result in Fig. 8.6d suggests that the wall thickness on OCT images were consistently under measured compared to histology measurements (i.e., a slope of 0.870 ± 0.045). This observation is also confirmed by the histogram as shown in Fig. 8.6e where the majority of the relative errors fell between -10% to 0. This might be due to the fact that the outer boundary delineated on OCT images based on intensity was underestimated from the actual outer boundaries. However, data in Fig. 8.6d still shows a reasonable linear correlation between OCT and histology measurements even when the outer boundaries of the bronchial wall is not clear.

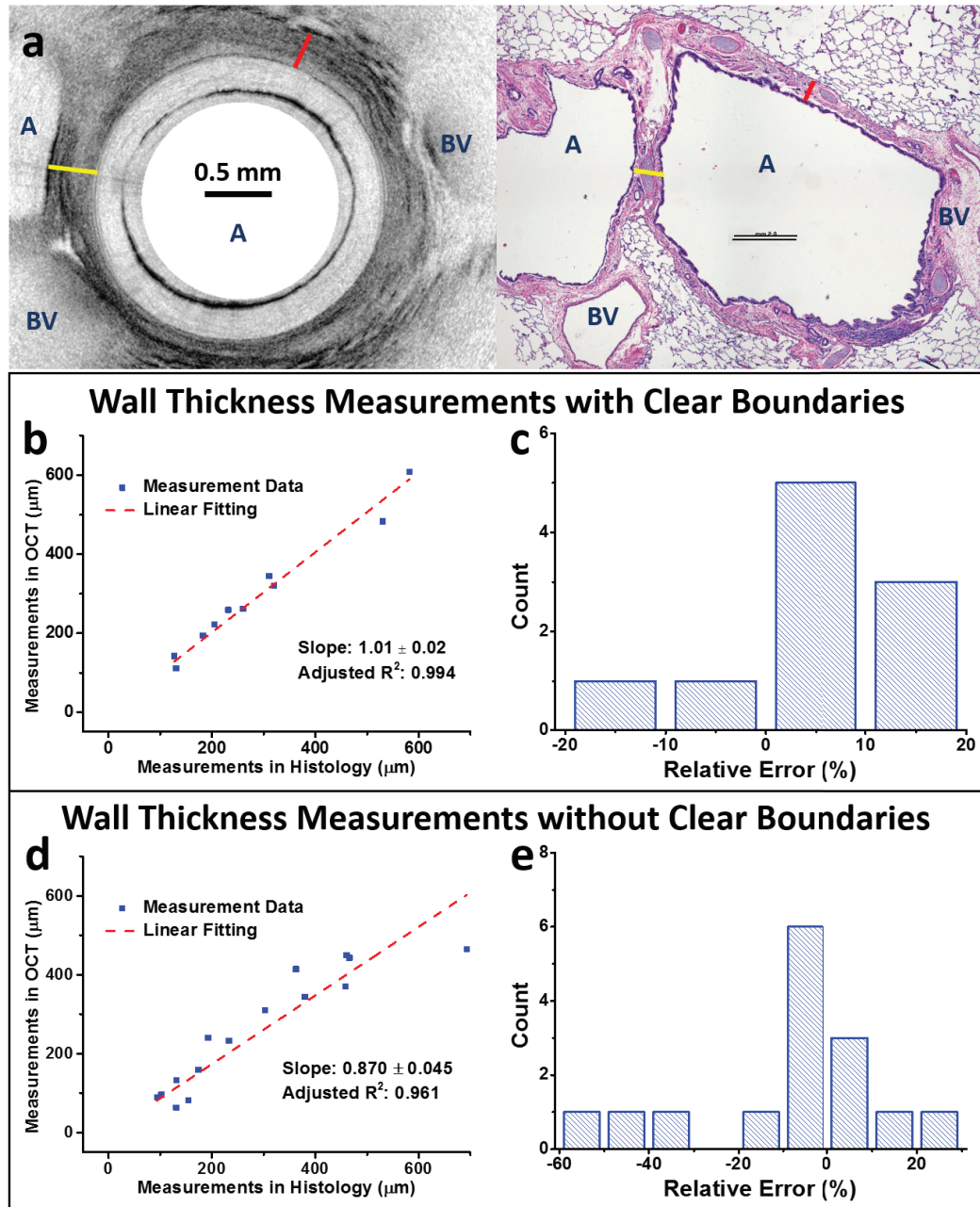


Figure 8.6 (a) An exemplary correlation pair of *in vivo* OCT images of canine bronchi and histopathology micrograph. Bronchial walls were picked and measured on both images. Yellow label shows a wall with clear boundaries on both sides whereas red label shows a wall without clear boundaries on both sides. A: airway; BV: blood vessel. Scale bar: 0.5 mm. (b and d) Correlations between OCT and histology measurements of the wall thickness if clear boundaries are (b) able to be identified or (d) hard to identify. (c and e) Histogram plots of the relative errors between the two measurements if clear boundaries are (b) able to be identified or (d) hard to identify.

One thing needs to be pointed out is that the correlation between OCT images and histopathology micrographs are imperfect (i.e., only within 1 mm accuracy) and tissue deformation was also not taken into account. Nevertheless, the preliminary results of the quantitative comparison between OCT and histology measurements of wall thickness shows that endoscopic OCT has a great potential of quantitatively analyzing the structures of the lower airway *in vivo*.

8.3.3 Dynamic OCT Imaging of Swine Lower Airways

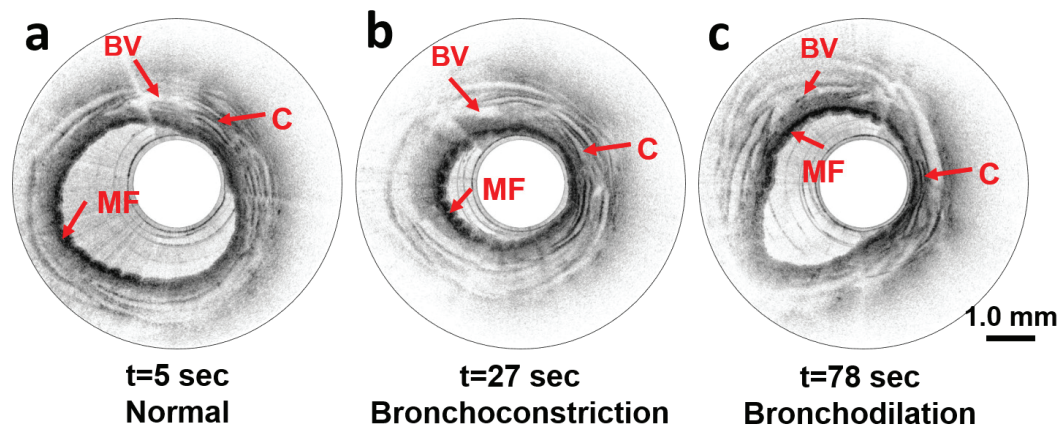


Figure 8.7 Three *in vivo* endoscopic OCT images of pig bronchi response (a) before, (b) during, and (c) after methocholine challenge. MF: mucosal folding; C: cartilage; BV: blood vessel. Scale bar: 1.0 mm.

Among the four methocholine challenged animals, two of them had noticeable response to the drug. Figure 8.7 shows three OCT images of the same location (or close locations) in a pig bronchi before (as shown in Fig. 8.7a), during (as shown in Fig. 8.7b), and after (as shown in Fig 8.7c) methocholine challenge. In all three phases, the OCT images clearly showed layered structures. In addition, with these images, luminal volumetric changes and morphological changes of the epithelium could be evidently identified; while the luminal area of the bronchi was greatly reduced with noticeable musical folding during the

methocholine challenge, the luminal area was partially restored and mucosal folding returned to the previous level after the effect of the drug was washed out.

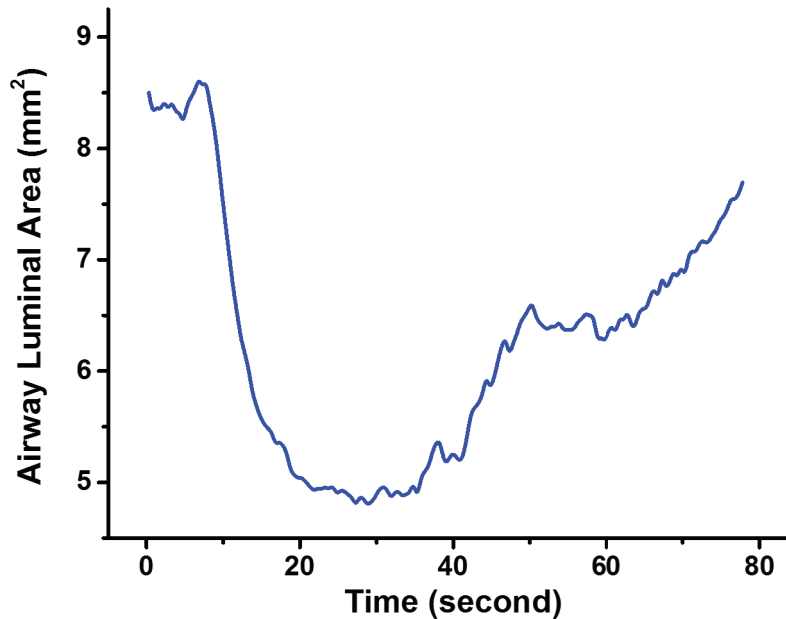


Figure 8.8 A time course of the luminal area of the pig bronchus response to the methocholine challenge.

By analyzing these *in vivo* OCT images, quantitative results can be drawn from the OCT dataset. Figure 8.8 shows that the luminal area of the pig bronchus was reduced during the bronchoconstriction and partially recovered to 90% of the previous level. The bronchoconstriction began at about 10 seconds after the injection (i.e., $t=0$ sec) and lasted for about 17 seconds. The most reduction of the luminal area ($\sim 50\%$) occurred about 27 seconds after the injection. Bronchodilation started from 27 seconds after the injection and lasted for about 50 seconds, which is much slower than bronchoconstriction.

Mucosal folding was also quantitatively analyzed. Three mucosal folding structures of similar size were chosen and tracked among all the OCT images; the heights and widths of these structures were measured. Averaged height and width of these mucosal folding structures as well as their standard deviations are shown in Fig. 8.9a. It is clearly shown

that mucosal folding is more evident as the folds were increased by ~43% in height and decreased by ~45% in width during the bronchoconstriction. Similar to the luminal area change, both height and width of the mucosal folding were partially recovered to the previous level during the bronchodilation. On the other hand, the averaged mucosal folding size remained more or less the same except for a spike increase just after the injection of the drug as shown in Fig. 8.9b.

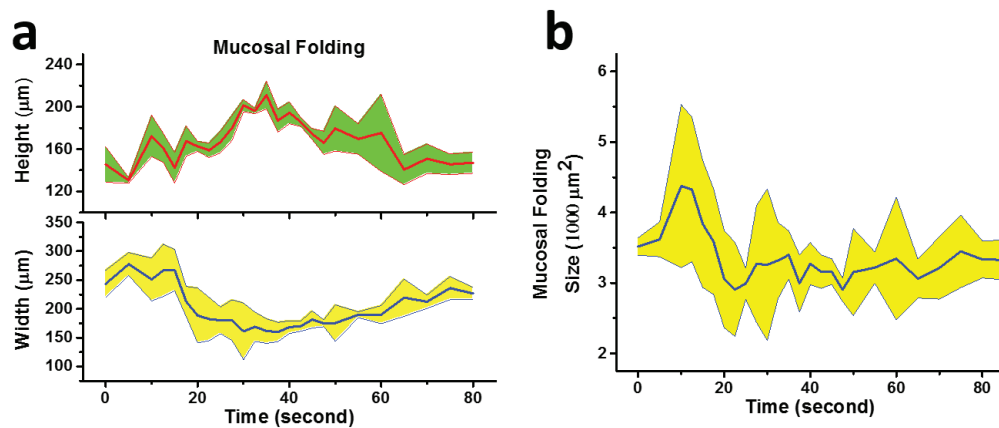


Figure 8.9 (a) Change of averaged height and width of mucosal folding with their standard deviations. (b) Change of averaged size of mucosal folding with its standard deviation.

8.4 Summary

In this chapter, we first introduced a brief background of lower airway imaging, in particular the limitations of current imaging modalities in lower airway imaging. The high-speed endoscopic OCT imaging of lower airways was then demonstrated in animal models. In addition, a correlation study was performed to show that *in vivo* endoscopic OCT has a potential of differentiating layered structures that were correlated with the *ex vivo* histopathology results. At last, dynamic endoscopic OCT imaging of lower airways was performed to monitor the airway response to methacholine in real time.

Chapter 9 Endoscopic Optical Coherence

Tomography in Upper Gastrointestinal Tract

Imaging

This chapter briefly reviews the background including the importance of esophageal imaging and the limitations of current clinic diagnosis. The OCT system and animal protocol are then discussed. Three studies have been conducted in esophagus imaging in this chapter, which are high-speed endoscopic OCT imaging of pig esophagus *in vivo* and human esophagectomy specimen *ex vivo*, a pilot study of *in vivo* assessment of cryoablation treated pig esophagus, and *in vivo* assessment of esophageal structures in a guinea pig model of eosinophilic esophagitis.

9.1 Background and Introduction

Esophageal cancer has the third lowest five-year survival rate of only 16% among all types of cancers, and the life quality of the patients who have surgical resection of esophagus is usually very poor. Over 95% of the esophageal cancer is either squamous cell carcinoma or adenocarcinoma [210]. The squamous cell carcinoma is more prevalent in Asian countries while adenocarcinoma is more common in Western Europe and the United States [211, 212]. Recent studies suggested that the incidence of esophageal adenocarcinoma (EAC) has increased six fold in the past three decades, and the increasing rate is faster than any other cancer [210]. Approximately 50% of all new EACs arise from patients with chronic gastroesophageal reflux disease (GERD) and Barrett's esophagus (BE) [213], and BE is thought to be responsible for at least 4% of all cancer deaths in the United States

[214]. BE, which is usually associated with chronic GERD, is an abnormal condition of the esophagus where the normal stratified squamous epithelium is replaced by specialized columnar epithelium found in lower GI tract (i.e., referred to as intestinal metaplasia). Although BE itself is asymptomatic, it is associated with an approximately 40-fold increase in risk of progression to dysplasia and adenocarcinoma over general population [215, 216]. Neoplastic changes in BE develop in stages from non-dysplastic metaplasia to increasing grades of dysplasia and eventually to adenocarcinoma. Therefore, early detection of esophageal cancer or esophageal premalignant lesions such as BE could significantly improve the survival rate and improve the life quality of the patients.

Current clinical diagnosis of BE is conducted by performing upper GI endoscopy followed by biopsies of the columnar lined esophagus [217]. The appearance of the mucosa of BE and normal epithelium are visually different under the endoscope. If abnormal mucosa is evident under the endoscope, multiple biopsies are then taken to look for intestinal metaplasia, dysplasia and other premalignant lesions. The current biopsy strategy, which takes biopsy samples at four circumferential quadrants at intervals of 1-2 cm along the esophagus, only covers 5% of susceptible area and yields a very high sampling error. Moreover, screening BE in selective populations at higher risks and surveillance of BE's progression are both recommended to use the same diagnostic [217].

Endoscopic ablation of BE is considered a relatively safe treatment and may lead to a regrowth of squamous epithelium [218]. However, residual BE remained after ablation may become subsquamous BE once the newly developed squamous epithelium grows over remnant BE [219]. Unfortunately, subsquamous BE is unable to be identified by current diagnostic method, leading to a high risk of developing EAC.

Endoscopic OCT has a capability of providing *in vivo* cross sectional images with an axial resolution of 1 – 15 μm and an imaging depth of 1 – 3 mm. Integrated with a standard upper GI endoscope, endoscopic OCT is an ideal tool for esophageal imaging. In particular, it has been proven that OCT is capable of identifying subsquamous BE [220]. Various OCT imaging probes have been developed to demonstrate that OCT can differentiate the layered structures of normal esophagus and identify abnormalities in diseased esophagus *in vivo* [70, 80, 83, 221-224]. Technical advances on laser source and photodetectors have significantly improved the imaging speed of the OCT system, making 3D OCT imaging possible. Meanwhile, large working distance OCT imaging probes could provide a full circumferential cross sectional image of the esophagus [74, 79]. Combining these two technologies together, there is a great potential in the surveillance/screening of the entire esophagus *in vivo* without any removal of esophageal tissue [225, 226].

Not only endoscopic OCT can provide a new imaging modality in clinics, it may also be a powerful tool in basic research. The pathogenesis of lots of GI diseases (e.g., eosinophilic esophagitis, inflammatory bowel disease and their link to oncogenesis, etc.) still remain unclear [227-230]. Most of these disease models have only been developed on small animals (e.g., mouse, rat, guinea pig, etc.) so far [231, 232]. Analysis of structural changes in these disease models is very important and could potentially unveil the pathogenesis of these diseases. However, the imaging modalities that could analyze structural changes *in vivo* on small animals is currently limited as an imaging resolution of micron scale is required. Interestingly, high-speed endoscopic OCT has the capability of providing such analysis on a volumetric dataset of the esophagus.

9.2 Material and Methods

In this chapter, we aimed to visualize the layered structures in the esophagus and assess the cryoablation effect on the esophagus using a swine model. We also demonstrated the possibility of using endoscopic OCT as a research imaging tool to study the thickness change of esophageal mucosa of eosinophilic esophagitis in a guinea pig model.

9.2.1 High-speed Endoscopic OCT System

The high-speed endoscopic OCT system used in this chapter was described in Chapter 3 to 7. Imaging parameter varied due to system upgrades (e.g., FDML laser sweeping speed). In short, two home built FDML laser sources were used here. Both of the sources have a central wavelength of 1310 nm and a full range sweeping range of ~ 150 nm, which provided an axial resolution of ~ 9.3 to 9.5 μm in air. The sweeping frequencies were 40 kHz and 220 kHz, respectively. Such swept laser source provide a frame rate of 10 and 55 frames per second when each frame contains 4096 A-scans.

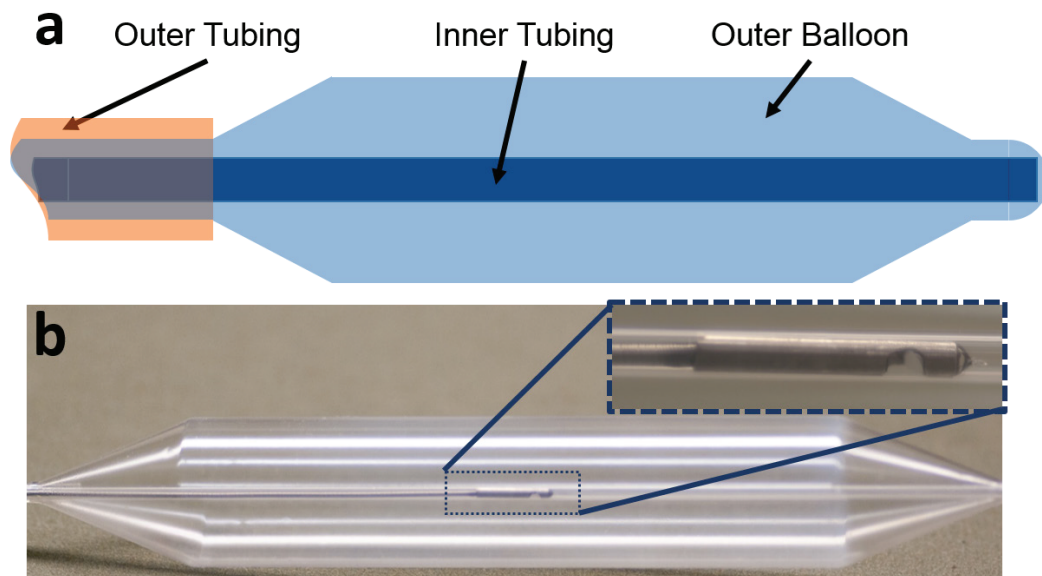


Figure 9.1 (a) A schematic of double lumen balloon. The scale in this schematic is not proportional to the actual balloon. (b) Photos of an OCT imaging probe inside an inflated double lumen balloon and the distal end of the OCT imaging probe (inset).

Three large working distance OCT imaging probes were designed and built with a working distance of 10.0 mm for acquiring 3D *in vivo* full circumferential OCT images of the pig esophagus. The basic parameters of those four imaging probes are listed in Table 9.1 (i.e., Probe No. 1, 2, and 3). The OCT imaging probes were then inserted into a double lumen balloon as illustrated in Fig. 9.1a. The outer balloon is transparent and inflatable, and has a maximal outer diameter of 18.0 mm when inflated. The inner diameter of the inner transparent tubing is ~ 1.40 mm where the OCT imaging probe can pass through. Ideally, the overall diameter of the double lumen balloon should be small enough to pass through the working channel on the commonly used upper GI endoscope (i.e., 2.8 – 6.0 mm). Current double lumen balloon cannot pass through a 2.8 mm working channel of an upper GI endoscope due to the size limit of the deflated outer balloon. The whole assembly of an inflated double lumen OCT imaging probe is shown in Fig. 9.1b. The total imaging depth was set either at 2.5 mm based on the calibration/clock signal from the Mach-Zehnder interferometer. The detection sensitivities of those OCT imaging probes were above 115 dB with 40 kHz FDML laser with an incident power of 15 – 20 mW at the sample arm. A short working distance OCT imaging probe was also used for acquiring 3D *in vivo* full circumferential OCT images of the guinea pig esophagus. The basic parameters of those four imaging probes are also listed in Table 9.1 (i.e., Probe #4). The performance of this imaging probe is similar to those described in the previous chapter. All the raw data generated from the high-speed endoscopic OCT system were processed, displayed and saved in real-time.

Probe No.	OD (mm)	WD1 (mm)	WD2 (mm)	Δx (μm)	BR (dB)	2-Pass Efficiency (dB)
1	1.27	10.38	9.88	23.5	< -58.3	> -3.51
2	1.27	10.16	9.66	25.7	< -59.0	> -3.30
3	1.27	11.20	10.70	21.2	< -58.5	> -3.71
4	1.27	1.84	0.45	16.0	< -58.9	> -1.74

Table 9.1 Basic parameters of four OCT imaging probes used in upper GI studies. Three of them are large working distance OCT imaging probes (#1, 2, and 3) for large animal imaging and the left one is a short working distance one for small animal imaging. OD: overall diameter of the imaging probe; WD1: working distance between the GRIN lens and the focal plane; WD2: working distance from the outer surface of the plastic tubing to the focal plane; Δx : lateral resolution; BR: back reflection; 2-Pass Efficiency: double pass efficiency.

9.2.2 Animal Protocols

Three pigs were used to test the performance of the high-speed endoscopic OCT system for esophageal imaging. During the experiments, a female pig was anesthetized and placed on a table in one of the animal facilities at the University of Washington or the Johns Hopkins University. An overtube was introduced into the esophagus. The deflated balloon was passed through the overtube and into the esophagus. An upper GI endoscope was inserted via the overtube to visually inspect the esophagus and find the region of interest. Once the OCT imaging probe was deployed into the targeted region, the double balloon was fully inflated and a 2 to 5 cm long segment of pig esophagus was imaged using a spiral scanning pattern with a 20 μm spacing between adjacent circumferential images. Among the pigs, one of them was treated with endoscopic spray cryoablation with pressured carbon dioxide [233, 234]. Endoscopic OCT imaging was performed immediately after the ablation treatment to monitor the acute structural changes after the treatment and assess the effect of cryoablation. Besides *in vivo* experiments, several *ex vivo* pig esophagus and

human esophagectomy specimens were also imaged using large working distance OCT imaging probes with a double lumen balloon.

The high-speed endoscopic OCT imaging was also applied to a guinea pig model of eosinophilic esophagitis to assess the structural changes of the esophagus. Two groups of male guinea pigs were imaged using endoscopic OCT system and each groups have 4 guinea pigs. Two groups of guinea pigs were actively sensitized by 3 intraperitoneal injection of 10 mg/kg ovalbumin (OVA) in saline every 48 hours. Three weeks after the last injection, all the animals were challenged with aerosolized 0.1% OVA for 30 seconds. One group of guinea pigs were only challenged once and endoscopic OCT imaging was performed before and after this challenge, whereas another group was challenged every morning for 3 weeks and endoscopic OCT imaging was performed once at the end. Prior to the OCT scan, animals were anesthetized by intraperitoneal injection of ketamine (80 mg/kg) and xylazine (7 mg/kg). A short working distance OCT imaging probe was then inserted into the esophagus to a depth of 10 cm past the incisor. The imaging probe was driven with a spiral scanning pattern with a 25 μm spacing between two adjacent circumferential images to obtain a 3D volumetric OCT dataset. The thickness of the esophageal layers were measured in the 3D dataset afterwards. In short, OVA sensitized animals were used as controls while guinea pigs challenged with OVA for 1 day and 3 weeks were used as acute and chronic inflammation models, respectively.

9.3 Results

9.3.1 Endoscopic OCT Esophageal Imaging

Microarchitectural structures of pig esophagus can be visualized *in vivo* in a cross sectional fashion with endoscopic OCT imaging system. Figure 9.2a shows one representative OCT

image snapshot of normal pig esophagus. Layered structures can be clearly identified, such as epithelium, lamina propria, muscularis mucosa, submucosa, and muscularis propria. A cutaway 3D image reconstructed from a series of 2D images is shown in Fig. 9.2b.

Human esophagectomy specimens were also imaged *ex vivo* using the same OCT imaging system. Figure 9.3a shows one representative OCT image snapshot of a human esophagectomy specimen from a patient with esophageal cancer. Unlike the normal esophagus, the layered structures on the abnormal specimen became less clear and lots of submucosal glands appeared on the OCT images (as indicated by red arrows in Fig. 9.3a). Similarly, a cutaway 3D image reconstructed from a series of 2D images is shown in Fig. 9.3b.

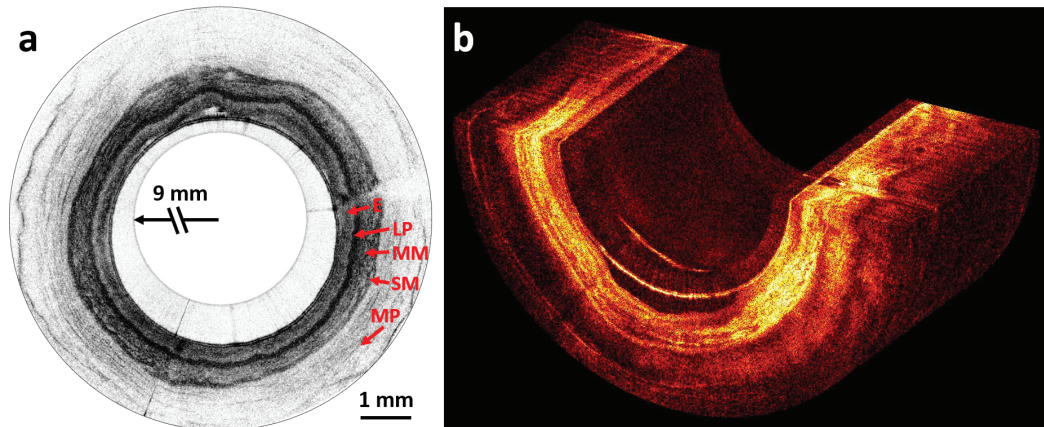


Figure 9.2 (a) Representative 2D circumferential OCT images of pig esophagus *in vivo*. The central void region is intentionally reduced in order to magnify the actual OCT image region. (b) A 3D reconstruction of OCT images of pig esophagus in a hot colormap. E: epithelium; LP: lamina propria; MM: muscularis mucosa; SM: submucosa; MP: muscularis propria. Scale bar: 1.0 mm

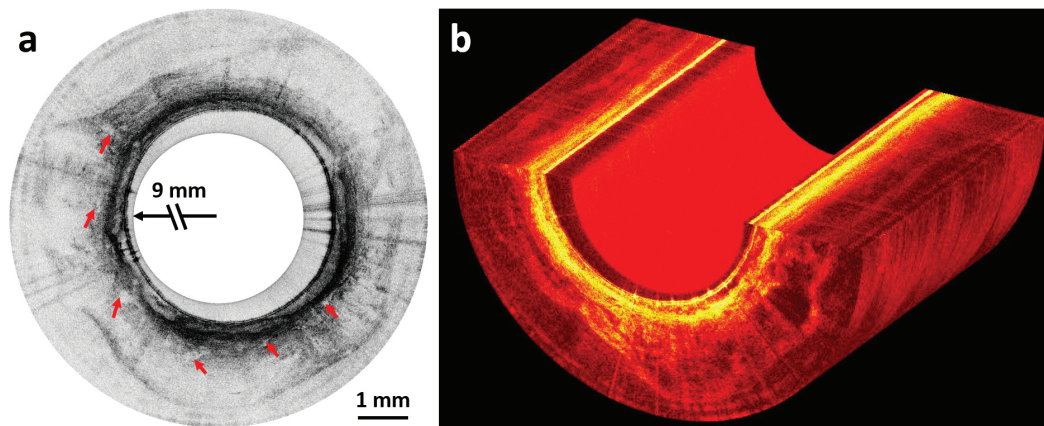


Figure 9.3 (a) Representative 2D circumferential OCT images of human esophagectomy specimen *ex vivo*. The central void region is intentionally reduced in order to magnify the actual OCT image region. Red arrows indicate submucosal glands (b) A 3D reconstruction of OCT images of human esophagectomy specimen in a hot colormap. Scale bar: 1.0 mm

9.3.2 *In vivo* Assessment of Cryoablation on Normal Pig Esophagus – A Pilot Study

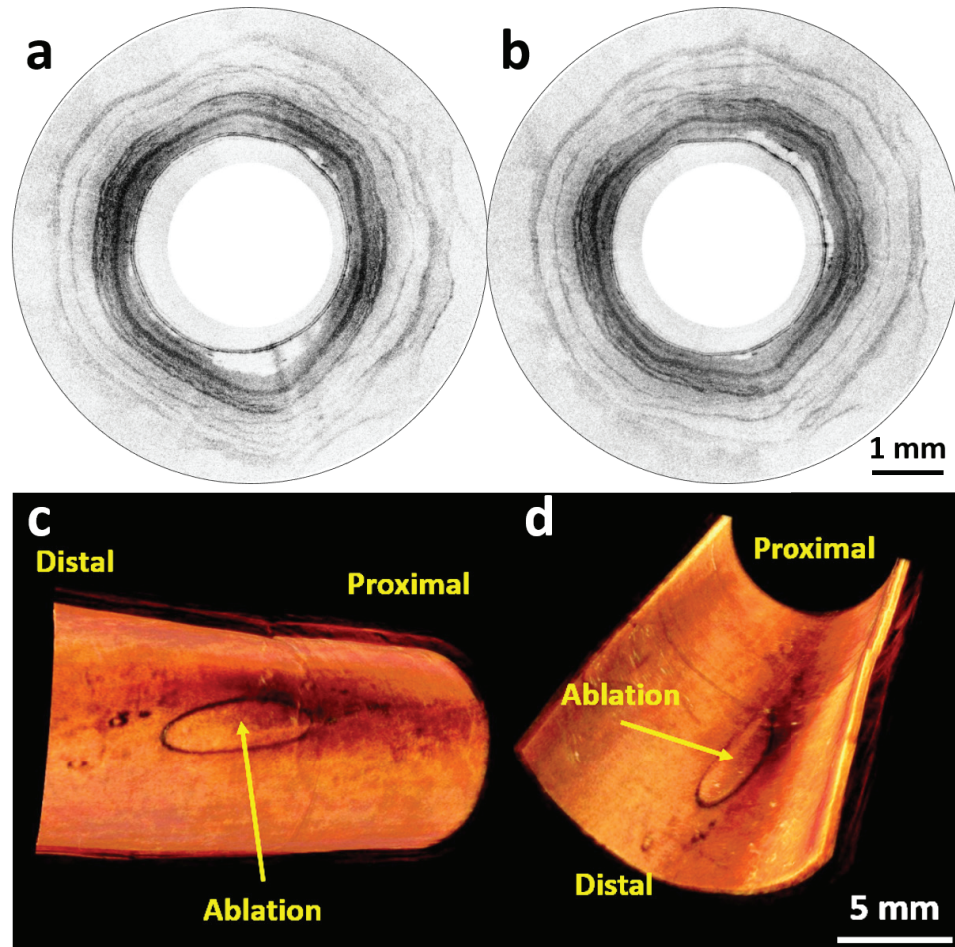


Figure 9.4 (a and b) Representative 2D circumferential OCT images of pig esophagus *in vivo* after cryoablation. (c and d) Different views of 3D reconstruction of OCT images of pig esophagus in a hot colormap. Scale bar: 1.0 mm in (a) and (b), 5.0 mm in (c) and (d)

One pig was used to image its esophagus after the animal was treated with cryoablation with pressured carbon dioxide. Figure 9.4a and 9.4b show two representative OCT image snapshots of pig esophagus after the cryoablation. Similar to Fig. 9.2a, layered structures can be identified from epithelium down to muscularis propria. In the cutaway 3D reconstruction images shown in Fig. 9.4c and 9.4d, a cryoablation site can be clearly visualized from different views (i.e., Fig. 9.4c was viewed from outside of the esophagus and Fig. 9.4 d was viewed from inner lumen of the esophagus).

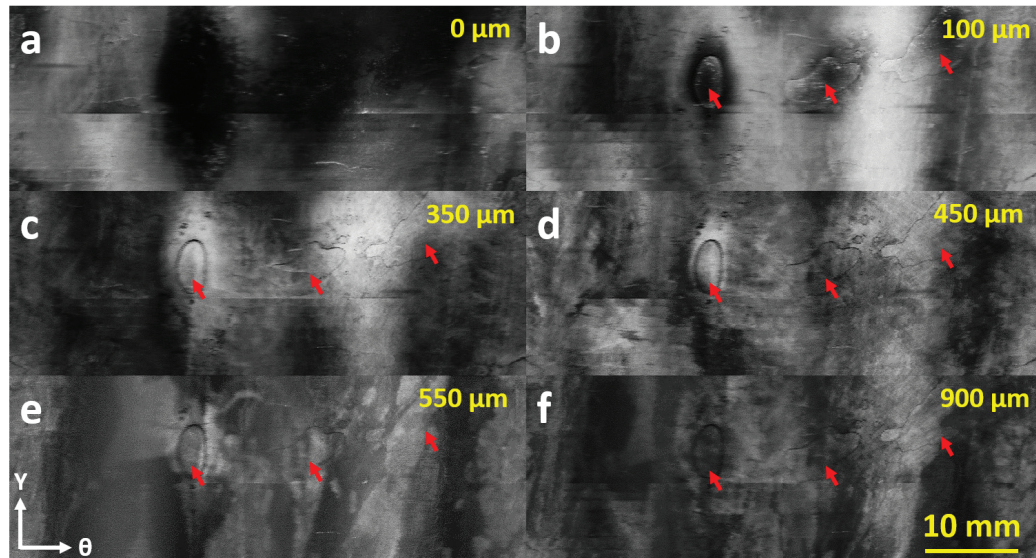


Figure 9.5 (a to f) *En face* images of pig esophagus *in vivo* after cryoablation at (a) 0 μm , (b) 100 μm , (c) 350 μm , (d) 450 μm , (e) 550 μm , and (f) 900 μm below the esophageal surface in an orthogonal view. Total field of view: $56.6 \times 20 \times 2.5$ mm (circumferential \times longitudinal \times depth). Red arrows indicates the cryoablation sites. Scale bar: 1.0 mm

The 3D dataset of the pig esophagus was then unwrapped along the circumferential direction in an orthogonal view. Six *en face* images of a thickness of ~ 50 μm at different depths are shown from Fig. 9.5a to 9.5f, which approximately correspond to (a) surface, (b) epithelium, (c) lamina propria, (d) muscularis mucosa, (e) submucosa, and (f) muscularis propria. Although the cryoablation is usually used to only treat layers in mucosa, cryoablation sites on this esophagus as indicated by red arrows could be identified from epithelium down to muscularis propria. Different gross characteristics are also shown on the *en face* images. For example, dense stratified squamous epithelium are shown as uniform high scattering signal in Fig. 9.5b; interwoven patterns shown in Fig. 9.5d and 9.5f suggest that smooth muscle fibers exist in the layers of muscularis mucosa and muscularis propria.

9.3.3 *In vivo* Assessment of Esophageal Structures in a Guinea Pig Model of Eosinophilic Esophagitis

Eight guinea pigs that were arranged into two groups were imaged using a high-speed endoscopic OCT imaging system. One of the groups was imaged before and after the OVA challenge. And twelve 3D datasets were acquired in total. Fig. 9.6 shows three representative OCT image snapshots and one longitudinal cross sectional OCT image of guinea pig esophagus acquired *in vivo* from one of the 3D datasets. The corresponding locations of three circumferential OCT images (i.e., Fig. 9.6a to 9.6c) are labeled as dotted red lines in longitudinal cross sectional OCT image as shown in Fig. 9.6d.

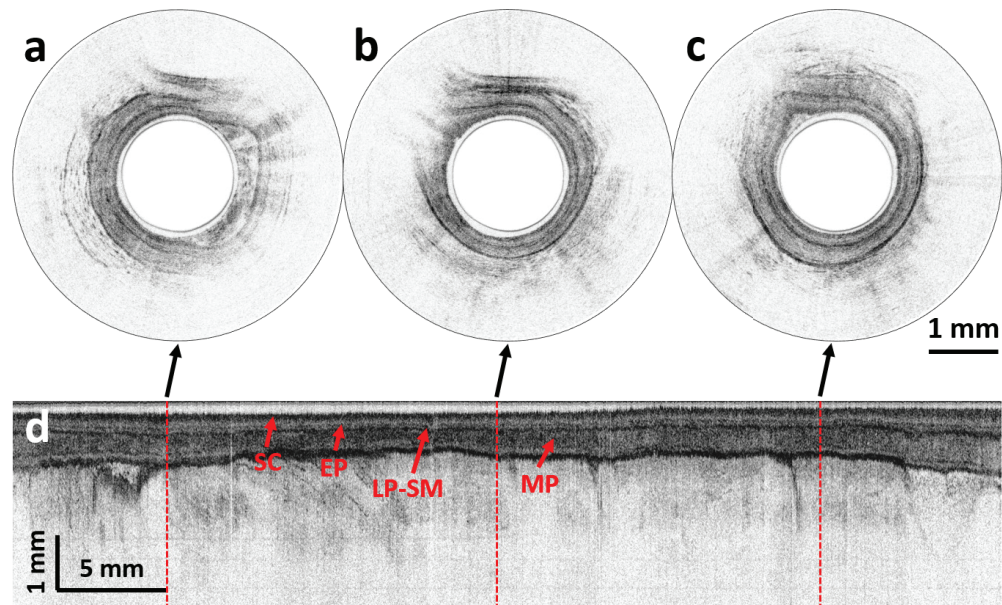


Figure 9.6 (a to c) Representative 2D circumferential OCT images of guinea pig esophagus *in vivo* at different longitudinal locations as labeled in (b). (b) A longitudinal cross sectional OCT images of guinea pig esophagus *in vivo*. SC: stratum corneum; EP: epithelium; LP: lamina propria; MM: muscularis mucosa; SM: submucosa; MP: muscularis propria. Scale bar: 1.0 mm in (a) to (c); 1.0 mm in depth direction of (d) and 5.0 mm in longitudinal direction of d.

Layered structures (e.g., stratum corneum, epithelium, muscularis propria) can be identified on both types of images. Other layers such as lamina propria, muscularis mucosa, and submucosa are thin in guinea pig, and cannot be always differentiated from each other on all the acquired OCT images.

The thickness of the esophageal layers were analyzed from the 3D datasets, which are categorized into 3 groups (i.e., control, acute, and chronic groups). The thickness was calculated from the measurement of the optical path on OCT images divided by an averaged refractive index of biological tissue (i.e., 1.38). Since the layers of lamina propria, muscularis mucosa, and submucosa are not always able to be differentiated, these three layers are grouped together. The measurements of the three layers shown in Fig. 9.7 are: (control v.s. acute and chronic) 64.8 ± 4.8 v.s. 68.3 ± 4.2 and 54.3 ± 4.9 μm in stratum corneum; 56.4 ± 2.6 v.s. 60.9 ± 3.8 and 58.0 ± 3.0 μm in epithelium; 199.7 ± 15.4 v.s. 205.6 ± 14.3 and 161.4 ± 8.3 μm in lamina propria to muscularis propria. The thicknesses of stratum corneum and epithelium didn't change among the groups. However it is suggested that there is a trend of decrease in the thickness of the layers from lamina propria to muscularis propria from control/acute group to chronic group, although no statistical significance was found (p value: 0.108 between control and chronic groups; 0.061 between acute and chronic groups). These findings are consistent with those concluded from the histopathology micrographs, which together suggests that there is no significant structural change in a guinea pig model of eosinophilic esophagitis.

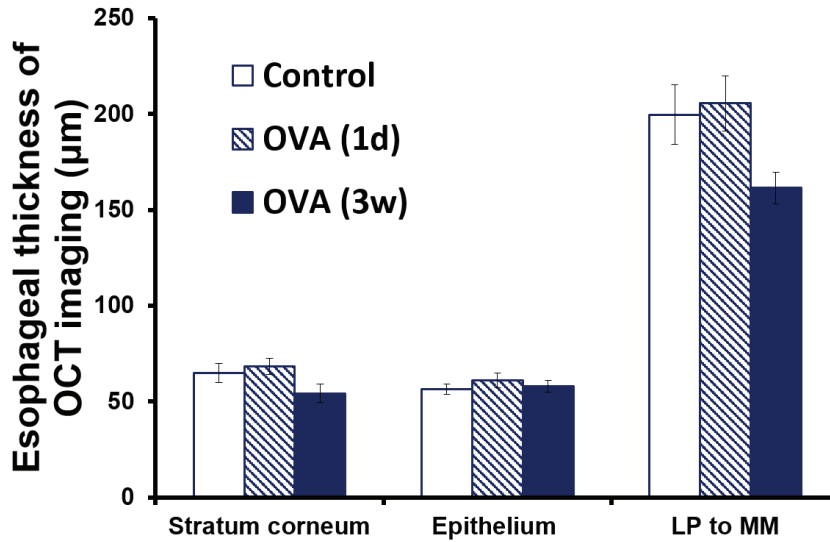


Figure 9.7. The thickness measurements of the esophageal layers on a guinea pig model based on the data acquired from the high-speed endoscopic OCT imaging system.

9.4 Summary

In this chapter, we first reviewed the background of esophageal imaging and the limitations of current clinic diagnosis. The high-speed endoscopic OCT imaging of pig esophagus *in vivo* and human esophagectomy specimen *ex vivo* was then demonstrated. Moreover, a pilot study of *in vivo* assessment of cryoablation treated pig esophagus was performed. At last, an *in vivo* experiment of a guinea pig model of eosinophilic esophagitis was conducted to assess esophageal structures change in real time.

Chapter 10 Ultrahigh Resolution Endoscopic Optical Coherence Tomography Imaging

This chapter briefly reviews the rationale of developing ultrahigh resolution endoscopic OCT imaging at the wavelength range of 800 nm. An ultrahigh resolution endoscopic OCT system is then discussed. Two preliminary studies, including guinea pig esophagus *in vivo* and guinea pig bronchus *ex vivo*, were used to demonstrate the performance of the system.

10.1 Introduction

In previous chapters, a portable high-speed endoscopic OCT imaging system at a central wavelength of 1300 nm that enabled translational imaging of internal luminal organs such as the gastrointestinal tract or airways was introduced. Due to technical difficulties, most OCT imaging probes developed so far were designed for working at the wavelength around 1300 nm, which provides an excellent axial resolution about 7-20 μm and an imaging depth about 2-3 mm [80, 191, 193-195, 197, 198]. Although this axial resolution is already much better than any other clinically used imaging modalities (e.g., ultrasound, MRI, etc.), a higher resolution that approaches low magnification histology result is highly desirable in order to resolve fine tissue structures such as airway smooth muscle, intestinal crypts, and structural changes associated with early stage diseases. Considering the quadratic dependence of the axial resolution on the center wavelength λ_c of the OCT light source (i.e. $\delta z \propto \lambda_c^2 / \Delta\lambda$ where $\Delta\lambda$ is the 3dB bandwidth of the source spectrum), compared to 1300 nm, it would be more convenient to achieve an ultrahigh axial resolution with a

broadband light source at 800 nm. In addition, an 800 nm source could also potentially provide improved image contrast owing to the increased light scattering and less tissue absorption at 800 nm. Ultrahigh-resolution OCT imaging at 800 nm with excellent contrast has been demonstrated with a bench-top system [41]. However, ultrahigh-resolution endoscopic OCT imaging at 800 nm remains challenging due to the difficulties in managing chromatic aberration and polarization over a broadband spectrum etc., and so far only a few achromatic endoscopic OCT setups have been reported [192, 196]. The designs in those endoscopes are rather complicated and expensive, involving multi-element achromatic microlenses. Besides, none of the endoscopic setups has the capability of performing high-speed three dimensional (3D) circumferential imaging over a large volume.

In this chapter, we are going to introduce an ultrahigh resolution endoscopic OCT system with a novel optical design of the OCT imaging probe that was recently developed.

10.2 Ultrahigh Resolution Endoscopic OCT System

The methods described in this section have been published in [235].

10.2.1 Light Source and Interferometer

Figure 10.1 illustrates the endoscopic spectral-domain OCT system at 800 nm which integrated a miniature OCT imaging probe in the sample arm. A broadband Ti:Sapphire laser with a central wavelength of 825 nm and a full width of half maximum ~ 150 nm was used as the light source (as shown in the inset of Fig. 10.1), which is highly linearly polarized and will significantly ease the polarization mode dispersion (PMD) management in such an endoscopic OCT system. One polarizer (indicated by PL in Fig. 10.1) was used

to control the total power sent to the interferometer and the output power from the catheter tip was kept at about 4 mW.

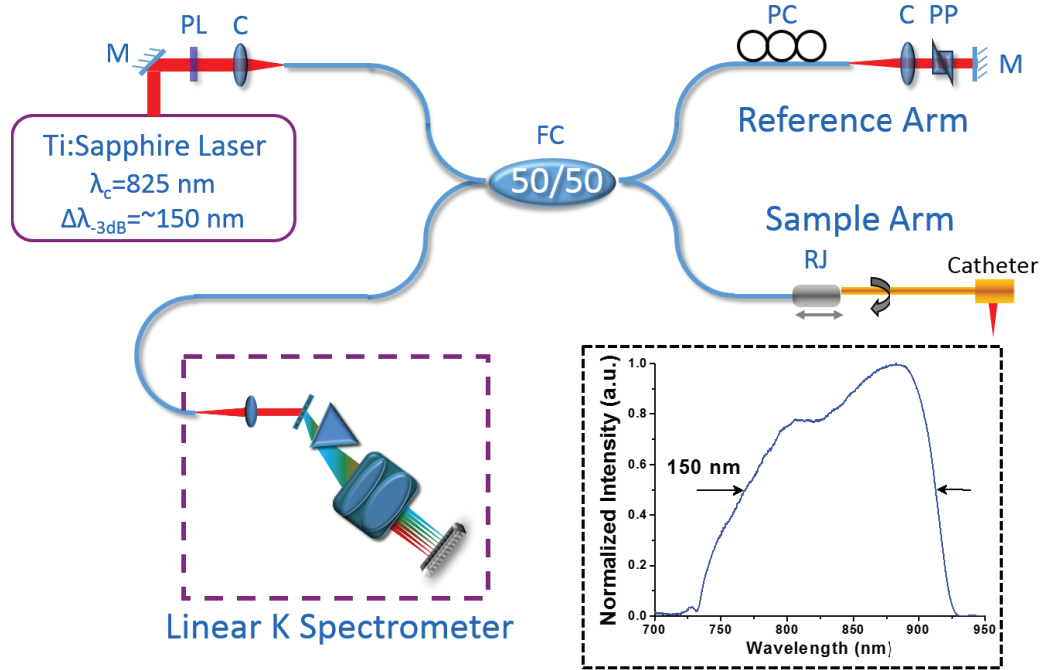


Figure 10.1 Schematic of the ultrahigh-resolution spectral-domain endoscopic OCT imaging system and the spectrum of the Ti:Sapphire laser source. C: multi-element achromatic collimator; CCD: line scan CCD; G: grating; M: mirror; MESL: multi-element scan lens; P: linear K mapping prism; PC: polarization controller; PL: polarizer; PP: prism pair; R: fiber-optic rotary joint.

The light from the laser was coupled into a single mode fiber (i.e., Corning HI-780).

A 50/50 broadband fiber coupler that was made of the same fiber (i.e., wavelength flattened coupler from Gould fiber optics), was used to form a Michelson interferometer as described in Chapter 5. In order to match the dispersion between the sample and the reference arm, a prism pair made of SF11 flint glass was inserted in the reference arm. The flint glass provides a much higher group velocity dispersion (GVD) and third-order dispersion (TOD) than crown glass (e.g., BK7) and optical fiber around 800 nm, and therefore more effectively minimizes the dispersion mismatch between the two arms while keeping a

considerably large air gap in the reference arm. A fiber polarization controller was placed in the reference to match the polarization states of the two arms to get the maximal fringe signal. In order to optimize the axial resolution, the spectra returned from both arms (measured at the detection port of the interferometer) were tuned separately to achieve a near Gaussian shape while maintaining maximum spectral overlap between the two arms. The axial resolution of the diffractive catheter based endoscopic OCT system was able to reach as high as $3.0\ \mu\text{m}$ in air as shown in Fig. 10.2. This was slightly worse than what was afforded by the laser source due to the suboptimal spectral throughput bandwidth of the fiber coupler and the collimators in the OCT system. It is noticed that the residual TOD mismatch between the two arms was almost negligible and can be further numerically compensated to slightly improve the side lobe of the point spread function (see in Fig. 10.2).

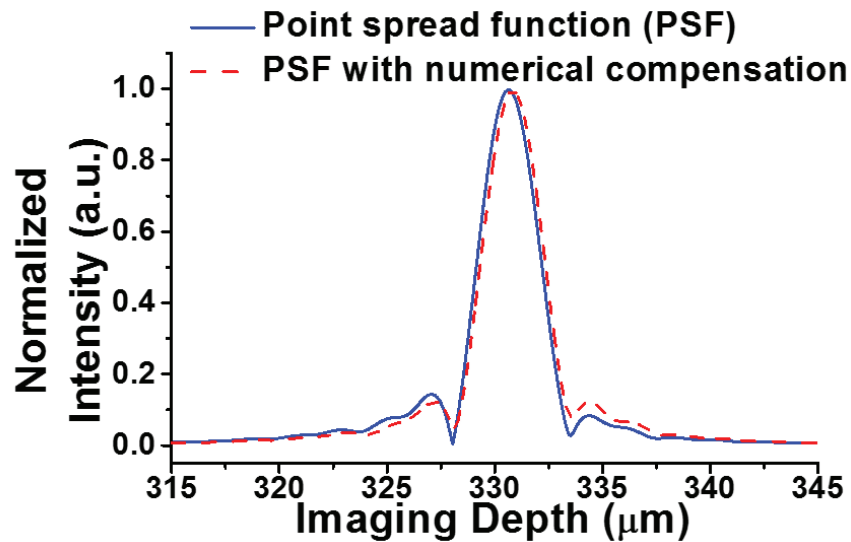


Figure 10. 2 Point spread function of the ultrahigh resolution endoscopic OCT system. Blue line is the point spread function transformed from the detected spectrum and red dashed line is the point spread function with a numerical compensation of residual third order dispersion.

10.2.2 Linear-in-wavenumber Spectrometer

For detection, a custom designed, home built broadband linear-in-wavenumber spectrometer was employed (as shown in Fig. 10.3a). The home built spectrometer, in principle, is similar to the one reported in [236], but covers a much broader spectrum. The function of a linear-in-wavenumber spectrometer in a SD-OCT system is similar to the real-time uniform K-space sampling method in an SS-OCT system introduced in Chapter 5. One of its advantages is that no calibration is required as the raw data from CCD can be directly used to perform FFT operation to get the depth-resolved signal. Another benefit is that the detection sensitivity would be improved. In this spectrometer, the light from a single mode fiber was first collimated by a custom made achromatic collimator. A volume holographic grating (1200 line pairs/mm, $\lambda_c = 830 \text{ nm}$, 80% transmission efficiency, from Wasatch Photonics) was used in the spectrometer to disperse the detected light. A BK7 prism with an apex angle of 56.4° was inserted after the grating to achieve a linear wavenumber distribution over a broad spectrum (750-950 nm). A custom designed multi element scan lens, which is made of four air gapped spherical lenses, was used to focus the linearly dispersed light onto a line scan CCD camera. The CCD (e2v AViiVA EM4) has 2048 pixels of $14 \mu\text{m}$ size that covers a 250 nm wavelength range with a line scan rate up to 70k/second at a 12 bit resolution.

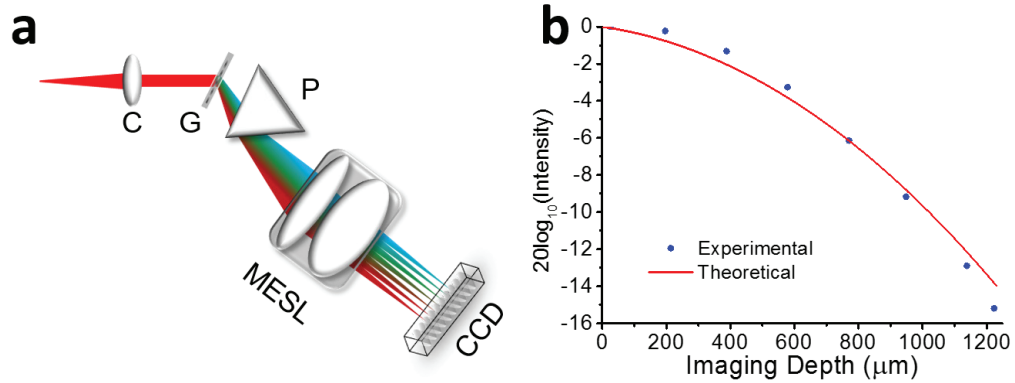


Figure 10.3 (a) Linear-in-wavenumber spectrometer and (b) detection sensitivity fall-off.

The imaging depth was calibrated to be 1.23 mm corresponding to a measured 16 dB detection sensitivity fall-off (see in Fig. 10.3b) using a form of $20\log[A(z)]$, where $A(z)$ is the intensity of the Fourier transformed interference signal at different depth z . The fall-off was close to its theoretical prediction, which used linear time invariant model that combined the effects of the grating resolution, the diffraction of a Gaussian beam, and finite CCD pixel size. The measured detection sensitivity of the endoscopic OCT system was around -105 dB at an imaging depth of 400 μm when the incident power on the sample was about 4 mW. OCT images were acquired, processed, displayed and stored in real-time with each frame consisting of 2048×2048 (lateral \times axial) pixels.

10.2.3 Diffractive Imaging Probe for Ultrahigh Resolution OCT Imaging

The major challenge in an ultrahigh resolution endoscopic OCT system is to develop a miniature OCT imaging probe that manages chromatic aberration and polarization over a broadband spectrum. The design of the previously reported imaging probes were rather complicated and expensive, involving multi-element achromatic microlenses. Here, we proposed a novel design of an imaging catheter that utilized a diffractive lens for chromatic aberration management, hereby named as diffractive imaging probe. Different from those

reported in [192, 196], the diffractive lens can be readily applied to a conventional imaging catheter that uses a GRIN lens, with almost no compromise to the catheter from factors such as diameter, weight, rigid length, etc..

Conventional refractive lenses use curved surface of the optical materials and Snell's law to form focusing power, which makes most of the refractive lenses show similar chromatic aberrations (i.e., a positive lens has higher focusing power with the light of shorter wavelength). On the other hand, diffractive lenses use thin circular micro structure patterns and laws of interference and diffraction to alter the phase of the light and form focusing power. The flexibility of the phase pattern can manipulate the light to almost any desired profile. Hence, a diffractive lens, which easily shows a reverse chromatic aberration with proper design (i.e., a positive lens has higher focusing power with the light of longer wavelength), can be used in management of the chromatic aberration in lens design as seen in Fig. 10.4, even in commercial lenses (e.g., Canon EF 70-300 mm f/4.5-5.6 DO [237]). Another advantage of diffractive lenses is that they are easy to be miniaturize, which makes them be a perfect candidate of the management of chromatic aberration in micro optics.

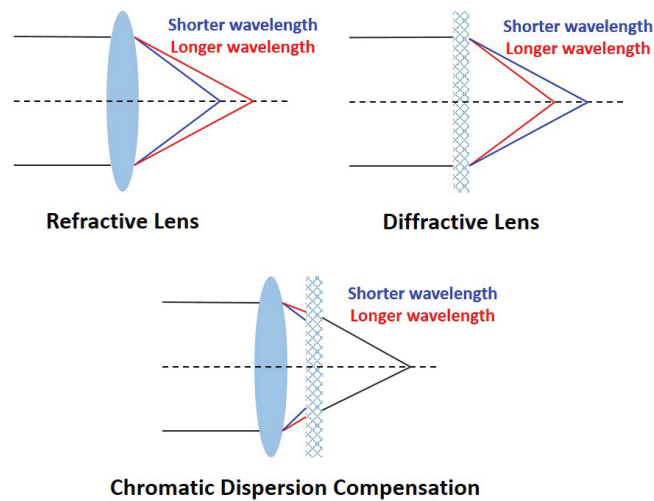


Figure 10.4 Schematic of the management of chromatic aberration by diffractive optic elements.

Gradient index (GRIN) lenses show a similar chromatic aberration to refractive lenses due to the optical property of the material. Therefore, using a diffractive lens to manage the chromatic aberration is similar to those situation with refractive lenses. Here, we first developed a Zemax model to simulate and optimize the optical design of the diffractive lens. Since the optical path is cylindrically symmetric, the Binary 2 surface was chosen to simulate the diffractive lens in the Zemax model. The Binary 2 phase profile can be described in the following polynomial expansion:

$$\Phi = M \sum_{i=1}^N A_i \rho^{2i}, \quad (7.1)$$

where M is the diffraction order that is usually 1, N is the number of polynomial coefficients in the series, A_i is the coefficient on the $2i^{th}$ power of ρ , which is the normalized radial aperture coordinate.

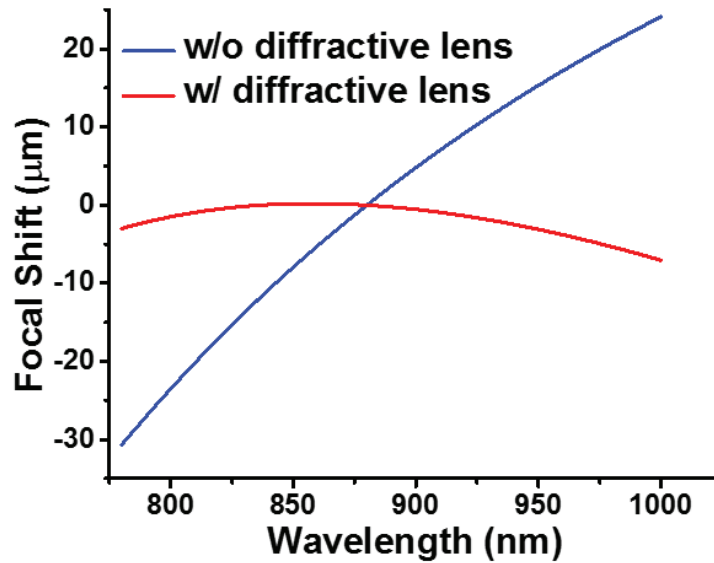


Figure 10.5 Zemax simulation result of the focal shift of an OCT imaging probe without a diffractive lens (in blue line) and with a diffractive lens (in red line).

In the Zemax model, we used two terms (i.e., $N = 2$) in the phase profile of the diffractive lens as described in Eq. (7.1). After optimization, the diffractive lens was a phase mask with circular phase retardation rings up to 7th order. According to the Zemax results, the focal shift of an OCT imaging probe as described in Chapter 7 is about $55 \mu\text{m}$ over a bandwidth of 220 nm at 800 nm wavelength range as displayed in blue line in Fig. 10.5. With the diffractive lens, however, the focal shift can be reduced about $8 \mu\text{m}$ at the same conditions as displayed in red line in Fig. 10.5. The performance of the diffractive imaging probe is close to a well corrected achromatic at this wavelength range.

Based on the simulation results, Fig. 10.6a illustrates the configuration of the diffractive catheter, which consists of a single-mode fiber (SMF), a 1-mm diameter glass rod, a 1-mm diameter GRIN lens, and a diffractive lens of an ~ 1 mm diameter. The combination of a glass rod and a GRIN lens with a proper length and pitch number allowed for maximal use of the limited numerical aperture (NA) of the 1-mm optics, and enabled the focusing of the beam to a designed focal point (i.e. 1.9 mm in our case) with a highest lateral resolution (i.e. $6.2 \mu\text{m}$ in our case) [198]. Due to the optical properties of the glass rod and GRIN lens, a significant amount of chromatic aberration is introduced in the imaging system (i.e., with a greater than $70 \mu\text{m}$ longitudinal focal shift for a wavelength range of 750 – 950 nm according to ray-tracing simulation). The diffractive lens was directly applied after the GRIN lens to alleviate the aforementioned chromatic aberration over the broad spectrum. The diffractive lens had a very weak focusing power causing only a small overall focal shift around $200 \mu\text{m}$, which has been taken into account during the imaging probe design. At the distal end of the catheter, a 45° micro reflector was attached

to the end of the probe to divert the focused beam 90° for side-viewing imaging. The total length of the diffractive imaging probe was measured to be ~1 meter.

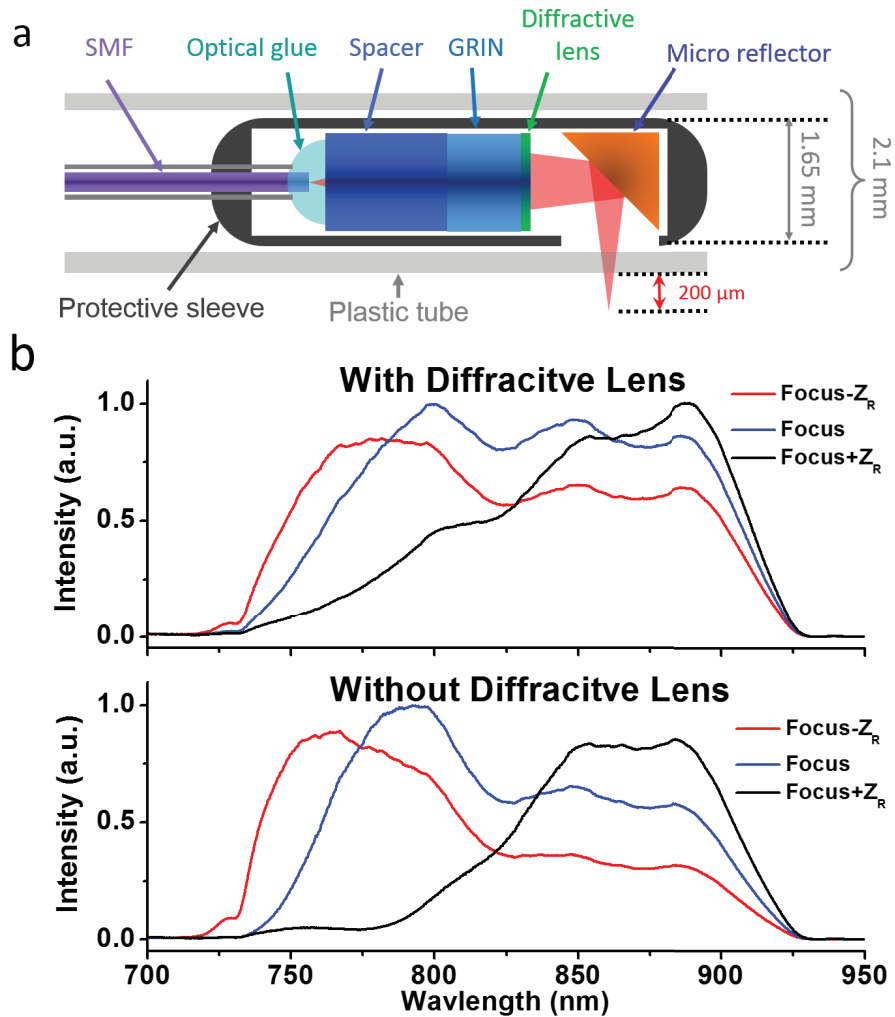


Figure 10.6 (a) Schematic of an ultrahigh-resolution OCT imaging probe utilizing a diffractive lens to alleviate chromatic aberration. (b) Reflected spectra of the imaging probes with a diffractive lens (upper panel) and without a diffractive lens (lower panel) when the mirror position was moved from the focal point by 1 Rayleigh range Z_r by an optical spectrum analyzer.

To show the effect of the diffractive lens on compensating chromatic aberration, the reflected spectrum by a mirror at the focal point of the catheter was compared with those reflected at one Rayleigh length Z_r away from the focal point as shown in the top

panel of Fig. 10.6b. As a comparison, the reflected spectra of a conventional imaging catheter with the same design but without a diffractive lens were also measured as shown in the lower panel of Fig. 10.6b. The results clearly demonstrated the reduction of chromatic aberration in the catheter with the aid of the diffractive lens. However, the reduction did not match the Zemax simulation results since the diffractive lens used in the probe was designed for the longer wavelength.

In order to achieve 3D circumferential scanning, a fiber rotary joint is required to couple the source light to the rotating diffractive catheter (and the backreflected light detected by the catheter to the OCT interferometer) through a stationary SMF. Most commercially available fiber rotary joints involve a pair of lenses for coupling light between a stationary and rotating SMF and are generally designed for the 1310/1550 nm spectral range. At the spectral range of 800 nm the chromatic aberration of optical materials is much larger and the mode field diameter of an SMF is smaller. As a result, a standard rotary joint becomes very challenging to use for coupling light between a stationary and a rotating SMF. Here, a mechanical coupling scheme similar to the one reported in [141] was employed as shown in Fig. 10.7a. In brief, a 126 μm capillary tube filled with an index matching liquid was used to connect a stationary fiber and the rotating catheter with the catheter rotated by a DC motor through a timing belt. The whole rotary unit was then mounted on a translational stage to enable 3D circumferential imaging. The measured throughput of the tubular rotary joint was greater than 90% and the fluctuation of the double-pass coupling efficiency during 360° rotation was less than 6% at a rotation speed of 10 revolutions per second (as shown in Fig. 10.7b).

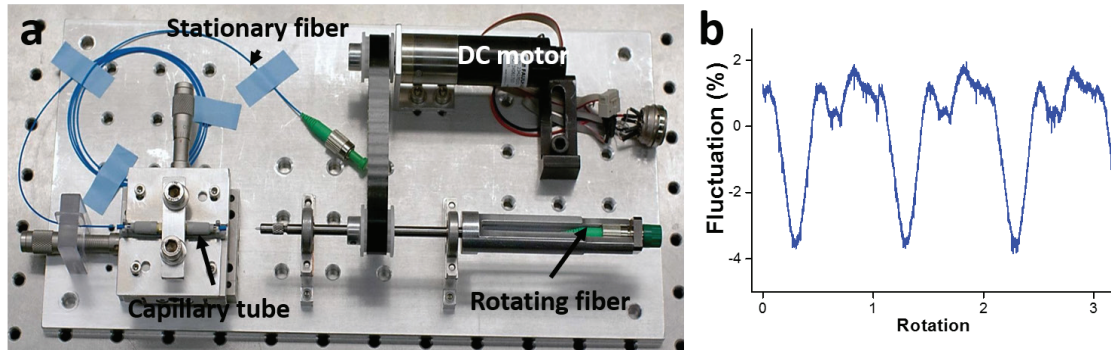


Figure 10.7 (a) Photo of fiber rotary joint and (b) fluctuation of the double-pass coupling efficiency of the fiber rotary joint.

10.3 Results

Some of the results described in this section have been published in [235].

10.3.1 *In vivo* Endoscopic OCT Esophageal Imaging

A preliminary study of 3D imaging of guinea pig esophagus *in vivo* was performed to test the performance of the ultrahigh-resolution diffractive imaging probe. The experiment was under an imaging protocol approved by the Johns Hopkins University Animal Care and Use Committee. For *in vivo* imaging, the A-scan rate of the line scan CCD was reduced to either 10 kHz or 20 kHz in order to match the rotation speed of the tubular fiber-optic rotary joint at 5 or 10 revolutions per second. A representative snapshot of 2D circumferential 800 nm ultrahigh resolution OCT images of a guinea pig esophagus *in vivo* was displayed in Fig. 10.8a. As a comparison, a series of 1300 nm high-speed OCT images of a guinea pig esophagus *in vivo* was displayed in Fig. 10.8b. A small region in two OCT images indicated by the dotted boxes in Figs. 10.8a and 10.8b are zoomed in by three times as shown in Figs. 10.8c and 10.8d, respectively. It is clearly shown that better axial resolution of 800 nm ultrahigh resolution endoscopic OCT imaging provided much better image quality and contrast over 1300 nm high-speed endoscopic OCT imaging.

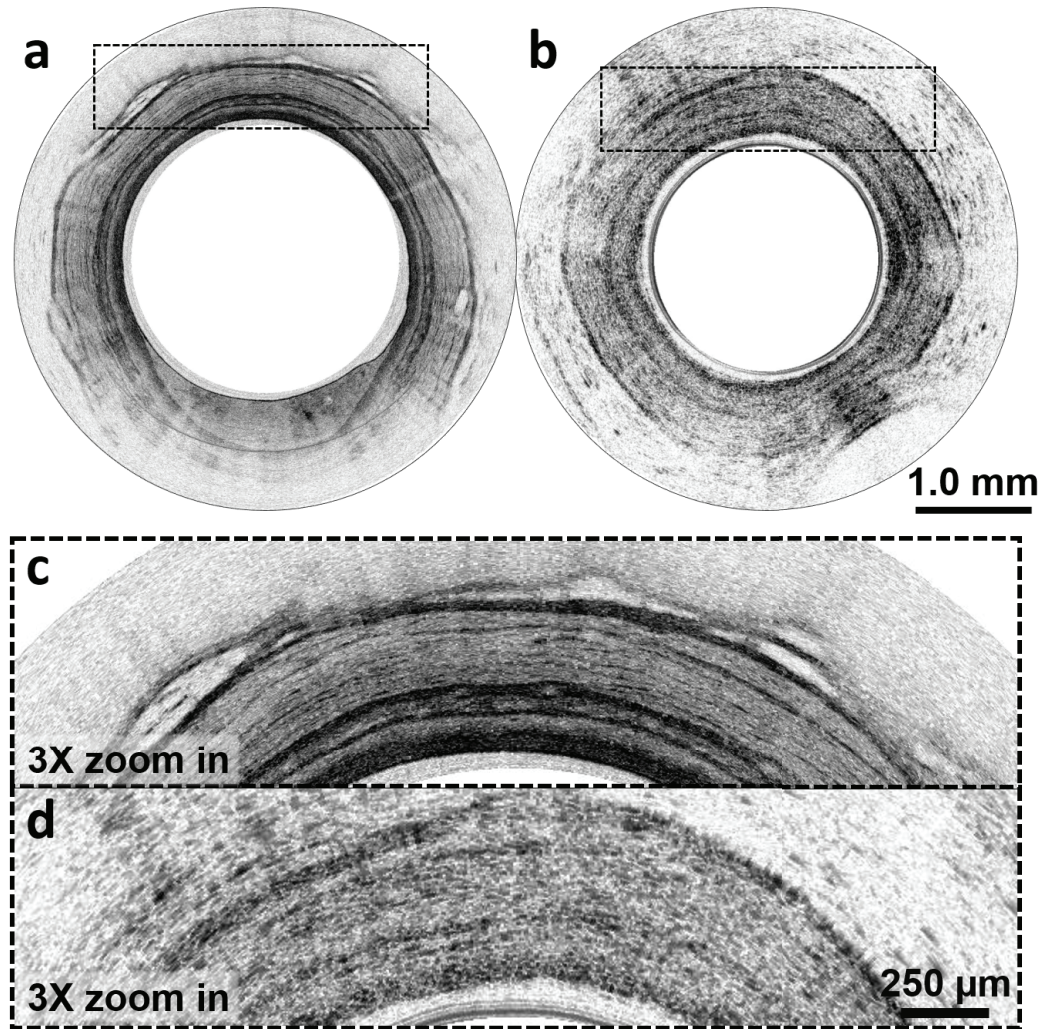


Figure 10.8 Representative snapshot of (a) 800 nm ultrahigh resolution OCT images and (b) 1300 nm high-speed OCT images of a guinea pig esophagus *in vivo*. (c) and (d) 3X zoomed-in regions of the dotted boxes in (a) and (b), respectively.

Furthermore, *in vivo* 800 nm ultrahigh resolution endoscopic OCT image was compared with *ex vivo* histology. A representative snapshot of 2D circumferential OCT images of a guinea pig esophagus *in vivo* is displayed in Fig. 10.9a while the corresponding Masson's trichrome stained histology is shown in Fig. 10.9b. To better visualize the fine structures on the OCT images and correlate those with histology, a small region in the OCT image and the histology micrograph as indicated by the dotted boxes in Figs. 10.9a and 10.9b are zoomed in by three times as shown in Figs. 10.9c and 10.9d, respectively. Good

correlation between OCT images and corresponding histology is evident on these zoomed-in images where all the layered esophageal structures, such as stratum corneum, epithelium, lamina propria, muscularis mucosae, submucosa, and muscularis propria, can be clearly identified. It is noticed that a thick layer of stratum corneum on the tissue surface provides strong scattering on the OCT images due to its high keratin content, and it can be clearly differentiated from the stratified epithelium layer below that exhibits less scattering. More interestingly, lamina propria and submucosa that contain abundant collagen fibers show very strong scattering signal on the zoomed-in OCT image (Fig. 10.9c), which is confirmed on the corresponding histology (Fig. 10.9d). Fine structures, such as a thin layer of muscularis mucosae that is embedded between lamina propria and submucosa can also be easily identified on the OCT image. Such structures are very hard to identify on 1310 nm OCT images. Figure 10.10 shows a cutaway view of a 3D image reconstructed from a series of 2D images along the longitudinal axis of the esophagus with a pitch of 10 μm .

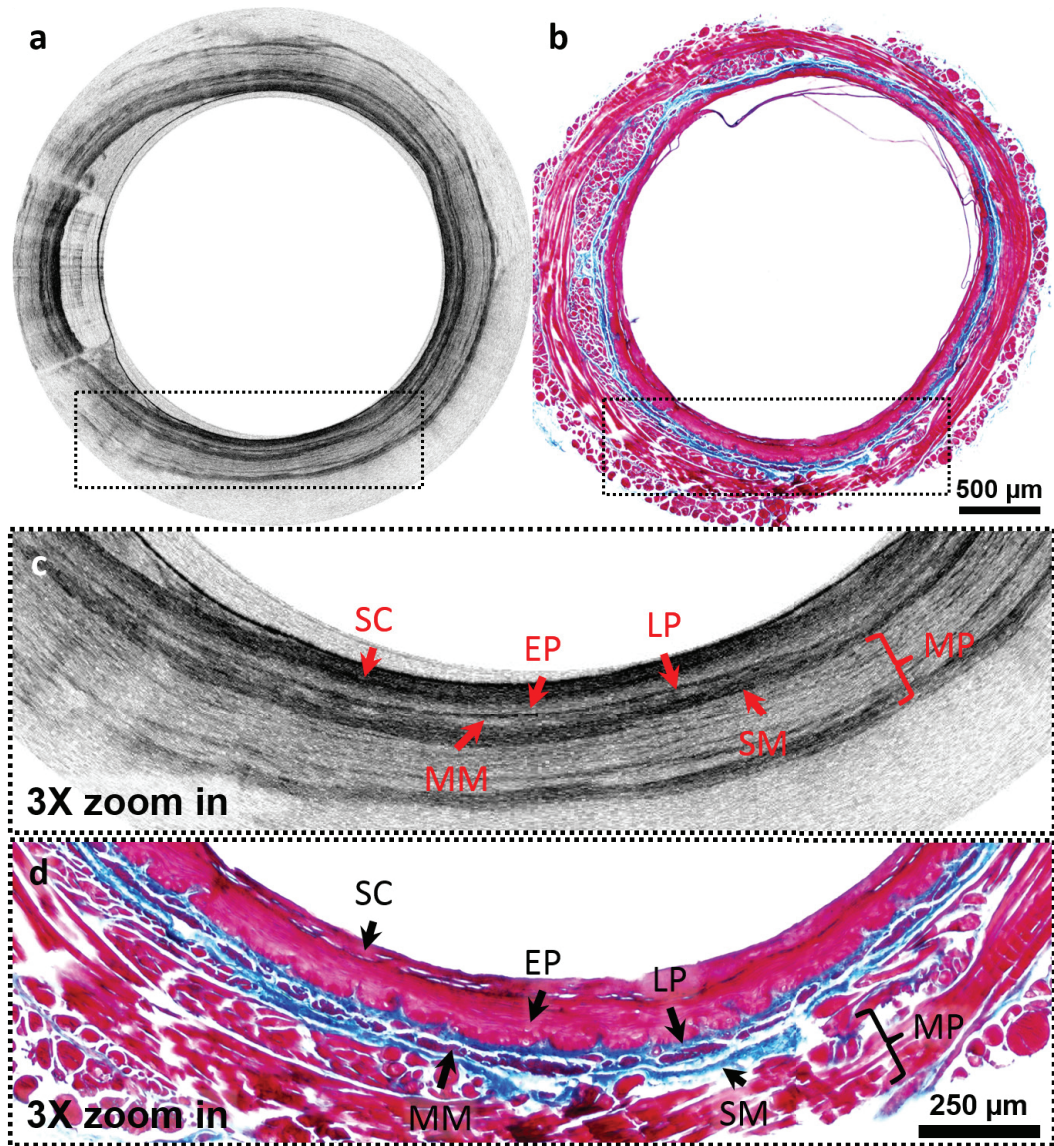


Figure 10.9 (a) Representative 2D circumferential *in vivo* OCT image of guinea pig esophagus and (b) its corresponding histology micrograph. (c) and (d) 3X zoomed-in regions of the dotted boxes in (a) and (b), respectively. SC: stratum corneum; EP: epithelium; LP: lamina propria; MM: muscularis mucosae; SM: submucosa; MP: muscularis propria. Scale bars: 500 μm in (a) and (b); 250 μm in (c) and (d).

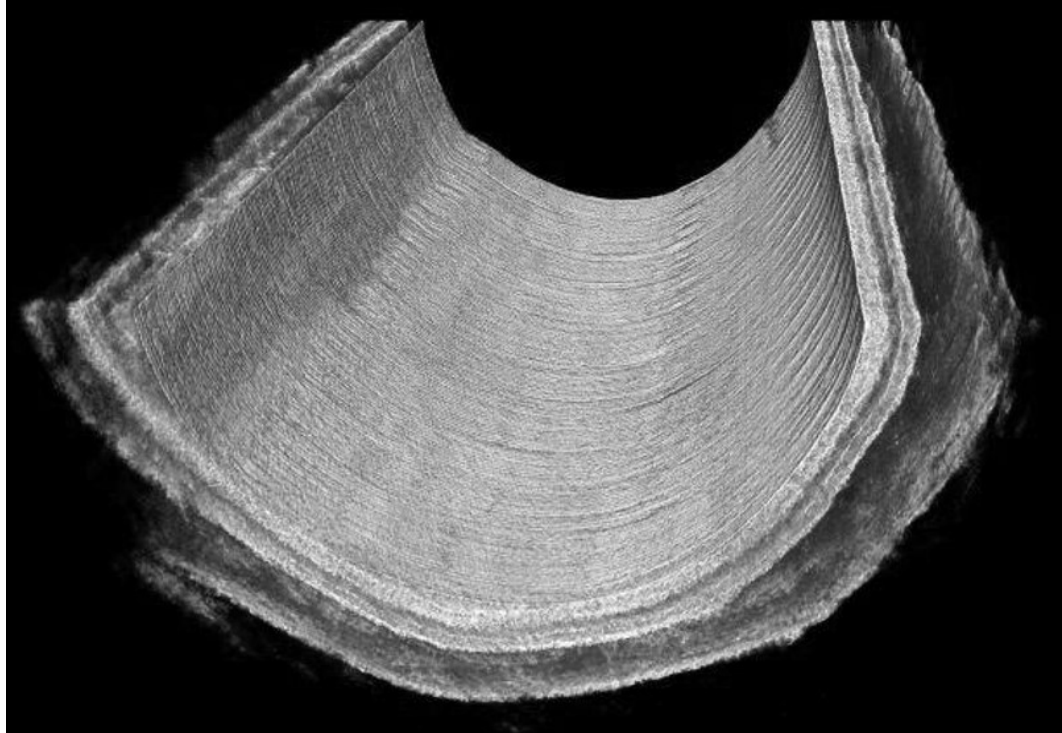


Figure 10.10 Cutaway view of a 3D reconstruction of 800 nm ultrahigh resolution endoscopic OCT image of guinea pig esophagus *in vivo*

10.3.2 *Ex vivo* Endoscopic OCT Bronchus Imaging

A similar study of guinea pig bronchus *ex vivo* as the one described in the last subsection was also performed. Two sets of correlation between 2D circumferential OCT images and *ex vivo* histology micrographs are displayed in Fig. 10.11, where OCT images are Figs. 10.11a and 10.11c and their corresponding histology are Figs. 10.11b and 10.11d, respectively. Structures, such as epithelium, cartilage, and smooth muscle, can be clearly identified on both sets of the images. Compared with 1300 nm high speed endoscopic OCT images shown in Chapter 9, layered structures, in particular smooth muscle, was able to be differentiated more clearly on 800 nm ultrahigh resolution endoscopic OCT images.

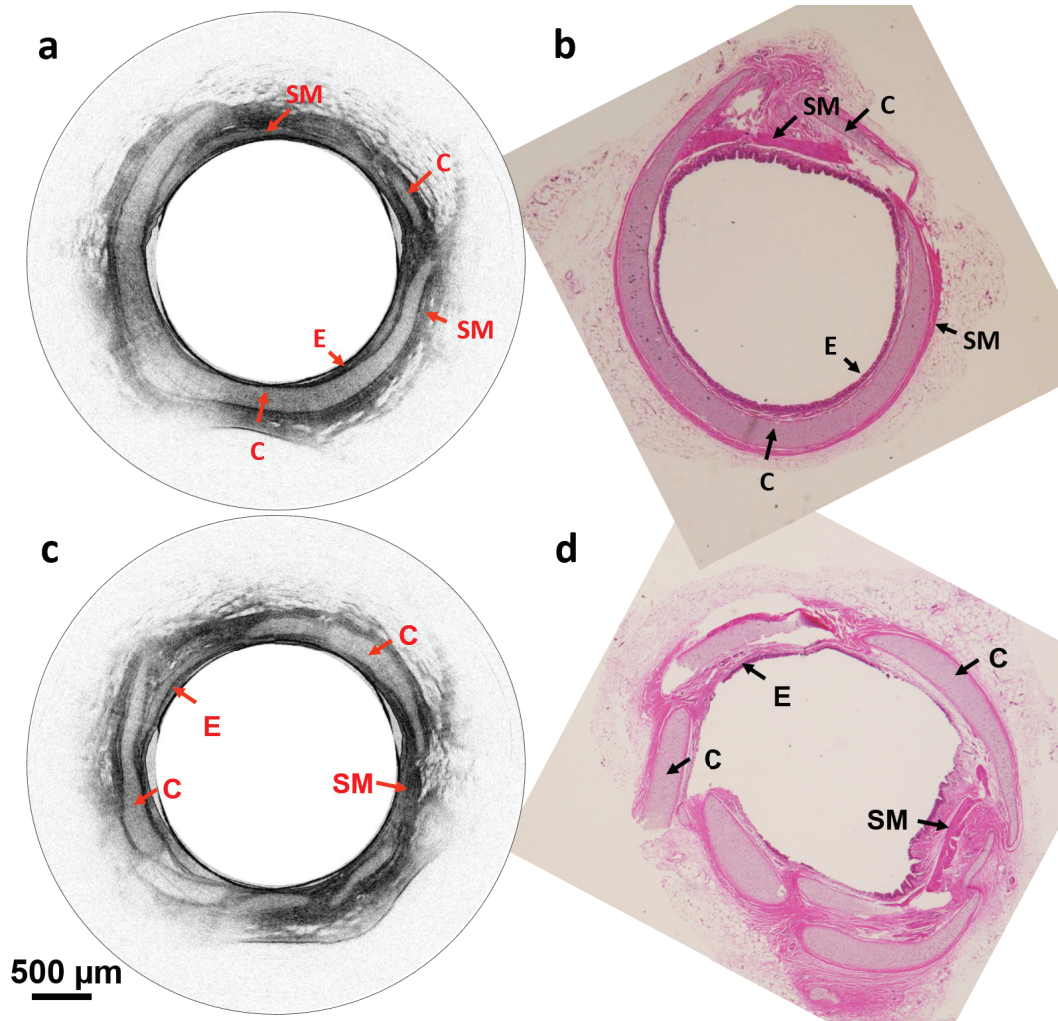


Figure 10.11 (a) and (c) are representative 2D circumferential *ex vivo* OCT image of guinea pig bronchus; (b) and (d) are its corresponding histology micrograph. E: epithelium; C: cartilage; SM: smooth muscle. Scale bars: 500 μm;

10.4 Summary

In this chapter, we first discussed the importance of ultrahigh resolution endoscopic OCT imaging. An 800 nm ultrahigh resolution endoscopic OCT system was then introduced, including a Ti:Sapphire ultrafast laser source, a Michelson interferometer, a linear-in-wavenumber broadband spectrometer, and the novel optical design of a diffractive OCT imaging probe. At last, two preliminary animal experiments demonstrate the performance

of the system and showed one of the directions in future development of endoscopic OCT imaging technology.

Chapter 11 OCT Contrast Enhancement and Endoscopic Multi-modal Imaging

This chapter describes another two projects related to OCT imaging during my Ph.D. study. The first project is on developing a cross-reference OCT imaging method to assess the optical properties of gold nanocages and to synthesize novel scattering-dominant gold nanocages that could be used as OCT contrast agents. The second project is to on developing a compact endoscopic multimodal imaging system that combined 1310 nm *en face* OCT and 1550 nm two photon fluorescence imaging.

11.1 Gold Nanocages as Optical Coherence Tomography Contrast Agent

The methods and results described in this section have been published in [238].

11.1.1 Introduction

The imaging contrast of OCT comes from the optical properties of biological tissue (i.e. scattering and absorption) and is often dominated by scattering in the near infrared (NIR) region. Unfortunately, the intrinsic OCT imaging contrast can be very weak in many cases for discerning pathological change. Similar to other clinically used medical imaging modalities, exogenous contrast agents have been used for enhance OCT imaging contrast and potentially gaining molecular specificity. An ideal OCT contrast agent is expected to have a small size (i.e. less than 100 nm) for effective systemic delivery, and should be strong in backscattering in order to reflect more photons that can be collected to the detector.

In addition, the contrast agents should be biocompatible and easy to conjugate for active targeting. Several types of contrast agents, such as core-shell microsphere, air-filled microbubbles, dyes and structured gold nanoparticles, have been developed for improving OCT contrast [239-246]. Most of them are either too large or are dominated by absorption (i.e., absorbing the imaging photons as opposed to enhancing backscattering). Gold nanocages are a relatively new class of structured nanoparticles with a hollow interior and a thin, porous, yet robust walls, synthesized using a galvanic replacement reaction between Ag nanocubes and HAuCl_4 in an aqueous solution [241, 247], which have a much larger extinction cross section (i.e., the sum of scattering and absorption) than other contrast agents in the NIR region while maintaining a relatively small size (i.e. ≤ 80 nm). More importantly, the optical properties of gold nanocages can be tailored by modulating the nanostructure geometric parameters including size, wall thickness and wall porosity. However, previously demonstrated gold nanocages are absorption dominant at a NIR region (i.e., 800 nm), which made the nanocages less attractive as an OCT contrast agent [240, 241]. Therefore, a new class of gold nanocages is desirable to enhance their scattering cross section over the total extinct cross section.

The optical properties of the OCT contrast agents should be ideally assessed in the development of the agents with a simple and quick yet accurate method. So synthesis conditions could be retuned in order to optimize the optical properties of the contrast agents. Typically the method of choice is the integrating sphere method, which has been used for quantitatively characterizing optical properties of scattering samples [248]; however, the results are sensitive to many experimental parameters and can often have large fluctuations. Thus a new and easy-to-use method is needed for rapid characterization of the contrast

agents. Characterization of optical properties using an OCT system has been investigated previously [246, 249, 250]. However, the effect of a focused incident beam in a scattering sample has not been carefully considered or eliminated in those models, which would reduce the accuracy of measurement results. In this section, a new generic method was proposed for quickly and accurately characterizing the optical properties of OCT contrast agents, including the total extinction, scattering, absorption and backscattering cross sections, by using an OCT system itself.

11.1.2 Characterizing Optical Properties by Using Cross-referencing OCT Imaging

The depth-dependent OCT backscattering intensity can be modeled as:

$$i(z) = K_1 \sqrt{\int_{\varphi=0}^{2\pi} \int_{\theta=0}^{\Theta} \mu'(\theta, \varphi) \sin \theta d\theta d\varphi} e^{-\mu_{ext} z} h(z), \quad (11.1)$$

where z is the imaging depth, φ and θ are respectively the azimuthal and polar angle in a spherical coordinate system, Θ is the half collection cone angle of the objective lens in the sample arm (and $\Theta = \sin^{-1}[NA]$, NA is the numerical aperture of the imaging objective lens), $\mu'(\theta)$ is the angular dependent differential scattering coefficient, μ_{ext} is the total extinction coefficient, K_1 is a system constant which depends on the detection system (such as the incident power and photo detector gain etc.), and $h(z)$ is the geometric factor function describing both the focusing and scattering effects on the imaging beam in a turbid medium as described previously [240, 251]. Considering the scattering is azimuthally symmetric in highly scattering samples and the NA of the imaging lens in most OCT systems is small (i.e. around 0.1 or even smaller), the equation can be reduced to [240, 251, 252]:

$$i(z) = K_1 \sin \frac{\Theta}{2} \sqrt{\mu_{bs}} e^{-\mu_{ext} z} h(z) = K \sqrt{\mu_{bs}} e^{-\mu_{ext} z} h(z), \quad (11.2)$$

where μ_{bs} is backscattering coefficient and $K = K_1 \sin \frac{\theta}{2}$ is a new system constant. We notice that there are three unknowns (i.e., K , μ_{bs} , μ_{ext}) and one function (i.e., $h(z)$) in Eq. (11.2). Extracting the unknowns, particularly those in a multiplicative form, from this equation by multi-parameter fitting generally yields very large errors and is not always feasible.

In order to overcome the challenges involved with direct curve fitting, the basic principle is to introduce one type of scattering nanoparticles, of which the optical properties (i.e. scattering, absorption, and backscattering cross-sections or coefficients) can be conveniently calculated. Mie theory was used for spherical particles [253] while discrete dipole approximation (DDA) was used for nonspherical ones. DDA is a numerical method for computing scattering of electromagnetic radiation by particles of arbitrary shape. Here an open source implementation package of DDA (i.e., DDSCAT) written in FORTRAN was chosen [254]. In this package, fast Fourier transform and conjugate gradient method are used to calculate convolution problem, which allows to calculate scattering by large particles (compared to the wavelength). In order to expedite the DDSCAT simulation speed, Intel FORTRAN Compiler [255] and Intel Math Kernel Library (MKL) [256] were used to optimize the code in the compilation time on a Linux operating system. When a noble metal particle that is emerged in a medium was numerically simulated in DDSCAT, a few considerations of parameter choice need to be taken in account. First of all, all the calculated wavelength is the wavelength in the medium instead of in vacuum; the dispersion relation of refractive index of the particle with respect to the wavelength should

be changed accordingly as well^{†††}. Secondly, due to the fact that the module of the complex refractive indices of the noble metals are usually large in the optical wavelength region, the wavelength in such metals are much smaller than the wavelength in vacuum. Therefore, the lattice spacing in DDSCAT should be adjusted accordingly to reduce the numeric error. However, too small lattice spacing would increase the computation time significantly. To balance between the numeric accuracy and the computation time, for example, the lattice spacing for gold in 800 nm should be 10 nm. More detailed explanation of the usage of this software is listed in Appendix A.

Two identical samples (phantoms) made of the given nanoparticles (e.g. silica nanospheres) with a known concentration are first prepared. The test nanoparticles (i.e. gold nanocages in our case) are then added to one of the phantoms (named test phantom), while the other phantom serves as the reference phantom. OCT imaging is then performed over the test and reference phantoms under the same experimental conditions (i.e., with the same incident power, focused spot size, focusing depth, etc.). The corresponding OCT signals are:

$$\begin{aligned}
 i_{ref}(z) &= K \sqrt{\mu_{bs}^{ref}} e^{-\mu_{ext}^{ref} z} h_{ref}(z) \\
 &\text{(for the reference phantom with only silica nanospheres),} \\
 i_{test}(z) &= K \sqrt{\mu_{bs}^{ref} + \mu_{bs}^{test}} e^{-(\mu_{ext}^{ref} + \mu_{ext}^{test})z} h_{test}(z) \\
 &\text{(for the test phantom with both silica and test nanoparticles).}
 \end{aligned} \tag{11.3}$$

Here $\mu_{bs}^{ref}(\mu_{ext}^{ref})$ and $\mu_{bs}^{test}(\mu_{ext}^{test})$ are the backscattering (and extinction) coefficients of reference and test phantoms, respectively; $h_{ref}(z)$ and $h_{test}(z)$ are the geometric factor

^{†††} Newest released DDSCAT v7.2 is able to automatically calculate the change of the wavelength by setting a parameter: refractive index of ambient medium.

functions in the reference and test phantom, respectively. If the scattering properties between reference and test phantoms do not differ dramatically (e.g., within an order of magnitude), it can be reasonably assumed (as confirmed experimentally in this paper) that the difference in the geometric factor function between the test and reference phantoms is negligible, i.e., $h_{ref}(z) \approx h_{test}(z)$. Therefore, by subtracting the logarithm of the two OCT signals in Eq. (11.3), we cancel out both the system constant and the geometric factor function and obtain the following depth-dependent cross-referencing function:

$$\ln i_{test}(z) - \ln i_{ref}(z) = -\mu_{ext}^{test} z + \frac{1}{2} \ln \left(\frac{\mu_{bs}^{test}}{\mu_{bs}^{ref}} + 1 \right). \quad (11.4)$$

Linear fitting can then be applied to Eq. (11.4) with respect to the imaging depth z , the slope of which gives the total extinction coefficient μ_{ext}^{test} of the test phantom. In addition, we will also obtain the y-intercept of the Eq. (11.4) (at $z = 0$) from the linear fitting, denoted as $b = \ln \left(\mu_{bs}^{test} / \mu_{bs}^{ref} + 1 \right) / 2$. Since the backscattering coefficient of the reference phantom μ_{bs}^{ref} can be precisely calculated by the scattering theory (or experimentally measured), the backscattering coefficient of the test sample μ_{bs}^{test} can then be easily found, i.e.,

$$\mu_{bs}^{test} = (e^{2b} - 1) \cdot \mu_{bs}^{ref}. \quad (11.5)$$

The next parameter to consider is the total scattering coefficient μ_{sca} of test nanoparticles, which can be deduced from the backscattering coefficient μ_{bs} of the test nanoparticles using $\mu_{bs} = k \cdot \mu_{sca}$, where k can be derived by the scattering theory for nanoparticles of a given size and shape (and by averaging over the nanoparticle orientations if the nanoparticle does not have a spherical shape). The absorption coefficient of the test

nanoparticles is then given by $\mu_{abs}^{test} = \mu_{ext}^{test} - \mu_{sca}^{test}$. This algorithm is fast and only involves OCT measurements. The above linear fitting procedure is very robust compared to the multivariable curve fitting procedure. More importantly, the new algorithm can provide a whole set of optical properties of the phantom made by the test nanoparticles, including μ_{ext}^{test} , μ_{sca}^{test} , μ_{abs}^{test} and μ_{bs}^{test} .

A validation experiment was first performed to verify it on mock nanoparticles. In this experiment, home synthesized silica nanospheres of 180 ± 20 nm diameter was used as the reference nanoparticles. The reference and test phantoms were made of 5% gelatin embedded with 50 and 100 mg/mL fused silica nanospheres, respectively. Therefore, the test and the reference nanoparticles are both at a concentration of 50 mg/mL in the 5% gelatin phantom. The optical properties, including the scattering (no absorption) and backscattering cross sections, of the fused silica nanosphere at the given concentration in the medium can be analytically predicted by the Mie scattering theory, and the angular dependent scattering pattern as shown in Fig. 11.1. OCT imaging was conducted using a 7-fs Ti:Sapphire laser as the light source with a center wavelength at 825 nm and a 3dB spectral bandwidth of ~ 150 nm. The NA of the imaging lens in the sample arm was about 0.1 and the averaged power on the sample arm was ~ 4 mW. OCT images of the two phantoms were acquired by scanning an imaging beam across the two side-by-side phantoms in order to maintain the same experimental conditions.

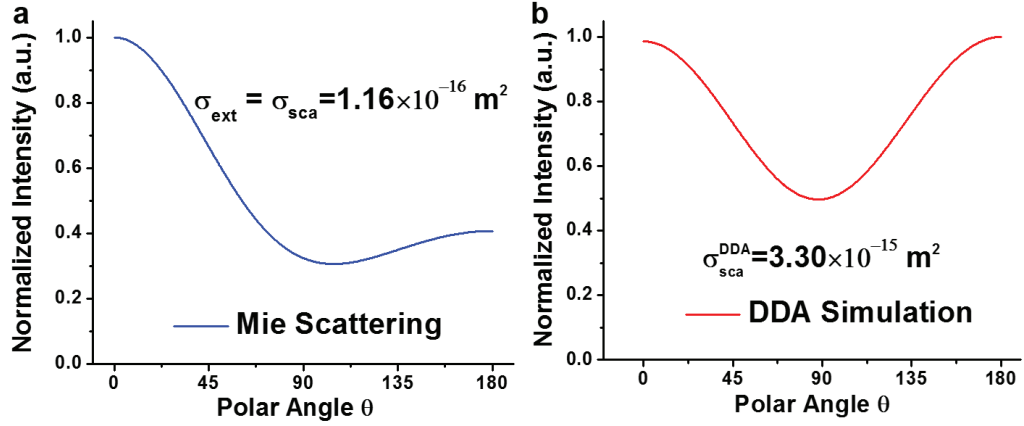


Figure 11.1. (a) Angular dependent scattering pattern of 180 nm silica nanospheres in a 5% gelatin phantom at the wavelength of 825 nm calculated by the Mie scattering theory. (b) Angular dependent scattering pattern of 75 nm gold nanocages in a 5% gelatin phantom at the wavelength of 825 nm calculated by a numerical method based on discrete dipole approximation (DDA). The scattering pattern is averaged over various nanoparticle orientations.

After OCT imaging of both phantoms, A-scan OCT intensity signals were obtained as a function of imaging depth by averaging along the B-scan direction in order to remove heterogeneity of the phantom samples and reduce the speckle noise. The first step is to extract the total extinction and back scattering coefficients from the averaged A-line signals (e.g., averaged over 500 A-lines). By applying the aforementioned algorithm to the test and reference A-scan OCT intensity signals, the extinction coefficient of test silica nanospheres was extracted in the test phantom (at a mass concentration of 50 mg/mL) as $\mu_{ext}^{test} = 0.640 \text{ mm}^{-1}$. To deduce the extinction cross section of a single fused silica nanosphere, we first need find out the molar concentration of the silica nanospheres in the test phantom by converting the mass concentration to the molar concentration. And the molar concentration was found to be $c^{test} = 9.88 \text{ nM}$. The extinction cross section of a fused silica nanosphere is then given by $\sigma_{ext} = \mu_{ext}^{test} / N_A c^{test} = 1.08 \times 10^{-16} \text{ m}^2$ (where N_A is Avogadro constant). This extinction cross section is very close to the theoretical value

$\sigma_{ext}^{Mie} = 1.16 \times 10^{-16} \text{ m}^2$ predicted by the Mie theory. The ratio of the backscattering coefficients of the test to the reference nanoparticles denoted by $\mu_{bs}^{test} / \mu_{bs}^{ref}$ can be found from Eq. (11.5), and the resulted value is 0.96 which is very close to the theoretical limit of 1 in this case (considering test and reference silica nanospheres had the same concentration in this experiment). We notice that the accuracy of the algorithm in determining the extinction coefficient and the backscattering ratio of the test and the reference nanoparticles is excellent; warranting that neglecting the geometric factor function $h(z)$ in Eq. (11.4) is safe.

The next step is to separate the total scattering and absorption coefficient of the test fused silica nanospheres from the total extinction coefficient. Since the backscattering coefficient of reference silica nanospheres was calculated by the Mie theory as $\mu_{bs}^{ref} = 0.695 \text{ mm}^{-1}$, we were able to deduce the backscattering coefficient of test silica nanospheres to be $\mu_{bs}^{test} = 0.667 \text{ mm}^{-1}$ (from Eq. (11.5)). From the scattering pattern predicted by the Mie theory (as shown in Fig. 11.1a), the ratio of the total scattering to the backscattering coefficient is $k = 1.008$. Therefore, the total scattering coefficient of test silica nanospheres is $\mu_{sca}^{test} = \mu_{bs}^{test} / k = 0.661 \text{ mm}^{-1}$, and the absorption coefficient of the test silica phantom is $\mu_{abs}^{test} = \mu_t^{test} - \mu_{sca}^{test} = -0.0214 \text{ mm}^{-1}$ (which, in theory, should be zero). It is noted that the relative errors in the extinction coefficient between the experimental measurements and theoretical predictions are within 7%, demonstrating the feasibility of the proposed cross-referencing method for optical properties characterization.

Similar experiments of different concentrations of fused silica nanospheres were repeated three times and all results showed that the relative measurement errors (i.e. the

variation in the characterization results) in the extinction and backscattering cross sections were no more than 3% among experiments, confirming the robustness of this method for optical properties characterization.

Two issues need to be considered in order to use the cross-referencing method properly. Firstly, in order to linearly fit the difference curve represented by Eq. (11.4), the A-scan OCT intensity signals from the reference and the test phantom need to be significantly above the noise floor of the OCT system. An alternative is to choose a segment from the entire depth profile of the OCT intensity. Secondly, the cross-referencing method assumes an approximation that the difference in the geometric factor function $h(z)$ in the test and reference phantom is negligible. In addition to the depth-dependent transparent-medium-equivalent point-spread function [257], also takes into account the scattering effect on the point-spread function in a turbid medium [251]. In theory, $h(z)$ would change as the scattering property changes and thus the two $h(z)$'s would not perfectly cancel out each other in the two A-scan signals (from Eq. (11.3) to Eq. (11.4)). However, from what we experimentally observed in the next subsection, the change in $h(z)$ was negligible even the scattering coefficient changed by about 2 mm^{-1} from the reference to test phantom.

11.1.3 Scattering-dominant Gold Nanocages

The basic protocol for synthesizing scattering-dominant gold nanocages is similar to the one reported previously [258] but with some modification. In essence, HAuCl_4 aqueous was titrated into a solution of silver nanocubes (of $\sim 68 \text{ nm}$ in edge length) as a template under room temperature and with a titration rate of 0.25 mL/minute . The templates were

gradually etched away, resulting in gold nanocages with hollow interiors and pores on the wall (as shown in inset of Fig. 11.2(a)). The optical properties (such as scattering, absorption, and SPR peak wavelength) of gold nanocages can be precisely tuned by controlling size, wall thickness and porosity. The optical properties of the gold nanocages were fully characterized by means of the cross-referencing OCT imaging described in the previous subsection, aiming to provide quick feedback to optimize nanocage synthesis conditions for achieving scattering dominating optical properties and thus OCT imaging contrast enhancement with the nanocages.

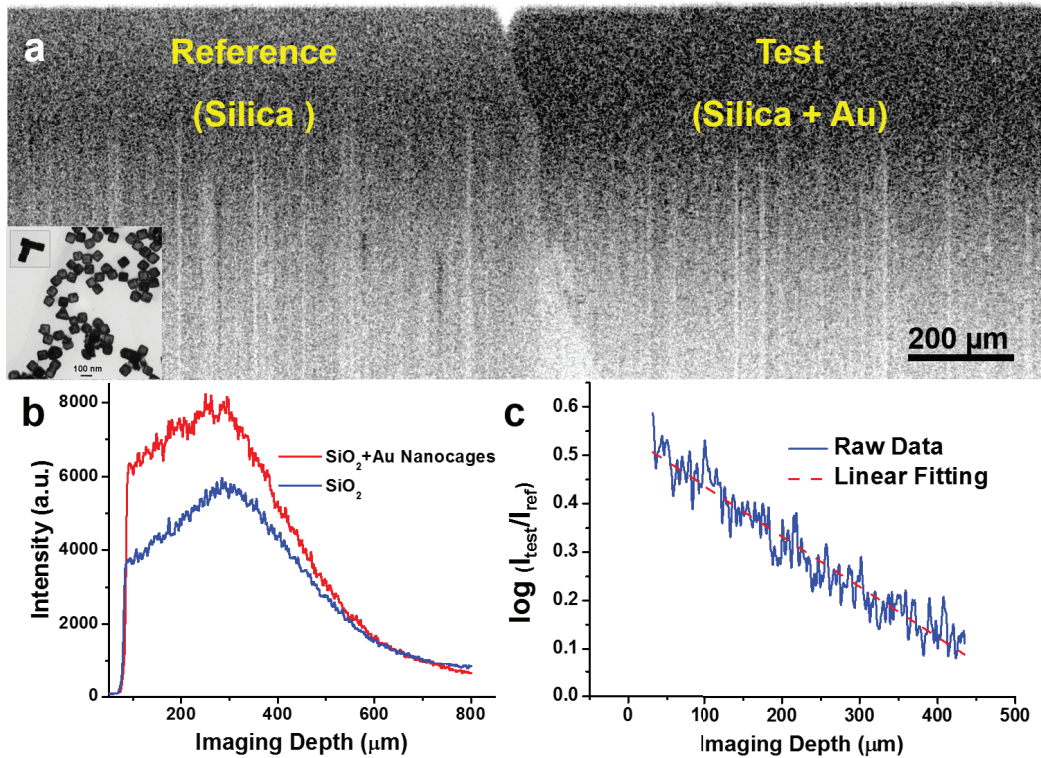


Figure 11.2. (a) OCT images of the phantoms without nanocages (left) and with nanocages (right). Inset: a TEM image of gold nanocages. (b) Intensity plots of the OCT signals on a linear scale as a function of imaging depth. (c) Ratio of the two signals in (B) on a logarithmic scale as a function of imaging depth. Scale bar: 200 μm in (a); 100 nm in inset in (a).

Similar to the experiment described in the previous subsection, two identical phantoms were made by embedding 50 mg/mL fused silica nanospheres into 5% gelatin,

whose optical properties again can be calculated using the Mie theory. Gold nanocages were added to one of the phantoms at a nominal concentration of 1.0 nM. OCT imaging of the test (with nanocages) and reference (without nanocages) phantoms were performed under the same conditions as mentioned in the previous subsection.

Figure 11.2a shows the OCT images of the reference phantom (on the left) and the test phantom (on the right), respectively, and the decay curves of the OCT intensity along imaging depth in both cases are given in Fig. 11.2b. Using the cross-referencing method, the extinction coefficient and the backscattering coefficient of gold nanocages in the test phantom were calculated from the slope and y-intercept of Eq. (11.4), and the resulted values are $\mu_{ext}^{Au} = 1.71 \text{ mm}^{-1}$ and $\mu_{bs}^{Au} = 1.34 \text{ mm}^{-1}$, where the backscattering coefficient $\mu_{bs}^{ref} = 0.695 \text{ mm}^{-1}$ of the reference nanoparticles (fused silica nanospheres) predicted by Mie theory was used for Eq. (11.5). Figure 11.2c shows the ratio of the two depth-dependent signals shown in Fig. 11.2b, and the nearly perfect linear relationship of this ratio versus imaging depth also implies that the potential difference in $h(z)$ of the test and reference phantoms can be safely neglected. To calculate the scattering coefficient of the nanocages from the backscattering coefficient, we need first to find the relationship constant k in $\mu_{bs}^{Au} = k_t \cdot \mu_{sca}^{Au}$. A numerical simulation method based on DDA was used to calculate the orientation averaged, angular dependent scattering pattern and the result is shown in Fig. 11.1b, from which the parameter k_t is found to be 1.385. The scattering coefficient of nanocages is then given by $\mu_{sca}^{Au} = \mu_{bs}^{Au} / k_t = 0.967 \text{ mm}^{-1}$. The absorption coefficient is thus $\mu_{abs}^{Au} = \mu_{ext}^{Au} - \mu_{sca}^{Au} = 0.743 \text{ mm}^{-1}$. We notice that the ratio of the scattering to the absorption coefficient is about 1.31, showing the scattering dominance in the optical

extinction coefficient. To independently validate the optical properties obtained from OCT phantom imaging, integrating sphere experiments were performed to directly measure the optical properties of the nanocages, where the ratio of scattering to absorption coefficient was found to be ~ 1.27 at the central wavelength (825 nm) of the OCT source, and this ratio was very close to the one obtained by cross-referencing OCT method. Taking into account the nanocage concentration (1 nM), the corresponding cross sections of a gold nanocage can be found as $\sigma_{ext} = 2.84 \times 10^{-15} \text{ m}^2$, $\sigma_{sca} = 1.61 \times 10^{-15} \text{ m}^2$ and $\sigma_{bs} = 2.23 \times 10^{-15} \text{ m}^2$. It is noted that the measured cross sections differ from the ones predicted by DDA simulations (i.e. $\sigma_{sca}^{DDA} = 3.30 \times 10^{-15} \text{ m}^2$ and $\sigma_{abs}^{DDA} = 1.95 \times 10^{-15} \text{ m}^2$). One major reason accounting for this discrepancy is the potential loss of gold nanocages during sample preparation which was inevitable; thus the actual concentration could be lower than the nominal one, underestimating the overall cross section values.

11.1.4 Contrast Enhancement of Gold Nanocages

The very first scattering-dominant gold nanocages were used as a contrast agent for *in vivo* OCT imaging of tumor on a xenograft mouse model. Three male Balb/c nude mice, 6–8 weeks of age and about 25 g of average weight, were obtained from Taconic Farmer (One Hudson City Centre, Hudson). Approximately 5×10^6 human epidermoid carcinoma cells (A-431) suspended in 50 μL PBS were injected subcutaneously into the ear of the mice where tumors developed in the ears of two of the three mice. 10 days after tumor cell inoculation, OCT imaging of the mouse tumor on the ear was performed before and after 4 fractionated tail vein injections (24 hours apart) of PEGylated gold nanocages (150 μL of 1nM solution per injection). The animal experimental procedures in this study were approved by the Johns Hopkins University IACUC.

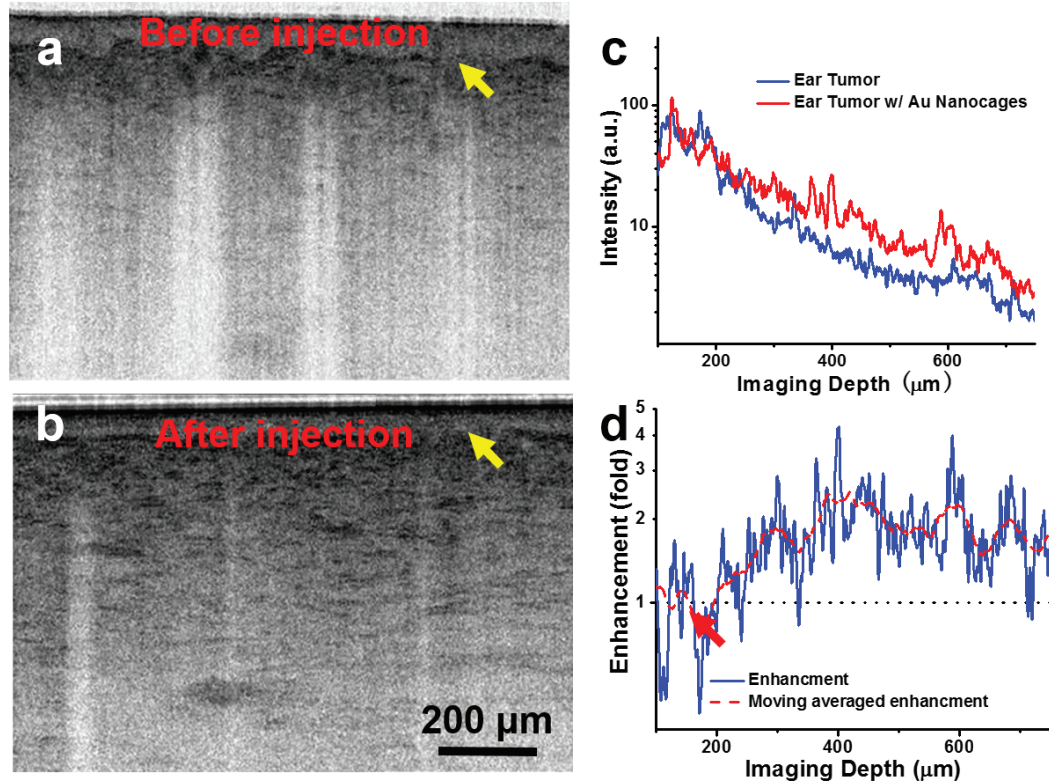


Figure 11.3. *In vivo* OCT images of a mouse ear tumor (induced with A431 cell line) (a) before and (b) after intravenous injection of gold nanocages, respectively. (c) Depth-dependent OCT intensity plots from the tumor on a logarithm scale before (blue curve) and after (red curve) the administration of gold nanocages. (d) The ratio of the two curves in (C) and its moving-average results on a logarithm scale. Scale bar: 200 μm

Figures 10.3a and 10.3b show representative OCT images of the tumor before and after the administration of gold nanocages, respectively; the corresponding decay curves on a logarithm scale are shown in Fig. 11.3c. It is evident that the presence of gold nanocages increases the backscattering in the tumor, thus enhancing OCT imaging contrast. More interestingly, fine structures were able to be observed after the injection of gold nanocages (as shown in Fig. 11.3b). It is noted that the contrast enhancement is approximately ~ 2.4 dB on average, and to the best of our knowledge, this is the highest OCT contrast enhancement by nanoparticles of a similar size and at a similar concentration. The contrast enhancement (in dB) and its moving average versus imaging depth are shown

in Fig. 11.3d, which suggest that the accumulation of the gold nanocages started $\sim 70 \mu\text{m}$ below the epidermis (where the tumor boundary is supposed to be as indicated by the arrows in Fig. 11.3a, 10.3b and 10.3d) and reached its peak around $300 \mu\text{m}$ beneath the surface.

11.2 Endoscopic Multi-modal Imaging System: Two-photon

Fluorescence and Optical Coherence Tomography

The method and results described in this section have been published in [259].

11.2.1 Introduction

Besides OCT, two-photon fluorescence (TPF) microscopy is recently developed as a high-resolution optical imaging modality. Both OCT and TPF hold a strong promise for performing noninvasive “optical biopsies” of biological tissues at a resolution approaching that of standard histology without the need for tissue removal. Different from OCT, TPF provides depth-resolved micron/submicron-scale images with an imaging contrast coming from endogenous or exogenous fluorophores, thus providing molecular or biochemical information about biological tissues beyond the capability of OCT [260]. The two complementary imaging modalities provide important yet different optical information based on unique contrast mechanisms. There is, hence, a strong motivation for developing an integrated platform for performing both OCT and TPF imaging. Previous works have demonstrated the possibility of combining the two imaging techniques using a bench-top scanning microscope platform [249, 261, 262], which involves free-space optics and is generally bulky. *In vivo* applications and potential clinical translation of the dual-modality imaging technology, particularly for imaging internal organs, requires a flexible and compact platform. In this section, a compact dual-modality imaging platform enables 1310

nm *en face* OCT and 1550 nm TPF imaging has been developed, consisting of a flexible miniature endomicroscope and small footprint fiber laser sources. The advantages of choosing these two wavelengths for this integrated multimodal imaging platform include: 1) compact fiber-optic light sources where components are widely available at both wavelengths; 2) capability of delivering both wavelengths in the same fiber (i.e., SMF-28e® or a double-clad fiber – DCF); and 3) similar propagation and dispersion characteristics at both wavelengths in the single-mode fiber SMF-28e® and the DCF.

11.2.2 Endoscope Design

The miniature multimodal endomicroscope was developed based on a previous reported [263, 264]. A schematic of this endomicroscope is shown in Fig. 11.4.a. In essence, an optical fiber was attached to a tubular piezoelectric (PZT) actuator of a 2.0 mm diameter, with a ~10-mm long fiber cantilever standing outside the PZT tube as shown in Fig. 11.4b. The outer surface of the piezoelectric tube is divided into four quadrants, forming two pairs of drive electrodes (i.e., $\pm x$ and $\pm y$). A circular scanning pattern is achieved when two orthogonal sinusoidal drive waveforms with a frequency at or near the mechanical resonant frequency (i.e., ~1.5 kHz in this case) of the fiber cantilever are applied to the two pairs of electrodes. By modulating the drive voltage with a slow sinusoidal envelope, a spiral scanning pattern is achieved (as illustrated in Fig. 11.4c).

The fiber employed in this endomicroscope is a customized DCF. The core diameter of the DCF is ~8 μm , similar to that of SMF-28e®, ensuring both 1550 nm TPF excitation light and 1310 nm OCT light can be delivered in single mode through the core. The DCF had a large inner cladding ($\phi 175 \mu\text{m}$) suitable for effective collection of the TPF

signal. The NA of the DCF core and inner cladding were 0.14/0.12 (at 1310 nm/1550 nm) and 0.267 (at 1550 nm), respectively.

The overall diameter of the endoscope is about 2.8 mm, including the protective metal tubing. The sweeping DCF tip was imaged to the sample by a miniature aspherical compound lens with a maximum NA of 0.8 and a magnification of ~ 0.22 (along the direction of fiber to sample) [265]. The micro compound lens offered a minimal chromatic focal shift from the OCT wavelength (1310 nm) to the TPF excitation wavelength (1550 nm), which was $\sim 10 \mu\text{m}$ in theory (according to ray tracing simulation) and $\sim 11 \mu\text{m}$ by experiment.

11.2.3 System Description

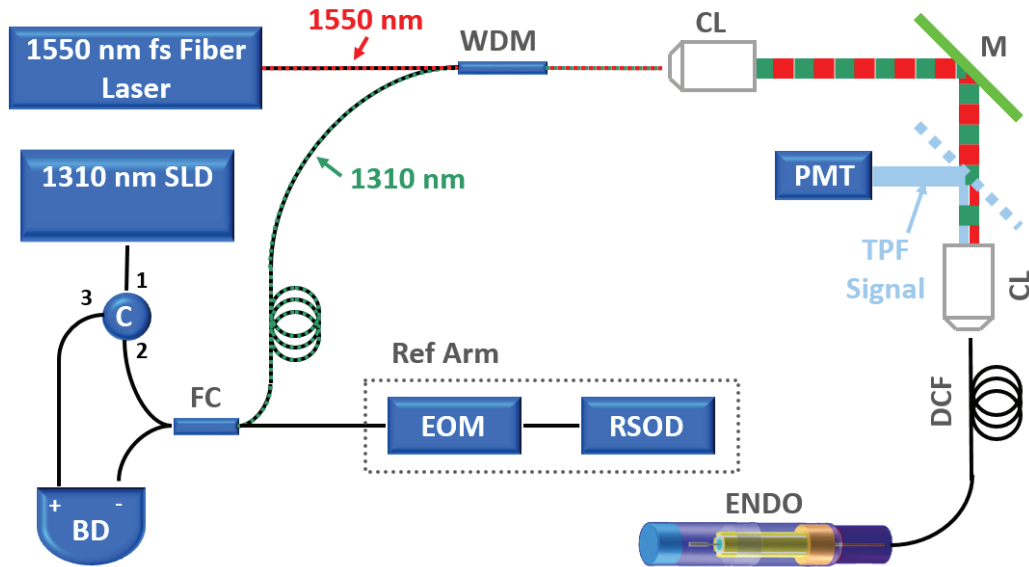


Figure 11.5. Schematic of TPF/OCT multimodal endomicroscope system. BD: balanced detector; C: circulator; CL: coupling lens; DCF: double-clad fiber; DM: dichroic mirror; ENDO: miniature endoscope; EOM: electro-optic modulator; FC: fiber coupler; LP: long pass filter; M: mirror; PMT: photomultiplier tube; RSOD: rapid scanning optical delay line; WDM: wavelength division multiplexer.

A schematic of the multimodal endomicroscopic system is illustrated in Fig. 11.5. The multimodal system consists of two modules: a 1550 nm TPF and a 1310 nm *en face* OCT

endomicroscopy systems. In the TPF module, a 1550 nm passive mode-locked amplified fiber laser generated ultrashort laser pulses (i.e., ~300 fs with a repetition rate of 42.5 MHz) with a maximum average power of ~155 mW in soliton mode as previously described in [265] so that the laser pulse remains relatively unchanged inside either the single-mode fiber (SMF-28e® or the customized DCF). Therefore, the TPF system does not require any further dispersion compensation [265]. Furthermore, reduced scattering at the NIR two-photon excitation and emission wavelengths potentially improves the imaging penetration depth. In the OCT module, the light generated by a fiber-coupled superluminescent diode served as a compact light source, which had a 13 mW output power and a central wavelength 1300 nm with a 3 dB bandwidth of 80 nm, was delivered into a Michelson interferometer of the OCT system. A high-isolation wavelength division multiplexer (WDM) made of SMF-28e® was employed to combine the 1310 nm OCT light source with the 1550 nm TPF excitation laser, which significantly simplified the procedure of integrating the two imaging modalities.

On the collection (i.e., return) path, in order to separate the TPF and the OCT signal, a customized dichroic mirror (i.e., DM in Fig. 11.5) of a transmission efficiency >90% for 1550 nm and >70% for 1310 nm and a reflectivity >99.97% for 700-900 nm was placed between the pair of coupling lenses. A photomultiplier tube (PMT) was used to collect the TPF signal reflected from the dichroic mirror. For OCT detection, although some of the backscattered OCT light from the sample entered the inner cladding of the DCF in the endoscope, the SMF-28e® in the sample arm of the OCT module (e.g. the WDM) can filter it out to avoid “ghost” OCT images. In order to perform optical heterodyne detection, an electro-optic modulator was inserted into the reference arm of the OCT module to introduce

a Doppler frequency. A rapid scanning optical delay line (RSOD) was used to compensate the dispersion mismatch between the two OCT arms and to select or scan the imaging depth as reported previously [266]. A balanced detection scheme was used in the OCT module to eliminate any DC components and increase the detection dynamic range.

It is noted that OCT and TPF imaging shares the same scanning endoscope but two independent detection paths; thus the two imaging modalities can run simultaneously with the same field of view and imaging speed. Different from a typical bench-top microscope system, the dual-modality endomicroscope system was drawn upon fiber optics except a short-distance free space to place the dichroic mirror and separate the OCT and fluorescence signals. The overall system is thus very compact and easy to use, which would be critical for future *in vivo* and clinical applications.

11.2.4 Results

Simultaneous TPF and OCT imaging was performed on cell culture and biological tissue (*ex vivo*) to test the performance of the multimodal endomicroscopic imaging platform. The resolutions were $\sim 2.5 \times 10.0 \mu\text{m}$ (lateral \times axial) in air for OCT and $\sim 1.2 \times 5.7 \mu\text{m}$ (lateral \times axial) for TPF imaging. Imaging was performed through a cover glass placed on top of the tissue sample and by a dry micro objective lens of a working distance $200 \mu\text{m}$ in air. The powers incident on the sample were ~ 30 to 50 mW (at 1550 nm for TPF) and $\sim 4.0 \text{ mW}$ (at 1310 nm for OCT). The sweeping range of the DCF fiber tip was either ~ 450 or $\sim 675 \mu\text{m}$ in this study, which resulted in a ~ 100 or $150 \mu\text{m}$ field of view on the sample after the micro compound lens. With a spiral scanning pattern, a frame rate of ~ 3.0 frames/second was achieved with each frame consisting of 512 spirals. The fluorescence

dye used for TPF imaging was indocyanine green (ICG) or ICG nanocapsules, which has an NIR emission peak around ~ 810 nm.

A431 cancer cells were incubated on a coverslip with anti-EGFR conjugated ICG micelles so that the cell membranes were immunostained with the ICG micelles [267, 268]. Figures 10.6a and 10.6b show one set of representative OCT and TPF images of the same cell culture sample acquired simultaneously with the multimodal imaging platform. The superimposed OCT and TPF image is shown in Fig. 11.6c where the whole cell topology can be easily identified with OCT while the cell membrane is enhanced under TPF imaging. As the cells were cultured on a flat coverslip and the sample was relatively transparent, any phase perturbation in the system could be manifested to visible artifacts on the OCT image such as the concentric ring patterns shown in Fig. 11.6a, which could be caused by the periodic instability in the galvanometer mirror in the reference arm.

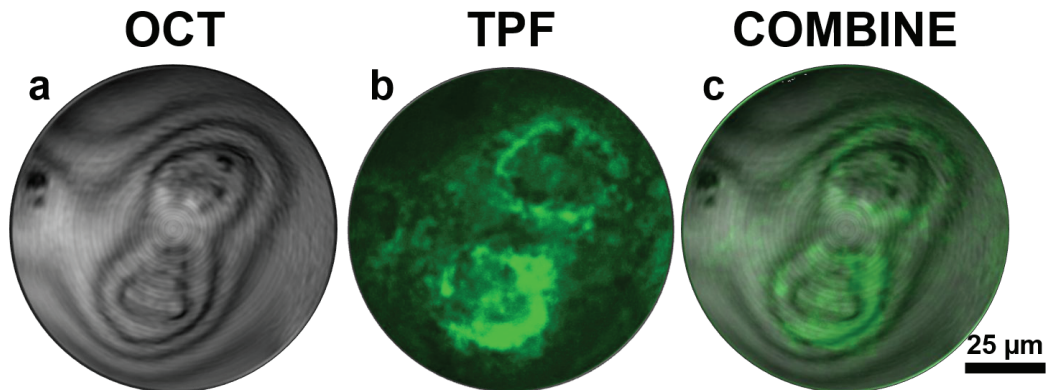


Figure 11.6. (a) OCT and (b) TPF images of A431 cancer cells immunostained with anti-EGFR conjugated ICG micelles. (c) Superposition of the OCT and TPF images. Scale bar: 25 μm

For tissue imaging, different samples from a nude mouse were harvested 15-20 min after local administration of 50 μL of 10 μM ICG solution. Figures 10.7a and 10.7b show representative OCT and TPF images taken simultaneously from adipose tissue. The adipocytes were clearly visualized under OCT with low reflectance from the large lipid

droplets within the adipocytes (indicated by red arrows). In comparison, the locally administrated ICG was found mainly diffused among the adipocytes as shown on the TPF image. The merged image from the two modalities is shown in Fig. 11.7c, and the OCT and TPF images overlap well, particularly around the cell membranes. In addition to cell culture imaging, simultaneous OCT and TPF imaging was also performed on tissue samples from the small intestine, and the representative OCT and TPF images are shown in Figs. 11.7d and 10.7e, respectively. The circular structures on the OCT image may represent the intestinal villi (indicated by blue arrows) with the lacteals (indicated by red arrows) shown as the areas of lower backscattering on the OCT image. Similar structures were visualized on the TPF image as well. The brighter fluorescent spots (indicated by yellow arrows) on the villi may suggest either the enterocytes or lymphocytes actively absorbed the ICG molecules. The superposed image is shown in Fig. 11.7f and the nice overlapping features suggest that the endoscopic multimodal imaging platform is able to produce well-correlated images even with highly scattering tissues.

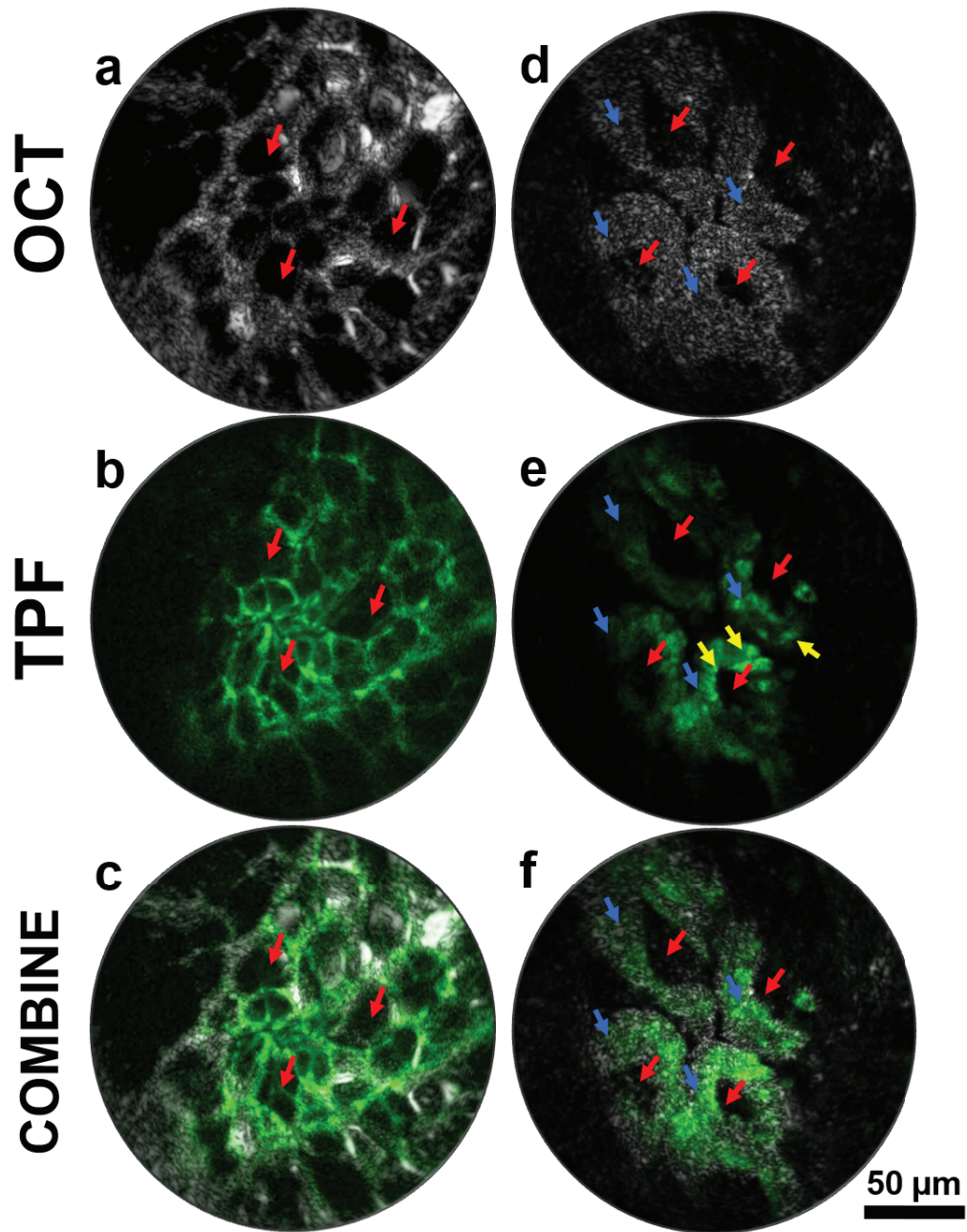


Figure 11.6. (a) OCT, (b) TPF and (c) superposed images of mouse adipose tissue with local ICG administration. Red arrow shown in (a) and (b) indicates one of the adipocytes visualized under both imaging modalities. (d) OCT, (e) TPF and (f) superposed images of mouse small intestine tissue with local ICG administration. Blue arrows shown in (d) and (e) indicate villus structures and red arrows indicate lacteals. The stronger fluorescence dots indicated by yellow arrows shown in (e) may be either enterocytes or lymphocytes. Both sets of images show great correlation between two imaging modalities. Scale bar: 50 μm

11.3 Summary

In this chapter, we described another two projects related to OCT imaging during my Ph.D. study. One of the projects was to develop a cross-reference OCT imaging method to assess the optical properties of gold particles and to synthesize novel scattering-dominant gold nanocages that could be used as OCT contrast agents. In this project, an average contrast enhancement of ~ 2.4 dB was achieved by the gold nanocages in an *in vivo* mouse tumor model. Another project was to develop a compact endoscopic multimodal imaging system that combined 1310 nm *en face* OCT and 1550 nm two photo fluorescence imaging. In this project, *ex vivo* experimental results suggested a potential of using optical imaging modalities with different contrast mechanism to provide complimentary diagnostic information.

Intended to be blank

Chapter 12 Conclusion and Future Perspective

12.1 Summary of Thesis Work

Optical coherence tomography (OCT) is an emerging high resolution optical imaging modality capable of providing cross-sectional images of tissue microanatomy *in vivo*. The non-invasiveness of OCT imaging provides optical biopsy with a resolution approaching standard histopathology, but without the need of tissue removal. The image contrast in OCT comes from the optical properties of the biological tissue and the change in tissue optical properties associated with various diseases at different stages offer the foundation of OCT assessment of the progression of the diseases. The axial resolutions of OCT ranges from 1 to 30 μm with a typical imaging penetration depth from 1 to 3 mm in most highly scattering tissues, which makes OCT well suited for imaging superficial epithelium where many diseases originate from. Technical advances on high speed wavelength swept laser and line scan detector array in the past decade has improved the imaging speed of OCT by 2 to 3 orders of magnitude. Real time OCT imaging and 3D OCT imaging has become not only possible but also popular in research laboratories as well as in clinics. Moreover, the fiber optic based miniature OCT imaging probe/endoscope, which is a critical component for *in vivo* OCT imaging of internal organs, have drawn more and more attentions.

The scope of the multidisciplinary, collaborative research presented in this dissertation was to develop a state-of-the-art high speed endoscopic OCT imaging system and to investigate its potential for *in vivo* assessment of the internal organs. The development of a high speed endoscopic OCT imaging system consists of the construction

of a high speed wavelength swept laser source (i.e., FDML), an optimized OCT interferometer, the development of a sophisticated software platform that is able to handle, process and display the huge dataset generated from the high speed OCT system, and the design and fabrication of robust miniature OCT imaging probes that can efficiently deliver the light source to the sample and collect the very weak signal from the sample. The clinical applications involved *in vivo* lower airway and esophageal 3D OCT imaging by using the high speed endoscopic OCT system. Two other OCT related projects were also discussed at the end of the dissertation.

The Fourier domain mode locked (FDML) laser is one of the wavelength swept laser ideal for a 3D swept source OCT imaging due to its unprecedented high sweeping rate, wide sweeping range, and high power output. A critical balance between a wavelength sweeping range and stable output power in a FDML laser has to be carefully chosen in order to optimize the operating performance of the laser. Counterintuitively, the dispersion and its effect to the laser performance only depends on the length of the laser cavity. Current bottleneck of the FDML sweeping rate is the mechanical response of the tunable filter to the driving frequency. In order to further improve the A-scan speed with the currently available tunable filter, a time multiplexing technique was employed in the FDML laser to form a buffered/double buffered FDML laser.

An OCT interferometer is a fundamental subsystem in an OCT system, where the OCT signal that provides depth-resolved information is generated from. An OCT interferometer was built based on Mach-Zehnder interferometer setup to (1) optimally utilize the output power of the laser and (2) implement balanced detection in order to achieve a shot-noise limited detection. A hardware based real-time uniform K-space

sampling was proposed and implemented to avoid a time consuming data processing procedure of interpolation and further improve the performance of the OCT system.

A flexible and sophisticated software developed for real time OCT imaging is a critical part of a high speed endoscopic OCT system. An OCT imaging software written in C/C++ was developed for data acquisition, data processing, data display, and data storage. Basic functions in the software were wrapped into separate modules so that they can be grouped and loaded into the software flexibly to fulfill different experimental requirements.

The basic requirements of an OCT imaging probe include: (1) the efficiency in delivering and collecting light to and from samples; (2) the robustness of the mechanical design; (3) the simplicity of the optical design so that the probe can be fabricated in a time and cost effective way. The optical designs of two types of side-viewing OCT imaging probe and the considerations behind these designs have been thoroughly discussed. Mechanical design and fabrication of these imaging probes were also mentioned.

Two internal organs were chosen to investigate the feasibility of using high-speed endoscopic OCT imaging system as an *in vivo* assessment tool for diseases, such as chronic obstructive pulmonary disease and Barrett's esophagus. Experimental results suggested that such a high speed system has a great potential to not only differentiate layered structures of the internal organs *in vivo*, but also dynamically monitor the structural changes and the treatment outcomes in real time.

Another two OCT related projects were discussed in the last chapter. The first one is to develop a cross-reference OCT imaging method to assess the optical properties of gold nanoparticles. By using this method, scattering-dominant gold nanocages was successfully synthesized for the first time. An averaged contrast enhancement of ~ 2.4 dB

was achieved by the gold nanocages in an *in vivo* mouse tumor model. The other project is to develop a compact endoscopic multimodal imaging system that combined 1310 nm *en face* OCT and 1550 nm two photo fluorescence imaging, both of which provides depth resolved *en face* images with distinctly different contrast mechanism.

12.2 Future Work

Future efforts for the high speed endoscopic OCT imaging system could be divided into three areas: (1) improvement of the imaging speed; (2) improvement of the imaging resolution; and (3) functional endoscopic OCT imaging.

First of all, the imaging speed of an endoscopic OCT system can be further improved to achieve real time 3D volumetric imaging. As a matter of fact, multimega Hz of imaging speed of OCT system has been demonstrated [168, 269]. However, there are still a few technical hurdles in order to apply such technology into endoscopic OCT applications. One of the technical obstacles is the scanning mechanism of the OCT imaging probe. Most of the miniature OCT imaging probes are proximal end driven; a rotation speed of a few hundreds to one thousand Hz of such a scanning mechanism is impractical for *in vivo* and clinical applications. Distal end scanning is, however, more appreciated for an ultrahigh speed endoscopic OCT imaging system. A distal scanning imaging probe has just been demonstrated at up to 3200 revolutions per second [270]. Another limitation is that the high-speed OCT systems have low detection sensitivity due to a higher bandwidth of the OCT signal. And an OCT imaging probe intends to collect less OCT signal and provide poorer transmission efficiency than a bulky OCT imaging lens because of its limited optical aperture and relatively simple optical design.

Secondly, most of the OCT imaging probes developed so far were designed to work at a wavelength around 1300 nm, which provides an axial resolution of 5 to 20 μm . However, a higher resolution is more desirable in order to resolve fine tissue structures such as airway smooth muscles, intestinal crypts. In addition, a short wavelength region is preferable due to the quadratic dependence of the axial resolution (i.e., $\Delta z \propto \lambda^2 / \Delta\lambda$). As described in Chapter 10, an ultrahigh resolution OCT imaging probe of an axial resolution of 3.0 μm was recently demonstrated in our lab to be able to acquire full circumferential ultrahigh resolution OCT images for the first time [271]. Therefore, a robust and portable ultrahigh resolution endoscopic OCT system should be preferably developed in a near future.

Finally, functional OCT has been proven to provide unique and useful information on bulky OCT setups, such as Doppler and phase retardation. Functional endoscopic OCT is highly desirable. For example, Doppler OCT provides optical microangiography images. However, its applications are highly restricted due to the limited access of the bulky imaging probe to the superficial or transparent biological samples. Combined with endoscopic OCT system, Doppler OCT would be able to provide microvascular information of the internal organs. Such information could bring a lot of opportunities in both research and clinical applications.

Intended to be blank

Appendix A DDSCAT

A.1. Introduction

DDSCAT is an open source package applying discrete dipole approximation (DDA) for calculating scattering and absorption of light by particle of arbitrary geometry and complex refractive index. It was developed in FORTRAN 90 by Bruce T. Drain and Piotr J. Flatau, who applied fast Fourier transform (FFT) and conjugate gradient method to calculate convolution problem in the DDA method [254].

A.2. Compilation of DDSCAT 7.0

The DDSCAT version used in this dissertation is 7.0 [272]. The original DDSCAT source code package was developed for Linux/Unix system, although it can be compiled on a Microsoft Windows system by using a Linux-like environment such as Cygwin [273] or a GNU development environment such as MinGW [274]. In order to properly compile DDSCAT on a native Microsoft Windows environment, the source code that manage the input and output was modified to functions that are supported on native Microsoft Windows environment. To expedite simulation speed, single precision floating point was used in the source code. In addition, Intel Math Kernel Library (MKL) was dynamically linked to the program in order to further improve the performance of the simulation [256]. Furthermore, Intel FORTRAN compiler was used to optimize the compilation procedure

on an Intel Core 2 CPU that supports the[255] instruction set extensions of MMX, SSE, SSE2 and SSE3 .

A.3. Applicability of DDSCAT 7.0

In order to get an accurate simulation result, there are a few considerations when using DDSCAT. First of all, the lattice spacing d should be small compared to the incident wavelength [254]:

$$|m|kd < 1, \quad (\text{L.1})$$

where m is the complex refractive index of the particle material, and $k = 2\pi/\lambda$ is the wavenumber.

Eq. (L.1) is valid when $|m-1| \leq 2$, which is a critical condition when simulation noble metals in the near-infrared region. When imaginary part of the complex refractive index m is large (which is the case of the noble metals in the near-infrared region), the numeric error of the simulation results tends to increase. The error can be reduced by reducing the lattice spacing smaller than the criterion shown in Eq. (L.1). However, too small lattice spacing would increase the computation time significantly. To balance between the numeric accuracy and the computation time, for example, the lattice spacing for gold in 800 nm should be 10 nm.

The choice of lattice spacing was test with simulations of a gold and silver nanosphere of a diameter of 60 nm. The simulation results were compared with Mie scattering theory and the relative error was within 2.5%.

A.4. Parameter File of DDSCAT 7.0

In order to execute the compiled DDSCAT, a parameter file named `ddscat.par` is required.

In the parameter file, the iterative algorithm and FFT method are specified along with other essential input parameters.

A.4.1 An example of `ddscat.par`

One file of `ddscat.par`, which was used for simulation of gold nanocages is displayed here:

```
1      ' ===== Parameter file for v7.0.7 ===== '
2      '**** Preliminaries ****'
3      'NOTORQ' = CMTORQ*6 (NOTORQ, DOTORQ) --either do or skip torque calculations
4      'PBCGS2' = CMDSOL*6 (PBCGS2, PBCGST, PETRKP) -- select solution method
5      'FFTMKL' = CMDFFT*6 (GPFAFT, FFTMKL)
6      'GKDLDR' = CALPHA*6 (GKDLDR, LATDR)
7      'NOTBIN' = CBINFLAG (NOTBIN, ORIBIN, ALLBIN)
8      '**** Initial Memory Allocation ****'
9      100 100 100 = dimensioning allowance for target generation
10     '**** Target Geometry and Composition ****'
11     'FROM_FILE' = CSHAPE*9 shape directive
12     60 60 60 = shape parameters 1 - 3
13     1 = NCOMP = number of dielectric materials
14     'alloy.tab' = file with refractive index 1
15     '**** Error Tolerance ****'
16     1.00e-5 = TOL = MAX ALLOWED (NORM OF |G>=AC|E>-ACA|X>)/(NORM OF AC|E>)
17     '**** Interaction cutoff parameter for PBC calculations ****'
18     5.00e-3 = GAMMA (1e-2 is normal, 3e-3 for greater accuracy)
19     '**** Angular resolution for calculation of <cos>, etc. ****'
20     0.5 = ETASCA (number of angles is proportional to [(3+x)/ETASCA]^2 )
21     '**** Wavelengths (micron) ****'
22     0.4 0.7 10 'LIN' 'LIN' = wavelengths (first,last,how many,how=LIN,INV,LOG)
23     '**** Effective Radii (micron) **** '
24     0.02954 0.02954 1 'LIN' = aeff (first,last,how many,how=LIN,INV,LOG)
25     '**** Define Incident Polarizations ****'
26     (0,0) (1.,0.) (0.,0.) = Polarization state e01 (k along x axis)
27     1 = IORTH (=1 to do only pol. state e01; =2 to also do orth. pol. state)
28     '**** Specify which output files to write ****'
29     1 = IWRKSC (=0 to suppress, =1 to write ".sca" file for each target orient.
```

```

30     1 = IWRPOL (=0 to suppress, =1 to write ".pol" file for each (BETA,THETA)
31     '**** Prescribe Target Rotations ****'
32     0. 0. 1 = BETAMI, BETAMX, NBETA (beta=rotation around a1)
33     0. 90. 3 = THETMI, THETMX, NTHETA (theta=angle between a1 and k)
34     0. 0. 1 = PHIMIN, PHIMAX, NPHI (phi=rotation angle of a1 around k)
35     '**** Specify first IWAV, IRAD, IORI (normally 0 0 0) ****'
36     0 0 0 = first IWAV, first IRAD, first IORI (0 0 0 to begin fresh)
37     '**** Select Elements of S_ij Matrix to Print ****'
38     6 = NSMELTS = number of elements of S_ij to print (not more than 9)
39     11 12 21 22 31 41 = indices ij of elements to print
40     '**** Specify Scattered Directions ****'
41     'LFRAME' = CMDFRM (LFRAME, TFRAME for Lab Frame or Target Frame)
42     2 = NPLANES = number of scattering planes
43     0. 0. 180. 10 = phi, thetan_min, thetan_max, dtheta (in deg) for plane 1
44     90. 0. 180. 10 = phi, thetan_min, thetan_max, dtheta (in deg) for plane 2

```


A.4.2 Explanation of Key Parameters in `ddscat.par`

There are a few key parameters in `ddscat.par` file. They are critical for simulation of gold nanoparticles, which will be explained in this subsection. Other parameters are described in [272].

Line 4 specifies the iterative algorithm. Among three supported algorithms, PBCGS2 has the fastest rate of convergence for noble metals. Line 5 specifies the FFT method. FFTMKL was recommended to get much better performance than the other method. GKDLDR was recommended for the lattice dispersion relation in Line 6. Line 11 specifies the choice of the particle. Here a customized cage shape file was created in a file named `shape.dat`. Line 14 specifies the name of the file that contains the complex refractive index with respect to the wavelength in the surrounding medium. In Line 22, all the calculated wavelength is specified, which is also the wavelength in the medium instead of in vacuum. Line 27 specifies how many polarization states need to be calculated. Since we are only interested in the cross sections (e.g., scattering and absorption cross sections), only one polarization state is required.

Intended to be blank

Bibliography

1. J. L. Prince, *Medical imaging signals and systems* (Pearson Prentice Hall, Upper Saddle River, N.J. :, 2006).
2. Alazartech, "ATS-SDK Release Notes" (2013), retrieved <http://www.alazartech.com/support/Download%20Files/ATS-SDK-ReleaseNotes-6.1.0.htm>.
3. B. Young and J. W. Heath, *Wheater's Functional Histology: A Text and Colour Atlas* (Churchill Livingstone/Elsevier, 2006).
4. R. Kariv, T. P. Plesec, J. R. Goldblum, M. Bronner, M. Oldenburgh, T. W. Rice, and G. W. Falk, "The Seattle Protocol Does Not More Reliably Predict the Detection of Cancer at the Time of Esophagectomy Than a Less Intensive Surveillance Protocol," *Clinical Gastroenterology and Hepatology* **7**, 653-658 (2009).
5. R. P. Burke, G. Michielon, and G. Wernovsky, "Video-assisted cardioscopy in congenital heart operations," *The Annals of Thoracic Surgery* **58**, 864-868 (1994).
6. Y.-C. Liu and A.-S. Chiang, "High-resolution confocal imaging and three-dimensional rendering," *Methods* **30**, 86-93 (2003).
7. A.-E. Stefan, K. Claes af, K. Svanberg, and S. Svanberg, "In vivo fluorescence imaging for tissue diagnostics," *Physics in Medicine and Biology* **42**, 815 (1997).
8. F. J. Wallace, "FIBER OPTIC ENDOSCOPY," *The Journal of urology* **90**, 324-334 (1963).
9. C. Xu, W. Zipfel, J. B. Shear, R. M. Williams, and W. W. Webb, "Multiphoton fluorescence excitation: new spectral windows for biological nonlinear microscopy," *Proceedings of the National Academy of Sciences* **93**, 10763-10768 (1996).
10. C. W. Hufeland, "Journal der practischen Arzneykunde und Wundarzneykunst," **24**(1806).
11. B. I. Hirshowitz, C. W. Peters, and L. E. Curtiss, "Preliminary report on a long fibroscope for examination of stomach and duodenum," *University Michigan Medical Bulletin* **23**, 178-180 (1957).
12. R. S. Kwon, D. G. Adler, B. Chand, J. D. Conway, D. L. Diehl, S. V. Kantsevov, P. Mamula, S. A. Rodriguez, R. J. Shah, L. M. Wong Kee Song, and W. M. Tierney, "High-resolution and high-magnification endoscopes," *Gastrointestinal Endoscopy* **69**, 399-407 (2009).
13. L. M. Wong Kee Song, D. G. Adler, J. D. Conway, D. L. Diehl, F. A. Farraye, S. V. Kantsevov, R. Kwon, P. Mamula, B. Rodriguez, R. J. Shah, and W. M. Tierney, "Narrow band imaging and multiband imaging," *Gastrointestinal Endoscopy* **67**, 581-589 (2008).
14. L. M. Wong Kee Song, D. G. Adler, B. Chand, J. D. Conway, J. M. B. Croffie, J. A. DiSario, D. S. Mishkin, R. J. Shah, L. Somogyi, W. M. Tierney, and B. T. Petersen, "Chromoendoscopy," *Gastrointestinal Endoscopy* **66**, 639-649 (2007).
15. Y. Wu, J. Xi, M. J. Cobb, and X. Li, "Scanning fiber-optic nonlinear endomicroscopy with miniature aspherical compound lens and multimode fiber collector," *Optics Letters* **34**, 953-955 (2009).

16. V. Subramanian and K. Raguath, "Advanced Endoscopic Imaging: A Review of Commercially Available Technologies," *Clinical Gastroenterology and Hepatology* (2013).
17. S. Kelly, K. M. Harris, E. Berry, J. Hutton, P. Roderick, J. Cullingworth, L. Gathercole, and M. A. Smith, "A systematic review of the staging performance of endoscopic ultrasound in gastro-oesophageal carcinoma," *Gut* **49**, 534-539 (2001).
18. R. H. Bardales, E. B. Stelow, S. Mallery, R. Lai, and M. W. Stanley, "Review of endoscopic ultrasound-guided fine-needle aspiration cytology," *Diagnostic Cytopathology* **34**, 140-175 (2006).
19. L. Varela-Lema, A. Fernández-Villar, and A. Ruano-Ravina, "Effectiveness and safety of endobronchial ultrasound–transbronchial needle aspiration: a systematic review," *European Respiratory Journal* **33**, 1156-1164 (2009).
20. E. M. Godfrey, S. M. Rushbrook, and N. R. Carrol, "Endoscopic ultrasound: a review of current diagnostic and therapeutic applications," *Postgraduate Medical Journal* **86**, 346-353 (2010).
21. M. C. McDaniel, P. Eshtehardi, F. J. Sawaya, J. S. Douglas Jr, and H. Samady, "Contemporary Clinical Applications of Coronary Intravascular Ultrasound," *JACC: Cardiovascular Interventions* **4**, 1155-1167 (2011).
22. D. Huang, E. Swanson, C. Lin, J. Schuman, W. Stinson, W. Chang, M. Hee, T. Flotte, K. Gregory, C. Puliafito, and J. Fujimoto, "Optical coherence tomography," *Science* **254**, 1178-1181 (1991).
23. J. M. Schmitt, "Optical coherence tomography (OCT): a review," *IEEE Journal of Selected Topics in Quantum Electronics* **5**, 1205-1215 (1999).
24. A. F. Fercher, W. Drexler, C. K. Hitzenberger, and T. Lasser, "Optical coherence tomography — principles and applications," *Reports on Progress in Physics* **66**, 239-303 (2003).
25. M. A. Duguay and A. T. Mattick, "Ultrahigh Speed Photography of Picosecond Light Pulses and Echoes," *Applied Optics* **10**, 2162-2170 (1971).
26. S. D. Personick, "Photon Probe—An Optical-Fiber Time-Domain Reflectometer," *Bell System Technical Journal* **56**, 355-366 (1977).
27. J. G. Fujimoto, S. Desilvestri, E. P. Ippen, C. A. Puliafito, R. Margolis, and A. Oseroff, "Femtosecond Optical Ranging in Biological-Systems," *Optics Letters* **11**, 150-152 (1986).
28. D. Stern, W. Z. Lin, C. A. Puliafito, and J. G. Fujimoto, "Femtosecond Optical Ranging of Corneal Incision Depth," *Investigative Ophthalmology & Visual Science* **30**, 99-104 (1989).
29. B. L. Danielson, "Optical Time-Domain Reflectometer Specifications and Performance Testing," *Applied Optics* **24**, 2313-2322 (1985).
30. K. Takada, I. Yokohama, K. Chida, and J. Noda, "New measurement system for fault location in optical waveguide devices based on an interferometric technique," *Applied Optics* **26**, 1603-1606 (1987).
31. R. C. Youngquist, S. Carr, and D. E. N. Davies, "Optical coherence-domain reflectometry: a new optical evaluation technique," *Optics Letters* **12**, 158-160 (1987).
32. Y. J. Rao and D. A. Jackson, "Recent progress in fibre optic low-coherence interferometry," *Measurement Science & Technology* **7**, 981-999 (1996).

33. A. F. Fercher, K. Mengedoht, and W. Werner, "Eye-length measurement by interferometry with partially coherent light," *Optics Letters* **13**, 186-188 (1988).
34. G. J. Tearney, B. E. Bouma, and J. G. Fujimoto, "High-speed phase- and group-delay scanning with a grating-based phase control delay line," *Optics Letters* **22**, 1811-1813 (1997).
35. G. Hausler and M. W. Lindner, "'Coherence Radar' and 'Spectral Radar'—New Tools for Dermatological Diagnosis," *BIOMEDO* **3**, 21-31 (1998).
36. R. Huber, M. Wojtkowski, K. Taira, J. Fujimoto, and K. Hsu, "Amplified, frequency swept lasers for frequency domain reflectometry and OCT imaging: design and scaling principles," *Opt. Express* **13**, 3513-3528 (2005).
37. T. Klein, W. Wieser, L. Reznicek, A. Neubauer, A. Kampik, and R. Huber, "Multi-MHz retinal OCT," *Biomed. Opt. Express* **4**, 1890-1908 (2013).
38. M. Choma, M. Sarunic, C. Yang, and J. Izatt, "Sensitivity advantage of swept source and Fourier domain optical coherence tomography," *Opt. Express* **11**, 2183-2189 (2003).
39. J. F. de Boer, B. Cense, B. H. Park, M. C. Pierce, G. J. Tearney, and B. E. Bouma, "Improved signal-to-noise ratio in spectral-domain compared with time-domain optical coherence tomography," *Optics Letters* **28**, 2067-2069 (2003).
40. R. Leitgeb, C. Hitzenberger, and A. Fercher, "Performance of fourier domain vs. time domain optical coherence tomography," *Opt. Express* **11**, 889-894 (2003).
41. W. Drexler, U. Morgner, R. K. Ghanta, F. X. Kartner, J. S. Schuman, and J. G. Fujimoto, "Ultrahigh-resolution ophthalmic optical coherence tomography," *Nature Medicine* **7**, 502-507 (2001).
42. W. Drexler, U. Morgner, F. X. Kärtner, C. Pitris, S. a. Boppart, X. D. Li, E. P. Ippen, and J. G. Fujimoto, "In vivo ultrahigh-resolution optical coherence tomography," *Optics Letters* **24**, 1221-1223 (1999).
43. E. A. Swanson, J. A. Izatt, C. P. Lin, J. G. Fujimoto, J. S. Schuman, M. R. Hee, D. Huang, and C. A. Puliato, "In vivo retinal imaging by optical coherence tomography," *Optics Letters* **18**, 1864-1866 (1993).
44. M. Wojtkowski, T. Bajraszewski, I. Gorczyńska, P. Targowski, A. Kowalczyk, W. Wasilewski, and C. Radzewicz, "Ophthalmic imaging by spectral optical coherence tomography," *American journal of ophthalmology* **138**, 412-419 (2004).
45. B. Potsaid, I. Gorczynska, V. J. Srinivasan, Y. Chen, J. Jiang, A. Cable, and J. G. Fujimoto, "Ultrahigh speed Spectral / Fourierdomain OCT ophthalmic imaging at 70,000 to 312,500 axial scans per second," *Opt. Express* **16**, 15149-15169 (2008).
46. I. Grulkowski, J. J. Liu, B. Potsaid, V. Jayaraman, C. D. Lu, J. Jiang, A. E. Cable, J. S. Duker, and J. G. Fujimoto, "Retinal, anterior segment and full eye imaging using ultrahigh speed swept source OCT with vertical-cavity surface emitting lasers," *Biomed. Opt. Express* **3**, 2733-2751 (2012).
47. J. Welzel, E. Lanke, R. Birngruber, and R. Engelhardt, "Optical coherence tomography of the human skin," *Journal of the American Academy of Dermatology* **37**, 958-963 (1997).
48. J. Welzel, C. Reinhardt, E. Lanke, C. Winter, and H. H. Wolff, "Changes in function and morphology of normal human skin: evaluation using optical coherence tomography," *British Journal of Dermatology* **150**, 220-225 (2004).

49. T. Gambichler, G. Moussa, M. Sand, D. Sand, P. Altmeyer, and K. Hoffmann, "Applications of optical coherence tomography in dermatology," *Journal of dermatological science* **40**, 85-94 (2005).
50. M. J. Cobb, R. A. Underwood, X. Li, M. L. Usui, Y. Chen, and J. Olerud, "Noninvasive assessment of cutaneous wound healing using ultrahigh-resolution optical coherence tomography," *BIOMEDO* **11**, 064002-064002-064011 (2006).
51. T. Gambichler, A. Orlikov, R. Vasa, G. Moussa, K. Hoffmann, M. Stücker, P. Altmeyer, and F. G. Bechara, "In vivo optical coherence tomography of basal cell carcinoma," *Journal of dermatological science* **45**, 167-173 (2007).
52. J. Welzel, M. Bruhns, and H. Wolff, "Optical coherence tomography in contact dermatitis and psoriasis," *Arch Dermatol Res* **295**, 50-55 (2003).
53. A. Golabchi, C. A. DiMarzio, and A. Gouldstone, "Multi angle view of lung using optical coherence tomography (OCT)," in 2012), 82270X-82270X-82276.
54. R. M. Lovering, S. B. Shah, S. J. P. Pratt, W. Gong, and Y. Chen, "Architecture of healthy and dystrophic muscles detected by optical coherence tomography," *Muscle & Nerve* **47**, 588-590 (2013).
55. J. a. Izatt, M. R. Hee, G. M. Owen, E. a. Swanson, and J. G. Fujimoto, "Optical coherence microscopy in scattering media," *Optics Letters* **19**, 590-592 (1994).
56. J. A. Izatt, M. D. Kulkarni, W. Hsing-Wen, K. Kobayashi, and M. V. Sivak, Jr., "Optical coherence tomography and microscopy in gastrointestinal tissues," *Selected Topics in Quantum Electronics, IEEE Journal of* **2**, 1017-1028 (1996).
57. S. Rais-Bahrami, A. W. Levinson, N. M. Fried, G. A. Lagoda, A. Hristov, Y. Chuang, A. L. Burnett, and L.-M. Su, "Optical Coherence Tomography of Cavernous Nerves: A Step Toward Real-Time Intraoperative Imaging During Nerve-Sparing Radical Prostatectomy," *Urology* **72**, 198-204 (2008).
58. Z. Yaqoob, J. Wu, and C. Yang, "Spectral domain optical coherence tomography: a better OCT imaging strategy," *BioTechniques* **39**, S6-13 (2005).
59. S. A. Boppart, M. E. Brezinski, B. E. Bouma, G. J. Tearney, and J. G. Fujimoto, "Investigation of Developing Embryonic Morphology Using Optical Coherence Tomography," *Developmental Biology* **177**, 54-63 (1996).
60. S. A. Boppart, G. J. Tearney, B. E. Bouma, J. F. Southern, M. E. Brezinski, and J. G. Fujimoto, "Noninvasive assessment of the developing *Xenopus* cardiovascular system using optical coherence tomography," *Proceedings of the National Academy of Sciences* **94**, 4256-4261 (1997).
61. B. Hoeling, A. Fernandez, R. Haskell, E. Huang, W. Myers, D. Petersen, S. Ungersma, R. Wang, M. Williams, and S. Fraser, "An optical coherence microscope for 3-dimensional imaging in developmental biology," *Opt. Express* **6**, 136-146 (2000).
62. S. Yazdanfar, M. Kulkarni, and J. Izatt, "High resolution imaging of in vivo cardiac dynamics using color Doppler optical coherence tomography," *Opt. Express* **1**, 424-431 (1997).
63. T. M. Yelbuz, M. A. Choma, L. Thrane, M. L. Kirby, and J. A. Izatt, "Optical Coherence Tomography: A New High-Resolution Imaging Technology to Study Cardiac Development in Chick Embryos," *Circulation* **106**, 2771-2774 (2002).
64. S. A. Boppart, M. E. Brezinski, and J. G. Fujimoto, "Optical coherence tomography imaging in developmental biology," in *Developmental Biology Protocols* (Springer, 2000), pp. 217-233.

65. D. Levitz, S. L. Jacques, M. T. Hinds, N. Choudhury, N. T. Tran, and S. R. Hanson, "Quantitative characterization of developing collagen gels using optical coherence tomography," *BIOMEDO* **15**, 026019-026019-026011 (2010).
66. C. Mason, J. F. Markusen, M. A. Town, P. Dunnill, and R. K. Wang, "The potential of optical coherence tomography in the engineering of living tissue," *Physics in Medicine and Biology* **49**, 1097 (2004).
67. L. E. Smith, M. Bonesi, R. Smallwood, S. J. Matcher, and S. MacNeil, "Using swept-source optical coherence tomography to monitor the formation of neo-epidermis in tissue-engineered skin," *Journal of Tissue Engineering and Regenerative Medicine* **4**, 652-658 (2010).
68. A. Sergeev, V. Gelikonov, G. Gelikonov, F. Feldchtein, R. Kuranov, N. Gladkova, N. Shakhova, L. Snopova, A. Shakhov, I. Kuznetzova, A. Denisenko, V. Pochinko, Y. Chumakov, and O. Streltsova, "In vivo endoscopic OCT imaging of precancer and cancer states of human mucosa," *Optics Express* **1**, 432-440 (1997).
69. G. J. Tearney, M. E. Brezinski, B. E. Bouma, S. A. Boppart, C. Pitris, J. F. Southern, and J. G. Fujimoto, "In Vivo Endoscopic Optical Biopsy with Optical Coherence Tomography," *Science* **276**, 2037-2039 (1997).
70. A. M. Rollins, R. Ung-arunyawee, A. Chak, R. C. K. Wong, K. Kobayashi, J. M. V. Sivak, and J. A. Izatt, "Real-time in vivo imaging of human gastrointestinal ultrastructure by use of endoscopic optical coherence tomography with a novel efficient interferometer design," *Optics Letters* **24**, 1358-1360 (1999).
71. Y. Pan, H. Xie, and G. K. Fedder, "Endoscopic optical coherence tomography based on a microelectromechanical mirror," *Opt. Lett.* **26**, 1966-1968 (2001).
72. A. R. Tumlinson, J. K. Barton, B. Povazay, H. Sattman, A. Unterhuber, R. A. Leitgeb, and W. Drexler, "Endoscope-tip interferometer for ultrahigh resolution frequency domain optical coherence tomography in mouse colon," *Opt. Express* **14**, 1878-1887 (2006).
73. W. Jung, D. T. McCormick, Y.-C. Ahn, A. Seppehr, M. Brenner, B. Wong, N. C. Tien, and Z. Chen, "In vivo three-dimensional spectral domain endoscopic optical coherence tomography using a microelectromechanical system mirror," *Opt. Lett.* **32**, 3239-3241 (2007).
74. J. Xi, L. Huo, Y. Wu, M. J. Cobb, J. H. Hwang, and X. Li, "High-resolution OCT balloon imaging catheter with astigmatism correction," *Opt. Lett.* **34**, 1943-1945 (2009).
75. H. Lu, M. Gargsha, Z. Wang, D. Chamie, G. F. Attizzani, T. Kanaya, S. Ray, M. A. Costa, A. M. Rollins, H. G. Bezerra, and D. L. Wilson, "Automatic stent detection in intravascular OCT images using bagged decision trees," *Biomed. Opt. Express* **3**, 2809-2824 (2012).
76. H. G. Bezerra, M. A. Costa, G. Guagliumi, A. M. Rollins, and D. I. Simon, "Intracoronary Optical Coherence Tomography: A Comprehensive Review Clinical and Research Applications," *JACC: Cardiovascular Interventions* **2**, 1035-1046 (2009).
77. G. J. Tearney, I.-K. Jang, and B. E. Bouma, "Optical coherence tomography for imaging the vulnerable plaque," *BIOMEDO* **11**, 021002-021002-021010 (2006).
78. G. J. Tearney, S. Waxman, M. Shishkov, B. J. Vakoc, M. J. Suter, M. I. Freilich, A. E. Desjardins, W.-Y. Oh, L. A. Bartlett, M. Rosenberg, and B. E. Bouma, "Three-

- Dimensional Coronary Artery Microscopy by Intracoronary Optical Frequency Domain Imaging," *JACC: Cardiovascular Imaging* **1**, 752-761 (2008).
79. H. L. Fu, Y. Leng, M. J. Cobb, K. Hsu, J. H. Hwang, and X. Li, "Flexible miniature compound lens design for high-resolution optical coherence tomography balloon imaging catheter," *Journal of Biomedical Optics* **13**, 060502-060502-060503 (2008).
 80. B. E. Bouma, G. J. Tearney, C. C. Compton, and N. S. Nishioka, "High-resolution imaging of the human esophagus and stomach in vivo using optical coherence tomography," *Gastrointestinal Endoscopy* **51**, 467-474 (2000).
 81. S. Jäckle, N. Gladkova, F. Feldchtein, A. Terentieva, B. Brand, G. Gelikonov, V. Gelikonov, A. Sergeev, A. Fritscher-Ravens, J. Freund, U. Seitz, S. Schröder, and N. Soehendra, "In Vivo Endoscopic Optical Coherence Tomography of Esophagitis, Barrett's Esophagus, and Adenocarcinoma of the Esophagus," *Endoscopy* **32**, 750-755 (2000).
 82. X. D. Li, S. A. Boppart, J. Van Dam, H. Mashimo, M. Mutinga, W. Drexler, M. Klein, C. Pitris, M. L. Krinsky, M. E. Brezinski, and J. G. Fujimoto, "Optical Coherence Tomography: Advanced Technology for the Endoscopic Imaging of Barrett's Esophagus," *Endoscopy* **32**, 921-930 (2000).
 83. M. J. Gora, J. S. Sauk, R. W. Carruth, K. A. Gallagher, M. J. Suter, N. S. Nishioka, L. E. Kava, M. Rosenberg, B. E. Bouma, and G. J. Tearney, "Tethered capsule endomicroscopy enables less invasive imaging of gastrointestinal tract microstructure," *Nat Med* **19**, 238-240 (2013).
 84. L. P. Hariri, M. B. Applegate, M. Mino-Kenudson, E. J. Mark, B. D. Medoff, A. D. Luster, B. E. Bouma, G. J. Tearney, and M. J. Suter, "Volumetric optical frequency domain imaging of pulmonary pathology with precise correlation to histopathology," *CHEST Journal* **143**, 64-74 (2013).
 85. S. Lam, B. Standish, C. Baldwin, A. McWilliams, J. leRiche, A. Gazdar, A. I. Vitkin, V. Yang, N. Ikeda, and C. MacAulay, "In vivo Optical Coherence Tomography Imaging of Preinvasive Bronchial Lesions," *Clinical Cancer Research* **14**, 2006-2011 (2008).
 86. A. M. D. Lee, K. Ohtani, C. MacAulay, A. McWilliams, T. Shaipanich, V. X. D. Yang, S. Lam, and P. Lane, "In vivo lung microvasculature visualized in three dimensions using fiber-optic color Doppler optical coherence tomography," *BIOMEDO* **18**, 050501-050501 (2013).
 87. S.-W. Lee, A. E. Heidari, D. Yoon, D. Mukai, T. Ramalingam, S. Mahon, J. Yin, J. Jing, G. Liu, Z. Chen, and M. Brenner, "Quantification of airway thickness changes in smoke-inhalation injury using in-vivo 3-D endoscopic frequency-domain optical coherence tomography," *Biomed. Opt. Express* **2**, 243-254 (2011).
 88. J. P. Williamson, J. J. Armstrong, R. A. McLaughlin, P. B. Noble, A. R. West, S. Becker, A. Curatolo, W. J. Noffsinger, H. W. Mitchell, M. J. Phillips, D. D. Sampson, D. R. Hillman, and P. R. Eastwood, "Measuring airway dimensions during bronchoscopy using anatomical optical coherence tomography," *European Respiratory Journal* **35**, 34-41 (2010).
 89. J. Xi, W. Mitnzer, R. Brown, R. Yung, and X. Li, "Real-time Three-Dimensional Dynamic Imaging of Lower Airway Using Swept Source Optical Coherence Tomography," in *Biomedical Optics and 3-D Imaging*, OSA Technical Digest (Optical Society of America, 2012), BTu3A.93.

90. X. Li and J. G. Fujimoto, "Optical Coherence Tomography," in *Encyclopedia of Biomaterials and Biomedical Engineering*, 2 ed., G. E. Wnek and G. L. Bowlin, eds. (Informa Healthcare USA, 2008), p. 3434.
91. E. Hecht, *Optics* (Addison-Wesley Longman, Incorporated, 2002).
92. M. O. Scully and S. Zubairy, *Quantum Optics* (Cambridge University Press, 1997).
93. J. A. Izatt and M. A. Choma, "Theory of Optical Coherence Tomography," in *Optical Coherence Tomography: Technology and Applications*, W. Drexler and J. G. Fujimoto, eds. (Springer, 2008), p. 47.
94. V. Yang, M. Gordon, B. Qi, J. Pekar, S. Lo, E. Seng-Yue, A. Mok, B. Wilson, and I. Vitkin, "High speed, wide velocity dynamic range Doppler optical coherence tomography (Part I): System design, signal processing, and performance," *Opt. Express* **11**, 794-809 (2003).
95. P.-L. Hsiung, X. Li, C. Chudoba, I. Hartl, T. H. Ko, and J. G. Fujimoto, "High-Speed Path-Length Scanning with a Multiple-Pass Cavity Delay Line," *Applied Optics* **42**, 640-648 (2003).
96. B. L. Danielson and C. D. Whittenberg, "Guided-Wave Reflectometry with Micrometer Resolution," *Applied Optics* **26**, 2836-2842 (1987).
97. J. F. de Boer, "Theory of Optical Coherence Tomography," in *Optical Coherence Tomography: Technology and Applications*, W. Drexler and J. G. Fujimoto, eds. (Springer, 2008), p. 147.
98. R. G. Lyons, *Understanding Digital Signal Processing* (Pearson Education, 2010).
99. D. C. Adler, Y. Chen, R. Huber, J. Schmitt, J. Connolly, and J. G. Fujimoto, "Three-dimensional endomicroscopy using optical coherence tomography," *Nat Photon* **1**, 709-716 (2007).
100. J. Xi, L. Huo, J. Li, and X. Li, "Generic real-time uniform K-space sampling method for high-speed swept-Source optical coherence tomography," *Opt. Express* **18**, 9511-9517 (2010).
101. K. K. H. Chan and S. Tang, "High-speed spectral domain optical coherence tomography using non-uniform fast Fourier transform," *Biomed. Opt. Express* **1**, 1309-1319 (2010).
102. K. Wang, Z. Ding, T. Wu, C. Wang, J. Meng, M. Chen, and L. Xu, "Development of a non-uniform discrete Fourier transform based high speed spectral domain optical coherence tomography system," *Opt. Express* **17**, 12121-12131 (2009).
103. S. Yun, G. Tearney, B. Bouma, B. Park, and J. de Boer, "High-speed spectral-domain optical coherence tomography at 1.3 μm wavelength," *Opt. Express* **11**, 3598-3604 (2003).
104. Z. Hu, Y. Pan, and A. M. Rollins, "Analytical model of spectrometer-based two-beam spectral interferometry," *Applied Optics* **46**, 8499-8505 (2007).
105. R. Huber, M. Wojtkowski, and J. G. Fujimoto, "Fourier Domain Mode Locking (FDML): A new laser operating regime and applications for optical coherence tomography," *Opt. Express* **14**, 3225-3237 (2006).
106. D. C. Adler, W. Wieser, F. Trepanier, J. M. Schmitt, and R. A. Huber, "Extended coherence length Fourier domain mode locked lasers at 1310 nm," *Opt. Express* **19**, 20930-20939 (2011).
107. I. Grulkowski, J. J. Liu, B. Potsaid, V. Jayaraman, C. D. Lu, J. Jiang, A. E. Cable, J. S. Duker, and J. G. Fujimoto, "Retinal, anterior segment and full eye imaging using

- ultra-high speed swept source OCT with vertical-cavity surface emitting lasers," *Biomed. Opt. Express* **3**, 2733-2751 (2012).
108. B. R. Biedermann, W. Wieser, C. M. Eigenwillig, and R. Huber, "Recent developments in Fourier Domain Mode Locked lasers for optical coherence tomography: Imaging at 1310 nm vs. 1550 nm wavelength," *Journal of Biophotonics* **2**, 357-363 (2009).
 109. S. Ishida and N. Nishizawa, "Quantitative comparison of contrast and imaging depth of ultra-high-resolution optical coherence tomography images in 800-1700 nm wavelength region," *Biomed. Opt. Express* **3**, 282-294 (2012).
 110. B. Považay, H. Sattmann, F. Zeiler, J. E. Morgan, C. Falkner-Radler, W. Drexler, C. Glittenberg, B. Hermann, A. Unterhuber, S. Blinder, and B. Hofer, "Three-dimensional optical coherence tomography at 1050nm versus 800nm in retinal pathologies: enhanced performance and choroidal penetration in cataract patients," *BIOMEDO* **12**, 041211-041211-041217 (2007).
 111. S. Radhakrishnan, A. M. Rollins, J. E. Roth, and et al., "Real-time optical coherence tomography of the anterior segment at 1310 nm," *Archives of Ophthalmology* **119**, 1179-1185 (2001).
 112. L. Kou, D. Labrie, and P. Chylek, "Refractive indices of water and ice in the 0.65- to 2.5- μm spectral range," *Appl. Opt.* **32**, 3531-3540 (1993).
 113. C.-F. Lin and B.-L. Lee, "Extremely broadband AlGaAs/GaAs superluminescent diodes," *Applied Physics Letters* **71**, 1598-1600 (1997).
 114. M. Ranjbaran and X. Li, "Performance-enhanced superluminescent diode with surface plasmon waveguide," *Opt. Express* **17**, 23643-23654 (2009).
 115. A. Unterhuber, B. Považay, B. Hermann, H. Sattmann, W. Drexler, V. Yakovlev, G. Tempea, C. Schubert, E. M. Anger, P. K. Ahnelt, M. Stur, J. E. Morgan, A. Cowey, G. Jung, T. Le, and A. Stingl, "Compact, low-cost Ti:Al₂O₃ laser for in vivo ultra-high-resolution optical coherence tomography," *Opt. Lett.* **28**, 905-907 (2003).
 116. P. Wagenblast, T. Ko, J. Fujimoto, F. Kaertner, and U. Morgner, "Ultra-high-resolution optical coherence tomography with a diode-pumped broadband Cr³⁺:LiCAF laser," *Opt. Express* **12**, 3257-3263 (2004).
 117. A. Unterhuber, B. Považay, B. Hermann, H. Sattmann, A. Chavez-Pirson, and W. Drexler, "In vivo retinal optical coherence tomography at 1040 nm - enhanced penetration into the choroid," *Opt. Express* **13**, 3252-3258 (2005).
 118. Thorlabs, "Superluminescent Diode 1050 nm SLD1050S" (2011), retrieved <http://www.thorlabs.com/thorcat/21600/SLD1050S-SpecSheet.pdf>.
 119. INPHENIX, "Super-Luminescent Light Emitting Diode Device IPSDD100X (1050nm)," (2012).
 120. P. J. Poole, M. Davies, M. Dion, Y. Feng, S. Charbonneau, R. D. Goldberg, and I. V. Mitchell, "The fabrication of a broad-spectrum light-emitting diode using high-energy ion implantation," *Photonics Technology Letters, IEEE* **8**, 1145-1147 (1996).
 121. L. Seung Yeol, Y. Jae Su, and L. Yong Tak, "Fabrication of self-aligned ridge waveguide lasers with spot-size converter for quantum well intermixed superluminescent diodes," *Semiconductor Science and Technology* **23**, 025013 (2008).
 122. Thorlabs, "Superluminescent Diode 1310 nm SLD1021S" (2011), retrieved <http://www.thorlabs.com/thorcat/19500/SLD1021S-SpecSheet.pdf>.

123. B. E. Bouma, G. J. Tearney, I. P. Bilinsky, B. Golubovic, S. A. Boppart, and J. G. Fujimoto, "Optical Coherence Tomographic Imaging Using a Mode Locked Cr⁴⁺:Forsterite Laser Source," in *Ultrafast Phenomena X*, P. Barbara, J. Fujimoto, W. Knox, and W. Zinth, eds. (Springer Berlin Heidelberg, 1996), pp. 143-144.
124. D. J. Ripin, C. Chudoba, J. T. Gopinath, J. G. Fujimoto, E. P. Ippen, U. Morgner, F. X. Kärtner, V. Scheuer, G. Angelow, and T. Tschudi, "Generation of 20-fs pulses by a prismless Cr⁴⁺:YAG laser," *Opt. Lett.* **27**, 61-63 (2002).
125. L. An, G. Guan, and R. K. Wang, "High-speed 1310 nm-band spectral domain optical coherence tomography at 184,000 lines per second," *BIOMEDO* **16**, 060506-060506-060503 (2011).
126. U. A. Systems, "Sensors Unlimited GL2048L InGaAs Linescan Camera for Spectral-domain OCT systems" (2013), retrieved <http://www.sensorsinc.com/downloads/GL2048L.pdf>.
127. S.-W. Lee, H.-W. Song, B.-K. Kim, M.-Y. Jung, S.-H. Kim, J.-D. Cho, and C.-S. Kim, "Fourier Domain Optical Coherence Tomography for Retinal Imaging with 800-nm Swept Source: Real-time Resampling in k-domain," *J. Opt. Soc. Korea* **15**, 293-299 (2011).
128. M. Born and E. Wolf, "Principles of optics : electromagnetic theory of propagation, interference and diffraction of light," E. Wolf and A. B. Bhatia, eds. (Cambridge University Press, Cambridge, UK ;, 2002).
129. X. Liu, M. J. Cobb, Y. Chen, M. B. Kimmey, and X. Li, "Rapid-scanning forward-imaging miniature endoscope for real-time optical coherence tomography," *Opt. Lett.* **29**, 1763-1765 (2004).
130. W. Piyawattanametha, R. P. J. Barretto, T. H. Ko, B. A. Flusberg, E. D. Cocker, H. Ra, D. Lee, O. Solgaard, and M. J. Schnitzer, "Fast-scanning two-photon fluorescence imaging based on a microelectromechanical systems two-dimensional scanning mirror," *Opt. Lett.* **31**, 2018-2020 (2006).
131. J. Wu, M. Conry, C. Gu, F. Wang, Z. Yaqoob, and C. Yang, "Paired-angle-rotation scanning optical coherence tomography forward-imaging probe," *Opt. Lett.* **31**, 1265-1267 (2006).
132. T. Xie, H. Xie, G. K. Fedder, and Y. Pan, "Endoscopic Optical Coherence Tomography with a Modified Microelectromechanical Systems Mirror for Detection of Bladder Cancers," *Appl. Opt.* **42**, 6422-6426 (2003).
133. J. M. Zara, S. Yazdanfar, K. D. Rao, J. A. Izatt, and S. W. Smith, "Electrostatic micromachine scanning mirror for optical coherence tomography," *Opt. Lett.* **28**, 628-630 (2003).
134. A. Jain, A. Kopa, P. Yingtian, G. K. Fedder, and X. Huikai, "A two-axis electrothermal micromirror for endoscopic optical coherence tomography," *Selected Topics in Quantum Electronics, IEEE Journal of* **10**, 636-642 (2004).
135. L. Huo, J. Xi, Y. Wu, and X. Li, "Forward-viewing resonant fiber-optic scanning endoscope of appropriate scanning speed for 3D OCT imaging," *Opt. Express* **18**, 14375-14384 (2010).
136. Y. Pan, Z. Li, C. R. Chu, and T. Xie, "Hand-held arthroscopic optical coherence tomography for in vivo high-resolution imaging of articular cartilage," *BIOMEDO* **8**, 648-654 (2003).

137. T. Xie, D. Mukai, S. Guo, M. Brenner, and Z. Chen, "Fiber-optic-bundle-based optical coherence tomography," *Opt. Lett.* **30**, 1803-1805 (2005).
138. G. J. Tearney, M. E. Brezinski, J. G. Fujimoto, N. J. Weissman, S. A. Boppart, B. E. Bouma, and J. F. Southern, "Scanning single-mode fiber optic catheter?endoscope for optical coherence tomography," *Opt. Lett.* **21**, 543-545 (1996).
139. T.-H. Tsai, B. Potsaid, M. F. Kraus, C. Zhou, Y. K. Tao, J. Hornegger, and J. G. Fujimoto, "Piezoelectric-transducer-based miniature catheter for ultrahigh-speed endoscopic optical coherence tomography," *Biomed. Opt. Express* **2**, 2438-2448 (2011).
140. A. R. Tumlinson, L. P. Hariri, U. Utzinger, and J. K. Barton, "Miniature Endoscope for Simultaneous Optical Coherence Tomography and Laser-Induced Fluorescence Measurement," *Appl. Opt.* **43**, 113-121 (2004).
141. X. Li, C. Chudoba, T. Ko, C. Pitris, and J. G. Fujimoto, "Imaging needle for optical coherence tomography," *Opt. Lett.* **25**, 1520-1522 (2000).
142. D. Lorensen, X. Yang, R. W. Kirk, B. C. Quirk, R. A. McLaughlin, and D. D. Sampson, "Ultrathin side-viewing needle probe for optical coherence tomography," *Opt. Lett.* **36**, 3894-3896 (2011).
143. Y. Wu, X. Jiefeng, H. Li, J. Padvorac, S. Eun Ji, S. A. Giday, A. A. Lennon, M. I. F. Canto, H. Joo Ha, and L. Xingde, "Robust High-Resolution Fine OCT Needle for Side-Viewing Interstitial Tissue Imaging," *Selected Topics in Quantum Electronics, IEEE Journal of* **16**, 863-869 (2010).
144. B. C. Quirk, R. A. McLaughlin, A. Curatolo, R. W. Kirk, P. B. Noble, and D. D. Sampson, "In situ imaging of lung alveoli with an optical coherence tomography needle probe," *BIOMEDO* **16**, 036009-036009-036004 (2011).
145. K. M. Tan, M. Shishkov, A. Chee, M. B. Applegate, B. E. Bouma, and M. J. Suter, "Flexible transbronchial optical frequency domain imaging smart needle for biopsy guidance," *Biomedical Optics Express* **3**, 1947-1954 (2012).
146. V. X. D. Yang, Y. X. Mao, N. Munce, B. Standish, W. Kucharczyk, N. E. Marcon, B. C. Wilson, and I. A. Vitkin, "Interstitial Doppler optical coherence tomography," *Opt. Lett.* **30**, 1791-1793 (2005).
147. W. Danling, B. V. Hunter, M. J. Cobb, and L. Xingde, "Super-Achromatic Rapid Scanning Microendoscope for Ultrahigh-Resolution OCT Imaging," *Selected Topics in Quantum Electronics, IEEE Journal of* **13**, 1596-1601 (2007).
148. A. R. Tumlinson, J. K. Barton, J. McNally, A. Unterhuber, B. Hermann, H. Sattmann, and W. Drexler, "An achromatized endoscope for ultrahigh-resolution optical coherence tomography," in 2005), 586110-586110-586117.
149. B. E. Bouma and G. J. Tearney, "Power-efficient nonreciprocal interferometer and linear-scanning fiber-optic catheter for optical coherence tomography," *Opt. Lett.* **24**, 531-533 (1999).
150. P. Herz, Y. Chen, A. Aguirre, J. Fujimoto, H. Mashimo, J. Schmitt, A. Koski, J. Goodnow, and C. Petersen, "Ultrahigh resolution optical biopsy with endoscopic optical coherence tomography," *Opt. Express* **12**, 3532-3542 (2004).
151. V. X. D. Yang, M. Gordon, S.-j. Tang, N. Marcon, G. Gardiner, B. Qi, S. Bisland, E. Seng-Yue, S. Lo, J. Pekar, B. Wilson, and I. Vitkin, "High speed, wide velocity dynamic range Doppler optical coherence tomography (Part III): in vivo endoscopic

- imaging of blood flow in the rat and human gastrointestinal tracts," *Opt. Express* **11**, 2416-2424 (2003).
152. J. Sun, S. Guo, L. Wu, L. Liu, S.-W. Choe, B. S. Sorg, and H. Xie, "3D In Vivo optical coherence tomography based on a low-voltage, large-scan-range 2D MEMS mirror," *Opt. Express* **18**, 12065-12075 (2010).
153. T. Chen, N. Zhang, T. Huo, C. Wang, J.-g. Zheng, T. Zhou, and P. Xue, "Tiny endoscopic optical coherence tomography probe driven by a miniaturized hollow ultrasonic motor," *BIOMEDO* **18**, 086011-086011 (2013).
154. J. Mavadia, J. Xi, Y. Chen, and X. Li, "An all-fiber-optic endoscopy platform for simultaneous OCT and fluorescence imaging," *Biomed. Opt. Express* **3**, 2851-2859 (2012).
155. P. R. Herz, Y. Chen, A. D. Aguirre, K. Schneider, P. Hsiung, J. G. Fujimoto, K. Madden, J. Schmitt, J. Goodnow, and C. Petersen, "Micromotor endoscope catheter for in vivo, ultrahigh-resolution optical coherence tomography," *Opt. Lett.* **29**, 2261-2263 (2004).
156. P. H. Tran, D. S. Mukai, M. Brenner, and Z. Chen, "In vivo endoscopic optical coherence tomography by use of a rotational microelectromechanical system probe," *Opt. Lett.* **29**, 1236-1238 (2004).
157. W. Eickhoff and R. Ulrich, "Optical frequency domain reflectometry in single-mode fiber," *Applied Physics Letters* **39**, 693-695 (1981).
158. U. Glombitza and E. Brinkmeyer, "Coherent frequency-domain reflectometry for characterization of single-mode integrated-optical waveguides," *Lightwave Technology, Journal of* **11**, 1377-1384 (1993).
159. E. Brinkmeyer and U. Glombitza, "High-resolution coherent frequency-domain reflectometry using continuously tuned laser diodes," in *Optical Fiber Communication*, 1991 OSA Technical Digest Series (Optical Society of America, 1991), WN2.
160. B. Golubovic, B. E. Bouma, G. J. Tearney, and J. G. Fujimoto, "Optical frequency-domain reflectometry using rapid wavelength tuning of a Cr⁴⁺:forsterite laser," *Optics Letters* **22**, 1704-1706 (1997).
161. S. H. Yun, C. Boudoux, G. J. Tearney, and B. E. Bouma, "High-speed wavelength-swept semiconductor laser with a polygon-scanner-based wavelength filter," *Optics Letters* **28**, 1981-1983 (2003).
162. R. Huber, D. C. Adler, and J. G. Fujimoto, "Buffered Fourier domain mode locking: unidirectional swept laser sources for optical coherence tomography imaging at 370,000 lines/s," *Optics Letters* **31**, 2975-2977 (2006).
163. K. Totsuka, K. Isamoto, T. Sakai, A. Morosawa, and C. Chong, "MEMS scanner based swept source laser for optical coherence tomography," in 2010), 75542Q-75542Q-75545.
164. S. Gloor, A. H. Bachmann, M. Epitoux, T. von Niederhäusern, P. Vorreau, N. Matuschek, K. Hsu, M. Duelk, and C. Vélez, "High-speed miniaturized swept sources based on resonant MEMS mirrors and diffraction gratings," in 2013), 85712X-85712X-85717.
165. THORLABS, "O-Band Booster Optical Amplifier BOA1132S" (2011), retrieved <http://www.thorlabs.com/thorcat/19400/BOA1132S-SpecSheet.pdf>.

166. W. Y. Oh, S. H. Yun, B. J. Vakoc, G. J. Tearney, and B. E. Bouma, "Ultrahigh-speed optical frequency domain imaging and application to laser ablation monitoring," *Applied Physics Letters* **88**, - (2006).
167. D. C. Adler, "Applications of Fourier Domain Mode Locked lasers for optical coherence tomography imaging," Ph.D. Dissertation (Massachusetts Institute of Technology, 2009).
168. W. Wieser, B. R. Biedermann, T. Klein, C. M. Eigenwillig, and R. Huber, "Multi-Megahertz OCT: High quality 3D imaging at 20 million A-scans and 4.5 GVoxels per second," *Optics Express* **18**, 14685-14704 (2010).
169. E. J. Jung, C.-S. Kim, M. Y. Jeong, M. K. Kim, M. Y. Jeon, W. Jung, and Z. Chen, "Characterization of FBG sensor interrogation based on a FDML wavelength swept laser," *Opt. Express* **16**, 16552-16560 (2008).
170. L. Q. LLC, "High Speed Optical Tunable Filter" (2012), retrieved http://www.lambdaquest.com/PDF/LQ_TF.pdf.
171. D. C. Adler, S.-W. Huang, R. Huber, and J. G. Fujimoto, "Photothermal detection of gold nanoparticles using phase-sensitive optical coherence tomography," *Opt. Express* **16**, 4376-4393 (2008).
172. V. J. Srinivasan, D. C. Adler, Y. Chen, I. Gorczynska, R. Huber, J. S. Duker, J. S. Schuman, and J. G. Fujimoto, "Ultrahigh-Speed Optical Coherence Tomography for Three-Dimensional and En Face Imaging of the Retina and Optic Nerve Head," *Investigative Ophthalmology & Visual Science* **49**, 5103-5110 (2008).
173. Nokia, "Qt Development Framework 4.8" (2011), retrieved <http://doc-snapshot.qt-project.org/4.8/index.html>.
174. GNU, "GNU Lesser General Public License 2.1" (1999), retrieved <http://www.gnu.org/licenses/lgpl-2.1.html>.
175. W. W. W. Consortium, "Extensible Markup Language" (2013), retrieved <http://www.w3.org/XML/>.
176. Microsoft, "Slim Reader/Writer (SRW) Locks" (2013), retrieved [http://msdn.microsoft.com/en-us/library/windows/desktop/aa904937\(v=vs.85\).aspx](http://msdn.microsoft.com/en-us/library/windows/desktop/aa904937(v=vs.85).aspx).
177. Alazartech, "Alazartech ATS9360" (2013), retrieved http://www.alazartech.com/products/ATS9360_v_1_2a.pdf.
178. J. Richter and C. Nasarre, *Windows Via C/C++* (Microsoft Press, 2011).
179. A. W. Schaefer, J. J. Reynolds, D. L. Marks, and S. A. Boppart, "Real-time digital signal processing-based optical coherence tomography and Doppler optical coherence tomography," *Biomedical Engineering, IEEE Transactions on* **51**, 186-190 (2004).
180. J. Su, J. Zhang, L. Yu, H. G. Colt, M. Brenner, and Z. Chen, "Real-time swept source optical coherence tomography imaging of the human airway using a microelectromechanical system endoscope and digital signal processor," *Journal of Biomedical Optics* **13**, 030506-030506-030503 (2008).
181. T. E. Ustun, N. V. Iftimia, R. D. Ferguson, and D. X. Hammer, "Real-time processing for Fourier domain optical coherence tomography using a field programmable gate array," *Review of Scientific Instruments* **79**, - (2008).
182. G. Liu, J. Zhang, L. Yu, T. Xie, and Z. Chen, "Real-time polarization-sensitive optical coherence tomography data processing with parallel computing," *Applied Optics* **48**, 6365-6370 (2009).

183. K. Zhang and J. U. Kang, "Real-time 4D signal processing and visualization using graphics processing unit on a regular nonlinear-k Fourier-domain OCT system," *Optics Express* **18**, 11772-11784 (2010).
184. J. Li, P. Bloch, J. Xu, M. V. Sarunic, and L. Shannon, "Performance and scalability of Fourier domain optical coherence tomography acceleration using graphics processing units," *Applied Optics* **50**, 1832-1838 (2011).
185. K. Zhang and J. U. Kang, "Real-time numerical dispersion compensation using graphics processing unit for Fourier-domain optical coherence tomography," *Electronics Letters* **47**, 309-310 (2011).
186. Y. Jian, K. Wong, and M. V. Sarunic, "Graphics processing unit accelerated optical coherence tomography processing at megahertz axial scan rate and high resolution video rate volumetric rendering," *Journal of Biomedical Optics* **18**, 026002-026002 (2013).
187. T. K. Group, (2013), retrieved <http://www.khronos.org/files/opengl-quick-reference-card.pdf>.
188. Nvidia, (2013), retrieved <https://developer.nvidia.com/cg-toolkit>.
189. Microsoft, (2013), retrieved [http://msdn.microsoft.com/en-us/library/windows/desktop/bb509561\(v=vs.85\).aspx](http://msdn.microsoft.com/en-us/library/windows/desktop/bb509561(v=vs.85).aspx).
190. S. A. Boppart, B. E. Bouma, C. Pitris, G. J. Tearney, J. G. Fujimoto, and M. E. Brezinski, "Forward-imaging instruments for optical coherence tomography," *Optics Letters* **22**, 1618-1620 (1997).
191. L. Huo, J. F. Xi, Y. C. Wu, and X. D. Li, "Forward-viewing resonant fiber-optic scanning endoscope of appropriate scanning speed for 3D OCT imaging," *Optics Express* **18**, 14375-14384 (2010).
192. D. L. Wang, B. V. Hunter, M. J. Cobb, and X. D. Li, "Super-achromatic rapid scanning microendoscope for ultrahigh-resolution OCT imaging," *IEEE Journal of Selected Topics in Quantum Electronics* **13**, 1596-1601 (2007).
193. D. C. Adler, C. Zhou, T. H. Tsai, J. Schmitt, Q. Huang, H. Mashimo, and J. G. Fujimoto, "Three-dimensional endomicroscopy of the human colon using optical coherence tomography," *Optics Express* **17**, 784-796 (2009).
194. H. L. Fu, Y. X. Leng, M. J. Cobb, K. Hsu, J. H. Hwang, and X. D. Li, "Flexible miniature compound lens design for high-resolution optical coherence tomography balloon imaging catheter," *Journal of Biomedical Optics* **13**(2008).
195. P. H. Tran, D. S. Mukai, M. Brenner, and Z. P. Chen, "In vivo endoscopic optical coherence tomography by use of a rotational microelectromechanical system probe," *Opt. Lett.* **29**, 1236-1238 (2004).
196. A. R. Tumlinson, B. Povazay, L. P. Hariri, J. McNally, A. Unterhuber, B. Hermann, H. Sattmann, W. Drexler, and J. K. Barton, "In vivo ultrahigh-resolution optical coherence tomography of mouse colon with an achromatized endoscope," *Journal of Biomedical Optics* **11**(2006).
197. H. Wang, W. Kang, T. Carrigan, A. Bishop, N. Rosenthal, M. Arruda, and A. M. Rollins, "In vivo intracardiac optical coherence tomography imaging through percutaneous access: toward image-guided radio-frequency ablation," *Journal of Biomedical Optics* **16**(2011).

198. J. F. Xi, L. Huo, Y. C. Wu, M. J. Cobb, J. H. Hwang, and X. D. Li, "High-resolution OCT balloon imaging catheter with astigmatism correction," *Optics Letters* **34**, 1943-1945 (2009).
199. D. Wang, L. Fu, X. Wang, Z. Gong, S. Samuelson, C. Duan, H. Jia, J. S. Ma, and H. Xie, "Endoscopic swept-source optical coherence tomography based on a two-axis microelectromechanical system mirror," *Journal of Biomedical Optics* **18**, 086005-086005 (2013).
200. Kinetron, "Kinetron Micro Motor" (2013), retrieved http://www.kinetron.nl/cms/publish/content/downloadaddocument.asp?document_id=15.
201. W. A. Reed, M. F. Yan, and M. J. Schnitzer, "Gradient-index fiber-optic microprobes for minimally invasive in vivo low-coherence interferometry," *Optics Letters* **27**, 1794-1796 (2002).
202. Y. Kawase, K. Hoshino, R. Yoneyama, J. McGregor, R. J. Hajjar, I.-K. Jang, and M. Hayase, "In vivo volumetric analysis of coronary stent using optical coherence tomography with a novel balloon occlusion-flushing catheter: A comparison with intravascular ultrasound," *Ultrasound in Medicine & Biology* **31**, 1343-1349 (2005).
203. J. Evans and M. Rosenquist, "'F=ma' optics," *American Journal of Physics* **54**, 876-876 (1986).
204. J. Evans, "Simple forms for equations of rays in gradient-index lenses," *American Journal of Physics* **58**, 773-773 (1990).
205. V. Kim and G. J. Criner, "Chronic Bronchitis and Chronic Obstructive Pulmonary Disease," *American Journal of Respiratory and Critical Care Medicine* **187**, 228-237 (2013).
206. P. F. Adams, M. E. Martinez, and J. L. Vickerie, "Summary health statistics for the U.S. population: National Health Interview Survey, 2009. National Center for Health Statistics," *Vital Health Statistics* **10**, 1-115 (2010).
207. "Expert Panel Report 3 (EPR-3): Guidelines for the Diagnosis and Management of Asthma—Summary Report 2007," *The Journal of Allergy and Clinical Immunology* **120**, S94-S138 (2007).
208. W. Dorffel, I. Fietze, D. Hentschel, J. Liebetrueth, Y. Ruckert, P. Rogalla, K. Wernecke, G. Baumann, and C. Witt, "A new bronchoscopic method to measure airway size," *European Respiratory Journal* **14**, 783-788 (1999).
209. R. H. Brown, W. Wizeman, C. Danek, and W. Mitzner, "In vivo evaluation of the effectiveness of bronchial thermoplasty with computed tomography," *Journal of Applied Physiology* **98**, 1603-1606 (2005).
210. B. Schlansky, A. J. Dimarino, D. Loren, A. Infantolino, T. Kowalski, and S. Cohen, "A survey of oesophageal cancer: pathology, stage and clinical presentation," *Alimentary Pharmacology & Therapeutics* **23**, 587-593 (2006).
211. J. Jeon, E. G. Luebeck, and S. Moolgavkar, "Age effects and temporal trends in adenocarcinoma of the esophagus and gastric cardia (United States)," *Cancer Causes & Control* **17**, 971-981 (2006).
212. S. Law and J. Wong, "Changing disease burden and management issues for esophageal cancer in the Asia-Pacific region," *Journal of Gastroenterology and Hepatology* **17**, 374-381 (2002).

213. M. Conio, A. J. Cameron, A. Chak, S. Blanche, and R. Filiberti, "Endoscopic treatment of high-grade dysplasia and early cancer in Barrett's oesophagus," *The Lancet Oncology* **6**, 311-321 (2005).
214. H. C. Wolfsen, "Present Status of Photodynamic Therapy for High-Grade Dysplasia in Barrett's Esophagus," *Journal of Clinical Gastroenterology* **39**, 189-202 (2005).
215. M. I. Canto, "Barrett's esophagus," *Gastrointestinal endoscopy clinics of North America* **15**, 83-92 (2005).
216. N. J. Shaheen, "Advances in Barrett's Esophagus and Esophageal Adenocarcinoma," *Gastroenterology* **128**, 1554-1566 (2005).
217. K. K. Wang and R. E. Sampliner, "Updated Guidelines 2008 for the Diagnosis, Surveillance and Therapy of Barrett's Esophagus," *Am J Gastroenterol* **103**, 788-797 (2008).
218. J. J. G. H. M. Bergman, "Diagnosis and therapy of early neoplasia in Barrett's esophagus," *Current Opinion in Gastroenterology* **21**, 466-471 (2005).
219. M. Mino-Kenudson, S. Ban, M. Ohana, W. Puricelli, V. Deshpande, M. Shimizu, N. S. Nishioka, and G. Y. Lauwers, "Buried Dysplasia and Early Adenocarcinoma Arising in Barrett Esophagus After Porfimer-photodynamic Therapy," *The American Journal of Surgical Pathology* **31**, 403-409 (2007).
220. M. J. Cobb, J. H. Hwang, M. P. Upton, Y. Chen, B. K. Oelschlager, D. E. Wood, M. B. Kimmey, and X. Li, "Imaging of subsquamous Barrett's epithelium with ultrahigh-resolution optical coherence tomography: a histologic correlation study," *Gastrointestinal endoscopy* **71**, 223-230 (2010).
221. W. Kang, H. Wang, Y. Pan, M. W. Jenkins, G. A. Isenberg, A. Chak, M. Atkinson, D. Agrawal, Z. Hu, and A. M. Rollins, "Endoscopically guided spectral-domain OCT with double-balloon catheters," *Optics Express* **18**, 17364-17372 (2010).
222. M. V. Sivak Jr, K. Kobayashi, J. A. Izatt, A. M. Rollins, R. Ung-runyawee, A. Chak, R. C. K. Wong, G. A. Isenberg, and J. Willis, "High-resolution endoscopic imaging of the GI tract using optical coherence tomography," *Gastrointestinal Endoscopy* **51**, 474-479 (2000).
223. G. J. Tearney, M. E. Brezinski, J. F. Southern, B. E. Bouma, S. A. Boppart, and J. G. Fujimoto, "Optical biopsy in human gastrointestinal tissue using optical coherence tomography," *Am J Gastroenterol* **92**, 1800-1804 (1997).
224. V. X. D. Yang, S.-j. Tang, M. L. Gordon, B. Qi, G. Gardiner, M. Cirocco, P. Kortan, G. B. Haber, G. Kandel, I. A. Vitkin, B. C. Wilson, and N. E. Marcon, "Endoscopic Doppler optical coherence tomography in the human GI tract: initial experience," *Gastrointestinal Endoscopy* **61**, 879-890 (2005).
225. M. J. Suter, M. J. Gora, G. Y. Lauwers, T. Arnason, J. Sauk, K. A. Gallagher, L. Kava, K. M. Tan, A. R. Soomro, T. P. Gallagher, J. A. Gardecki, B. E. Bouma, M. Rosenberg, N. S. Nishioka, and G. J. Tearney, "Esophageal-guided biopsy with volumetric laser endomicroscopy and laser cautery marking: a pilot clinical study," *Gastrointestinal Endoscopy* **79**(2014).
226. B. J. Vakoc, M. Shishko, S. H. Yun, W.-Y. Oh, M. J. Suter, A. E. Desjardins, J. A. Evans, N. S. Nishioka, G. J. Tearney, and B. E. Bouma, "Comprehensive esophageal microscopy by using optical frequency-domain imaging (with video)," *Gastrointestinal Endoscopy* **65**, 898-905 (2007).

227. R. J. Xavier and D. K. Podolsky, "Unravelling the pathogenesis of inflammatory bowel disease," *Nature* **448**, 427-434 (2007).
228. S. J. Galli, M. Tsai, and A. M. Piliponsky, "The development of allergic inflammation," *Nature* **454**, 445-454 (2008).
229. C. L. Sears and D. M. Pardoll, "Perspective: Alpha-Bugs, Their Microbial Partners, and the Link to Colon Cancer," *Journal of Infectious Diseases* **203**, 306-311 (2011).
230. J. P. Abonia and M. E. Rothenberg, "Eosinophilic Esophagitis: Rapidly Advancing Insights," *Annual Review of Medicine* **63**, 421-434 (2012).
231. M. E. Rothenberg, "Biology and Treatment of Eosinophilic Esophagitis," *Gastroenterology* **137**, 1238-1249 (2009).
232. A. Mizoguchi, "Animal Models of Inflammatory Bowel Disease," in *Progress in Molecular Biology and Translational Science*, P. M. Conn, ed. (Academic Press, 2012), pp. 263-320.
233. H. B. Xue, H. H. Tan, W. Z. Liu, X. Y. Chen, N. Feng, Y. J. Gao, Y. Song, Y. J. Zhao, and Z. Z. Ge, "A pilot study of endoscopic spray cryotherapy by pressurized carbon dioxide gas for Barrett's esophagus," *Endoscopy* **43**, 379-385 (2011).
234. M. I. Canto, "8. Barrett's esophagus – A perfect target for cryo-ablation," *Cryobiology* **66**, 344-345 (2013).
235. J. Xi, A. Zhang, Z. Liu, W. Liang, L. Y. Lin, S. Yu, and X. Li, "Diffractive catheter for ultrahigh-resolution spectral-domain volumetric OCT imaging," *Opt. Lett.* **39**, 2016-2019 (2014).
236. Z. Hu and A. M. Rollins, "Fourier domain optical coherence tomography with a linear-in-wavenumber spectrometer," *Opt. Lett.* **32**, 3525-3527 (2007).
237. C. Inc., "A Compact, Reduced-Weight Telephoto Lens" (2012), retrieved http://www.canon.com/technology/canon_tech/explanation/ef.html.
238. J. Xi, Y. Chen, and X. Li, "Characterizing optical properties of nano contrast agents by using cross-referencing OCT imaging," *Biomedical Optics Express* **4**, 842-851 (2013).
239. J. K. Barton, J. B. Hoying, and C. J. Sullivan, "Use of microbubbles as an optical coherence tomography contrast agent," *Acad. Radiol.* **9**, S52-S55 (2002).
240. H. Cang, T. Sun, Z.-Y. Li, J. Chen, B. J. Wiley, Y. Xia, and X. D. Li, "Gold nanocages as contrast agents for spectroscopic optical coherence tomography," *Opt. Lett.* **30**, 3048-3050 (2005).
241. J. Chen, F. Saeki, B. J. Wiley, H. Cang, M. J. Cobb, Z.-Y. Li, L. Au, H. Zhang, M. B. Kimmey, X. D. Li, and Y. Xia, "Gold nanocages: bioconjugation and their potential use as optical imaging contrast agents," *Nano Lett.* **5**, 473-477 (2005).
242. A. M. Gobin, M. H. Lee, N. J. Halas, W. D. James, R. A. Drezek, and J. L. West, "Near-infrared resonant nanoshells for combined optical imaging and photothermal cancer therapy," *Nano Lett.* **7**, 1929-1934 (2007).
243. F. Hao, C. L. Nehl, J. H. Hafner, and P. Nordlander, "Plasmon resonances of a gold nanostar," *Nano Lett.* **7**, 729-732 (2007).
244. T. M. Lee, A. L. Oldenburg, S. Sitafalwalla, D. L. Marks, W. Luo, F. J.-J. Toublan, K. S. Suslick, and S. A. Boppart, "Engineered microsphere contrast agents for optical coherence tomography," *Opt. Lett.* **28**, 1546-1548 (2003).
245. T. S. Troutman, J. K. Barton, and M. Romanowski, "Optical coherence tomography with plasmon resonant nanorods of gold," *Opt. Lett.* **32**, 1438-1440 (2007).

246. C. Xu, D. Marks, M. Do, and S. Boppart, "Separation of absorption and scattering profiles in spectroscopic optical coherence tomography using a least-squares algorithm," *Opt. Express* **12**, 4790-4803 (2004).
247. S. E. Skrabalak, J. Chen, Y. Sun, X. Lu, L. Au, C. M. Cobley, and Y. Xia, "Gold Nanocages: Synthesis, Properties, and Applications," *Accounts of Chemical Research* **41**, 1587-1595 (2008).
248. L. M. Hanssen and K. A. Snail, "Integrating spheres for mid- and near infrared reflection spectroscopy," in *Handbook of Vibrational Spectroscopy*, J. M. Chalmers and P. R. Griffiths, eds. (John Wiley & Sons, Ltd, 2002), pp. 1175-1192.
249. N. Bosschaart, D. J. Faber, T. G. v. Leeuwen, and M. C. G. Aalders, "Measurements of wavelength dependent scattering and backscattering coefficients by low-coherence spectroscopy," *J. Biomed. Opt.* **16**, 030503-030503 (2011).
250. F. E. Robles and A. Wax, "Separating the scattering and absorption coefficients using the real and imaginary parts of the refractive index with low-coherence interferometry," *Opt. Lett.* **35**, 2843-2845 (2010).
251. T. G. van Leeuwen, D. J. Faber, and M. C. Aalders, "Measurement of the axial point spread function in scattering media using single-mode fiber-based optical coherence tomography," *IEEE J. Sel. Top. Quant.* **9**, 227-233 (2003).
252. J. M. Schmitt, A. Knüttel, A. Gandjbakhche, and R. F. Bonner, "Optical characterization of dense tissues using low-coherence interferometry," *P. Soc. Photo-Opt. Ins.* **1889**, 197-211 (1993).
253. W. Hergert and T. Wriedt, *The mie theory: basics and applications* (Springer, 2012).
254. B. T. Draine and P. J. Flatau, "Discrete-dipole approximation for scattering calculations," *J. Opt. Soc. Am. A* **11**, 1491-1499 (1994).
255. I. Corporation, "Intel FORTRAN Compilers" (2012), retrieved <http://software.intel.com/en-us/fortran-compilers>.
256. I. Corporation, "Intel Math Kernel Library" (2012), retrieved <http://software.intel.com/en-us/intel-mkl>.
257. T. S. Ralston, D. L. Marks, P. Scott Carney, and S. A. Boppart, "Interferometric synthetic aperture microscopy," *Nature Phys.* **3**, 129-134 (2007).
258. S. E. Skrabalak, L. Au, X. Li, and Y. Xia, "Facile synthesis of Ag nanocubes and Au nanocages," *Nat. Protocols* **2**, 2182-2190 (2007).
259. J. Xi, Y. Chen, Y. Zhang, K. Murari, M.-J. Li, and X. Li, "Integrated multimodal endomicroscopy platform for simultaneous en face optical coherence and two-photon fluorescence imaging," *Optics Letters* **37**, 362-364 (2012).
260. W. Denk, J. H. Strickler, and W. W. Webb, "Two-photon laser scanning fluorescence microscopy," in *Science*, (1990), pp. 73-76.
261. S. A. Boppart, "Multimodality microscopy of cell dynamics in three-dimensional engineered and natural tissues," in *Complex Medical Engineering, 2009. CME. ICME International Conference on*, (2009), 1-7.
262. S. Tang, T. B. Krasieva, Z. Chen, and B. J. Tromberg, "Combined multiphoton microscopy and optical coherence tomography using a 12-fs broadband source," in *Journal of Biomedical Optics*, (SPIE, 2006), p. 020502.
263. X. M. Liu, M. J. Cobb, Y. Chen, M. B. Kimmey, and X. D. Li, "Rapid-scanning forward-imaging miniature endoscope for real-time optical coherence tomography," *Opt. Lett.* **29**, 1763-1765 (2004).

264. M. T. Myaing, D. J. MacDonald, and X. D. Li, "Fiber-optic scanning two-photon fluorescence endoscope," *Opt. Lett.* **31**, 1076-1078 (2006).
265. K. Murari, Y. Zhang, S. Li, Y. Chen, M.-J. Li, and X. D. Li, "Compensation-free, all-fiber-optic, two-photon endomicroscopy at 1.55 μ m," *Opt. Lett.* **36**, 1299-1301 (2011).
266. Y. Chen and X. D. Li, "Dispersion management up to the third order for real-time optical coherence tomography involving a phase or frequency modulator," *Opt. Express* **12**, 5968-5978 (2004).
267. Y. P. Chen, T. G. Jabbour, and X. D. Li, "Bioconjugated ICG/Dox-Micellar Nanocapsules for Optical Molecular Imaging and Targeted Therapy," in *OSA Technical Digest (CD)* (Optical Society of America, 2010), BTuC6.
268. V. B. Rodriguez, S. M. Henry, A. S. Hoffman, P. S. Stayton, X. D. Li, and S. H. Pun, "Encapsulation and stabilization of indocyanine green within poly(styrene-alt-maleic anhydride) block-poly(styrene) micelles for near-infrared imaging," *Journal of Biomedical Optics* **13**, 014025-014010 (2008).
269. T. Klein, W. Wieser, C. M. Eigenwillig, B. R. Biedermann, and R. Huber, "Megahertz OCT for ultrawide-field retinal imaging with a 1050nm Fourier domain mode-locked laser," *Optics Express* **19**, 3044-3062 (2011).
270. T. Wang, W. Wieser, G. Springeling, R. Beurskens, C. T. Lancee, T. Pfeiffer, A. F. W. van der Steen, R. Huber, and G. v. Soest, "Intravascular optical coherence tomography imaging at 3200 frames per second," *Optics Letters* **38**, 1715-1717 (2013).
271. J. F. Xi, A. Zhang, Z. Liu, Y. S., and X. D. Li, "Diffractive Catheter for Ultrahigh-resolution Spectral-domain Volumetric OCT Imaging," *Optics Letters* **39**(2014).
272. B. T. Draine and P. J. Flatau, "User Guide to the Discrete Dipole Approximation Code DDSCAT 7.0" (2008), retrieved <http://arxiv.org/abs/0809.0337>.
273. I. Red Hat, "Cygwin" (2013), retrieved <http://www.cygwin.com/>.
274. M. Project, "MinGW" (2012), retrieved <http://mingw.org/>.

CURRICULUM VITAE

The Johns Hopkins University School of Medicine

Jiefeng Xi

09/27/2014

Name

Date of this version

Educational History:

Ph.D. expected	2014	Program in Biomedical Engineering Mentors: Xingde Li, Ph.D.	Johns Hopkins School of Medicine
Ph. D. student	2009	Bioengineering	University of Washington
M.S.	2005	Optical Engineering	Tsinghua University
B.S.	2002	Precision Instruments	Tsinghua University

Scholarships, fellowships, or other external funding:

Name	Source	Inclusive date	Amount
Siebel Scholar	Siebel Foundation	07/25/2013	\$35,000.00

Academic and other honors at Hopkins and elsewhere

Date	Name of the award	Source
04/2012	Best Student Poster Award	OSA
04/2012	Best Student Poster Award	OSA

Publications

1. A. Q. Zhang, **J. F. Xi**, W. X. Liang, T. Gao, X. D. Li, "Generic Pixel-wise Speckle Detection in Fourier-domain OCT Images," *Optics Letters*, 39, 4392-4395 (2014).
2. **J. F. Xi**, A. Q. Zhang, Z. Y. Liu, W. X. Liang, Lih Y. Lin, S. Y. Yu, X. D. Li, "Diffractive catheter for ultrahigh-resolution spectral-domain volumetric OCT imaging," *Optics Letters* 39, 2016-2019 (2014) .
3. J. Chen, **J. F. Xi**, Y. Tian, G. S. Bova, H. Zhang, "Identification, prioritization and evaluation of glycoproteins for aggressive prostate cancer using quantitative glycoproteomics and antibody-based assays on tissue specimens," *Proteomics*, 13, 2268-77 (2013)
4. **J. F. Xi**, Y. P. Chen, X. D. Li, "Characterizing the Optical Properties of Nano Contrast Agents by Using Self-referencing OCT Imaging," *Biomedical Optics Express*, 4, 842-851 (2013).

5. J. Mavadia*, **J. F. Xi***, Y. P. Chen, X. D. Li, "An all-fiber-optic endoscopy platform for simultaneous OCT and fluorescence imaging," *Biomedical Optics Express* 3, 2851-2859 (2012). (*: equal contribution)
6. Y. Zhang, M. L. Akins, K. Murari, **J. F. Xi**, M. J. Li, K. Luby-Phelps, M. Mahendroo, X. D. Li, "A compact fiber-optic SHG scanning endomicroscope and its application to visualize cervical remodeling during pregnancy," *Proceedings of the National Academy of Sciences* 109, 12878-12883 (2012).
7. **J. F. Xi**, Y. Chen, Y. Zhang, K. Murari, M. J. Li, X. D. Li, "Integrated multimodal endomicroscopy platform for simultaneous en face optical coherence and two-photon fluorescence imaging," *Optics Letters* 37, 362-364 (2012).
8. K. Murari J. Mavadia, **J. F. Xi**, X. D. Li, "A self-starting, self-regulating Fourier domain mode locked fiber laser for OCT imaging," *Biomedical Optics Express* 2, 2005-2011 (2011).
9. Y. Wu, Y. Zhang, **J. F. Xi**, M. J. Li, X. D. Li, "Fiber-optic nonlinear endomicroscopy with focus scanning by using shape memory alloy actuation," *Journal of Biomedical Optics* 15, 060506-3 (2010).
10. Y. Wu, **J. F. Xi**, L. Huo, J. Padvorac, E. J. Shin, S. A. Giday, A. M. Lennon, M. I. Canton, J. H. Hwang, X. D. Li, "Robust high-resolution fine OCT needle for side-viewing interstitial tissue imaging," *IEEE Journal of Selected Topics in Quantum Electronics* 16, 863-869 (2010) (invited paper).
11. L. Huo, **J. F. Xi**, Y. Wu, X. D. Li, "Forward-viewing resonant fiber-optic scanning endoscope of appropriate scanning speed for 3D OCT imaging," *Optics Express* 18, 14375-14384 (2010).
12. **J. F. Xi**, L. Huo, J. Li, X. D. Li, "Generic real-time uniform K-space sampling method for high-speed swept-Source optical coherence tomography," *Optics Express* 18, 9511-9517 (2010).
13. **J. F. Xi**, L. Huo, Y. C. Wu, M. J. Cobb, J. H. Hwang, X. D. Li, "High-resolution OCT balloon imaging catheter with astigmatism correction," *Optics Letters* 34, 1943-1945 (2009).
14. Y. Wu, Y. Leng, **J. F. Xi**, X. D. Li, "Scanning all-fiber-optic endomicroscopy system for 3D nonlinear optical imaging of biological tissues," *Optics Express* 17, 7907-7915 (2009).
15. Y. Wu, **J. F. Xi**, M. J. Cobb, X. D. Li, "Scanning fiber-optic nonlinear endomicroscopy with miniature aspherical compound lens and multimode fiber collector," *Optics Letters* 34, 953-955 (2009).
16. J. Chen, D. Wang, **J. F. Xi**, L. Au, A. Siekkinen, A. Warsen, Z. Y. Li, H. Zhang, Y. N. Xia, X. D. Li, "Immuno gold nanocages with tailored optical properties for targeted photothermal destruction of cancer cells," *Nano Letters* 7, 1318-1322 (2007).
17. **J. F. Xi**, Q. Li, J. Wang, "Numerical simulation of Bessel beams by FDTD employing the superposition principle," *Optik* 118, 315-318 (2007).
18. Q. Li, J. Wang, J. Xu, **J. F. Xi**, G. Jin, "Experimental Research on Focusing Property of Radially Polarized Beam Based on Solid Immersion Lens," *Optical Review*, 13, 283-287 (2006).

1. J. Mavadia, **J. F. Xi** and X. D. Li, "Multi-modal Endoscopy: OCT and Fluorescence," in *Optical Coherence Tomography: Technology and Applications*, 2nd edition, Wolfgang Drexler, James G. Fujimoto, in press

First Author Oral and Poster Presentations

1. **J. F. Xi**, R. Yung, W. Mitzner, R. H. Brown, X. D. Li, "Real-time Assessment of Dynamics in Lower Airway Using High Speed Endoscopic OCT," in Oral presentation, BioS, SPIE Photonics West, San Francisco, CA (2014), 8927-38.
2. **J. F. Xi**, Y. P. Chen, X. D. Li, "Characterization of Optical Properties of OCT Contrast Agents by Using Self-referencing OCT Algorithm," in Oral presentation, BioS, SPIE Photonics West, San Francisco, CA (2013), 8571-38.
3. **J. F. Xi**, W. Mitzner, R. Brown, R. Yung, X. D. Li, "Real-time Three-Dimensional Dynamic Imaging of Lower Airway Using Swept Source Optical Coherence Tomography," in Poster presentation and paper, OSA Biomedical Optics Topical Meeting, Miami, FL (2012), BTu3A.93.
4. **J. F. Xi**, R. Yung, W. Mitzner, R. Brown, X. D. Li, "Real-time Three-dimensional Dynamic Imaging of Airways Reactivity Using Optical Coherence Tomography," in Oral presentation, BioS, SPIE Photonics West, San Francisco, CA (2012), 8213-08.
5. **J. F. Xi**, Y. Chen, J. Mavadia, X. D. Li, "Gold nanocages with tunable surface plasmon resonance peaks as contrast agents for optical coherence tomography," in Poster presentation, NIH Inter-Institute Workshop on Optical Diagnostic and Biophotonic Methods from Bench to Bedside 2011, Bethesda, MD (2011), NIH100-89.
6. **J. F. Xi**, Y. Zhang, L. Huo, X. D. Li, "Integrated en face Optical Coherence Endomicroscopy and Two-photon Fluorescence Endomicroscopy for Simultaneous Multimodal Imaging," in Oral presentation, BioS, SPIE Photonics West, San Francisco, CA (2011), 7889-42.
7. **J. F. Xi**, L. Huo, X. D. Li, "3D FD-OCT Imaging with Resonant Fiber-optic Scanning Endoscope in a Rectangular Field of View," in Oral presentation, BioS, SPIE Photonics West, San Francisco, CA (2011), 7889-46.
8. **J. F. Xi**, L. Huo, J. S. Li, and X. D. Li, "Real-time Calibration for High-speed Swept-Source OCT," in Poster presentation and paper, OSA Biomedical Optics Topical Meeting, Miami Beach, FL (2010), JMA42.
9. **J. F. Xi**, M. J. Cobb, L. Huo, K. Hsu, J. H. Hwang, X. D. Li, "Improved Optics Design for High-resolution OCT Balloon Imaging Catheter," in Oral presentation, BioS, SPIE Photonics West, San Jose, CA (2009), 7168-34.
10. **J. F. Xi**, H. L. Fu, Y. Leng, M. J. Cobb, D. J. MacDonald, J. H. Hwang, X. D. Li, "High-resolution Ballon Catheter based on Swept Source OCT for Systematic Esophagus Imaging," in Oral presentation, BioS, SPIE Photonics West, San Jose, CA (2008), 6847-09.

Patents

1. X. D. Li, **J. F. Xi**, L. Huo, Y. Wu, and J. H. Hwang, "Astigmatism correction on high-resolution side-viewing fiber-optic catheter," US Patent Pending

2. X. D. Li, **J. F. Xi**, L. Huo, “Generic Real-time Uniform K-space Sampling Method for High-speed Swept-Source Optical Coherence Tomography,” US Patent Pending
3. X. D. Li, **J. F. Xi**, J. Mavadia, “All-fiber-optic multimodal endoscope/catheter imaging platform for simultaneous optical coherence tomography and fluorescence imaging,” US Patent Pending
4. X. D. Li, A. Q. Zhang, **J. F. Xi**, “Methods for Color Corrected OCT Imaging Endoscope/ Catheter to Achieve High-resolution,” US Patent Pending
5. X. D. Li, A. Quinones-Hinojosa, E. McVeigh, K. Chaichina, C. Kut, **J. F. Xi**, “Quantitative Tissue Property Mapping for Real-time Tumor Detection and Interventional Guidance,” US Patent Pending